High power continuous-wave frequency conversion in the visible and ultraviolet using diamond

By

Hadiya Jasbeer

A thesis submitted to Macquarie University

for the degree of Doctor of Philosophy

Department of Physics and Astronomy

May 2017

MACQUARIE
University
SYDNEY·AUSTRALIA

Typeset in LaTeX 2_ε.

Except where acknowledged in the customary manner, the material presented in this thesis is, to the best of my knowledge, original and has not been submitted in whole or part for a degree in any university.

Hadiya Jasbeer

Acknowledgements

I greatly acknowledge the power of God almighty without whose will; I could not have completed this project.

Firstly, I would like to thank my supervisor Rich Mildren, a diamond laser wizard, whose immense support helped me all throughout the project. I don't think that I would have completed the project and submitted my thesis without his constant encouragement and help. Thank you so much, Rich, for the time you have invested in my project and for enhancing my knowledge. You are truly a great mentor and I feel really lucky to have you as my supervisor. I would like to thank my co-supervisor Robert Williams, for his generous help and contributions in all the stages of my project. He was the person to whom I constantly approach, probably every day, whenever I encounter any problems in my project. As I am his first student, I am sure he would be equally happy and thrilled at my successful thesis completion. All I can say to Rob is big thanks from the bottom of my heart, as I have no words to express my gratitude towards you. The next person I would like to thank is Aaron MacKay, whom I used to approach for anything and everything all throughout my project. He has facilitated everything in the lab, from equipment to ideas. Thank you very much, Aaron, for your constant help and encouragement. I would also like to thank Ondrej Kitzler, a man with lots of ideas, for setting up the platform for building my thesis. His positive attitude towards approaching any scientific problem and constant pouring of ideas has helped me immensely in completing my experiments. I always get a confidence and positive energy after having a discussion with him. Big thanks to Ondra for his help, encouragement, and feedbacks all throughout my project.

I must give special thanks to Chris Baldwin for investing his time to edit my thesis. He was always welcoming and had spent a lot of time in reading my thesis and editing it even

in the midst of his busy schedule. Many thanks to Soumya, for being with me inside and outside the academia. She was the person who was there with me for more than 10 years and I would cherish each and every moment that I had spent with her. I should also thank Oliver Lux, for his cheerful smile, positive energy, and valuable discussions which helped me a lot in my project.

Outside the diamond group, I would like to thank Jipeng Lin, for helping me in Matlab coding during my initial period of PhD and Krystyna Drozdowicz-Tomsia for her assistance with the Raman microscope. I must also thank Andrew Lee for giving me ideas as well as necessary equipment for the intracavity doubling experiments. I extend my sincere thanks to Sandhya Clement for her supportive and encouraging words during my stressful days of PhD. Also, many thanks to Vineeth Benyamin, who is doing his PhD in UNSW, for helping me in editing my thesis.

Now I would like to thank the most important person in my personal as well as professional life, my better half, Jasbeer. He had to sacrifice his professional life and had to leave his job back in India to accompany me to Sydney for my studies. The stress he had undergone as a result of it cannot be expressed in words. Thank you so much for being with me and sharing my feelings at every point in my life. Next, I would like to thank my father V.A.M. Ashrof and my mother Aneesa. Being from a middle-class family, they literally sacrificed their life for upbringing me and to give me the best education. It is all because of their efforts and prayers that I could reach up to what I am now. Even during my PhD period, my father used to spend the time to collect academic papers and books which are relevant to my field. My mother's prayers and encouraging words were the one of the major motivation for me to complete my studies. Many thanks to my brother Hafis Rahman for being my companion to share my thoughts and feelings. He gave me an immense amount of confidence for my life inside and outside academia. I would also like to thank my father in law Musthafa Azeez and my mother in law Amina Musthafa for their prayers and support.

Last but definitely not the least I would like to extend my thanks and love to our kid who started growing inside me when I started writing my thesis. Both of us were writing the thesis together and the mental interaction with him/her was the major source of motivation to complete the thesis. Now eagerly waiting for the time to welcome him/her.

Hence, this thesis is the final output of help and support I have received from a lot of people, the most important ones are mentioned here. But I am sure there are a lot more

people who have directly and indirectly contributed to my thesis. Thank you all!

Finally, let me dedicate this thesis to my husband Jasbeer and our cute little kid.

Abstract

Solid-state Raman lasers are a convenient technology for shifting the wavelength of conventional lasers to exotic wavelengths with enhanced brightness. Recently, diamond has emerged as an outstanding Raman medium due to its capacity for power handling with demonstrations of very high output powers (hundreds of watts) in the continuous wave regime. To date, these demonstrations have been performed in the near-infrared. However, there is demand for continuous high brightness output at shorter wavelengths (visible and UV). This thesis aims to address this challenge by intracavity nonlinear frequency mixing.

As nonlinear mixing is a polarization dependent process, the polarization behaviour of the Raman laser is critical to efficient operation. Thus as a first step, this thesis investigates the polarization properties of external cavity diamond Raman lasers including a detailed investigation of anomalous polarization effects that had been previously reported.

In-grown stress-induced birefringence in the diamond is identified as critical to the polarization behaviour. Birefringence was characterized using Mueller polarimetry, a technique that provides a complete description of the Mueller matrix. Surprisingly, substantial circular retardance is observed in some locations of the sample and of sufficient magnitude to induce errors in measurements obtained using more standard polarimetric techniques such as Metripol. The analysis finds that the most significant parameter influencing the laser performance is the linear birefringence axis direction. This parameter is found to dictate the threshold for laser operation and the polarization of the Stokes output. These outcomes provide a firm basis for selecting crystals, optimizing the beam location in the crystal and optimizing the input pump polarization.

The knowledge was used to develop a high power intracavity frequency doubled CW

diamond Raman laser operating in quasi-CW mode. Using an external cavity Raman configuration and 1064 nm pumping, a 620 nm laser of output power 30 W and M^2<1.1, parameters that are difficult to achieve presently using any other laser technology. The critical design parameters that affects the visible conversion efficiency was evaluated experimentally. Furthermore, a model was developed to predict design parameters for optimum laser performance and power scaling.

The concepts were also adapted to a DRL pumped at 532 nm. First Stokes output in the yellow (573 nm) was demonstrated with 15 W and 22.7% conversion efficiency. A model for the laser is presented to optimize efficiency and further increase power. The results were used to predict the design for deep-UV generation, a wavelength range that is otherwise very challenging to generate with high power in the CW regime.

Contents

1

Introduction

With the advent of the first laser in 1960 by Theodore Maiman [1], lasers have become an integral part of the modern world, with applications ranging from bar code readers and media disc players to communication, sensors, military equipment, medical diagnostics and therapeutics. Over the last five decades, various laser technologies have been developed based on gas, liquid, and solid-state gain media covering wavelengths ranging from deep ultraviolet (UV) to far infrared (IR) in discrete as well as continuously tunable wavelengths. These lasers operate over a wide range of timescales, from pulsed (with pulse duration less than a femtosecond) to the continuous wave (CW) regime, with varying powers and energies. Among these technologies, solid-state lasers are preferred over fluid-based lasers as they are practically more convenient to handle and are generally more compact. The most widely used solid-state lasers are based on glass/crystalline host materials doped with rare-earth or transition metal ions [2, 3] generating high average powers and/or high pulse energies and high beam brightness from ultrashort pulses to continuous wave output with low production and maintenance cost.

CW lasers are often necessary for applications where uninterrupted and highly monochromatic radiation are required. They have a wide range of applications such as in spectroscopy, flow cytometry, atom cooling, remote sensing, laser inspection, material processing, forensics, laser displays, and medical diagnostics and treatments. The first CW laser was demonstrated in 1961 using a He-Ne gas mixture as the gain medium and emitting at 1153 nm [4]. A year later, the first visible CW laser, emitting at 633 nm, was demonstrated using the same gain medium [5]. Since then, the major thrust has shifted towards developing efficient and powerful CW lasers operating over a wide range of wavelengths. The 1960s witnessed some other notable developments including argon ion lasers, CO_2 lasers, dye lasers, Nd:YAG lasers, and semiconductor lasers [6–10]. Gas/fluid lasers were initially the most successful owing to their better thermal management capability. However, owing to their practical difficulties, the research focus has progressively shifted towards solid-state laser technologies.

Although many solid-state technologies have been investigated, there is still an ongoing need for high power and high brightness sources at many wavelengths. For example, semiconductor diode lasers cover a wide wavelength range from UV to mid-IR, but suffer from poor beam quality at high powers. This is a result of the fact that power scaling involves increasing emitting apertures size and by using diode emitter arrays, thus leading to highly divergent output. On the other hand, solid state lasers, including fiber lasers offer high output powers with good beam quality but have a limited range of wavelengths [11]. Many of the above mentioned CW laser applications are not adequately fulfilled by current sources. Hence there is a need for new technology that simultaneously address both the wavelength diversity and brightness, especially in the visible and ultraviolet (UV) spectral region.

1.1 Frequency conversion of CW lasers

Currently, nonlinear frequency conversion is relied upon as the main tool for generating the wavelengths that are otherwise difficult to achieve using conventional laser technologies. Nonlinear frequency conversion is the result of interaction of a light wave with the material, leading to changes in the spatial and temporal distribution of electric charges. The magnitude of induced polarization (dipole moment per unit volume) depends on the applied electric field ($\mathbf{E}$) and optical susceptibilities by [12],

$$\mathbf{P}(t) = \chi^{(1)}\mathbf{E}(t) + \chi^{(2)}\mathbf{E}^2(t) + \chi^{(3)}\mathbf{E}^3(t) + ... \tag{1.1}$$

where $\chi^{(1)}$ is the linear susceptibility, $\chi^{(2)}$ and $\chi^{(3)}$ are the second-order and third-order non-linear optical susceptibilities. Here, $\chi^{(1)}$ is a second-rank tensor, $\chi^{(2)}$ is a third-rank tensor, $\chi^{(3)}$ is a fourth rank tensor and so on. For large electric field strengths, the second and third terms become significant giving rise to a wide range of nonlinear optical phenomena. The second term gives rise to second-order nonlinear effects such as second harmonic generation (SHG), sum frequency generation (SFG) and difference frequency generation (DFG) whereas the third term gives rise to third-order nonlinear optical effects such as third harmonic generation, intensity-dependent refractive index (also called optical Kerr effect), saturable absorption, two-photon absorption, stimulated Raman scattering (SRS) and stimulated Brillouin scattering (SBS). While third-order nonlinearity occurs in all the materials, second-order nonlinearity is exhibited only in non-centrosymmetric crystals.

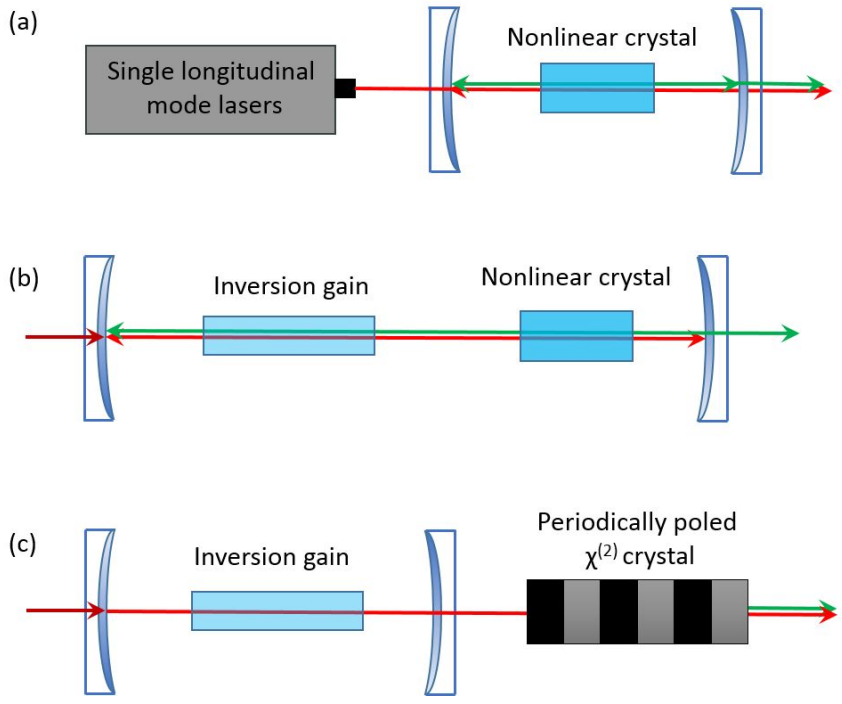

Figure 1.1: Basic concepts for nonlinear frequency conversion in the CW regime: (a) external cavity resonant enhancement, (b) intracavity, and (c) single pass conversion using periodically-poled crystals.

Nonlinear frequency conversion in the CW regime is challenging because of the large

intensities needed to drive the nonlinear process. Hence, resonant schemes are usually employed, such as external resonant cavity frequency conversion [13–19], and intracavity frequency conversion [20–25] in which the fundamental and/or frequency shifted beams are resonated in the cavity (Fig. 1.1 (a) and (b)). In an external cavity, the mirror spacing requires precise locking to provide a resonance with the laser frequency, so the technique is only suitable for single longitudinal mode pump lasers precisely tuned to the cavity mode. The intracavity frequency conversion technique, which utilizes a single resonator for both the fundamental as well as the frequency converted beams, provides an approach for efficient conversion of multi-mode pump lasers. Another approach is the use of periodically-poled materials (Fig.1.1 (c)) which provide a method to phase-match in materials and for propagation directions that yield a high nonlinearity [26–33]. Due to their high effective nonlinear coupling, periodically-poled crystals enable efficient conversion of external beams without resonant enhancement.

From a commercial point of view, the most widely used and simplest approach is based on intracavity SHG of rare-earth based crystalline lasers. Many laser pointers and visible CW lasers for ophthalmology, for example, are based on SHG of Nd^{3+} doped solid state lasers using crystals such as lithium triborate (LBO) and Potassium titanyl phosphate (KTP). The concept has been readily extended to frequency tripling and quadrupling to generate a range of discrete wavelengths [34–39].

Sum frequency mixing is also employed for frequency shifting rare-earth doped crystalline lasers. For example, 50 W of 589 nm laser was developed from SFG of 1064 nm and 1320 nm outputs from separate Nd:YAG lasers using LBO crystal [40, 41] for applications in laser-guide stars. However, these approaches provide only a limited range of new wavelengths according to the available pump wavelengths and their sum frequency combinations.

Optical parametric oscillators (OPOs) offer the important property of shifting to longer wavelengths and provide wide wavelength tunability ranging from blue to far-IR spectral regions covering almost the entire visible spectrum [42–49]. However, like SHG and SFG, these systems require strict phase-matching conditions and temperature stability for its operation and hence are more sophisticated.

A significant development in exploring a wide range of wavelengths is the vertical external cavity surface emitting lasers (VECSEL) that generate wavelengths ranging from blue to red up to 20 W in the yellow region [21, 50] and up to 64 W in the green [51]. However, obtaining

good beam-quality at higher powers is still a challenge.

Power scaling in these systems based on the $\chi^{(2)}$ nonlinearity is challenging as stability and efficiency are influenced by an effect called thermal dephasing. Although the nonlinear optical crystals used are ideally non-absorbing, small amounts of absorption become important as the heating of the crystal perturbs the relative phase of the intensity fields (phase-matching), which is critical to achieve high conversion efficiency [27, 29, 30]. In addition, the beam quality is difficult to maintain at higher powers [26, 52].

1.2 CW Raman lasers

Raman lasers, based on SRS, are another important technology for frequency conversion, where the pump photons interact with the material optical phonons to generate Stokes photons frequency shifted by the phonon frequency ω_r, as shown in Fig. 1.2. The process is considered to be automatically phase-matched as the phase mismatch between the pump and Stokes photons are taken up by the optical phonons (further discussed in Sec 1.1.2), thus making the process insensitive to temperature and angle. The principle of automatic phase-matching forms the basis for Raman beam clean-up, where an aberrated pump beam generates a diffraction limited Stokes beam. The process also allows the generation of higher-order Stokes via cascading of lower order Stokes photons.

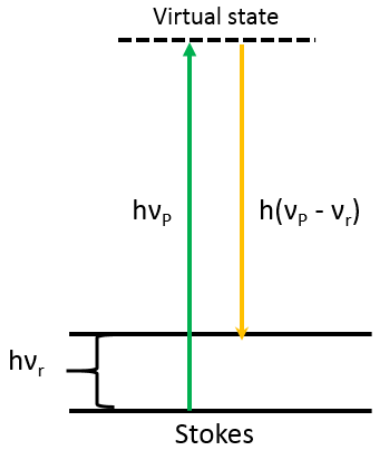

Figure 1.2: Energy level diagram of Raman sacttering.

1.2.1 Stimulated Raman scattering

Raman scattering was first theoretically predicted by Smekal *et al.* in 1923 [53] and was first observed by Raman and Krishnan in 1928 [54]. SRS was first observed by Woodbury and Ng in 1962 [55] of Hughes Aircraft Company while working with a pulsed ruby laser. Eckhardt *et al.* gave the explanation for the new line observed, as the Raman line of the NO_2 functional group from nitrobenzene in the Kerr cell used for Q-switching the ruby laser [56]. Since then, many scientists have contributed to the theoretical description of SRS [57–60].

The theory of SRS will be briefly introduced here in preparation for developing the concepts used to model CW Raman laser operation in this thesis. A quantum mechanical treatment of Raman scattering was performed by Penzkofer *et al.* [57] by describing the physical system as a Hamiltonian consisting of components representing the molecular system H_{m}, electromagnetic field H_{em} and the interaction between the molecular vibration and the electromagnetic field H_{int}. The interaction of a quantized electromagnetic field with a two energy level quantum system results in Raman scattering.

The interaction of the electromagnetic field with the material induces a polarization which is proportional to the dipole moment p and the number of molecules N_0. The induced dipole moment is

$$p\left(z,t\right)=\alpha E\left(z,t\right), \tag{1.2}$$

and the polarization vector is

$$P=N_0\alpha E\left(z,t\right), \tag{1.3}$$

where E is the electric field and the molecular polarizibility α is expanded as a function of the local coordinate q according to Placzek [61],

$$\alpha=\alpha_0+\frac{\partial\alpha}{\partial q}q+.... \tag{1.4}$$

When an electromagnetic field interacts with the material, the molecule oscillates thereby periodically changing the polarizability. This results in the modulation of refractive index in time ($n\left(t\right)=\epsilon\left(t\right)^{1/2}=\left[1+4\pi N\alpha\left(t\right)\right]^{1/2}$) of the coherently oscillating molecules resulting in frequency side bands separated by the resonant frequency of the oscillator ω_{r}, which results in Stokes and anti-Stokes frequency shifts.

The total scattered Stokes generation rate is the difference between the number of Stokes photons generated at the expense of the pump photon and the reverse process of loss of Stokes photons and the generation of pump photons [57],

$$\frac{dm_{\mathrm{S}}}{dt} = N\left(\frac{\partial\alpha}{\partial q}\right)^2 \frac{4\pi^3}{n_{\mathrm{P}} n_{\mathrm{S}}^2 mc} I_{\mathrm{P}} \sum_{k_{\mathrm{S}}} \frac{\omega_{\mathrm{S}}}{\omega_{\mathrm{r}}} \left(\mathbf{e_P}.\mathbf{e_S}\right)^2 \left(1 + m_{\mathrm{S}} + m_{\mathrm{m}}\right) \delta\left(\omega_{\mathrm{S}} - \omega_{\mathrm{P}} + \omega_{\mathrm{r}}\right), \tag{1.5}$$

where $m_{\mathrm{P,S,m}}$ are the occupation numbers for the pump, Stokes mode and phonon vibration, $N = N_0/V$; N_0 is the number of molecules in the interaction volume V, I_{P} is the pump intensity $I_{\mathrm{P}} = \left(\frac{\hbar\omega_{\mathrm{P}} c}{n_{\mathrm{P}} V}\right) \sum_{k_{\mathrm{P}}} m_{\mathrm{P}}$, $\omega_{\mathrm{P,S,r}}$ are the angular frequencies of pump, Stokes and phonon vibration and $e_{\mathrm{P,S}}$ are the polarization vectors of pump and Stokes.

Equation. 1.5 consists of three terms. The first term (with the 1 in the bracket) corresponds to the spontaneous Raman scattering. The second term (proportional to m_{S}) corresponds to growth in the Stokes mode due to stimulated Raman scattering. The third term, which corresponds to the material vibration, is small due to large damping of the optical phonons and can generally be neglected.

From Eq. 1.5, the rate of growth of an individual Stokes photon with wave number k_{S} is [57]

$$\frac{\mathrm{d}m\left(k_{\mathrm{S}}\right)}{dt} = N\left(\frac{\partial\alpha}{\partial q}\right)^2 \frac{4\pi^3}{n_{\mathrm{P}} n_{\mathrm{S}}^2 mc} I_{\mathrm{P}} \sum_{k_{\mathrm{S}}} \frac{\omega_{\mathrm{S}}}{\omega_{\mathrm{r}}} \left(\mathbf{e_P}.\mathbf{e_S}\right)^2 \left(1 + m\left(k_{\mathrm{S}}\right)\right) \rho\left(\omega_{\mathrm{S}} - \omega_{\mathrm{P}} + \omega_{\mathrm{r}}\right), \tag{1.6}$$

where $\rho\left(\omega\right)$ is the spectral distribution determined by the molecular transition and linewidth of the pump laser. For a homogeneous broadening of the molecular transition and narrow linewidth pump laser, the spectral distribution $\rho\left(\omega\right)$ is expected to be Lorentzian [57],

$$\rho\left(\omega_{\mathrm{S}} - \omega_{\mathrm{P}} + \omega_{\mathrm{r}}\right) = \frac{\Gamma/\pi}{\left(\omega_{\mathrm{S}} - \omega_{\mathrm{P}} + \omega_{\mathrm{r}}\right)^2 + \Gamma^2}. \tag{1.7}$$

where Γ denotes the linewidth which is inversely proportional to the dephasing time T_2 of the physical system. From Eqs. 1.6 and 1.7, it is seen that the growth of Stokes photons depends on the frequency of the Stokes photons and the linewidth Γ. When the occupation number $m\left(k_{\mathrm{S}}\right) \gg 1$, an exponential growth of the Stokes photons is predicted by Eq. 1.6. The maximum small-signal gain g_{S} for Raman scattering is obtained at the centre of the Raman line ($\omega_{\mathrm{S}} = \omega_{\mathrm{P}} - \omega_{\mathrm{r}}$) [57],

$$g_S = N\left(\frac{\partial\alpha}{\partial q}\right)^2 \frac{4\pi^2\omega_S}{n_P n_S c^2 m\omega_r\Gamma}. \tag{1.8}$$

Thus, g_S is proportional to the material parameter $\left(\frac{\partial\alpha}{\partial q}\right)^2$ and T_2. Also, g_S depends on the wavelength; higher gain is expected for shorter Stokes wavelengths.

From Eq. 1.6, the rate of growth of Stokes photons depends on the dot product of pump and Stokes polarization vectors, which is valid in the case of a two energy level molecular gas system. However, in general, the polarizability described by Eq. 1.4 is a tensor (the Raman tensor, $R = \frac{d\alpha}{dq}$) with off-diagonal elements according to the symmetry of the mode of vibration. In this general case, the Raman gain coefficient is,

$$g_S = \frac{4\pi^2 N\omega_S}{n_S n_P c^2 m\omega_r\Gamma}(e_P R e_S)^2. \tag{1.9}$$

1.2.2 Raman laser intensity equations

Initially the Stokes power increases linearly due to spontaneous scattering and when a sufficient number of Stokes photons are present, growth becomes exponential due to SRS with the small-signal Raman gain given by Eq. 1.9. Once the number of Stokes photons are large, the dynamics may be readily described by a classical treatment of electromagnetic field [12]. Here the vibrational mode is described as a simple harmonic oscillator with resonant frequency ω_r and damping constant γ due to the influence of the pump laser field. The equation of motion for the molecular vibration is [12]

$$\frac{d^2q}{dt^2} + 2\gamma\frac{dq}{dt} + \omega_r^2 q = \frac{F(t)}{m}, \tag{1.10}$$

where $F(t)$ is the force inducing the molecular vibration and m is the reduced mass. When both pump and Stokes fields are present, the total electric field is written as

$$E(z,t) = A_P \exp\left[i\left(k_P z - \omega_P t\right)\right] + A_S \exp\left[i\left(k_S z - \omega_S t\right)\right] + c.c, \tag{1.11}$$

and the amplitude of the molecular vibration is [12]

$$q(\omega_{PS}) = \frac{\left(\frac{\partial\alpha}{\partial q}\right) A_P A_S^*}{m\left(\omega_r^2 - \omega_{PS}^2 - 2i\omega_{PS}\gamma\right)}, \tag{1.12}$$

where $\omega_{PS} = \omega_P - \omega_S$. From Eq. 1.3, the nonlinear part of the polarization is given by,

$$P^{\mathrm{NL}}(z,t) = N_0\left(\frac{\partial\alpha}{\partial q}\right)\left[q\left(\omega_{\mathrm{PS}}\right)e^{i(Kz-\omega_{\mathrm{PS}}t)} + c.c\right]\left[A_{\mathrm{P}}e^{i(k_{\mathrm{P}}z-\omega_{\mathrm{P}}t)} + A_{\mathrm{S}}e^{i(k_{\mathrm{S}}z-\omega_{\mathrm{S}}t)}\right], \quad (1.13)$$

where $K = k_{\mathrm{P}} - k_{\mathrm{S}}$. The nonlinear polarization contains several frequency components, of which the one oscillating with frequency ω_{S} is the Stokes polarization. The complex amplitude of the Stokes polarization helps in determining its spatial evolution and is given by [12]

$$P\left(\omega_{\mathrm{S}}\right) = N\left(\frac{\partial\alpha}{\partial q}\right)q^*\left(\omega_{\mathrm{PS}}\right)A_{\mathrm{P}}e^{ik_{\mathrm{S}}z} = 6\epsilon_0\chi_{\mathrm{R}}^{(3)}\left(-\omega_{\mathrm{S}};\omega_{\mathrm{P}},-\omega_{\mathrm{P}},\omega_{\mathrm{S}}\right)|A_{\mathrm{P}}|^2A_{\mathrm{S}}e^{ik_{\mathrm{S}}z}, \quad (1.14)$$

where the third order nonlinear susceptibility $\chi_{\mathrm{R}}^{(3)}$ is [62]

$$\chi_{\mathrm{R}}^{(3)}\left(-\omega_{\mathrm{S}};\omega_{\mathrm{P}},-\omega_{\mathrm{P}},\omega_{\mathrm{S}}\right) = \frac{N\left(\frac{\partial\alpha}{\partial q}\right)^2\left(\omega_{\mathrm{r}}^2-\omega_{\mathrm{PS}}^2\right) - iN\left(\frac{\partial\alpha}{\partial q}\right)^2 2\omega_{\mathrm{PS}}\gamma}{6\epsilon_0 m\left[\left(\omega_{\mathrm{r}}^2-\omega_{\mathrm{PS}}^2\right)^2 + 4\omega_{\mathrm{PS}}^2\gamma^2\right]}, \quad (1.15)$$

and is related to g_{S} by,

$$g_{\mathrm{S}} = -\frac{6\omega_{\mathrm{S}}}{c^2\epsilon_0 n_{\mathrm{S}}n_{\mathrm{P}}}\mathrm{Im}\chi_{\mathrm{R}}^{(3)}. \quad (1.16)$$

The rate equations for the pump and Stokes fields for a Raman laser are obtained from Helmholtz's equation of interacting waves (propagating in the z direction), assuming that the interacting waves are harmonic in time (second derivatives are neglected here) [63],

$$\frac{n}{c}\frac{\partial E}{\partial t} + \frac{\partial E}{\partial z} + \frac{1}{2\epsilon_0 cn}E = \frac{i\omega}{2\epsilon_0 cn}P_{\mathrm{NL}}. \quad (1.17)$$

Here, the induced polarization P_{NL} due to the material vibration described by Eq. 1.13 is the driving term for the electromagnetic waves in Eq. 1.17. The spatial evolution of Stokes and pump wave amplitudes and intensities ($I = |E|^2 cn\epsilon_0/2$) obtained from Eq. 1.14 and Eq. 1.17 are given by [62]

$$\frac{\mathrm{d}A_{\mathrm{S}}}{\mathrm{d}z} = i\frac{3\omega_{\mathrm{S}}\chi_{\mathrm{R}}^{(3)}\left(\omega_{\mathrm{S}}\right)}{cn_{\mathrm{S}}}\left|A_{\mathrm{P}}^2\right|A_{\mathrm{S}}, \quad (1.18)$$

$$\frac{\mathrm{d}A_{\mathrm{P}}}{\mathrm{d}z} = i\frac{3\omega_{\mathrm{P}}\chi_{\mathrm{R}}^{(3)}\left(\omega_{\mathrm{P}}\right)}{cn_{\mathrm{P}}}\left|A_{\mathrm{S}}^2\right|A_{\mathrm{P}}, \quad (1.19)$$

$$\frac{\mathrm{d}I_{\mathrm{S}}}{\mathrm{d}z} = -\frac{6\omega_{\mathrm{S}}}{c^2\epsilon_0 n_{\mathrm{S}}n_{\mathrm{P}}}\mathrm{Im}\chi_{\mathrm{R}}^{(3)}\left(\omega_{\mathrm{S}}\right)I_{\mathrm{P}}I_{\mathrm{S}}, \quad (1.20)$$

$$\frac{\mathrm{d}I_\mathrm{P}}{\mathrm{d}z} = -\frac{6\omega_\mathrm{P}}{c^2\epsilon_0 n_\mathrm{S} n_\mathrm{P}}\mathrm{Im}\chi_\mathrm{R}^{(3)}(\omega_\mathrm{P})\, I_\mathrm{P} I_\mathrm{S}. \tag{1.21}$$

From Eq. 1.18, the spatial evolution of the Stokes wave depends on $|A_\mathrm{P}|^2$ and thus is independent on the phase of the pump wave. As a result, phase distortions in the pump wave are not directly transferred to the Stokes wave — this forms the basis for the aforementioned automatic phase matching of the SRS interaction. Since $\omega_\mathrm{PS} = \omega_\mathrm{P} - \omega_\mathrm{S}$ is positive, the imaginary part of $\chi_\mathrm{R}^{(3)}(\omega_\mathrm{S})$ is negative and Eq. 1.20 implies that the Stokes is amplified. Also, using the susceptibility identities, $\chi_\mathrm{R}^{(3)}(\omega_\mathrm{P})$ is positive, indicating that the Stokes wave grows at the expense of the pump wave. The amplified Stokes wave, in turn, beats more strongly with the pump beam, resulting in stronger molecular oscillations and further amplification of the Stokes.

The steady state rate equations for CW Raman lasers (pump and Stokes waves are time-independent) are obtained from Eq. 1.16, 1.20 and 1.21 after introducing absorption loss coefficients for pump and Stokes $\alpha_\mathrm{P,S}$ [58, 64, 65],

$$\begin{aligned}\frac{\partial I_\mathrm{P}}{\partial z} &= -g_\mathrm{P} I_\mathrm{P} I_\mathrm{S} - \alpha_\mathrm{P} I_\mathrm{P},\\ \frac{\partial I_\mathrm{S}}{\partial z} &= g_\mathrm{S} I_\mathrm{P} I_\mathrm{S} - \alpha_\mathrm{S} I_\mathrm{S}.\end{aligned} \tag{1.22}$$

where $g_\mathrm{S} = g_\mathrm{P}\omega_\mathrm{S}/\omega_\mathrm{P}$ is the small-signal gain coefficient given in Eq. 1.8. These equations form the backbone to the CW diamond Raman laser models developed in Chapters 4 and 5.

1.2.3 CW Raman laser technologies

The first CW Raman lasers were demonstrated in ammonia [66, 67], neon [68] and sodium vapour [69]. These lasers used near atomic/molecular resonant Raman transitions to attain enough gain for Stokes conversion in a single pass; however, the pump can be tuned only over narrow regions near the resonance. The first "off-resonant" CW Raman laser was demonstrated by Brasseur *et al.* in H_2 utilizing a resonantly pumped cavity [70] opening up the potential for widely tunable CW Raman lasers. Gases have often been the preferred Raman media owing to their lower scattering losses, large Raman shift ($\sim$ 2900-4200 cm^{-1}) and higher threshold for other detrimental nonlinear effects such as self-focussing [71]. H_2, D_2 and CH_4 were the most widely used [70, 71] owing to their higher Raman gain among the

other gaseous media. However, they suffer from severe thermal effects, low gain (compared to crystalline counterparts), optical breakdown and large physical size which sets a limit on their range of applications [71]. In order to access a wide range of wavelengths with high power and brightness, a combination of properties such as high Raman gain, good thermal and mechanical properties and wide transmission band is highly desired.

In parallel with these developments, optical fibers were also being used as promising Raman gain media as they allow high pump intensities to be maintained over a longer distance due to optical confinement [72]. In addition, the heat generated can be distributed over a longer distance, thus enabling simplified management of the thermal load. CW output powers up to 1.28 kW with a lower threshold at 1120 nm has been demonstrated with Raman fiber lasers [72–74]. However, they suffer from linewidth broadening at elevated powers which poses problems for subsequent harmonic conversion.

Crystalline Raman media exhibit higher Raman gain, much smaller spectral broadening than glasses (but higher than gases), and wide transmission. The first bulk crystalline CW Raman laser was demonstrated by Grabtchikov *et al.* using barium nitrate as the Raman medium as it has the highest Raman gain amongst common Raman crystals [75]. Since then, a variety of Raman crystals have been used including $Ba(NO_3)_2$, $BaWO_4$, $KGd(WO_4)_2$, $KY(WO_4)_2$, silicon and so on (comparison of properties of selected Raman crystals are provided in Sec.1.3). Recent research in CW Raman lasers has mainly focussed on crystalline Raman media and glass and hollow-core gas-filled fibers.

As SRS is a third-order nonlinear optical effect, pumping at high intensities is required to reach the threshold for net gain (typically much higher than the $\chi^{(2)}$ processes). In order to minimize the threshold, the cavity is often made resonant for the Stokes, and the pump is either resonated together with the Stokes or single/double passed in the cavity. The basic Raman laser configurations can be broadly divided into two categories: intracavity (Fig. 1.3 (a)) and external cavity configurations (Fig. 1.3 (b) and (c)).

In an intracavity Raman laser configuration, the Raman gain material is placed inside the pump laser cavity [76–80], which is made resonant for both the fundamental and first Stokes. This enables efficient energy extraction from the laser gain medium as well as efficient conversion of fundamental to the first Stokes in the Raman crystal. Intracavity Raman lasers are an important technology providing efficient, low-threshold wavelength conversion from diode lasers to exotic wavelengths. The major concern for this class is the significant thermal

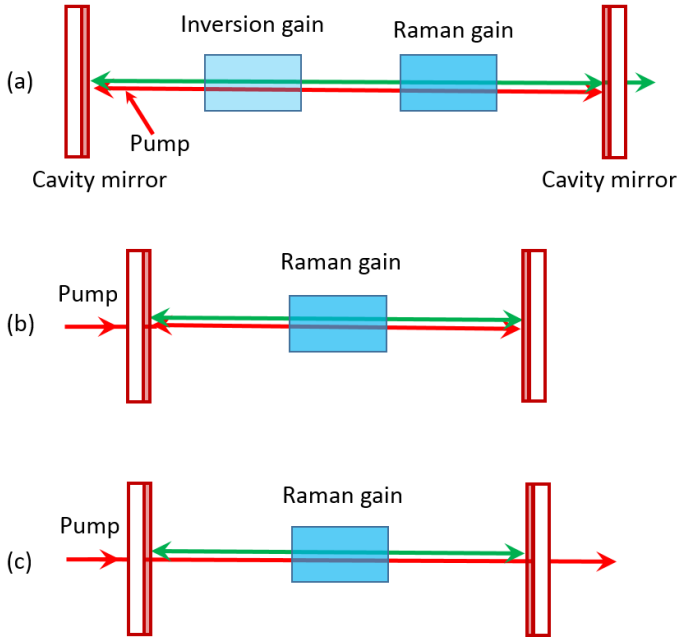

Figure 1.3: Basic configurations used in CW Raman lasers: (a) intracavity (b) doubly-resonant and (c) singly-resonant.

loading arising from the laser gain medium as well as from the Raman gain medium. Hence, such resonators need to manage two thermal lenses and this has put a limit on the maximum power achieved to a few watts [76]. A variation of intracavity Raman laser is the self-Raman laser in which a single crystal (e.g. $KGd(WO_4)_2$, $Pb(WO_4)_2$, $GdVO_4$ doped with Nd^{3+} and Yb^{3+} ions) is used for the generation of the fundamental wavelength as well as frequency shift through SRS process [81, 82]. This design is utilized for developing very compact and robust laser sources. However, the combined heat load due to the inversion and SRS processes also makes power scaling challenging.

In an external cavity Raman laser configuration, the Raman medium is placed in a resonator entirely separated from the pump laser. As a result, the thermal effects in the laser and the Raman gain medium can be managed separately. The external cavity Raman lasers include doubly-resonant cavity with resonating pump and Stokes (Fig. 1.3 (a)) and singly-resonant cavity with only Stokes resonating in the cavity (and the pump is either single or double passed)(Fig. 1.3 (b)). Resonantly-enhanced pumping has been demonstrated in gaseous Raman media [70, 83–85] with thresholds as low as a few milliwatts. But like resonantly-enhanced second harmonic generation, these systems require single longitudinal mode pump sources that are locked to a cavity resonance (or vice versa). Moreover, it

requires more complex mirror coatings to resonate both the pump and the Stokes. In order to avoid these complexities, non-resonant (single/double pass pumped) external cavity Raman lasers are used at the expense of a much higher threshold. Hence, strong focusing and low intracavity losses are critical for reducing the threshold and for efficient operation [86]. In all Raman crystals but diamond, the combination of high threshold and low thermal conductivity makes efficient operation problematic [75, 87]. That is, the pump powers needed to achieve threshold are typically enough to cause substantial thermal degradation (through impurity absorption as well as SRS) so that practical efficiencies have not been achieved.

Recently, diamond has emerged as an important high brightness CW conversion material due chiefly to its high thermal conductivity but also useful because of its wide transparency range and large Raman shift [88–91]. A further key advance has been its use together with the external cavity configuration to further simplify thermal management of the system. An external cavity diamond Raman laser (DRL) was first reported by Kitzler *et al.* with 10 W of 1240 nm Stokes output with 49.7% slope efficiency in the near-IR [87]. Output power has since been further increased to 381 W for periods of 10 ms (approximately a thousand times longer than the transient thermal time-constant) with conversion efficiencies as high as 61% [92, 93]. To date, the pumps used have been exclusively limited to Nd and Yb lasers operating near 1064 nm, however the technology is promising for being readily adaptable to other CW laser pumps.

1.2.4 CW Raman laser technology with intracavity frequency conversion: Visible and UV generation

The wavelength diversity of Raman lasers is greatly increased by combining intracavity frequency mixing techniques such as SHG and SFG. The first intracavity frequency mixed Raman laser was demonstrated in the pulsed regime by Ammann in 1979 using an arc-lamp pumped Q-switched $Nd : YAlO_3$ crystal and an intracavity lithium iodate crystal. Lithium iodate, having both second and third order nonlinearity, was used as the Raman crystal and frequency mixing crystal to generate four lines in the yellow to red spectral region [94]. Much later, in 2007, Dekker *et al.* demonstrated the first CW intracavity doubled Raman laser using $Nd : GdVO_4$ as the laser crystal, KGW as the Raman crystal and LBO as the frequency doubling crystal generating 704 mW CW power at 588 nm and 1.5 W of quasi-CW

power [95]. Since then, intracavity Raman lasers with intracavity doubling have demonstrated a range of wavelengths in the yellow and orange spectral region with up to 10 W of CW power using a range of pump lasers, Raman crystals and doubling crystals [96–107].

External cavity Raman lasers with intracavity doubling have been reported in the pulsed regime to generate visible and UV outputs [108, 109], but to date not in the CW regime. Since diamond solves a major thermal problem, the high intracavity powers (of the order of tens of kilowatts) in an external cavity DRL open up the possibility of exploring wavelengths in the visible by intracavity frequency mixing and is the central topic of this thesis.

1.3 Diamond as a Raman medium

Diamond is an extreme optical material and has a range of applications in optics such as in nano-photonics and optomechanics, intracavity heat spreaders, high power laser windows, synchrotron and x-ray optics and quantum information processing, apart from Raman lasers [111–115]. High thermal conductivity, wide bandgap and wide transmission window are a few of its outstanding properties pertinent to optical and photonic applications. As this thesis is focussed on the application of diamond as a Raman gain medium, properties in this context will be introduced here. A comparison of such properties with other commonly used Raman crystals is presented in Tab. 1.1.

The Raman gain coefficient is a fundamentally important parameter determining Raman laser performance. A high gain coefficient provides lower threshold, relaxed constraints on optical coatings and allows the choice of shorter crystals. The Raman gain of diamond is relatively high compared to most other Raman crystals (See Tab. 1.1) due to its high density, small mass and large $\mathrm{d}\alpha/\mathrm{d}q$ (deformation potential) [119]. Like all Raman crystals, the Raman gain coefficient of diamond increases with decreasing Stokes wavelength (see Eq. 1.9) as shown in Fig. 1.4. Measurements by several groups at various pump wavelengths range from 8-15 cm/GW in the IR and 15-20 cm/GW in the visible [120–122].

The power range of Raman lasers is limited, primarily due to thermal effects arising from the decay of optical phonons involved in the SRS process and impurity/defect absorption. The thermal conductivity of diamond, which is orders of magnitude higher compared to other commonly used Raman crystals and those listed in Tab. 1.1, is thus an outstanding feature for providing a high power advantage. Furthermore, diamond possesses a positive

Table 1.1: Comparison of properties of various Raman crystals [116–118].

Crystal	$LiIO_3$	$Ba(NO_3)_2$	$BaWO_4$	$KGd(WO_4)_2$	$KY(WO_4)_2$	Silicon	Diamond
Crystal structure	Hexagonal uniaxial	Cubic isotropic	Tetragonal uniaxial	Monoclinic biaxial	Monoclinic biaxial	Cubic isotropic	Cubic isotropic
Raman shift (cm^{-1})	770, 822	1047.3	924	768, 901	765, 905	521	1332.3
Raman gain at 1064 nm (cm/GW)	4.8	11	8.5	3.5	3.6	20@1550 nm	10-12
Transmission range (nm)	310-400	350-1800	260-5000	340-5500	350-5500	1100-6000	230-3800 and >6500
Thermal conductivity (WmK^{-1})	4	1.17	3	2.6(a)	3.3	153	2200
				3.8(b)	(averaged over		
				3.4(c)	3 directions)		
Thermal expansion coefficient ($\times 10^{-6}K^{-1}$)	28	18.2	4-6(a)	4(a)	1.83 (N_p)	3	1.1
	46(c)		23(c)	1.6(b)	10.29 (N_m)		
				8.5(c)	15.94 (N_g)		
$\frac{dn}{dT}$ ($\times 10^{-6}K^{-1}$)	-95	-20	<-9.0	-4.3-5.5	-14.6 (N_m)	215	15
					-8.9 (N_m)		
					-12.4 (N_m)		

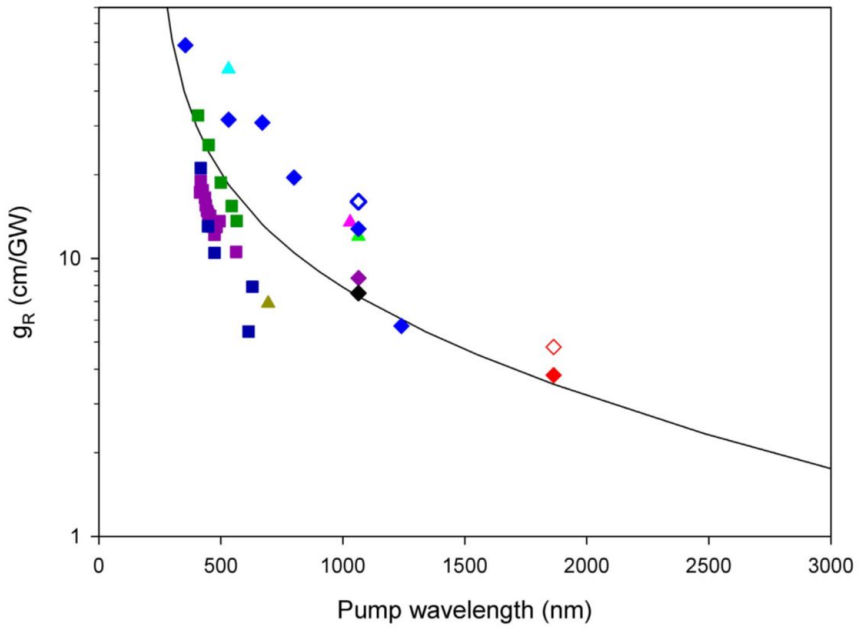

Figure 1.4: Raman gain coefficient as a function of wavelength measured using various techniques [120].

and moderate value of temperature coefficient of refractive index (dn/dT). From all these parameters, heating in diamond results in positive thermal lens of magnitude several orders weaker than other Raman crystals.

Diamond has a transparency range from UV to IR because of its UV absorption edge and the absence of first-order infrared absorption. As shown in Fig. 1.5, the absorption spectrum is featureless from the wavelength range 230 nm to 2600 nm and beyond 6200 nm. The major features that affect the wavelength dependence of absorption are UV-edge absorption (wavelength less than 225 nm) and infrared lattice absorption of moderate strength between 2600-6200 nm [119].

Synthetic diamond typically contains a host of defects and impurities, especially nitrogen, arising from growth conditions (the details of which are given in Sec.1.3.2) that affect the absorption properties. Fig. 1.6 shows the dependence of absorption coefficient of CVD grown diamond on the amount of nitrogen concentration, determined using laser calorimetry at 532 nm and 1064 nm. Crystals with 100 ppb nitrogen content have an order of magnitude higher absorption coefficient than crystals with 20 ppb nitrogen content. It is also to be noted that the absorption coefficient is higher in the visible, with values around 0.001-0.005 cm^{-1}

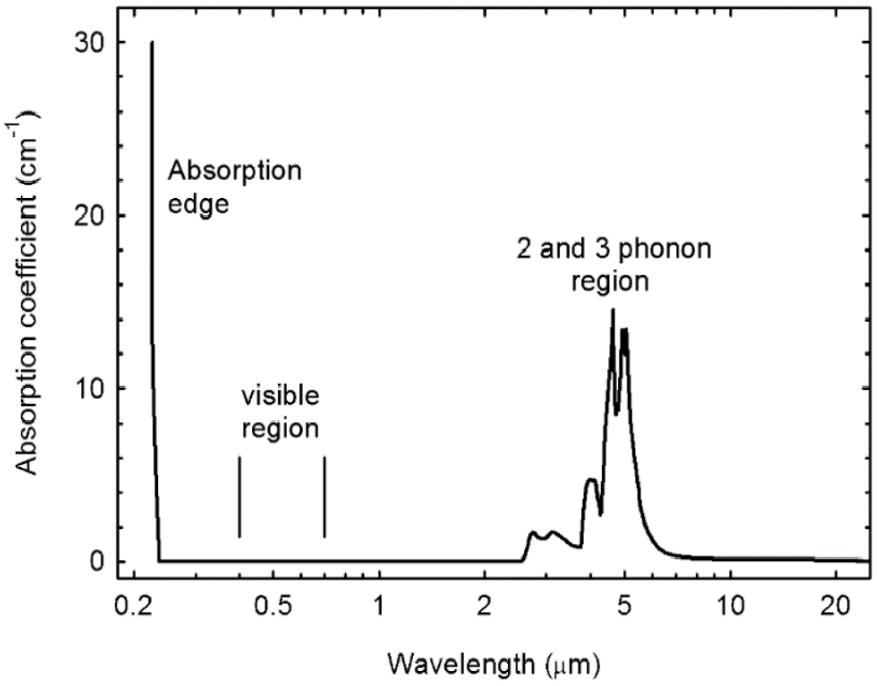

Figure 1.5: Intrinsic absorption spectrum of diamond from UV to far IR [123].

at 532 nm, as opposed to less than 0.001 cm^{-1} at 1064 nm. The diamond crystals used in this thesis have approximately 20-40 ppb nitrogen content and hence have an absorption coefficient in the range 0.001-0.004 cm^{-1}.

1.3.1 Polarization dependence of SRS in diamond

Like $\chi^{(2)}$ nonlinear interactions, SRS is a polarization dependent process (see Eq. 1.9), and gain is dependent on the pump and Stokes polarisations. The polarization behaviour is determined by the Raman scattering tensors associated with its crystal structure. Understanding the polarization behaviour of the Raman gain medium is critical to performance optimization.

Like silicon, diamond has a cubic structure, where each carbon atom is covalently bonded to four other carbon atoms. It belongs to $O_h^7 - Fd\bar{3}m$ consisting of two interpenetrating face-centered cubic (FCC) lattices displaced along the body diagonal of the cubic cell by one-quarter of the length of the diagonal, as shown in Fig. 1.7.

The major crystallographic directions and dimensions of the single-crystal diamond used in this thesis are shown in Fig. 1.8. The diamonds are grown by CVD along the [100] direction. The long dimension of the crystal [110], which is perpendicular to the growth direction, is typically used as the propagation direction [87, 92, 124, 125], owing to lower

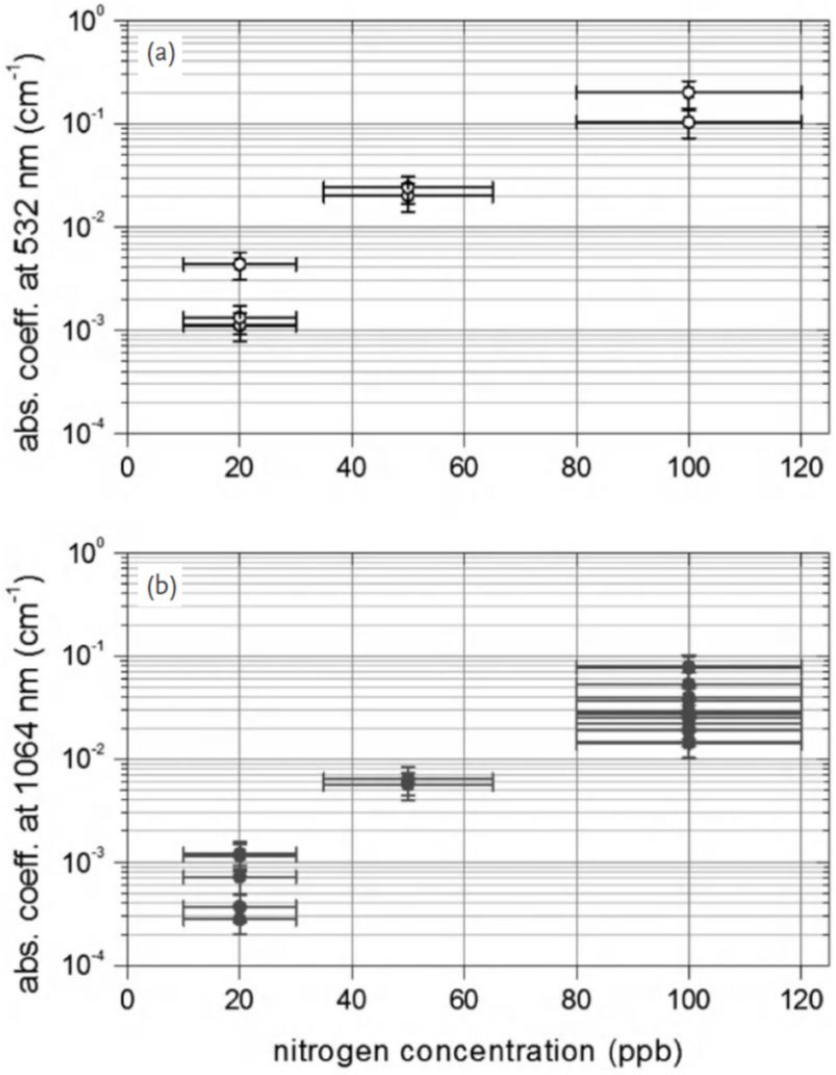

Figure 1.6: Absorption coefficient of single crystal CVD diamond with nitrogen concentrations of 20, 50 and 100 ppb at (a) 532nm and (b) 1064 nm. The error bars are attributed to the uncertainty in the calorimetric measurements and due to variations in the growth conditions [123].

residual stress along this direction (discussed further in Sec.1.3.2).

The first-order Raman scattering corresponds to the vibrational modes involving the relative displacement of carbon atoms along the direction of carbon-carbon bonds ($\langle 111 \rangle$ direction – see Fig. 1.7). At the zone centre of phonon dispersion, the longitudinal and two transverse vibrational branches converge resulting in a triply degenerate Raman mode. The Raman frequency ω_r at room temperature is 1332.3 cm^{-1} [119].

The triply degenerate Raman tensors for propagation along $\langle 110 \rangle$ propagation direction

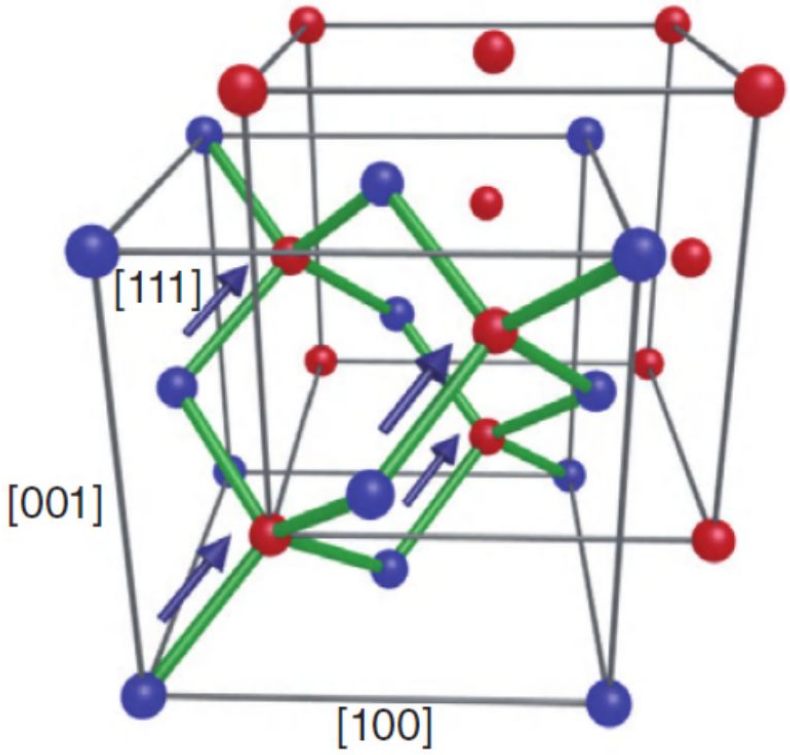

Figure 1.7: Diamond crystal structure showing the two interpenetrating FCC lattices (in red and blue) [119]. The arrow (in blue) shows the direction of Raman vibrational mode along [111].

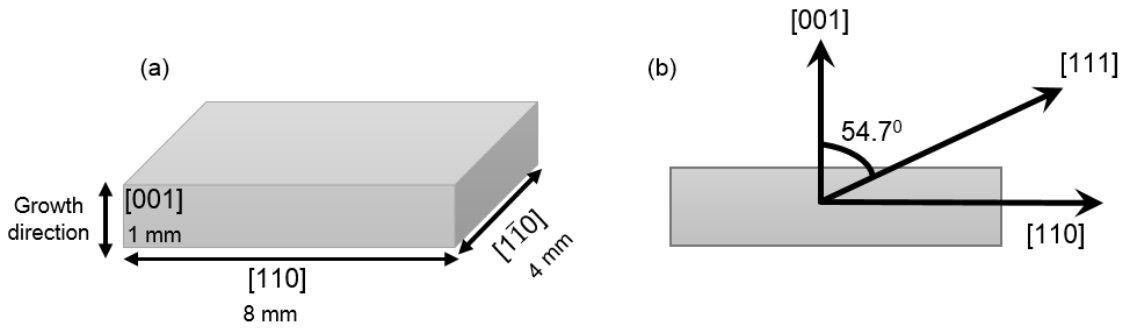

Figure 1.8: Dimensions and crystallographic orientation of diamond samples (a) side view and (b) end view.

are given by [126],

$$R_1 = \begin{bmatrix} 0 & 0 & \frac{d}{\sqrt{2}} \\ 0 & 0 & \frac{d}{\sqrt{2}} \\ \frac{d}{\sqrt{2}} & \frac{d}{\sqrt{2}} & 0 \end{bmatrix}, R_2 = \begin{bmatrix} 0 & 0 & \frac{d}{\sqrt{2}} \\ 0 & 0 & -\frac{d}{\sqrt{2}} \\ \frac{d}{\sqrt{2}} & -\frac{d}{\sqrt{2}} & 0 \end{bmatrix}, R_3 = \begin{bmatrix} d & 0 & 0 \\ 0 & -d & 0 \\ 0 & 0 & 0 \end{bmatrix}. \quad (1.23)$$

By substituting in Eq. 1.9, it can be readily shown that the gain coefficient is a strong function of pump and Stokes polarization. A maximum value is obtained for the pump and Stokes polarizations oriented parallel to ⟨111⟩ direction [116], which is oriented at an angle 54.7° from the [001] direction for the chosen propagation direction, as shown in Fig. 1.8 (b). More details on the polarization dependence of Raman gain in the diamond will be discussed in Chapter 3.

1.3.2 Stress in diamond and its effect on optical properties

Recent studies have shown that the polarization behaviour of CW diamond Raman lasers deviates significantly from that predicted by the Raman tensors [93, 127]. In the pulsed regime, the Stokes polarization varies continuously with pump polarization, which is consistent with the Raman tensors. For example, for a vertically polarized pump, the Stokes polarization is horizontal and for a horizontally polarized pump, the Stokes polarization is randomly oriented. Also, for a pump polarized along ⟨111⟩, the Stokes polarization is collinear with the pump (see Sec. 3.1 for more details). However, in the CW case, the Stokes polarization remains fixed and switches between two orthogonal polarizations as the pump polarization is rotated (see Sec. 3.3.2 for more details). This deviation in the polarization behaviour has been proposed to be due to stress induced birefringence present in the diamond [93, 127]. Hence, it is necessary to understand and characterize the causes and effects of stress in diamond to obtain a more complete picture of the polarization behaviour.

Although diamond is a cubic crystal and ideally isotropic, stress causes anisotropies that affect its optical properties. Stress induced birefringence is the most obvious effect, but another of potential importance is that it lifts the degeneracy of the phonon modes resulting in splitting and/or a shift in the Raman line [128–137].

The stress is caused by defects and impurities (especially nitrogen) introduced during growth. Of the two main categories of growth – high-pressure-high-temperature (HPHT) technique and chemical vapour deposition (CVD) technique – CVD has been considered to be the most viable technique for producing high optical quality single crystals with low

absorption and birefringence ("Type IIa").

CVD growth utilizes a hydrocarbon gas, such as methane diluted in hydrogen. The hydrogen dissociates in the chamber and facilitates preferential deposition of diamond instead of graphite. The atomic hydrogen helps in etching away any sp^2-bonded phases. Growth takes place at low pressure (0.01-0.1 bar) and substrate temperatures around 700 – 1400°C. The gas mixture is ionized in order to produce reactive species for high-quality crystal growth [111, 123]. The ionization activation is achieved using techniques such as the hot filament, arc-jet, combustion flame, and microwave plasma. Microwave plasma CVD (MPCVD) is currently the most effective technique for majority of optical and electronic applications [111, 123].

To date, single-crystals have only been grown homo-epitaxially and usually on a {100} – oriented diamond substrate [123]. Other substrates yield polycrystalline diamond which suffers much larger scattering, particularly for near-IR wavelengths and shorter [123]. Also, due to the random orientation of crystal domains, the effective Raman gain coefficient is not as high as that achievable for single crystal.

A controlled amount of dopant, such as nitrogen, is added to the gas phase in order to accelerate the growth process as well as for surface stabilization [111, 123]. Impurities may also be introduced through air leaks in the chamber and/or from impurities in the source gases. These impurities lead to the formation of lattice defects, which increase in density with the growth rate. Thus, there is a trade-off between the absorption loss and the growth rate [123].

In general, there are three types of defects that lead to stress: point defects, line defects, and planar defects [123]. A 2-dimensional representation of the major types of point and line defect are depicted in Fig. 1.9. Point defects may be caused by self-interstitial carbon atoms, foreign interstitial atoms, edge substitutional atoms and vacancies resulting in spatial variation in the lattice structure. However, the density of point defects is usually lower in high optical quality diamond and hence does not play a significant role in contributing to birefringence [123].

Line defects (shown in Fig. 1.9) are caused by dislocations originating either in the substrate or in the epitaxial interface [139–142]. This is mainly due to the lattice errors caused by the substrate damage or surface contamination at the epitaxial interface. It may also be caused by dislocations in the substrate that propagate up to the growth layer [123].

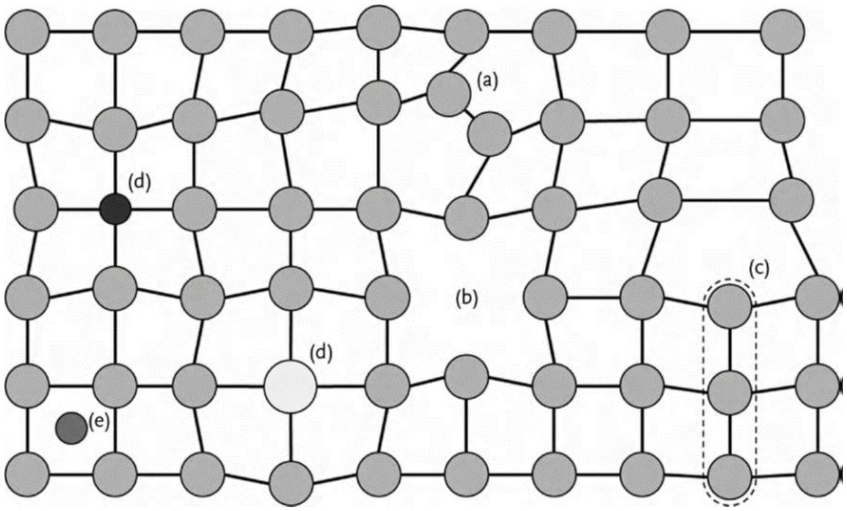

Figure 1.9: 2-D depiction of defects in diamond. (a) Point defect due to self-interstitial carbon atom, (b) point defect due to a vacancy (c), line defect due to edge dislocation, (d) point defect due to an edge substitutional atom and (e) point defect due to a foreign interstitial atom [138].

X-ray topographic studies of single crystal CVD diamonds show that the dislocations have directions close to the [001] growth direction and are predominantly of two types: edge dislocations and 45° mixed dislocations [143]. Edge dislocations normally arise when there are groups of dislocations originating in isolated points. Edge dislocations have been shown to produce a petal-shape birefringence pattern as shown in Fig. 1.10 [141]. 45° mixed dislocations were also observed when the substrate surface was deliberately damaged before growth and can be largely avoided by careful substrate preparation [143].

Planar defects are generally caused by twinning of lattice planes [123, 144]. Twinning in diamond generally occurs in the {111} plane, where the twinned domain is rotated by 180° with respect to the parent crystal. This leads to incoherent lattice boundaries between neighbouring twinned and untwinned regions leading to planar defects [123]. The twinned domain may grow into macroscopic defects that exert strain on the neighbouring lattice.

The aforementioned defects lead to complex and non-uniform birefringence patterns with spatially-varying axis directions of linear birefringence. The magnitude of birefringence has been observed to be reduced significantly by minimising the density of edge dislocations, achieved by selecting growth substrates with a low density of surface dislocations and damage [123, 145]. The effect of dislocation density on the birefringence is detailed in Ref. [123]

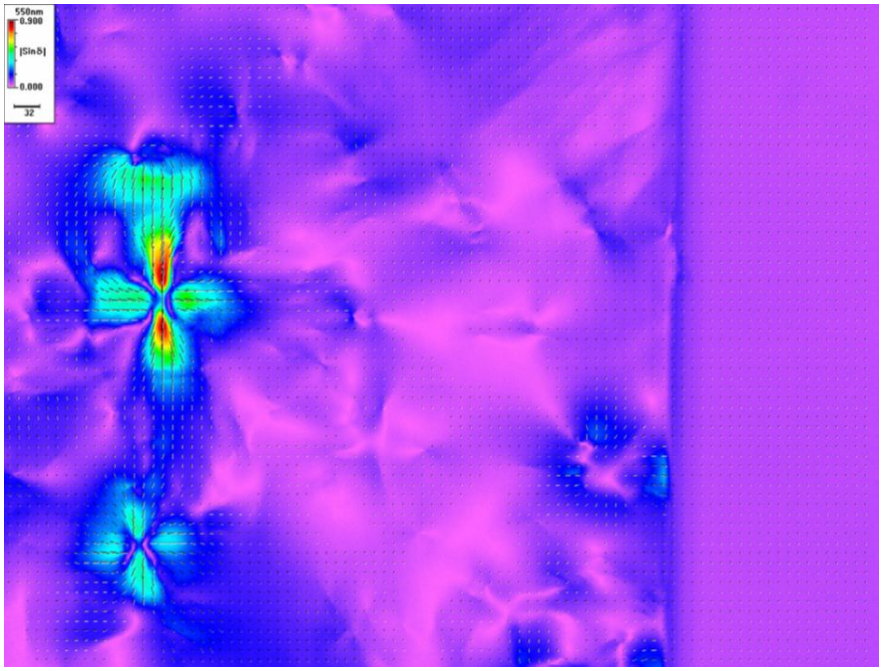

Figure 1.10: Petalled birefringence pattern due to edge dislocation [141]. The small dashed lines in the map show the direction of the birefringence axis.

and is shown in Fig. 1.11. It is seen that the birefringence magnitude is decreased from samples A to C as the edge dislocation density is reduced. Also, the linear birefringence magnitude is usually an order of magnitude higher along the growth direction than along the perpendicular [110] direction. For sample C, with the lowest dislocation density, the birefringence Δn is of the order of 10^{-5} in the growth direction and of the order of 10^{-6} along the [110] direction [123, 145]. Δn was found to be greater than 10^{-4} for regions with dense clusters of dislocations [123].

The diamond material used in Raman lasers has been almost exclusively CVD-grown and oriented perpendicular to the growth direction for low residual birefringence. This type of material has led to efficient DRLs (> 50%) under a wide range of pulse formats (ultrafast, nanosecond and CW) and wavelength range (UV to mid-infrared). For the CW regime, further investigation is required to understand the detailed role of stress in influencing threshold, efficiency, and perturbing polarisation away from the expected behaviour (from Raman tensors). Understanding stress effects is crucial for optimizing performance and further diversifying the wavelength range through (polarization-dependent) nonlinear harmonic mixing.

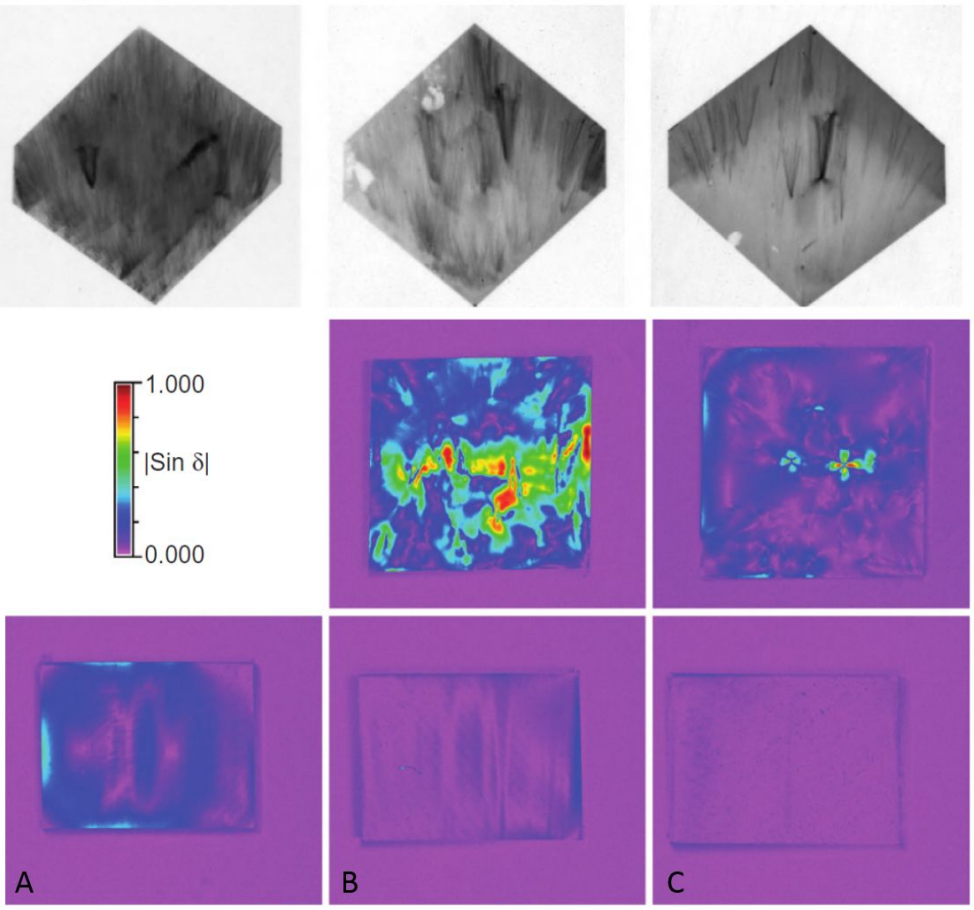

Figure 1.11: Birefringence map of three samples A, B and C with decreasing edge dislocation density. The top row shows X-ray topographic images of three samples (A to C) with decreasing edge dislocation densities. The middle and bottom rows show birefringence maps viewed parallel and perpendicular to the growth direction respectively [123].

1.4 Thesis outline

The primary aim of this thesis is to extend the wavelength range of CW DRLs using intracavity doubling to generate high power and high beam quality lasers in the visible and UV spectral regions.

Chapter 2 presents a detailed birefringence characterization of laser-grade CVD-grown diamond including an examination of linear and circular components. The birefringence was characterised for several samples along the propagation direction using the Metripol technique and also the more complete Mueller polarimetric technique. The latter revealed that significant circular birefringence occurs in some crystal locations. The significance of

the presence of circular birefringence on Metripol measurement accuracy and laser behaviour was analysed using Jones calculus. Stress effects along the growth direction were also characterized to further elucidate their role in perturbing laser performance as well as interpreting the birefringence behaviour observed in the propagation direction. This chapter provides a firm basis for analysing the DRL behaviour as a function of polarisation.

The detailed effects of birefringence on external cavity DRL performance is presented in Chapter 3. The dependence of threshold and output polarization is characterized as a function of input polarization and compared with the polarization behaviour of DRLs reported to date. An analysis based on the Raman tensors is used to yield insights into the Raman gain behaviour in the presence of birefringence and better understand the departure from the behaviour seen to date in pulsed lasers. Design rules for crystal selection and low threshold operation are established. The results of this chapter are also likely to be relevant to polarization behaviour of other high-Q factor diamond lasers such as intracavity CW DRLs and synchronously pumped ultrafast DRLs.

Intracavity frequency doubling in a DRL is investigated in Chapter 4. A linear cavity using an intracavity LBO crystal is used to obtain high power output with high beam quality at 620 nm, using a 1064 nm quasi-CW pump. The choice of the nonlinear crystal is discussed. An analytical model is presented to provide guidance for increasing efficiency and further increasing power. By considering the thermal effects in diamond and LBO, output saturation is forecast for the case of indefinitely long CW durations.

In chapter 5, the wavelength range is extended further by utilising a 532 nm pump laser. A first Stokes laser at 573 nm laser is demonstrated and analysed to understand the behaviour in the visible and contrast it with that seen in the near-infrared. Ways to improve the laser performance by varying the design parameters are investigated using an analytical model. Extending this system to incorporate intracavity frequency doubling to generate UV is discussed by considering the choice of nonlinear crystal and laser design.

Finally, Chapter 6 summarises the major findings and future implications.

2

Stress effects in laser grade single crystal CVD diamond

This chapter presents a detailed characterization of the in-grown stress present in laser-grade diamond samples with the underlying motivation to decipher its effect on the polarization characteristics of Raman laser behaviour. The two major consequences of stress – birefringence and Raman frequency shift – are investigated in detail. While the birefringence is anticipated to affect the polarization characteristics of Raman lasers, perturbations to the centre Raman frequency along the line of sight may result in a reduction in the overall Raman gain (if the shifts are greater than the Raman linewidth). To date, the birefringence characterization of CVD diamond has only been focussed on linear birefringence, predominantly using Metripol technique. This chapter provides a comprehensive birefringence characterization along the propagation direction of Raman lasers ([110] direction) and along the (orthogonal) growth direction ([001] direction).

Firstly, characterization of the magnitude and direction of linear birefringence for two

diamond samples is investigated using Metripol polarimetry. The study was further extended to include other birefringence effects such as circular birefringence and dichroism using the more complete technique of Mueller polarimetry. Significant circular retardance was measured in at least one of the samples causing inaccuracies in the measured values of linear retardance. Furthermore, the origin of birefringence along the [110] direction was investigated by measuring the stress effects including linear birefringence and Raman frequency shifts along the perpendicular direction in the crystal (the growth direction [001]).

2.1 Techniques for characterizing stress

The birefringence properties of a sample can be deduced by analyzing the polarization of the incoming and outgoing beams. Birefringence characterization using a pair of crossed polarizers is the simplest and most commonly used technique, however, it is limited to the measurement of the magnitude of linear birefringence alone [146, 147]. The information on both the magnitude and direction of linear birefringence is obtained by utilizing a polarization modulation technique where the sample is placed in between a circular polarizer and a rotating linear analyzer. Although this technique has been widely used for precisely measuring the linear birefringence, the process is highly time-consuming [146, 148]. A variation of this technique that is less complicated is the Metripol technique, which is extensively used in this chapter.

2.1.1 Metripol polarimetry

The Metripol method [149] was performed using an in-house system to determine both the magnitude and direction of linear retardance of the optical sample. The experimental setup for the Metripol polarimetry is shown in Fig. 2.1. It consisted of a collimated, narrow-band, incoherent beam (in this case from an incandescent lamp, 589-nm notch filter and a collimating lens) passing through a rotatable polarizer, the optical sample, followed by a quarter waveplate and an analyzing polarizer. The analyzing polarizer was set to 45° with respect to the fast axis of the quarter waveplate and a 10 cm focal length lens was used to image the end face of the diamond onto a silicon CCD camera (Spiricon SP620U).

The amplitude of the emerging light is obtained by multiplying the Jones matrices of all

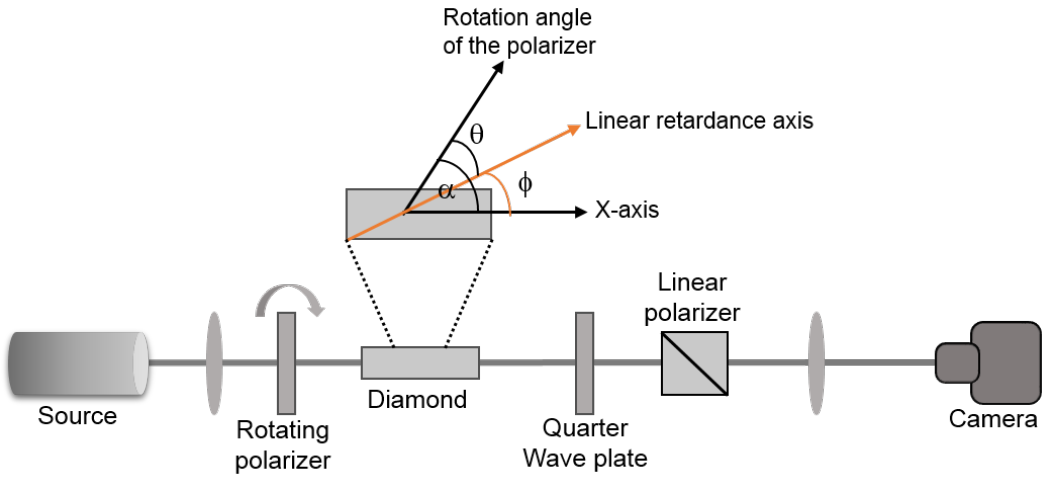

Figure 2.1: Experimental arrangement of the Metripol technique. The upper inset diagram shows the angle variables used in the text as viewed along the propagation direction through the sample.

the polarizing elements [149]

$$\mathbf{A} = \frac{1}{2}\begin{bmatrix} 1 & 1 \\ 1 & 1 \end{bmatrix}\begin{bmatrix} e^{\frac{i\pi}{4}} & 0 \\ 0 & e^{\frac{-i\pi}{4}} \end{bmatrix}\begin{bmatrix} e^{\frac{i\delta}{2}} & 0 \\ 0 & e^{\frac{-i\delta}{2}} \end{bmatrix}\begin{bmatrix} \cos\theta & \sin\theta \\ -\sin\theta & \cos\theta \end{bmatrix}\begin{bmatrix} 1 \\ 0 \end{bmatrix}, \tag{2.1}$$

for $\theta = \alpha - \phi$, where α is the polarizer rotation angle (with respect to the horizontal), ϕ is the orientation of the linear retardance axis of the sample (with respect to the horizontal) (see Fig. 2.1) and δ is the magnitude of linear retardance.

The normalized intensity of the transmitted light after passing through the sample and the polarization elements is given by

$$\frac{I}{I_0} = A^*.A = \frac{1}{2}\left[1 + \sin 2\left(\alpha - \phi\right)\sin\delta\right] \tag{2.2}$$

thus the transmitted intensity as a function of rotatable polarizer angle is a sine curve whose amplitude is $\sin\delta$ and phase is ϕ. The birefringence Δn is then obtained from δ using the relation

$$\Delta n = \frac{\delta\lambda}{2\pi L} \tag{2.3}$$

where λ is the wavelength of the light used and L is the length of the sample.

The polarizer was rotated in steps of 10° and the transmitted light was captured by the CCD camera. The intensity recorded at each pixel, corresponding to a specific location in the diamond, was fitted to a sine curve as a function of α from which the amplitude and

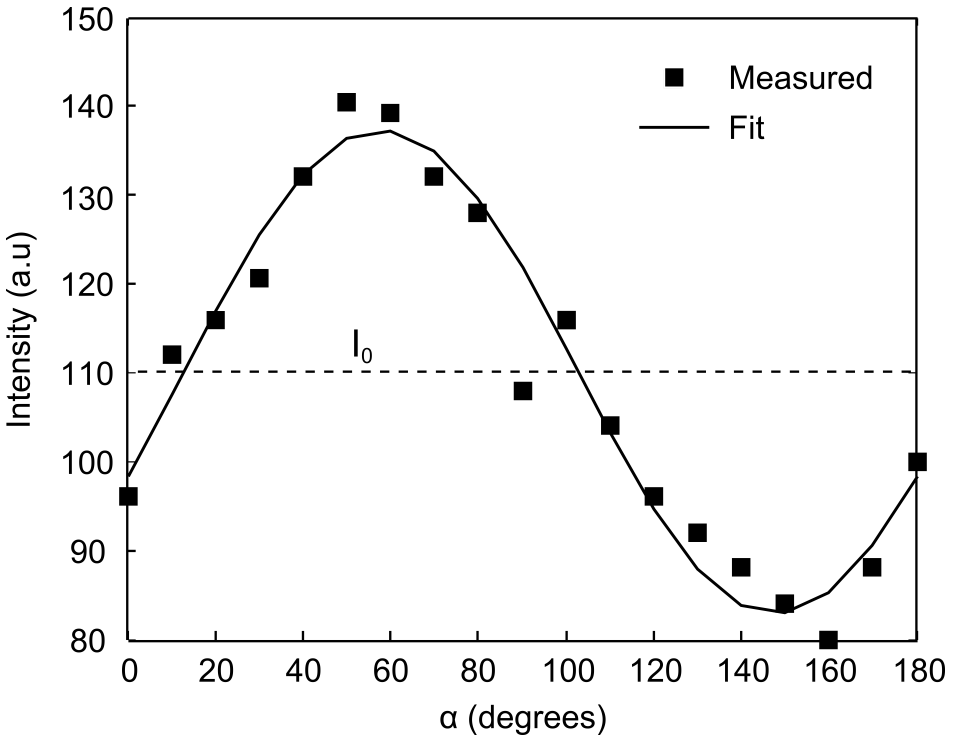

Figure 2.2: Intensity of the exiting beam as a function of rotation angle of the polarizer for a selected location in the diamond. The curve shows the fitted sine curve to the data points.

phase values were extracted to provide the magnitude and direction of linear retardance. The fitting of the experimental data to the sine curve was done using a custom Matlab code. Fig. 2.2 shows the intensity of the exiting beam as a function of the rotation angle of the polarizer for an arbitrary pixel. For this pixel, the magnitude of linear retardance is 29° and the corresponding direction is 12.5°. The process is repeated to obtain a map showing the magnitude and direction of linear retardance at each location in the sample. The measurement uncertainty was calculated to be ±2.5° ($\Delta n = \pm 5 \times 10^{-7}$) due to imperfect waveplate used in the experiment.

2.1.2 Mueller polarimetry

The Metripol technique is limited to the measurement of linear birefringence only and may lead to measurement inaccuracies if other polarization properties such as circular birefringence and/or dichroism are present. Multiple photoelastic modulators have been used to gain more information on these additional birefringence effects and thus to accurately measure linear birefringence [150–153]. The technique used in this chapter, Mueller polarimetry, utilizes four photoelastic modulators to measure the complete birefringence characteristics

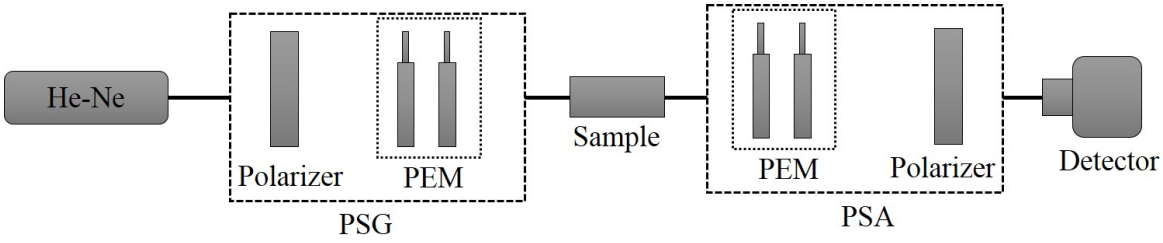

Figure 2.3: Basic experimental arrangement of Mueller polarimetry.

of CVD diamond.

Mueller polarimetry, the principles of which are described in Ref. [151], was performed using a commercially available Mueller polarimeter (Exicor 150 XT from Hinds Instruments). The basic experimental arrangement of the Mueller polarimetry consists of a He-Ne laser (operating at 632.8 nm), four computer-controlled polarization modulating photoelastic modulators (PEM), two linear polarizers, the optical sample and a photodetector as shown in Fig. 2.3. A linear polarizer and a pair of PEMs acts as the polarization state generator (PSG), that generates any elliptical state of polarization. Similarly, another set of PEMs and a linear polarizer acts as the polarization state analyzer (PSA), that can achieve the extinction of the known elliptical state of polarization generated by PSG. Here, the instrument launches a variety of known polarization states from the He-Ne laser and PSG, which passes through the length of the sample, whose polarization is modulated by the birefringence in the sample. At the same time, the transmitted state of polarization from the sample corresponding to each launched state of polarization is analysed using PSA and a photodetector. Through the Mueller analysis of the recorded data (Ref. [151]), the system calculates all sixteen Mueller matrix elements of the sample under test, thereby providing a complete polarization behaviour of the sample.

Note that, both the Metripol and Mueller polarimetry are based on intensity variations as a function of polarization and are therefore unaffected by scattering and absorption in diamond.

2.1.3 Raman microscopy

Apart from birefringence, stress also leads to a splitting and/or a shift in the Raman frequency of the material. Raman microscopy with spatially resolved techniques such as mapping and depth profiling is employed, in order to determine the magnitude of stress and its spatial

distribution in the crystal.

A confocal microscope equipped with Raman spectrometer (Renishaw RM1000 Micro-Raman spectrometer) was used to record the Raman spectra as a function of position in the diamond sample. A 2400 lines/mm grating and 50 μm slit provided 5 cm^{-1} spectral resolution. A frequency doubled Nd:YAG laser at 532 nm was used as the excitation source. A 50× objective lens with numerical aperture of 0.75 provided a 1 μm probe beam spot size. A motorized stage was used to raster the sample in the X-Y plane in 25 μm steps. As discussed below, no splitting of the spectrum was observed. Thus it was sufficient to characterize the Raman spectra at each point using a Gaussian function that captured the width and the peak position. The resolution of the peak shift measurement was 0.17 cm^{-1} for a single pixel. By averaging over many pixels in a particular region of interest, the effective resolution of the peak position increased to 0.025 cm^{-1} or approximately 50 times less than the Raman linewidth.

2.2 Linear and circular birefringence along [110] direction

This section presents the stress characterization of two laser-grade diamond samples (A and B) with dimensions $8 \times 4 \times 1$ mm typically used in Raman lasers. Both the samples are from the same batch, with nitrogen impurity content approximately 20-40 ppb. The dimensions and crystallographic orientations are illustrated in Fig. 1.8 (see Sec.1.3.1).

Figures. 2.4 shows the maps of the magnitude and direction of linear retardance and circular retardance along the [110] direction (through the 1×4 mm end) obtained using Metripol and Mueller polarimetry of two samples A and B.

For sample A, the qualitative features from the two methods are similar, showing a complex birefringence pattern across the sample. Both the Metripol and Mueller measurements reveal extended features in the growth direction in the central region of the crystal, and to the right of centre, with linear retardance up to 55° (Δn up to 1.2×10^{-5}) as measured using Mueller polarimetry and up to 50° (Δn up to 1.1×10^{-5}) using Metripol. From Fig. 2.4, it can be seen that the values obtained using Mueller substantially differ from the Metripol values depending upon the magnitude and handedness of circular retardance (refer bottom map). Both measurement methods also show that the direction of linear retardance varies markedly across the sample from $-90°$ to $+90°$. Quantitatively, the linear retardance direction obtained

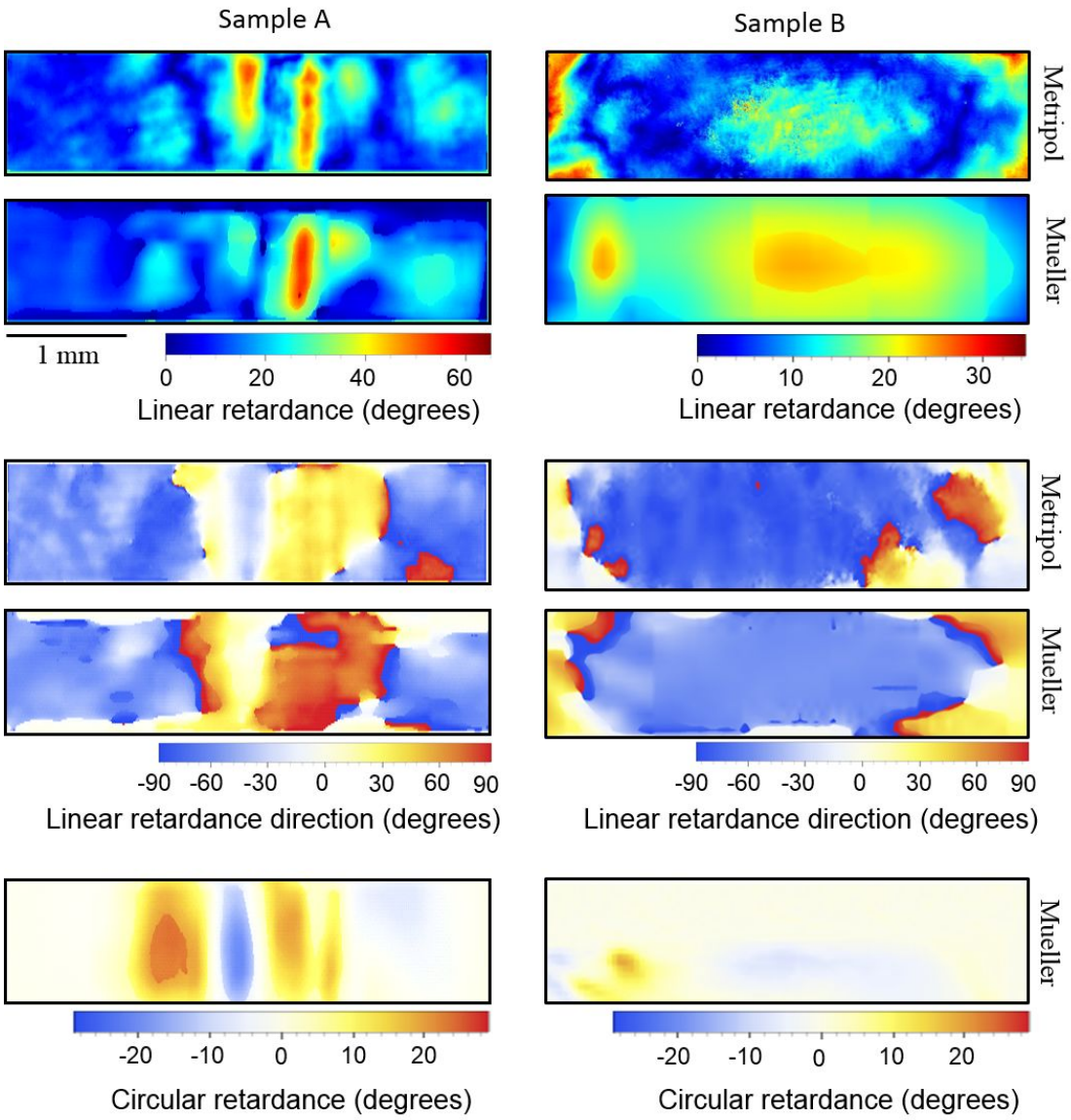

Figure 2.4: Metripol and Mueller polarimetry-obtained values of linear retardance magnitude, direction and circular retardance for samples A and B. Positive and negative values correspond to dextro and levo rotation respectively. 0° represents the $[1\bar{1}0]$ (horizontal in figure) direction.

using both techniques differ from each other by approximately 5° to 15° across the map. This is attributed to two causes: small errors in the orientation and the quality of the broadband quarter waveplate used in the Metripol measurements. In addition, as with the magnitude of linear retardance, there are notable discrepancies between Metripol and Mueller in the central of the crystal where there is significant circular retardance. In this sample, circular retardance values of up to 28° are observed in some locations in the sample. As a stack

of waveplates with varying magnitude and direction of linear retardance can be reduced to a single waveplate and rotator [154–156], some circular retardance is expected. However, it is interesting that the magnitude of circular retardance is up to approximately half of the maximum linear retardance observed in the crystal.

For sample B, the qualitative features obtained from both the techniques are similar to sample A. Fig. 2.4 shows that both the magnitude and orientation of linear retardance is uniform across the large central region of the sample. The magnitude of linear retardance is measured to be up to 25° (Δn up to 5.5×10^{-6}). Negligible circular retardance is measured across the whole sample except at a small region towards the left corner with a circular retardance of about 13°. The magnitude of linear retardance measured using Mueller is systematically higher than for Metripol across the sample by up to 7°. This offset is slightly higher than for sample A and is attributed to an offset error in the analyzing polarizer orientation (see Fig. 2.1) with respect to the quarter waveplate. The linear retardance direction obtained using each technique are generally consistent within a small margin (5°) consistent with the small circular retardance over most of the sample area. Note that the retardance values towards the edges in Mueller measurements might contain invalid data (and thus the larger discrepancy between Metripol and Mueller) due to beam blocking.

Of the other polarization characteristics measured using Mueller polarimetry (eg. linear and circular dichroism), none were detected in significant quantities in either of these samples.

Although the two samples characterized here are from the same batch, there is a considerable difference in the birefringence properties exhibited by both the crystals. Sample A exhibits relatively large linear and circular retardance magnitudes and more complex behaviour of these across the sample.

2.2.1 Effect of circular retardance on Metripol measurements

Since it was observed that the linear birefringence (especially the orientation of linear birefringence) measured using the two techniques deviate significantly in the regions with circular retardance, it is necessary to quantify the effect of circular retardance on the accuracy of the Metripol determined linear retardance.

The Jones matrix of the sample in Eq. 2.1 assumes that the sample possesses only linear retardance. When the circular retardance χ is introduced into the Jones matrix of the sample

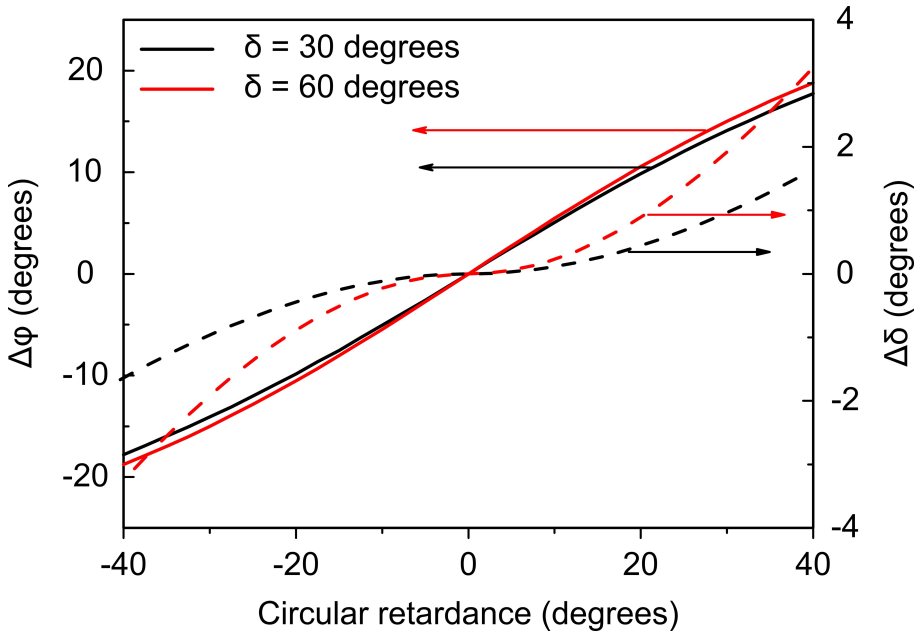

Figure 2.5: Shift in Metripol measured magnitude (dashed lines) and direction (full lines) of linear retardance as a function of circular retardance. Black and red lines indicate the values for $\delta = 30°$ and $\delta = 60°$ respectively.

under test, it can be expressed as [149]

$$M = \begin{bmatrix} e^{\frac{i\delta}{2}} & -2\chi\frac{\sin\frac{\delta}{2}}{\delta} \\ 2\chi\frac{\sin\frac{\delta}{2}}{\delta} & e^{\frac{-i\delta}{2}} \end{bmatrix}. \tag{2.4}$$

Thus the Jones matrix that describes the transmitted intensity through the entire Metripol setup becomes

$$\mathbf{A''} = \frac{1}{2}\begin{bmatrix} 1 & 1 \\ 1 & 1 \end{bmatrix}\begin{bmatrix} e^{\frac{i\pi}{4}} & 0 \\ 0 & e^{\frac{-i\pi}{4}} \end{bmatrix}\begin{bmatrix} e^{\frac{i\delta}{2}} & -2\chi\frac{\sin\frac{\delta}{2}}{\delta} \\ 2\chi\frac{\sin\frac{\delta}{2}}{\delta} & e^{\frac{-i\delta}{2}} \end{bmatrix}\begin{bmatrix} \cos\theta & \sin\theta \\ -\sin\theta & \cos\theta \end{bmatrix}\begin{bmatrix} 1 \\ 0 \end{bmatrix} \tag{2.5}$$

The effect of non-zero χ causes a shift in the amplitude and phase of the Metripol curve which thus affects the Metripol measured magnitude and direction of the linear retardance. Fig. 2.5 shows the shift in Metripol measured magnitude and direction of linear retardance with circular retardance. The magnitude and direction of linear retardance increases with positive circular retardance and decreases with negative circular retardance. The shift is higher for larger values of linear retardance magnitude. For example, for a region in the sample having maximum linear retardance magnitude of 55° oriented at 75°, and circular retardance of 25°, the Metripol-determined values for the magnitude and direction of the linear retardance are 53° and 60° respectively. Accordingly, in the Metripol birefringence map of

Sample A (Fig. 2.4), areas that have significant circular retardance have errors attributable to circular retardance of up to 5° in magnitude and 27° in orientation. In the central region of sample A, the Metripol-determined values of magnitude and direction of linear retardance are found to be higher than the Mueller-determined values because of negative circular retardance in this area. Thus, in regions of the crystal with significant circular retardance, the Metripol-determined values of linear birefringence magnitude and direction are deduced to be perturbed and inaccurate.

2.3 Birefringence and piezo-Raman effect for the (001) plane

2.3.1 Measurements

In order to elucidate the cause of circular birefringence observed through the [110] face in sample A, the stress effects along the perpendicular direction ([001] growth direction) was investigated in detail using Metripol polarimetry and Raman microscopy, as shown in Fig. 2.6. The Metripol polarimetry was used here, as the primary interest was to characterize the stress distribution through the [001] face rather than the details of each Mueller matrix component. Also, it was more convenient to use Metripol as it was an in-house system and therefore more accessible. As seen in Figs. 2.6 (a) and (b), the magnitude and direction of linear retardance as viewed along the [001] direction shown complex behaviour across the crystal face. Magnitudes up to 60° are observed, which, given the much shorter path length through this direction of the crystal, correspond to Δn values up to 1.1×10^{-4} or an order of magnitude higher than the linear birefringence measured along [110] as expected for the growth direction (see also Sec.1.3.3) [145, 157]. Here again, we can see a clear correlation between the patterns in magnitude and birefringence axis direction. On the left side of the image, there are patterns aligned nearby the [010] direction. A notable feature with two-fold symmetry is observed on the right-hand side slightly above centre.

Fig. 2.6 (c) shows the shift of the Raman centre frequency for back-scattering along the [001] direction. No broadening of the peak was observed within the measurement uncertainty indicating that the sampling volume is smaller than the granularity of the stress pattern. The shift is calculated with respect to the minimum stress value obtained at the bottom left-hand side of the birefringence map. A similar map is obtained for the laser focused 0.5 mm below the sample surface, indicating that the map is representative of the stress field throughout the

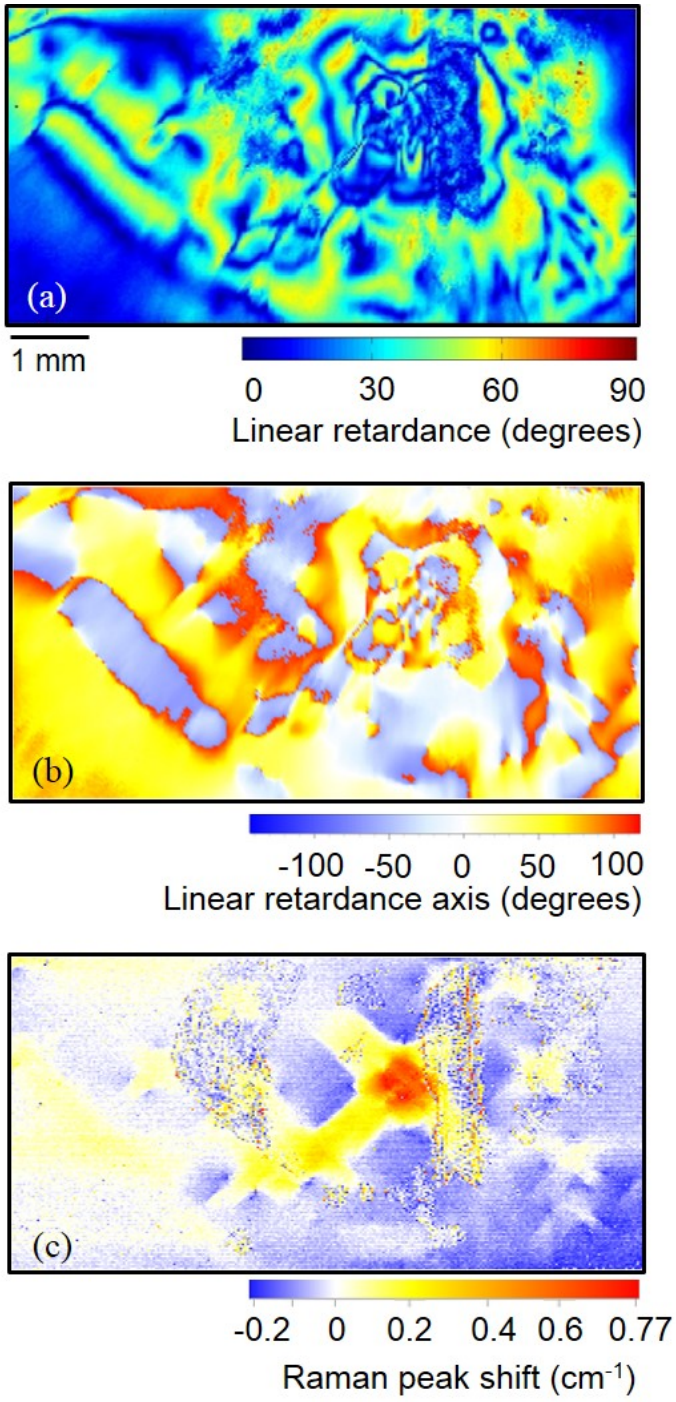

Figure 2.6: (a) Magnitude, (b) direction of linear retardance across (001) plane obtained from Metripol (0° represents [110] direction) and (c) a map of the shift in the Raman centre frequency as measured by Raman back-scattering from the (001) surface of sample A.

1 mm-thick sample. Both positive and negative shifts in Raman frequency were observed but the individual spectra showed no splitting of the Raman line. This is consistent with the polarization selection rules for Raman scattering studied by Kaenel *et al.*, where only a

singlet peak is observed for back-scattering from a (001) surface, in the cases of uniaxial or biaxial stresses acting in the (001) plane [130]. In diamond, positive and negative shifts correspond to compressive stress and tensile stress respectively [134, 137, 158].

The Raman frequency map contains features that correspond to the two main features in the Metripol images; stress features that are elongated in the [010], and a region of large frequency shift that coincides with the two-fold symmetric pattern (on the right-hand side above centre). It is interesting to note that this latter region has the largest frequency shift while having relatively low birefringence. The maximum peak shift is +0.7 cm^{-1}, approximately half the Raman linewidth in diamond (1.5 cm^{-1} [119, 159, 160]). On-average along the length of the crystal (along [110]), the magnitude of the shift is less than 0.13 cm^{-1}. Since this is a small fraction of the Raman linewidth (1.5^{-1}) and occupies only a fraction of length, we do not expect a significant stress-induced decrease in the Raman gain of this crystal for beams propagating along the [110].

The correspondence between the birefringence and Raman frequency shift observed can be understood by considering the effect of stress on the piezo-Raman and piezo-optic tensor, and is described below. The analysis below is focussed in particular on interpreting the observed behaviour in the anomalous region right-of-centre in the maps showing low birefringence and a large Raman shift.

2.3.2 Piezo-optic effect

This section evaluates the effect of stress on birefringence in terms of piezo-optic (or stress-optic) tensor components.

For a linear strain, the stress (σ_{kl}) and strain (ϵ_{ij}) tensors are related by Hooke's law as [161]

$$\epsilon_{ij} = s_{ijkl}\sigma_{kl} \tag{2.6}$$

where s_{ijkl} is the 4th rank elastic compliance tensor. For diamond, a cubic crystal, the elastic compliance tensor in the Voigt abbreviated notation (see Appendix A for more details) is

given by [131]

$$s = \begin{bmatrix} s_{11} & s_{12} & s_{12} & 0 & 0 & 0 \\ s_{12} & s_{11} & s_{12} & 0 & 0 & 0 \\ s_{12} & s_{12} & s_{11} & 0 & 0 & 0 \\ 0 & 0 & 0 & s_{44} & 0 & 0 \\ 0 & 0 & 0 & 0 & s_{44} & 0 \\ 0 & 0 & 0 & 0 & 0 & s_{44} \end{bmatrix}, \tag{2.7}$$

Hooke's law can also be written as

$$\sigma_{ij} = c_{ijkl}\epsilon_{kl}, \tag{2.8}$$

where c_{ijkl} is the 4th rank elastic stiffness tensor and the elastic stiffness and compliance tensors are related by [161]

$$\begin{aligned} c_{11} &= \frac{s_{11} + s_{12}}{(s_{11} - s_{12})(s_{11} + 2s_{12})}, \\ c_{12} &= \frac{-s_{12}}{(s_{11} - s_{12})(s_{11} + 2s_{12})}, \text{ and} \\ c_{44} &= \frac{1}{s_{44}}. \end{aligned} \tag{2.9}$$

The change in dielectric impermittivity tensor (which is related to Δn) due to an applied stress σ_{ij} is given by [162]

$$\zeta_{ij} = \pi_{ijkl}\sigma_{kl} \qquad i, j, k, l = 1, 2, 3, \tag{2.10}$$

where π_{ijkl} is the fourth rank piezo-optic tensor (or stress-optic tensor), or in terms of strain is given by

$$\zeta_{ij} = p_{ijkl}\epsilon_{kl} \qquad i, j, k, l = 1, 2, 3, \tag{2.11}$$

where p_{ijkl} is the fourth rank photoelastic tensor which is related to the piezo-optic tensor by

$$\pi_{ijkl} = p_{ijmn}s_{mnkl} \qquad i, j, k, l, m, n = 1, 2, 3. \tag{2.12}$$

For a biaxial stress, Eq. 2.10 in the Voigt abbreviated notation becomes

$$\zeta_\lambda = \begin{bmatrix} \pi_{11} & \pi_{12} & \pi_{12} & 0 & 0 & 0 \\ \pi_{12} & \pi_{11} & \pi_{12} & 0 & 0 & 0 \\ \pi_{12} & \pi_{12} & \pi_{11} & 0 & 0 & 0 \\ 0 & 0 & 0 & \pi_{44} & 0 & 0 \\ 0 & 0 & 0 & 0 & \pi_{44} & 0 \\ 0 & 0 & 0 & 0 & 0 & \pi_{44} \end{bmatrix} \begin{bmatrix} \sigma_{11} \\ \sigma_{22} \\ 0 \\ 0 \\ 0 \\ 0 \end{bmatrix} \tag{2.13}$$

$$= \begin{bmatrix} \sigma_{11}\pi_{11} + \sigma_{22}\pi_{12} \\ \sigma_{11}\pi_{12} + \sigma_{22}\pi_{11} \\ \sigma_{11}\pi_{12} + \sigma_{22}\pi_{12} \\ 0 \\ 0 \\ 0 \end{bmatrix}, \tag{2.14}$$

where the birefringence Δn is given in terms of ζ_λ as

$$\Delta n = (n_0 - \frac{n_0^3}{2}\zeta_1) - (n_0 - \frac{n_0^3}{2}\zeta_2). \tag{2.15}$$

When the birefringence is viewed along the [001] direction, which is the case in Fig. 2.6, Eq. 2.15 becomes

$$\Delta n = \frac{n_0^3}{2}(\sigma_{22} - \sigma_{11})(\pi_{11} - \pi_{12}). \tag{2.16}$$

Hence, for a biaxial stress along the [001] direction, the birefringence is proportional to the difference between the stress components σ_{11} and σ_{22} (along [010] and [100] directions).

2.3.3 Piezo-Raman effect

As discussed in Chapter 1 (Sec.1.2.1), the Raman signal depends on the pump and Stokes polarization vectors according to Eq. 1.9. The three Raman tensors correspond to the three first-order Raman modes of the diamond lattice which, in the absence of strain, are degenerate (ω_0). In the presence of strain, the degeneracy may be lifted and the Raman lineshape is broadened. In order to understand the role of stress in forming the observed piezo-Raman

map, an analysis was performed similar to that of Wolf [131] for silicon. Here the Raman frequency shift for backscattered polarization components of the incident light are evaluated.

For a linear strain, the frequencies ω_{i} of the optical phonon modes of diamond are given by the solution of the eigenvalues of the secular equation given by [128, 131, 163]

$$\begin{vmatrix} P\epsilon_{11}+Q(\epsilon_{22}+\epsilon_{33})-\lambda & 2R\epsilon_{12} & 2R\epsilon_{31} \\ 2R\epsilon_{12} & P\epsilon_{22}+Q(\epsilon_{11}+\epsilon_{33})-\lambda & 2R\epsilon_{23} \\ 2R\epsilon_{31} & 2R\epsilon_{23} & P\epsilon_{33}+Q(\epsilon_{11}+\epsilon_{22})-\lambda \end{vmatrix} = 0, \tag{2.17}$$

where P, Q and R are the phonon deformation potentials (the parameters that describe the dependence of phonon frequencies on the strain), ϵ_{11}, ϵ_{22}, ϵ_{33} are the normal strain components and ϵ_{12}, ϵ_{23}, ϵ_{31} are the shear strain components and $\lambda_{\mathrm{i}} = \omega_{\mathrm{i}}^2 - \omega_0^2$. This equation has three solutions for the eigenvalues λ_1, λ_2, λ_3 and thus three frequencies ω_1, ω_2 and ω_3.

The stress induced Raman shift for each peak is given by $\Delta\omega_{\mathrm{i}} = \omega_{\mathrm{i}} - \omega_0$. In most cases, the frequency shift (less than 1 cm^{-1} for diamond) is small compared to ω_0 (1332 cm^{-1}) and hence ω_i+$\omega_0 \simeq 2\omega_0$. Hence

$$\Delta\omega_i = \omega_i - \omega_0 \simeq \frac{\lambda_i}{2\omega_0} \qquad i = 1, 2, 3. \tag{2.18}$$

If we assume the shear stress components are zero, then using Eq. 2.6 the stress tensor can be expressed as [131]

$$\begin{aligned} \epsilon_{11} &= s_{11}\sigma_{11} + s_{12}\sigma_{22} + s_{12}\sigma_{33}, \\ \epsilon_{22} &= s_{12}\sigma_{11} + s_{11}\sigma_{22} + s_{12}\sigma_{33}, \\ \epsilon_{33} &= s_{12}\sigma_{11} + s_{12}\sigma_{22} + s_{11}\sigma_{33}, \\ \epsilon_{12}, \epsilon_{23}, \epsilon_{13} &= 0, \end{aligned} \tag{2.19}$$

and Eq. 2.17 becomes

$$\begin{vmatrix} P\epsilon_{11}+Q(\epsilon_{22}+\epsilon_{33})-\lambda & 0 & 0 \\ 0 & P\epsilon_{22}+Q(\epsilon_{11}+\epsilon_{33})-\lambda & 0 \\ 0 & 0 & P\epsilon_{33}+Q(\epsilon_{11}+\epsilon_{22})-\lambda \end{vmatrix} = 0, \tag{2.20}$$

from which the eigenvalues is solved as

$$\lambda_1 = P\epsilon_{11} + Q(\epsilon_{22} + \epsilon_{33})$$

$$\lambda_2 = P\epsilon_{22} + Q(\epsilon_{11} + \epsilon_{33})$$
$$\lambda_3 = P\epsilon_{33} + Q(\epsilon_{11} + \epsilon_{22}). \tag{2.21}$$

From Eqs. 2.18, 2.19 and 2.21, the shift in Raman peaks is expressed as

$$\begin{aligned}
\Delta\omega_1 &= \frac{1}{2\omega_0}[(Ps_{12} + Q(s_{11} + s_{12}))(\sigma_{22} + \sigma_{33}) + (Ps_{11} + 2Qs_{12})\sigma_{11}],\\
\Delta\omega_2 &= \frac{1}{2\omega_0}[(Ps_{12} + Q(s_{11} + s_{12}))(\sigma_{11} + \sigma_{33}) + (Ps_{11} + 2Qs_{12})\sigma_{22}],\\
\Delta\omega_3 &= \frac{1}{2\omega_0}[(Ps_{12} + Q(s_{11} + s_{12}))(\sigma_{11} + \sigma_{22}) + (Ps_{11} + 2Qs_{12})\sigma_{33}].
\end{aligned} \tag{2.22}$$

The intensity of each of these Raman shifted frequencies is calculated to determine the Raman frequencies that are visible for a chosen polarization direction of the incident and scattered light. The total Raman intensity is given by [131, 164]

$$I = C\sum_{i=1}^{3} d^2 f_{\mathrm{i}}^2, \tag{2.23}$$

where C is a proportionality constant and f_{i} is defined as

$$f = \begin{bmatrix} f_1 \\ f_2 \\ f_3 \end{bmatrix} = \begin{bmatrix} e_{2\mathrm{P}}e_{3\mathrm{S}} + e_{3\mathrm{P}}e_{2\mathrm{S}} \\ e_{3\mathrm{P}}e_{1\mathrm{S}} + e_{1\mathrm{P}}e_{3\mathrm{S}} \\ e_{1\mathrm{P}}e_{2\mathrm{S}} + e_{2\mathrm{P}}e_{1\mathrm{S}} \end{bmatrix}, \tag{2.24}$$

where e_{P} and e_{S} are the polarization vectors of the incident and scattered light given by

$$e_{\mathrm{P}} = \begin{bmatrix} e_{1\mathrm{P}} & e_{2\mathrm{P}} & e_{3\mathrm{P}} \end{bmatrix}, e_{\mathrm{S}} = \begin{bmatrix} e_{1\mathrm{S}} & e_{2\mathrm{S}} & e_{3\mathrm{S}} \end{bmatrix}. \tag{2.25}$$

For backscattering from the diamond surface along the Z direction ([001] in both crystal direction and Cartesian direction), only the X ([100] Cartesian direction or $[1\bar{1}0]$ crystal direction) and Y ([010] Cartesian direction or [110] crystal direction) components of the polarization vectors will be non-zero. Hence, the polarization vectors are given by

$$e_{\mathrm{P}} = \begin{bmatrix} e_{1\mathrm{P}} & e_{2\mathrm{P}} & 0 \end{bmatrix}, e_{\mathrm{S}} = \begin{bmatrix} e_{1\mathrm{S}} & e_{2\mathrm{S}} & 0 \end{bmatrix}. \tag{2.26}$$

Eq. 2.24 thus becomes

$$f = \begin{bmatrix} 0 \\ 0 \\ e_{1\mathrm{P}}e_{2\mathrm{S}} + e_{2\mathrm{P}}e_{1\mathrm{S}} \end{bmatrix}, \tag{2.27}$$

and hence only the third peak $\Delta\omega_3$ will be visible in this configuration, consistent with the observations in Sec.2.3.

For a biaxial stress in the (001) plane observed by back-scattering along the [001] direction, the shift in Raman frequency can be obtained from Eq. 2.22 as

$$\begin{aligned}\Delta\omega_R &= \frac{1}{2\omega_0}[(\sigma_{11}+\sigma_{22})(Ps_{12}+Q(s_{11}+s_{12}))] \\ &= -8.1576\times10^{-10}(\sigma_{11}+\sigma_{22}).\end{aligned} \tag{2.28}$$

Evaluation of Eq. 2.28 enables the stress values to be determined. The values of P and Q were calculated from the mode-Gruneisen parameter γ_G ($\gamma_G = -(P+2Q)/6\omega_0^2$) and the factor $(P-Q)/2\omega_0^2$ given in Ref. [165]. The values of s_{11} and s_{12} were calculated from the elastic stiffness constants c_{11} and c_{12} given in Ref. [166] using Eq. 2.9. The maximum frequency shift of +0.7 cm^{-1} corresponds to biaxial stress $(\sigma_{11}+\sigma_{22})$ of 0.86 GPa. For the case of uniaxial stress (stress features elongated in the [010] direction), the maximum peak shift is approximately 0.25 cm^{-1} which corresponds to a stress value of 0.3 GPa. Regions of the crystal with negative frequency shift indicate the action of tensile biaxial stress.

From the piezo-optic and piezo-Raman analysis, birefringence is proportional to the difference between the stress components and the Raman frequency shift is proportional to the sum of the stress components for a biaxial stress acting along the (001) plane. Hence, the two-fold symmetric feature of low Δn and high $\Delta\omega_R$ seen in Fig. 2.6 is consistent with a transversely isotropic stress field (σ_{11} approximately equal to σ_{22}) in the (100) plane. For uniaxially stressed regions (σ_{11} or σ_{22} approximately equal to 0), $\Delta\omega_R$ increases with Δn which is consistent with scenarios on the left-hand side of the crystal.

2.3.4 Correlation between top and end-on mapping

Fig. 2.7 reveals that the extended stripe feature in the birefringence map as viewed end-on in the [110] direction coincides with the strong two-fold feature in the (001) birefringence map (and thus also the corresponding feature in the piezo-Raman map, described in Sec.2.3.1). Following the discussions in Sec.1.3.2, bundles of edge dislocations lying near parallel to a (001) direction give rise to stress induced birefringence patterns with a 2-fold symmetric petals as shown in Fig. 1.10 [141] which is similar to the two-fold symmetric birefringence pattern of sample A in the (001) plane (Fig. 2.7). Hence, the most likely cause of this symmetric pattern in the (001) plane which results in the extended stripe pattern when

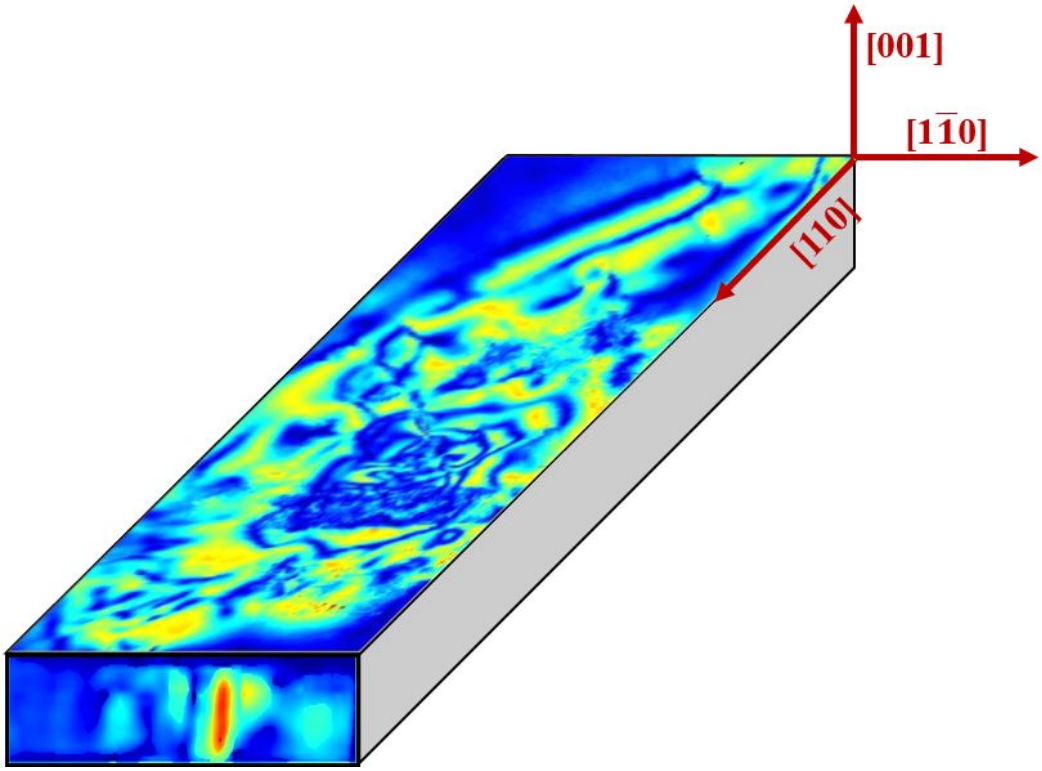

Figure 2.7: Maps of linear birefringence magnitude an measured through the (110) and top (001) faces for sample A.

viewed end-on (along the [110] direction) is due to the such edge dislocations and thus may be the cause of large circular retardance observed in Fig. 2.4.

2.4 Discussion

As discussed in Chapter 1, the polarization behaviour of CW DRLs deviated significantly from that predicted by the Raman tensors and this has been attributed to stress-induced birefringence [93, 127]. Hence, the detailed birefringence characterization performed in this chapter can be used to understand the influence of birefringence in the polarization behaviour of CW DRLs and is the main theme of Chapter 3. Sample A is appropriate for evaluating the birefringence dependence on polarization behaviour as it exhibited the largest variation in the birefringence properties, thus providing a sufficiently large set to understand the polarization behaviour as a function of birefringence. Sample B, with its relatively uniform and lower birefringence, is anticipated to be a more suitable candidate for DRL

operation. The investigation on the dependence of laser performance on birefringence in the following Chapter will assist in the choice of selecting the appropriate diamond samples and the optimum locations within each crystal.

Apart from Raman lasers, stress induced birefringence in diamond is known to influence the properties of polarization sensitive devices such as intracavity heat spreaders [112]. Low loss operation was found to be achieved by rotating the sample to match the direction of linear birefringence or by using a diamond with lower birefringence. The detailed characterization including circular birefringence presented here is likely to provide a more comprehensive understanding of the birefringence dependence on polarization sensitive devices such as intracavity heat spreaders.

2.5 Chapter summary

The birefringence properties of two single crystal CVD diamonds along the [110] were characterized using Metripol and Mueller polarimetry. One sample (B) showed a uniform birefringence with negligible circular retardance over most of the sample region. The other (A) revealed much more varied behaviour with an extended feature along the growth direction as well as significant circular retardance almost of the order of linear birefringence. The effect of the circular component in the linear retardance measurement of Metripol was studied using Jones matrix analysis. It was found that the presence of circular retardance leads to errors in Metripol measured linear birefringence. Hence, a complete polarization characterization technique such as Mueller polarimetry is a generally more appropriate tool for characterizing CVD diamonds.

The stress characterization using Metripol and Raman microscopy in the perpendicular plane ((001) plane) provided insights into the origin of the observed birefringence along [110]. It was found that the region of high linear and circular birefringence (along [110]) coincides with a two-fold symmetric pattern characterized by large $\Delta\omega_R$ but lower birefringence (as viewed along the (001) plane). The most likely cause of this pattern is the edge dislocation originating from the growth substrate surface.

Tensor analysis showed that the two-fold symmetric pattern is consistent with a biaxial stress field which perturbs the Raman frequency but has little effect on the birefringence magnitude. Raman shifts of up to 0.7 cm^{-1} were measured which correspond to biaxial stress

values of up to 0.86 GPa. Along the length of the crystal ([110] direction), the average Raman shift is less than 10% of the Raman linewidth. Hence, a reduction in the Raman gain is not expected along the usual propagation direction for Raman lasers. Uniaxial stresses were also observed with maximum Raman shift up to 0.25 cm^{-1}.

The comprehensive stress characterization presented in this chapter, apart from being important for Raman lasers, may also impact other polarization sensitive devices such as intracavity heat spreaders and on-chip diamond lasers.

The main results of this chapter were published in Hadiya Jasbeer, Robert J. Williams, Ondrej Kitzler, Aaron McKay, Soumya Sarang, Jipeng Lin and Richard P. Mildren, "Birefringence and piezo-Raman analysis of single crystal CVD diamond and effects on Raman laser performance", JOSA B, Vol 3, No 5, pp. B56–B64 (2016).

3

The effects of diamond birefringence in CW DRLs

Birefringence is known to affect the operation of various laser systems such as Nd:YAG lasers [167], VECSELs [168], and microchip solid-state lasers [169]. In this chapter, the effect of birefringence on the performance of CW DRLs is investigated in detail.

Polarization characteristics of low-Q (such as nanosecond pulsed) DRLs were found to be in accordance with the theoretically predicted polarization dependence of Raman gain [124]. However, as introduced in Chapter 1, the polarization behaviour in the CW regime deviated significantly from those theoretical predictions. Moreover, the observed variability in Stokes polarization as a function of pump polarization was attributed to stress-induced birefringence in diamond [127]. Since the Raman gain depends on both the pump and Stokes polarizations, any deviation of the polarization behaviour affects the Raman gain and thus the laser performance. Hence, it is critical to study the impact of birefringence on the polarization dynamics as a means to optimize its performance.

The comprehensive birefringence characterization of CVD single crystal diamond performed in Chapter 2 is utilized here to study the laser performance across the crystal. Laser characteristics such as threshold, output polarization, and pump depolarization were measured as a function of pump polarization across the crystal with a range of birefringence properties. The results were compared with the polarization behaviour of pulsed DRLs. In order to better understand the discrepancy between both the cases, an analysis based on Raman tensors was used to provide insights into the Raman gain in the presence of birefringence.

3.1 Polarization dependence of Raman gain in diamond

Following the discussions in Chapters 1 and 2, the Raman gain coefficient corresponding to the triply degenerate Raman tensors is obtained from Eq. 1.9

$$g_{\mathrm{S}} = \frac{4\pi^2 N \omega_{\mathrm{S}}}{n_{\mathrm{S}} n_{\mathrm{P}} c^2 m \omega_{\mathrm{r}} \Gamma} \sum_{i=1}^{3} (e_{\mathrm{P}} R e_{\mathrm{S}})^2. \tag{3.1}$$

Here, the total Raman gain may be broken down into contributions from each Raman mode to provide additional insights into the functional polarization dependence. Fig. 3.1 shows the individual components of Raman gain (g_{s1}, g_{s2} and g_{s3}, corresponding to the three Raman modes), and their linear combination g_{S} as a function of pump and Stokes polarizations. The 0° in Fig 3.1 represents the horizontal $\langle 1\bar{1}0 \rangle$ direction.

When varying the pump polarization, the Stokes output polarization is expected to follow the maximum Raman gain. The first two gain coefficients, g_{s1} and g_{s2} are similar, with a maximum value of 0.5 (represented by white loci in Fig. 3.1). The third component, g_{s3}, has a maximum gain along 0° (parallel to $\langle 1\bar{1}0 \rangle$) for all the pump polarizations.

The total Raman gain, g_{s}, exhibits the following behaviour: For a $\langle 1\bar{1}0 \rangle$-polarized pump, the gain is uniform for all the Stokes polarizations. For small angles of pump polarization, the gain has a maximum for a Stokes polarization near 45°. This angle counter-rotates as the pump polarization angle is increased. For a $\langle 111 \rangle$-oriented pump, the Stokes polarization is collinear and the Raman gain attains its maximum value which is 33% higher than for 0° and 90° pump polarizations. Upon further rotation of the pump polarization, the Stokes polarization continues to rotate until at a pump polarization angle parallel to $\langle 1\bar{1}0 \rangle$ there is a flip in the Stokes polarization by 90°. Note that when the pump polarization is parallel

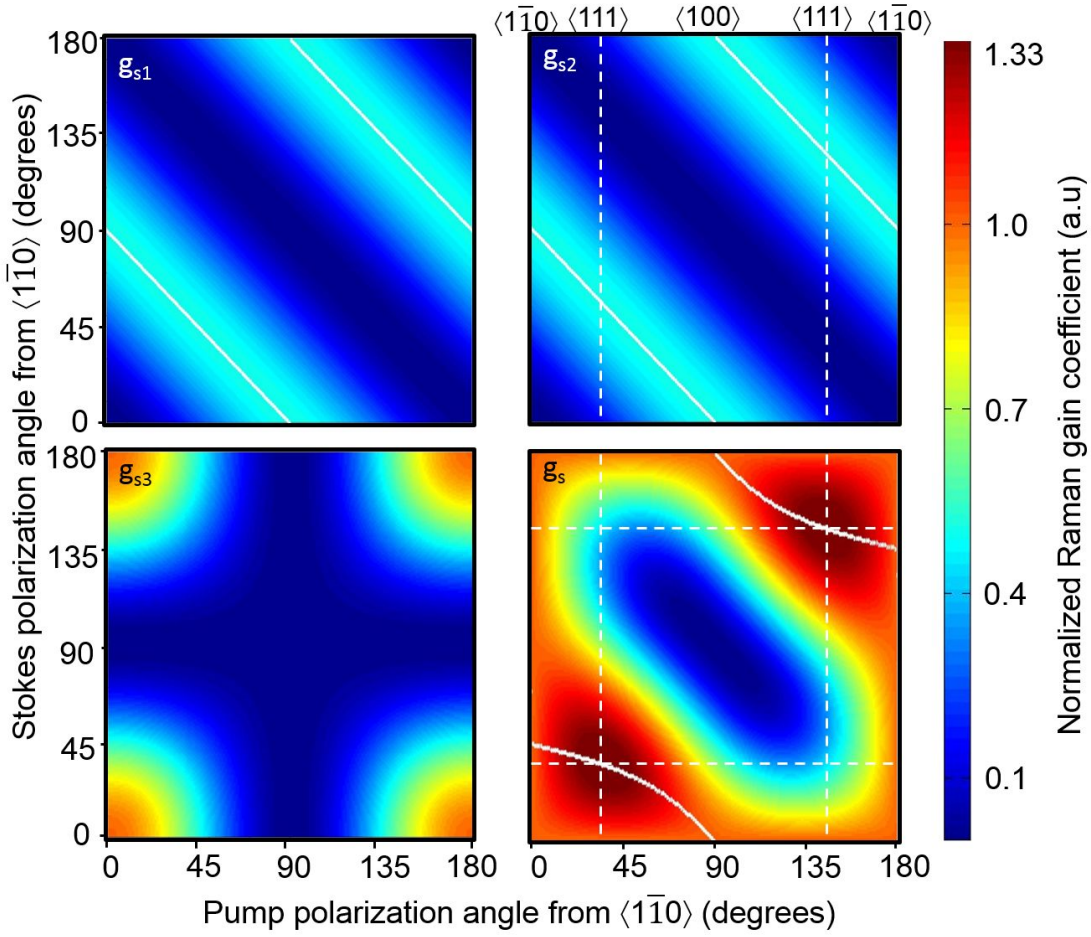

Figure 3.1: The normalized Raman gain for propagation along the ⟨110⟩ direction as a function of pump and Stokes polarizations. The first three panels represent the individual components of Raman gain (g_{s1}, g_{s2} and g_{s3}) corresponding to the three Raman modes and the fourth panel represent the total gain (g_s). Notable directions in diamond are represented by white dashed lines and the maximum Raman gain is shown by the white loci.

to ⟨111⟩, the pump and Stokes polarizations are parallel to the two interpenetrating face-centered cubic lattices that vibrate against each other to generate the first order Raman mode (see Fig. 1.7, Sec.1.3.1) [116, 124, 170].

3.2 Polarization properties of low-Q pulsed DRLs

The polarization characteristics of pulsed (low-Q) DRLs reported by Sabella *et al.* [124] agrees well with polarization dynamics of Raman gain described in the previous section

(Sec. 3.1). The diamond sample used in their experiment was a 6.9 mm long AR coated type IIa single crystal CVD diamond (Element Six, UK) with birefringence Δn of the order of 10^{-6} (along [110] direction) as measured using Metripol polarimetry. A linearly polarized Q-switched Nd:YAG laser at 1064 nm with powers up to 4.5 W, pulse duration of 10 ns at 5 kHz repetition rate was used for pumping the DRL. The output coupling for the first Stokes was 50%, making it low-Q for the first Stokes.

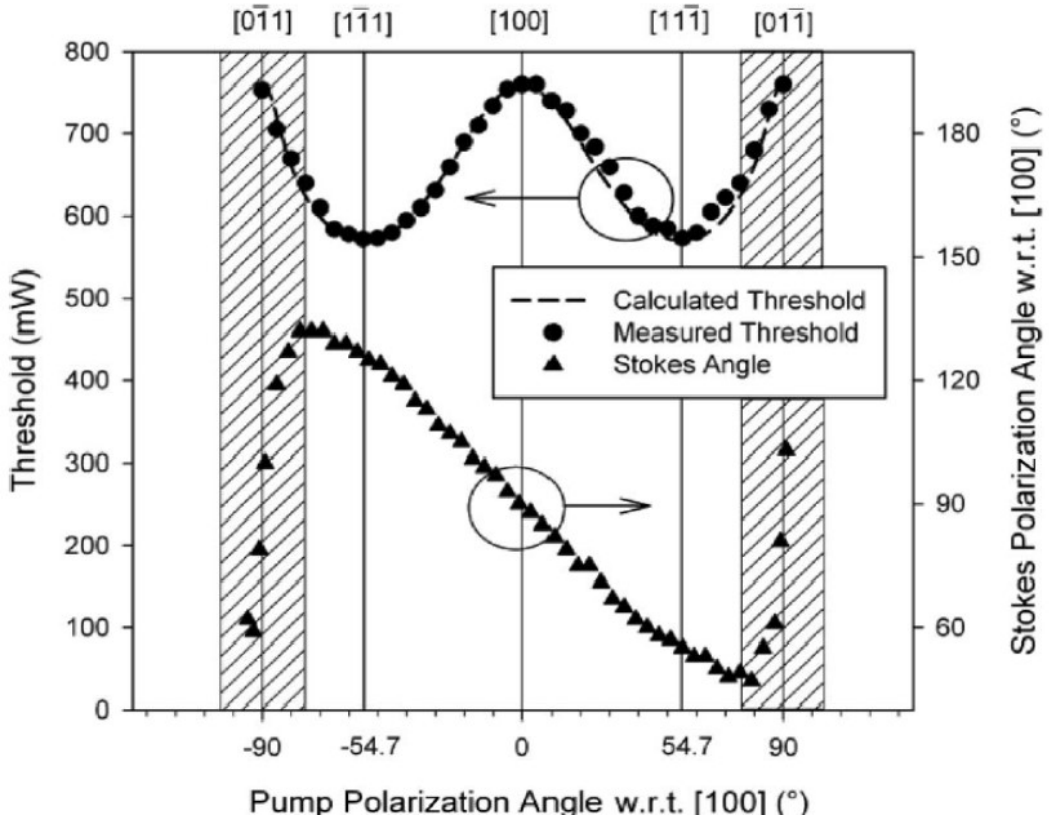

Figure 3.2: Threshold and Stokes polarization as a function of pump polarization angle in a low-Q diamond Raman laser. Figure taken from Sabella *et al.* [124].

Fig. 3.2 shows the measured (full circles) and calculated (dashed line) threshold and measured Stokes polarization angle (full triangles) as a function of pump polarization. Note that here, angles are measured from the [100] crystal direction. A minimum threshold (maximum Raman gain) was obtained when the pump polarization is aligned to the $\langle 111 \rangle$ direction and the maximum thresholds were obtained when aligned to the [110] and [100] directions, all consistent with the Raman gain plot of Fig. 3.1. Likewise, the measured Stokes polarization as a function of pump polarization is also consistent with that predicted by the locus of maximum gain in the plot. For the case of pump polarized along [110], the Stokes polarization was linearly polarized but in a random direction as expected for the two

orthogonal Stokes components of equal gain.

3.3 Polarization properties of high-Q DRLs

In this section, the laser performance is characterized for several selected locations across the diamond and correlated with the measured birefringence data at each location. The Stokes polarization, threshold, and pump depolarization were measured as a function of pump polarization angle by selecting regions in the crystal with a range of birefringence properties. Sample A (characterized in Chapter 2) is chosen as the Raman gain material as it exhibited the largest variation of birefringence along the laser propagation direction ([110] direction).

3.3.1 Experiment

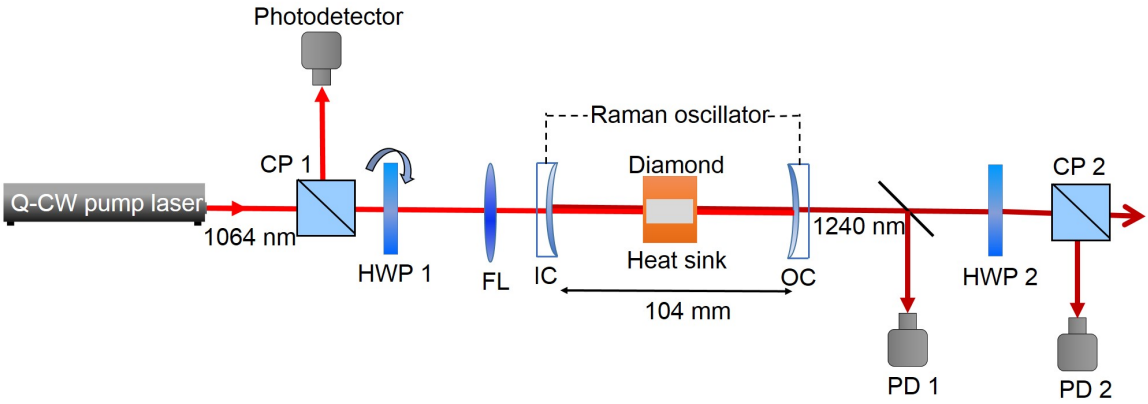

Figure 3.3: Experimental arrangement for measuring laser threshold and polarization characteristics: CP-cube polarizer, HWP-half wave plate, FL-focussing lens, IC-input coupler, OC-output coupler and PD-photodiode.

Fig. 3.3 shows the experimental arrangement providing simultaneous characterization of the Stokes polarization, lasing threshold and pump depolarization. The pump source was a quasi-CW-pumped Nd:YAG laser with horizontally polarized output at 1064 nm, operating at 40 Hz repetition rate and 1% duty cycle (pulse duration approximately 250 μs). Variable attenuation of the pump beam was achieved with a half-wave plate and polarizing cube. The diamond laser cavity was a 104 mm-long near-concentric resonator consisting of concave mirrors with 50 mm radii of curvature. The input coupler was highly transmitting (>97%) at

the pump and highly reflecting (99.98%) at the 1240 nm first Stokes. The output coupler was highly reflecting at the pump and provided 0.5% transmission at the first Stokes wavelength. The AR-coated diamond (Sample A) was placed in the centre of the cavity. A 50 mm focusing lens was used to focus the pump beam into the middle of the diamond.

The diamond was placed on an X-Y-Z translation stage, allowing different regions in the crystal to be investigated. An IR camera was used to monitor the pump spot in the diamond in order to correlate the position in the diamond with the birefringence map, with an accuracy of 0.3-mm. This procedure enabled regions of the crystal to be probed across a range of birefringence parameters. Since the beam sizes ($\sim$ 40 μm) are much smaller than the birefringence features (typically > 500 μm – refer Chapter 2), it is valid to use the polarimetry maps to obtain accurate values for birefringence parameters that are applicable to the entire beam area. Note that the mounting procedure for the diamond, which is similar to the polarimetry measurements, adds negligible stress to the crystal compared to the in-grown values. Our experience has shown that large forces are required to perturb the stress field.

The six regions (marked A, B, C, D, E and F in Fig. 3.4) were selected as these provided a range of δ, Φ and χ values and was a sufficiently large set to characterize the observed features in polarization behaviour. Regions A and F have the least amount of circular retardance (2°); B, C, D and E have circular retardance of 12°, 18°, −13° and 17°, respectively. The magnitudes and directions of linear and circular retardance for these regions are summarized in Tab. 3.1.

A half-wave plate (HWP 1 in Fig. 3.3) was used to rotate the injected pump polarization. In the following sections, the polarization angles are quoted with respect to the $\langle 1\bar{1}0\rangle$ direction (the horizontal direction in the laboratory frame of reference). The total output Stokes power was monitored using an InGaAs photodiode (PD 1 in Fig. 3.3). The Stokes degree of polarization and its principle direction were determined using a half-wave plate and cube polarizer combination (by rotating the half-wave plate and measuring the extinction).

The depolarized pump power was monitored as a function of injected pump polarization as a check of the linear retardance axis measured using the Metripol technique and verifying the region in the diamond with respect to the birefringence map. This was achieved by removing the input coupler and measuring the backreflected, depolarized pump power on a photodetector.

Measurements were performed for six regions of the crystal as shown in Fig. 3.4. Table 3.1 shows the summary of the laser characteristics such as the Stokes polarization, threshold and

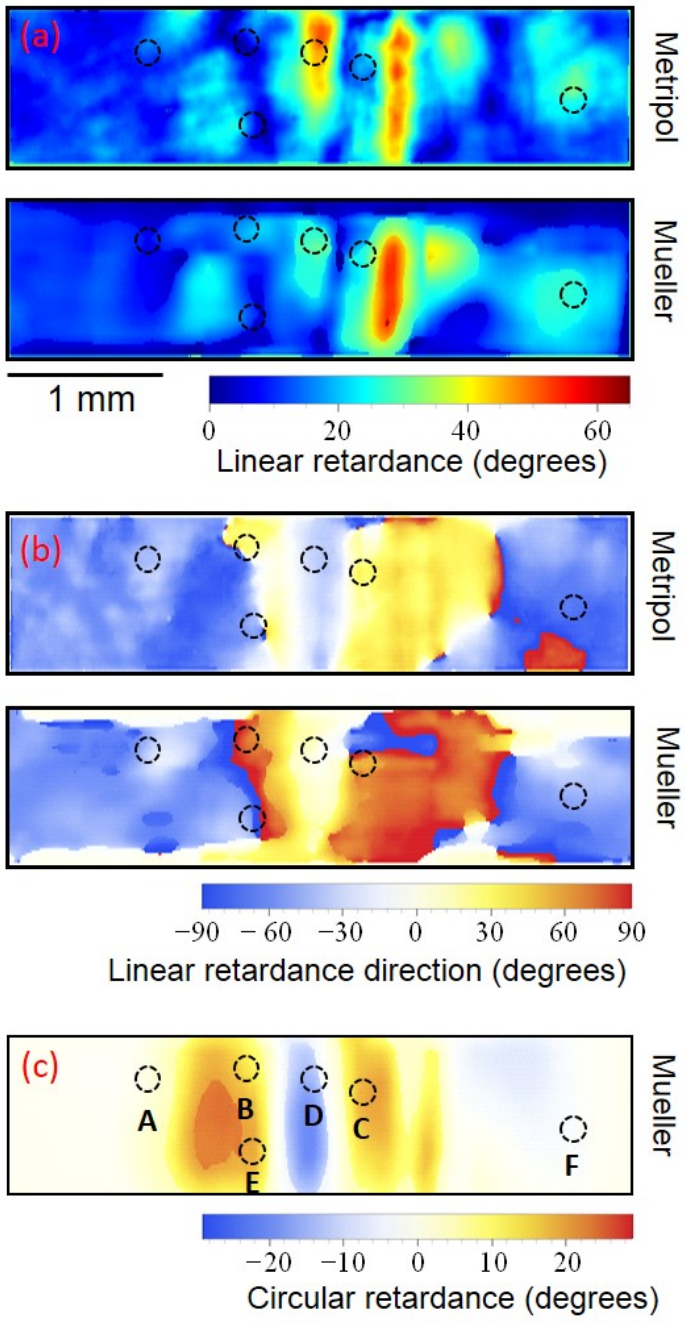

Figure 3.4: Metripol and Mueller polarimetry-obtained values of (a) linear retardance magnitude and (b) direction. (c) Circular retardance obtained from Mueller polarimetry for sample A. 0° represents the $[1\bar{1}0]$ (horizontal in figure) direction. The black circles A, B, C, D, E and F mark the six regions that were characterized under Raman laser operation. The circle diameter (0.3 mm) indicates the uncertainty in location of the laser spot.

pump depolarization for all the six regions investigated. The major focus of the following result is on the four regions A-D, which exhibit a range of representative polarization behaviours.

3.3.2 Results

Fig. 3.5 shows the output Stokes polarization (top row), measured and calculated threshold (middle row) and pump depolarization (bottom row) as a function of pump polarization. In each case, the Stokes polarization remains fixed to either of two orthogonal linear polarizations depending on the pump polarization. This is distinctly contrasting behaviour to that seen in low Q DRLs. For all regions except D, the Stokes polarization is observed to switch between the orthogonal polarizations at a point in the cycle. The switching points, and the orthogonal polarizations, vary substantially for each region. The minimum threshold for the different regions ranges from 18 to 55 W.

For region A, which has low circular retardance (2.5°), the linear birefringence axes obtained from Metripol (40°) and Mueller (46°) are in fair agreement. The two Mueller-obtained axis values closely match the two orthogonal Stokes polarizations (45° and 135°). Region F also exhibited a similar behaviour (see Tab. 3.1). No significant pump depolarization was observed for region A as expected because of the low linear birefringence value ($\Delta n = 1.6 \times 10^{-6}$).

Regions B and C have significant circular retardance which substantially perturbs the Metripol-determined direction of linear retardance. The direction obtained using the pump depolarization measurement matches the Metripol measurement as expected, since both measurements are unable to deconvolve the contributions of circular and linear retardance (see black dotted lines coinciding with the minimum of pump depolarization). For both the regions, the Stokes polarizations are aligned closer to the Mueller-determined linear retardance axis. Region E also exhibits a similar behaviour as seen in Tab. 3.1.

As for B and C, region D also has large circular retardance and thus large difference between the linear retardance directions obtained using Metripol (24°) and Mueller (2°) polarimetry. Here, as the circular retardance is negative, the Metripol determined axis direction is overvalued unlike B, C and E. Region D is also unique in that the output Stokes polarization state is constant at 178° for all pump polarizations, closer to the Mueller determined birefringence direction. The reason for this is explained in the following section.

Table 3.1: Summary of the magnitude and direction of linear and circular retardance (measured using Metripol and Mueller polarimetry), pump depolarization, Stokes polarization and minimum threshold for the crystal locations A, B, C, D, E and F indicated in Fig. 3.4

	Region A	Region B	Region C	Region D	Region E	Region F
Δn (Metripol)	1.4×10^{-6}	2.5×10^{-6}	4.5×10^{-6}	7.2×10^{-6}	2.2×10^{-6}	4.8×10^{-6}
Δn (Mueller)	1.6×10^{-6}	3.9×10^{-6}	5.3×10^{-6}	6.7×10^{-6}	3.1×10^{-6}	5.2×10^{-6}
Principle axis (Metripol)	40°	40°	46°	26°	43°	41°
Principle axis (Mueller)	45°	59°	71°	1.7°	59°	37°
Circular retardance (Mueller)	2.5°	12°	18.3°	−13.2°	17°	2°
Depolarization axes	—	40°	50°	30°	40°	40°
Stokes polarization	45° and 135°	50° and 140°	62° and 152°	178° - no flip	52° and 142°	34° and 124°
Minimum threshold	18 W	24 W	25 W	53.5 W	27 W	28 W

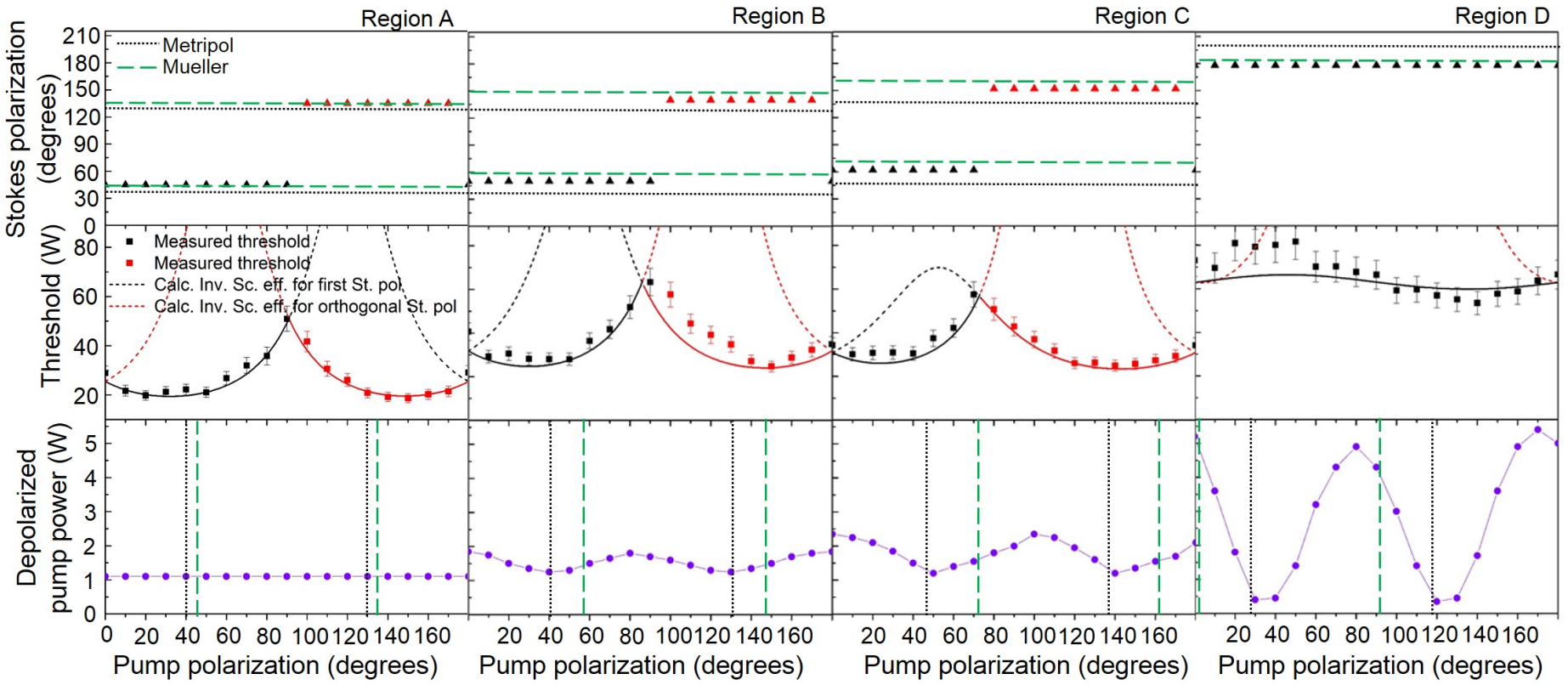

Figure 3.5: Laser properties as a function of pump polarization for regions A, B, C and D. Top row: Stokes polarization (black and red triangular marker) along with the linear retardance axis direction obtained by Metripol (black dotted line) and Mueller (green dashed line). Middle row: threshold for the orthogonal Stokes polarizations measured (black and red rectangular markers) and calculated (black and red dashed and full lines). The full lines indicate the calculated threshold corresponding to the polarization state with the highest Raman gain. Bottom row: measured pump depolarization (violet circular markers). As for the top row, the Metripol and Mueller measured linear retardance axis directions are also shown.

The Metripol determined linear birefringence direction again coincides with the direction obtained using pump depolarization measurement.

3.4 Analysis and discussion

The above results reveal that the Stokes polarization is, in all cases, fixed to either of the axes of linear retardance. This is in stark contrast to the case of low-Q (nanosecond-pulsed) diamond Raman lasers whose polarization dynamics are dictated by the Raman tensors.

Insights into the cause of the contrasting behaviour are obtained by calculating the Raman gain (and hence threshold) as a function of pump polarization for the measured output Stokes polarization. The dependence of Raman laser threshold on pump polarization was calculated according to the Raman gain in Eq. 3.1, using the measured Stokes polarizations for each region. This was then scaled to the measured threshold to account for the variations in diamond coating losses, surface quality, and cavity alignment. The middle row of Fig. 3.5 shows the measured threshold (red and black rectangular markers) and calculated threshold (red and black full and dashed lines) using the observed Stokes polarizations.

It is seen that the Stokes polarization is fixed to the retardance axis that provides the highest gain according to the injected pump polarization. For example for A, the threshold for 45° Stokes polarization is less than the threshold for 135° for pump polarizations in the range 0° to 91°, whereas the threshold for 135° Stokes polarization is less than for the 45° for pump polarizations in the range 92° to 180°. Hence, we observe that the output polarization switches between birefringence axis directions according to which has the highest gain. A similar behaviour is observed for B, C, E and F. For D, the threshold for 178° Stokes polarization is less than its orthogonal polarization over the entire range of pump polarization angles which is consistent with the absence of a transition in the measured Stokes polarization. Note that the dashed curves in Fig. 3.5 represent the gain behaviour for the Stokes polarization of lower gain than its orthogonal counterpart.

The maximum gains for all the spots except D are each of a similar magnitude because their birefringence axes are oriented close to the $\langle 111 \rangle$ crystal direction (see Fig. 3.1). This is consistent with the similar minimum threshold observed for these regions (18-28 W). The minimum threshold for D (50 W) is notably higher, partially due to the Stokes polarization being well away from the direction of maximum gain. Note that slight variations in the

coating and surface quality at each location, as well as precise alignment (which affects the pump/stokes mode overlap), also contribute to the spread of observed thresholds.

These results show that even weak stress-induced birefringence in the diamond crystal ($\Delta n \sim 10^{-6}$) affects the performance of CW DRLs, fixing the output polarizations to the local birefringence axes, and thereby determining the maximum Raman gain coefficient achievable as a function of pump polarization. As the Stokes polarization is fixed to the local linear birefringence axis, pumping along $\langle 111 \rangle$ no longer provides maximum gain in all cases but only when Stokes polarization is aligned to $\langle 111 \rangle$. Hence, if the birefringence axis is not parallel to $\langle 111 \rangle$, the gain coefficient is less than the maximum achievable.

The results, for regions A-F and all other regions investigated, show no clear correlation between the magnitude of linear or circular retardance and DRL performance, although a more careful measurement over a wider range of linear and circular retardance might reveal some effects.

The cause of the observed characteristic behaviour in the high-Q regime is explained in broad terms by considering the number of round trips of the Stokes photons before exiting the cavity given by

$$N = \frac{\tau_c}{\tau_r}, \tag{3.2}$$

where the average intracavity Stokes life-time $\tau_c = \frac{t_r}{T+2\alpha_d L_d+\kappa}$, $\tau_r = \frac{2l}{c}$ is the round-trip time for the resonator of length l, c is the speed of light, T is the transmission of the output coupler, L_d is the length of the diamond, α_d is the distributed loss including absorption and scattering losses and κ includes other losses such as coating, birefringence, and diffraction losses. Here, l is 104 mm, T is 0.5%, L_d is 8 mm, α_d is approximately 0.2%/cm and κ is approximately 0.3%, hence the Stokes photons make around 100 round-trips inside the cavity and in each trip accumulate phase retardances. For typical birefringence values in the diamond (10^{-6}), the accumulated retardance over such a number of trips equates to the order of 1-2 wavelengths and thus is expected to be an important factor in dictating polarization state behaviour. In contrast, for low-Q DRLs using an output coupler of 50%, the Stokes photons make approximately 2 round-trips and hence the accumulated effects of birefringence are greatly reduced. This provides an intuitive explanation for the contrasting polarization behaviour of low and high Q DRLs. Further investigation is required to more fully understand the cavity-Q dependence of the competition between birefringence and Raman gain in determining the Stokes polarization. This involves the development of a comprehensive model for solving the

polarization eigenmodes of the resonator, for example, by utilizing Jones matrix formalism. Such a model is also expected to elucidate the contributions of the magnitudes of linear and circular retardance in determining the polarization behaviour.

The severity of problems associated with birefringence may be reduced by improving the diamond growth conditions and thereby reducing the defects that cause birefringence. Indeed, it is apparent that material quality has already improved over the period of this thesis work with more recent diamond crystals exhibiting more uniform birefringence across the whole aperture with magnitudes of the order of 10^{-6}. Use of diamond grown by other techniques such as the high-pressure high-temperature (HPHT) technique may also provide a way to alleviate birefringence problems. In addition, engineering the stress in diamond so as to have a uniform stress distribution with the birefringence axis closer to $\langle 111 \rangle$ would aid in improving the laser performance.

Although the effect of stress was investigated in an external cavity DRL, the results can readily be extended to other high-Q DRLs such as in intracavity Raman lasers and synchronously pumped ultrafast diamond Raman lasers.

3.5 Chapter conclusions

The Stokes polarization in the investigated CW DRL is determined primarily by the local birefringence axis direction unlike the case of nanosecond-pulsed DRLs for which the output polarization follows the maximum Raman gain for a given pump polarization. Since the Raman gain is dependent on both pump and Stokes polarizations, a minimum threshold is obtained for locations in diamond where the retardance axis and pump polarization are aligned close to the $\langle 111 \rangle$ direction. This result explains why some crystals or some regions in the crystal exhibited an improved performance compared to others, and thereby provides the design considerations for selecting the appropriate crystal. The greater susceptibility of CW devices to birefringence is attributed to the much greater number of round-trips for the Stokes beam through the diamond medium. These results have direct implication for improving the performance of CW DRLs and intracavity doubled DRLs. Apart from diamond, the results are also likely to impact Raman lasers based on other isotropic Raman media such as silicon and barium nitrate. These results may also be of importance to other high-Q systems, such

as intracavity diamond Raman lasers and synchronously pumped ultrafast Raman lasers.

The main results of this chapter were published in Hadiya Jasbeer, Robert J. Williams, Ondrej Kitzler, Aaron McKay, Soumya Sarang, Jipeng Lin and Richard P. Mildren, "Birefringence and piezo-Raman analysis of single crystal CVD diamond and effects on Raman laser performance", JOSA B, Vol 3, No 5, pp. B56–B64 (2016).

4

CW visible generation by intracavity frequency doubling

This chapter focusses on developing high power and high brightness lasers sources in the visible, specifically addressing the red spectral region. Many applications ranging from optical storage, laser scanning and printing, interferometry, atom cooling and spectroscopy would benefit from laser sources in the red. Also, red lasers find its place in photodynamic therapy (PDT), as the majority of PDT sensitizers are activated in this spectral region.

The most prominent technologies for red generation are intracavity frequency doubling of 1.3 μm transition of rare-earth doped lasers [39, 171–173], frequency doubling of semiconductor disk lasers (SDLs) [174, 175], Pr^{3+}-doped $LiYF_4$ lasers [176–178], VECSELs [179, 180] and laser diodes [181]. However, these technologies are either limited in power (maximum achieved up to approximately 15 W), beam quality or both.

As discussed in Chapter 1, external cavity DRLs have proved to be an excellent platform for generating high power and high brightness output at exotic wavelengths. To date, CW

DRLs have been demonstrated in the near-IR achieving high output Stokes power (381 W) and conversion efficiency (61%) with greater than 20 kW intracavity Stokes power [92]. The high intracavity Stokes power in these systems is convenient for enabling efficient intracavity frequency doubling to the red spectral region. Also, the approach offers the advantage of being applicable to multi-longitudinal mode pumps since the cavity is non-resonant with the input, in contrast to alternatives based on external resonant enhancement cavities (see also Sec.1.1 for more details).

This chapter presents the first demonstration of intracavity frequency doubling in a CW DRL. The critical design parameters affecting the visible conversion efficiency are evaluated experimentally. A model for the laser is presented and used to identify the route to optimized efficiency at current and elevated power levels. In addition, the prospects for scaling this technology to power levels in excess of 100 W output power are analyzed.

4.1 Choice of the nonlinear crystal

A linear cavity is utilized to demonstrate intracavity frequency doubling in a CW DRL, as this type of cavity offers simplicity in mirror alignment and system analysis, and reduced mirror losses compared to more complex folded cavity designs. Such complex cavity designs may be used to further optimize the frequency doubling efficiency by generating a separate waist in the LBO, thus providing additional design flexibility. However, in such cases, the increased losses introduced by the additional mirror surface and astigmatic effects need to be considered in the design. In order to achieve efficient conversion of the near-IR Stokes to the visible, the first step to consider is the choice of the nonlinear crystal compatible with the chosen linear cavity design.

The primary crystal parameters to be considered for efficient frequency doubling are obtained from the conversion efficiency equation [3],

$$\frac{P_{2\omega}}{P_{\omega}} = L_{\chi 2}^{2} K \frac{P_{\omega}}{A} \frac{\sin^{2}\left(\frac{\Delta k L_{\chi 2}}{2}\right)}{\left(\frac{\Delta k L_{\chi 2}}{2}\right)^{2}}, \tag{4.1}$$

where $P_{2\omega}$ is the frequency doubled power, P_{ω} is the fundamental power (in this case intracavity Stokes power), $L_{\chi 2}$ is the length of the nonlinear crystal, $A = \pi w_{\mathrm{LBO}}^{2}$ is the area of the fundamental beam (in this case the Stokes beam) with radius w_{LBO} in the LBO,

$K = 2\eta^3\omega_S^2 d_{\text{eff}}^2$, $\eta = \sqrt{\mu_0/\epsilon_0\epsilon} = 377/n_0$ $[V/A]$ is the plane-wave impedance, ω_S is the frequency of the Stokes beam, and d_{eff} is the effective nonlinear coefficient of the crystal. The units of d_{eff} is $[As/V^2]$ which includes ϵ_0 and is equivalent to $8.855 \times 10^{-12} d_{eff}$ [m/V] when ϵ_0 is excluded. Δk is the phase mismatch between the fundamental wave and the second harmonic wave, given by $\Delta k = \frac{4\pi}{\lambda_S}(n_1 - n_2)$, where λ_S is the wavelength of the Stokes beam and $n_{1,2}$ are the indices of refraction for the fundamental and frequency doubled beams.

For the case where perfect phase-matching is satisfied ($\Delta k = 0$), Eq. 4.1 becomes [3],

$$\frac{P_{2\omega}}{P_\omega} = \Gamma P_\omega, \tag{4.2}$$

where $\Gamma = \dfrac{L_{\chi 2}^2 K}{A}$. From Eqs. 4.1 and 4.2, the key parameters for efficient frequency conversion are d_{eff} and crystal length as well as acceptance angle and bandwidth to ensure $\Delta k \approx 0$. Since the divergence of the Stokes beam in the linear cavity used here is approximately 9.4 mrad, the acceptance angle of the nonlinear crystal should ideally be greater than this value. Non-critical phase matching is preferred over critical phase matching due to smaller beam walk-off, wider acceptance angle and practical simplicity in laser alignment (as the crystal may be temperature tuned).

Table. 4.1 compares key properties of potential nonlinear crystals that are feasible for frequency doubling 1240 nm Stokes. Among the nonlinear crystals listed, BBO, BIBO and $LiIO_3$ offer type I phase matching with relatively high d_{eff}. However, these crystals are critically phase-matched and hence suffer from a larger walk-off angle, smaller angular tolerance, and narrower acceptance angle. LBO, on the other hand, allows non-critical phase matching and thus possesses smaller beam walk-off, larger angle tolerance, wider acceptance angle and band-width, with a moderate d_{eff} value. Hence, LBO is better suited to SHG conversion of 1240 nm Stokes in the present resonator design.

In order to achieve non-critical phase matching in LBO, the crystal should be cooled to approximately 282 K, which is below room temperature. However, this would likely lead to condensation and a high risk of coating damage. Alternatively, the crystal can be operated at elevated temperatures and close to non-critical phase matching, providing tolerable walk-off and acceptance angles, by choosing a crystal cut with phase matching angles close to 90°. In these experiments, an LBO cut at $\theta = 85.8°$ and $\phi = 0°$ and heated to 310.8 K is used for implementing SHG of Stokes.

Table 4.1: Comparison of various nonlinear crystals used for 1240-620 nm wavelength conversion. Data were taken from SNLO software.

Crystal	Phase-matching configuration	d_{eff}(pm/V)	walk-off (mrad) $[\omega(e), \omega(o), 2\omega]$	Angle tolerance (mrad cm)	Acceptance angle (mrad cm) $[e, o]$	Acceptance band-width $(cm^{-1}cm)$ $[e, o]$
LBO	Type I	0.824	3.78, 3.78, 0	10.25	20.50, 20.50	317.5, 317.5
BBO	Type I	2.00	0, 0, 51.6	0.73	1.46, 1.46	70.35, 70.35
	Type II	1.48	65.09, 0, 65.93	1.12	85.99, 1.14	35.00, 351.66
BIBO	Type I	2.22	0, 0, 16.56	2.10	4.21, 4.21	34.02, 34.02
	Type II	1.97	0, 83.36, 0	0.78	0.78	14.84,103.42
KDP	Type I	0.264	0, 0, 27.38	1.52	3.04, 3.04	60.51, 60.51
	Type II	0.315	17.66, 0, 23.29	2.89	15.04, 3.58	77.10, 32.79
$LiIO_3$	Type I	2.09	0, 0, 66.62	0.50	1.00, 1.00	19.72, 19.72
	Type II	0.106	76.77, 0, 79.66	0.81	23.50, 0.84	12.69, 47.66

4.2 Experimental arrangement

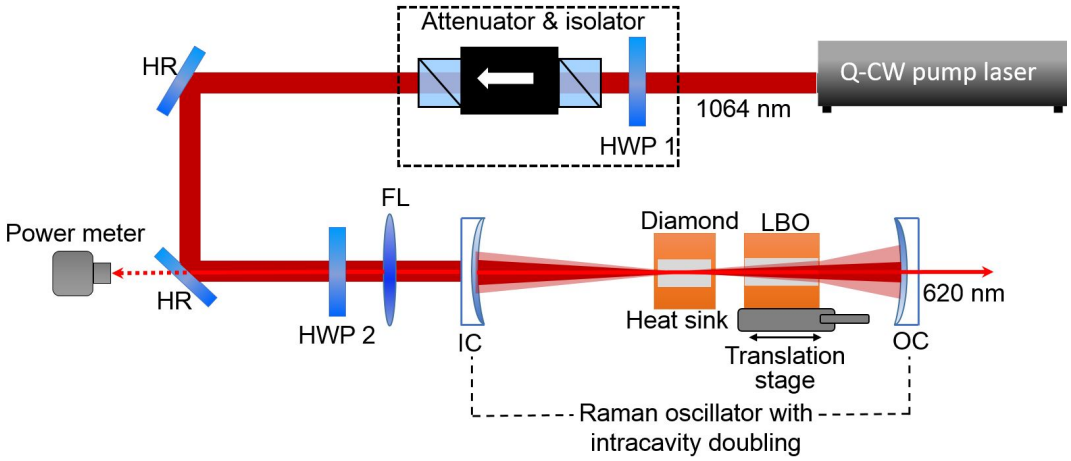

Figure 4.1: Experimental arrangement of an external cavity DRL with intracavity frequency doubling: HWP-half-wave plate, FL-focussing lens, HR-higly reflecting mirror, IC-input coupler, and OC-output coupler.

Figure. 4.1 shows the experimental arrangement for the CW DRL with intracavity frequency doubling to generate 620 nm visible output. The pump source was the same as that used in Chapter 3: a quasi-CW-pumped Nd:YAG laser at 1064 nm, operating at 40 Hz repetition rate and 1% duty cycle with a pulse duration of 250 μs. A half-wave plate (HWP 1) and a polarizing cube were used to achieve variable attenuation of the pump beam and a Faraday rotator provided isolation from the back-reflected pump. A half-wave plate (HWP 2 in Fig. 4.1) was used to control the pump polarization with respect to the diamond axes.

The Raman laser cavity consisted of a 107.5 mm long near-concentric resonator consisting of an input coupler (radius of curvature = 50 mm), diamond as the Raman gain medium, LBO as the frequency doubler and an output coupler (radius of curvature = 50 mm). A focusing lens (50 mm focal length) was used to focus the pump beam into the middle of the AR coated diamond, which was sample B, characterized in Chapter 2. The LBO (temperature tuned to 310.8 K) was placed on a translation stage so as to change its position with respect to the waist of the Stokes mode, thus controlling the width of the Stokes beam in the LBO and thus the nonlinear output coupling. The input coupler was highly transmissive for the pump (>97%), highly reflective for the 1240 nm first Stokes (99.98%) and partially transmissive for the 620 nm second harmonic output (66%). The output coupler was highly reflective for

the pump and provided 0.5% transmission for the first Stokes and 30% transmission for the second harmonic output. Since the input and output couplers are neither AR nor HR coated for 620 nm, the generated SHG power exits through both the cavity mirrors. The generated SHG power was measured from one of the HR mirrors (as indicated in Fig. 4.1) and calibrated using the transmissivities of the output coupler, input coupler, focussing lens (FL), half-wave plate (HWP 2) and the HR mirror at 620 nm.

4.3 Experimental results - Laser performance

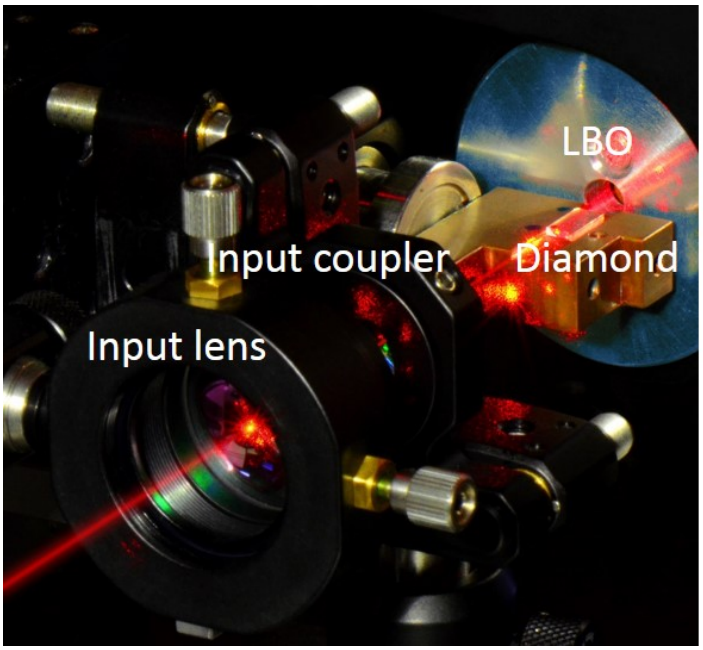

Figure 4.2: Photograph showing 620 nm laser emission in the intracavity doubled CW DRL. The red beam on the lower left has been digitally enhanced for clarity.

After optimizing the LBO position (as discussed further below), the laser behaviour was characterized. Fig. 4.3 shows the generated SHG power, Stokes power leaked through the output coupler (as a result of 0.5% T at 1240 nm) and residual pump power as a function of injected pump power. At a pump power of 97 W, the onset of 1240 nm residual first Stokes output and 620 nm second harmonic output (as shown in Fig.4.2) was observed simultaneously. Above threshold, the SHG power increased monotonically up to a maximum of 30 W limited by the available pump power (204 W) achieving a maximum conversion efficiency of 14.9%. Fig. 4.4 shows the beam quality measurements for the SHG output, revealing an M^2 of 1.1.

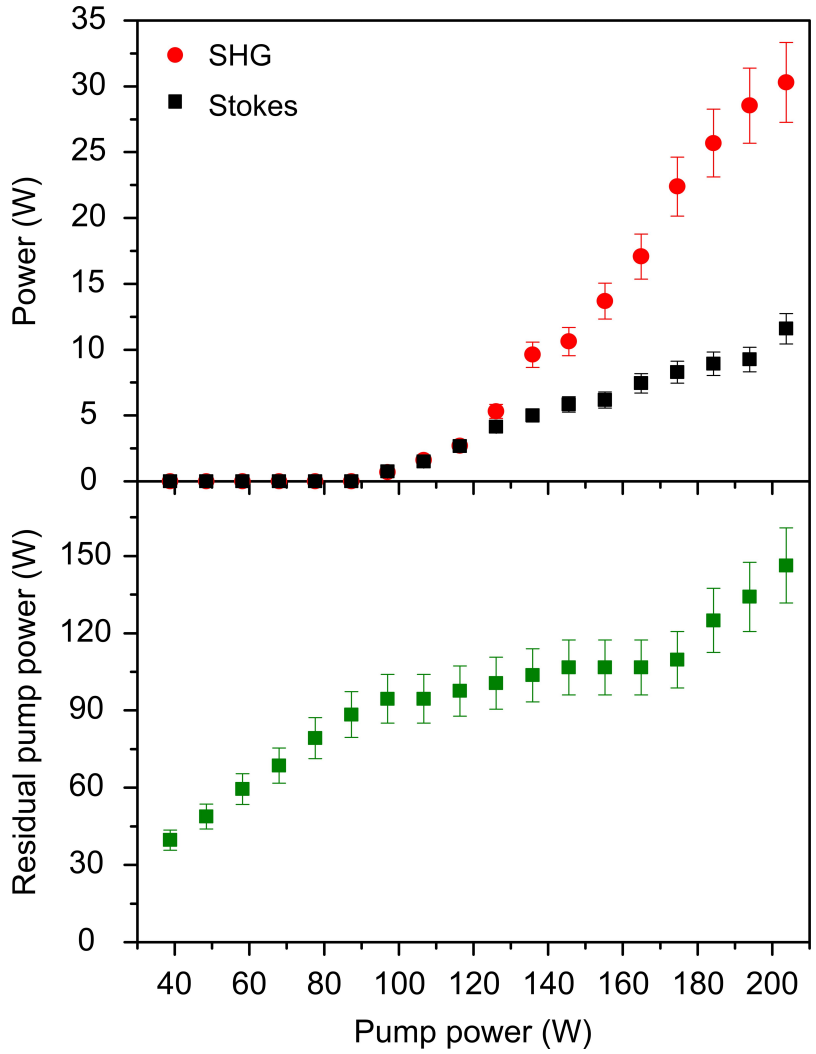

Figure 4.3: On-time SHG and Stokes power (top figure) and residual pump power (bottom figure) as a function of incident pump power for w_{LBO} = 155 μm for a diamond-LBO separation of 12 mm. The error bars indicate the variation of measured power in the power meter.

The Stokes power leakage from the output coupler was 11.6 W for a pump power of 204 W. As a function of injected pump power, the residual pump power increased linearly until threshold and then remains approximately constant up to 180 W of injected pump due to pump depletion by the first Stokes. Beyond 180 W, the residual pump was observed to increase monotonically up to the maximum injected power. Although an increase in residual pump power may signal the onset of cascaded second Stokes generation (1485 nm), however, in this case, the threshold pump power for second Stokes generation could not be attained owing to the high transmission of 1485 nm for both the input and output couplers (T at

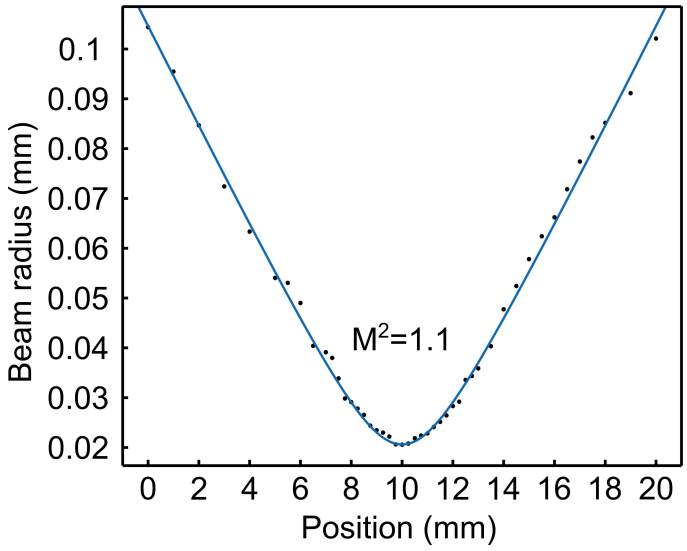

Figure 4.4: Beam radius as a function of position through the beam waist, which was used to calculate the M^2 of 620 nm output at the power level of 30 W.

1485 nm for input coupler is 98% and output coupler is 84%). Other explanations may include poor overlap between the pump and Stokes mode, owing to slight misalignment of the cavity. Further investigation at higher pump powers is required to understand the cause of this behaviour.

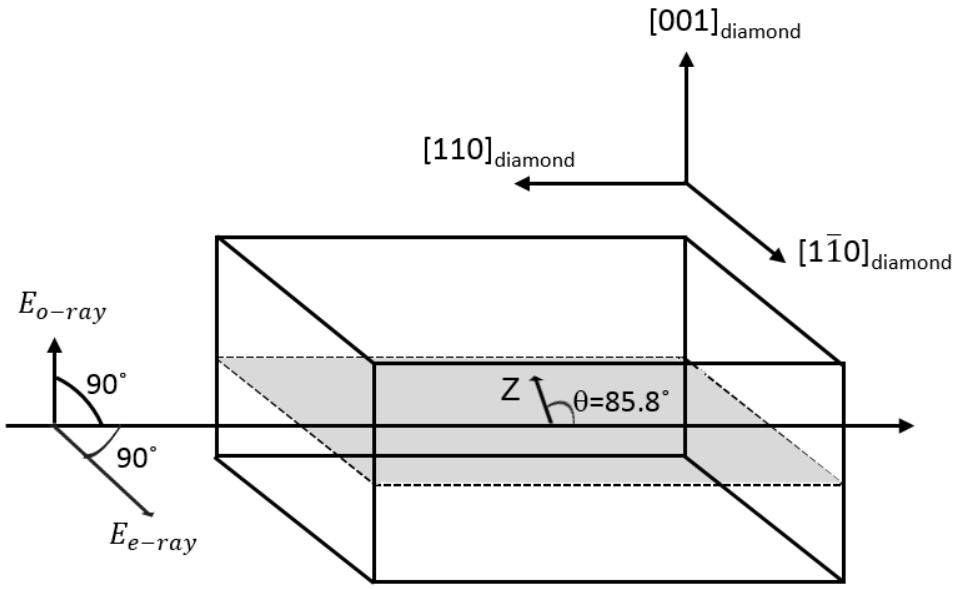

Figure 4.5: Relationships between the ordinary and extra-ordinary rays in the LBO (cut at θ = 85.8°) and the diamond crystallographic orientation. Z indicates the optic axis.

The SHG and the first Stokes output was measured to be vertically and horizontally polarized respectively for all pump polarizations. Since the dominant birefringence element in the cavity is LBO with its optic axis in the horizontal plane containing the diamond $\langle 1\bar{1}0 \rangle$ (see Fig. 4.5), the measured Stokes polarization is consistent with the results in Chapter 3. The vertical SHG polarization is consistent with the type I phase matching conditions (1240(e)+1240(e) = 620(o)).

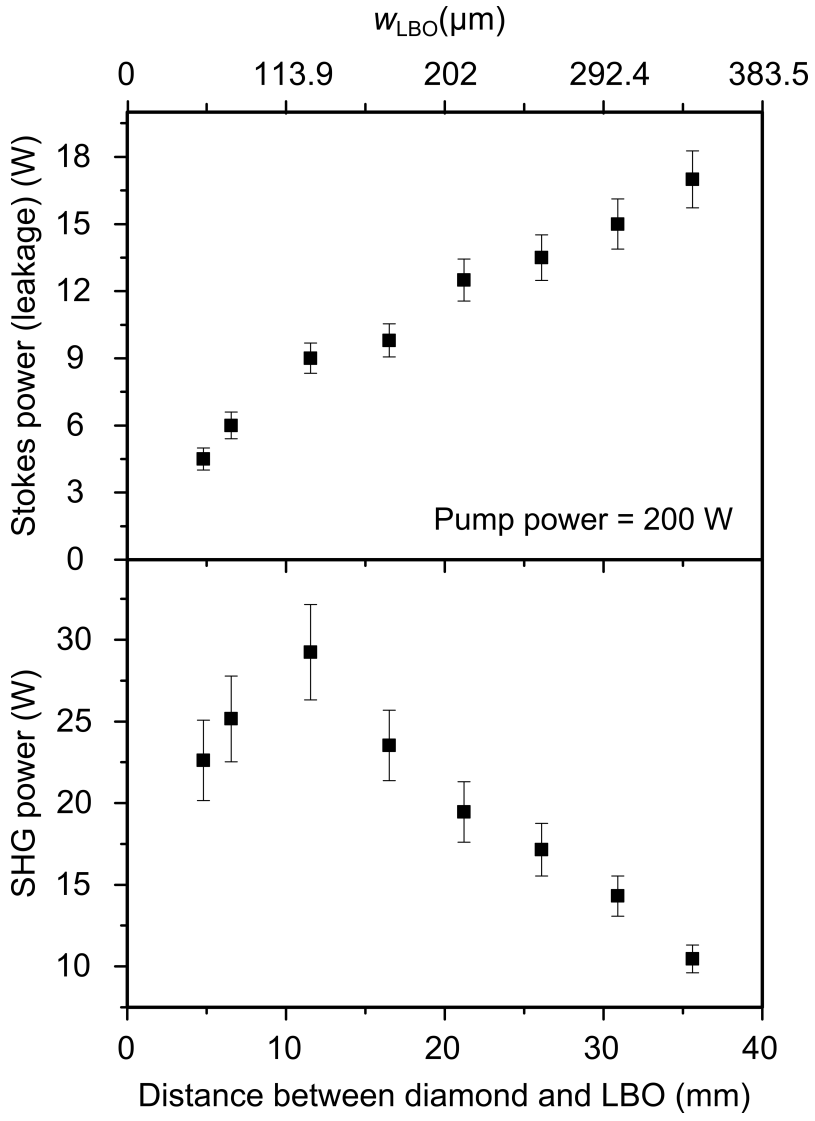

Figure 4.6: On-time Stokes power leakage (top figure) and SHG power (bottom figure) as a function of diamond-LBO separation for pump power of 200 W. The beam width of the Stokes in LBO is shown in the top X-axis.

Fig. 4.6 shows the laser output power as a function the diamond-LBO separation distance. The Stokes beam radius in the LBO (see top axis) was calculated using PSST software

(used for modelling laser cavity) using the radii of curvature of input and output couplers, measured cavity length and the distance between the diamond and LBO. The Stokes leakage (top figure) from the cavity increases with separation distance. This is consistent with the expected offsetting of SHG to higher power and hence greater build-up of intracavity Stokes power. Over the same range, the SHG power (bottom figure) increases initially up to the 30 W maximum at a diamond-LBO separation of 12 mm (corresponding to a Stokes beam width in the LBO of 155 μm) and decreases thereafter. For separations less than optimum, over-coupling occurs where the high rate of Stokes-SHG conversion leads to low Stokes field, hence reduced pump depletion and lower SHG power. Conversely, under-coupling occurs for larger than optimum separations and in which Stokes-SHG conversion is low despite the high Stokes field and strong depletion of the pump beam.

The detailed output characteristics for the under-coupled regime are shown in Fig. 4.7. When compared to the optimum condition (Fig. 4.3), this regime is characterized by a much higher intracavity Stokes field and consequently much higher depletion. (Note that operation in the over-coupled regime was not investigated in detail due to a higher risk of LBO coating damage under extended operation.)

The output spectrum (see Fig. 4.8 acquired with an Ocean Optics spectrometer) shows a strong second harmonic output at 620 nm and a weak SFG output at 573 nm between the pump and the first Stokes. The SFG signal is weak as the phase-matching conditions are not fulfilled, however, shows the potential for extending the wavelength range of DRL using SFG.

4.4 Laser model

A model has been developed to provide guidance for improving the performance and predicting the performance at elevated power levels of an intracavity doubled CW DRL. This model was adapted from an analytical model for CW DRL by Kitzler *et al.* [86]. The rate equations for the pump and Stokes intensity fields described in Sec.1.2.2 (Eq. 1.22) are adapted to include a nonlinear output coupling loss term for the intracavity Stokes field corresponding to the SHG output. Also note that this model explicitly includes the depletion of the pump beam. The major assumptions used in the model are:

- the pump, Stokes, and SHG beams are all Gaussian;

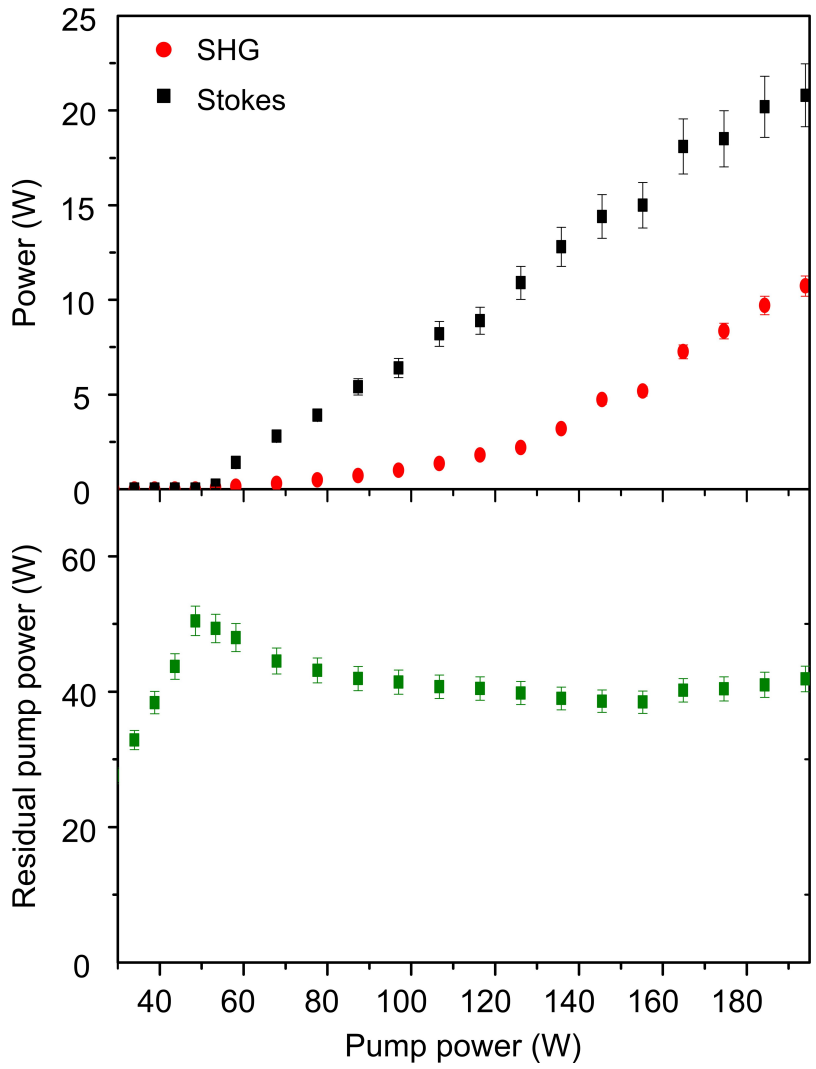

Figure 4.7: On-time SHG and Stokes power (top figure) and residual pump power (bottom figure) as a function of incident pump power for w_{LBO} = 550 µm (under-coupling) for a diamond-LBO separation of 40 mm. The error bars indicate the variation of measured power in the power meter.

- a low gain system in which the z-dependence of the intracavity Stokes intensity inside the cavity is taken to be constant;

- thermal effects are negligible (these are considered separately in Sec. 4.7).

The growth of the intracavity Stokes field and the depletion of the single pass pump beam are given by (from Sec.1.2.2) [86]

$$\frac{\mathrm{d}I_{\mathrm{S}}^{int}(r,z)}{\mathrm{d}z} = g_{\mathrm{S}} I_{\mathrm{P}} I_{\mathrm{S}}^{int} - \alpha_{\mathrm{S}} I_{\mathrm{S}}^{int},$$

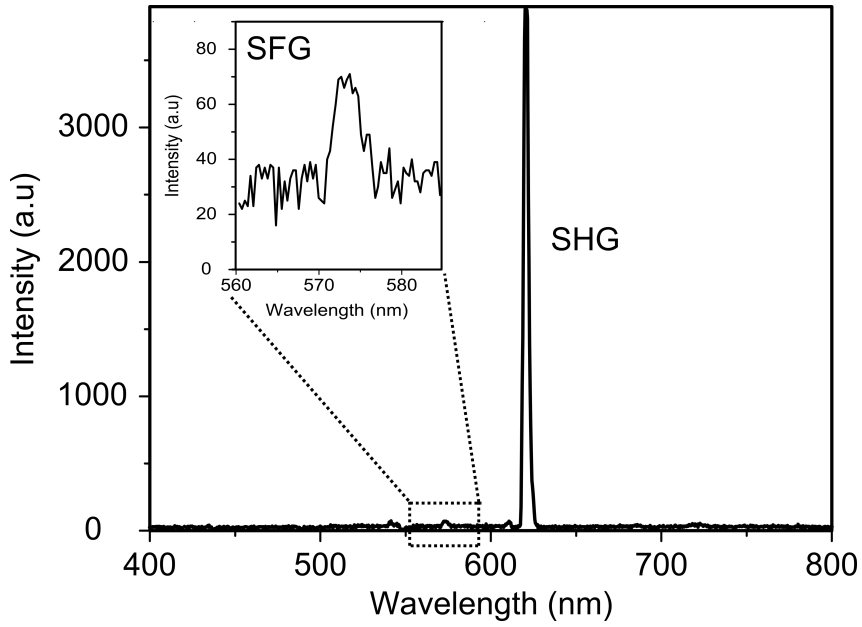

Figure 4.8: Output spectrum obtained when pumping with 1064 nm laser. The inset corresponds to the signal at the sum frequency of the pump and Stokes. Note that the small peaks at 547 nm and 613 nm account for the room light emissions.

$$\frac{\mathrm{d}I_{\mathrm{P}}(r,z)}{\mathrm{d}z} = -\frac{g_{\mathrm{S}}}{\eta} I_{\mathrm{P}} I_{\mathrm{S}}^{int} - \alpha_{\mathrm{P}} I_{\mathrm{P}}, \tag{4.3}$$

where I_{P} and I_{S}^{int} are the pump and intracavity Stokes intensities respectively, $\eta = \lambda_{\mathrm{P}}/\lambda_{\mathrm{S}}$ is the quantum defect of the inelastic Raman scattering process, and α_{S}, α_{P} are the parasitic losses at the Stokes and pump wavelengths respectively.

Assuming that the losses are small in a single pass of the Raman crystal , the volume integration in polar coordinates (r from 0 to ∞ and θ from 0 to 2π) of the equation for pump depletion in 4.3 becomes [86]

$$\frac{\mathrm{d}P_{\mathrm{P}}(z)}{\mathrm{d}z} = -\frac{2g_{\mathrm{S}}}{\pi\eta} P_{\mathrm{P}}(z) P_{\mathrm{S}}^{int}(z) \frac{1}{w_{\mathrm{P}}^2(z) + w_{\mathrm{S}}^2(z)}, \tag{4.4}$$

where $w_{\mathrm{P,S}}$ is the pump and Stokes beam waists. Above the threshold, the pump power decays rapidly on passage through the crystal as is necessary for an efficient single- or double-pass pumped laser. Since the dependence of intracavity Stokes intensity on z is neglected, Eq. 4.4 can be solved by separation of variables to give [86, 127]

$$P_{\mathrm{Res}} = P_{\mathrm{P}} \exp\left(-G P_{\mathrm{S}}^{int}\right), \tag{4.5}$$

where P_{Res} is the residual pump power and G is the Raman gain in the focussed geometry

given by

$$G = \frac{2g_S}{\eta}\frac{\arctan(\zeta)}{\Lambda}. \tag{4.6}$$

The dimensionless parameter ζ depends on the the diamond length L_d and confocal parameters of pump (b_P) and Stokes (b_S) according to

$$\zeta = \frac{L_d}{\sqrt{b_P b_S}}\sqrt{\frac{\eta' + b_{PS}}{\eta' b_{PS} + 1}}, \tag{4.7}$$

where $b_{PS} = b_P/b_S$ and $\eta' = \lambda'_P/\lambda'_S = \left(\lambda_P n_S M_P^2\right) / \left(\lambda_S n_P M_S^2\right)$. The parameter Λ, defined as

$$\Lambda = \frac{1}{2}\sqrt{\lambda'_P \lambda'_S}\sqrt{\left(\eta' + \frac{1}{\eta'}\right) + \left(b_{PS} + \frac{1}{b_{PS}}\right)}, \tag{4.8}$$

contains the gain reduction factor for the pump and Stokes wavelength mismatch (first bracket in Eq. 4.8) and beam overlap mismatch (second bracket in Eq. 4.8).

The Stokes power generated P_S^{gen}, according to the conservation of energy is the difference between the pump and residual pump power scaled to the quantum defect

$$\begin{aligned} P_S^{gen} &= \eta\left(P_P - P_{Res}\right) \\ &= \eta P_P\left[1 - \exp\left(-GP_S^{int}\right)\right]. \end{aligned} \tag{4.9}$$

The intracavity Stokes power generated is lost from the cavity via three ways: absorption and scattering loss from the diamond and the LBO (P_S^{loss}), first Stokes leaking through the output coupler (P_S^{OC}), and nonlinear output coupling due to frequency doubling (P_{SHG}). The total crystal loss for the Stokes, which include distributed losses terms for absorption and scattering loss (α_d for diamond and $\alpha_{\chi 2}$ for LBO) as well as reflection losses from the crystal faces (κ – total reflection loss from diamond and LBO) is given by

$$P_S^{loss} = \left(\alpha_d L_d + \alpha_{\chi 2} L_{\chi 2} + \kappa\right) P_S^{int}. \tag{4.10}$$

In a linear cavity, half of the intracavity power propagates towards right and half towards the left. The Stokes power leakage through the output coupler with transmission T for the Stokes is given by

$$P_S^{OC} = \frac{T}{2}P_S^{int}. \tag{4.11}$$

The nonlinear output coupling due to SHG is (from Eq. 4.2)

$$P_{SHG} = \Gamma\left(P_S^{int}\right)^2. \tag{4.12}$$

Substituting Eqs. 4.10, 4.11 and 4.12 in Eq. 4.9 leads to a solution predicting the required pump power for a certain intracavity Stokes power (and thus generated SHG)

$$P_{\mathrm{P}} = \frac{\left(T + 2\alpha_{\mathrm{d}}L_{\mathrm{d}} + 2\alpha_{\chi 2}L_{\chi 2} + 2\kappa\right) P_{\mathrm{S}}^{int} + 2\Gamma \left(P_{\mathrm{S}}^{int}\right)^2}{2\eta \left[1 - \exp\left(-GP_{\mathrm{S}}^{int}\right)\right]}. \tag{4.13}$$

The first term in the brackets takes into account the Stokes leakage through the output coupler and parasitic losses in the cavity. The second term which depends on the square of the intracavity Stokes power corresponds to the SHG. Eq. 4.13 can be also written in terms of SHG and output coupled Stokes power:

$$P_{\mathrm{P}} = \frac{\left(T + 2\alpha_{\mathrm{d}}L_{\mathrm{d}} + 2\alpha_{\chi 2}L_{\chi 2} + 2\kappa\right) P_{\mathrm{S}}^{OC} + TP_{\mathrm{SHG}}}{\eta T \left[1 - \exp\left(\frac{-2GP_{\mathrm{S}}^{OC}}{T}\right)\right]}. \tag{4.14}$$

The threshold pump power $P_{\mathrm{P}}^{\mathrm{th}}$ is obtained by limiting the intracavity Stokes power in Eq. 4.13 to zero

$$P_{\mathrm{P}}^{\mathrm{th}} = \frac{\left(T + 2\alpha_{\mathrm{d}}L_{\mathrm{d}} + 2\alpha_{\chi 2}L_{\chi 2} + 2\kappa\right)}{2G\eta}. \tag{4.15}$$

Thus the threshold pump power depends on the Stokes output coupling, parasitic crystal losses, Raman gain coefficient and pump and Stokes focussing parameters.

In the experiment investigated above, the pump undergoes two passes through the diamond (the output coupler is HR for the pump) and thus experiences additional depletion. Assuming that the residual pump follows the same path during the second pass (from Eq. 4.5)

$$P_{\mathrm{Res}} = P_{\mathrm{P}} \exp\left(-2GP_{\mathrm{S}}^{int}\right). \tag{4.16}$$

The relation between pump and intracavity Stokes power for second harmonic output given by Eq. 4.13 becomes

$$P_{\mathrm{P}} = \frac{\left(T + 2\alpha_{\mathrm{d}}L_{\mathrm{d}} + 2\alpha_{\chi 2}L_{\chi 2} + 2\kappa\right) P_{\mathrm{S}}^{int} + 2\Gamma \left(P_{\mathrm{S}}^{int}\right)^2}{2\eta \left[1 - \exp\left(-2GP_{\mathrm{S}}^{int}\right)\right]}, \tag{4.17}$$

Likewise the threshold pump power given in Eq. 4.15 becomes

$$P_{\mathrm{P}}^{\mathrm{th}} = \frac{\left(T + 2\alpha_{\mathrm{d}}L_{\mathrm{d}} + 2\alpha_{\chi 2}L_{\chi 2} + 2\kappa\right)}{4G\eta}, \tag{4.18}$$

and thus reduces by half compared to single pass. Eqs. 4.16, 4.17 and 4.18 can be used to predict the key trends in Stokes, SHG, and residual pump power. Fig. 4.9 shows examples of model output corresponding to the over-, optimally- and under-coupled regimes for a general set of parameters which highlight the contrasting behaviour in each.

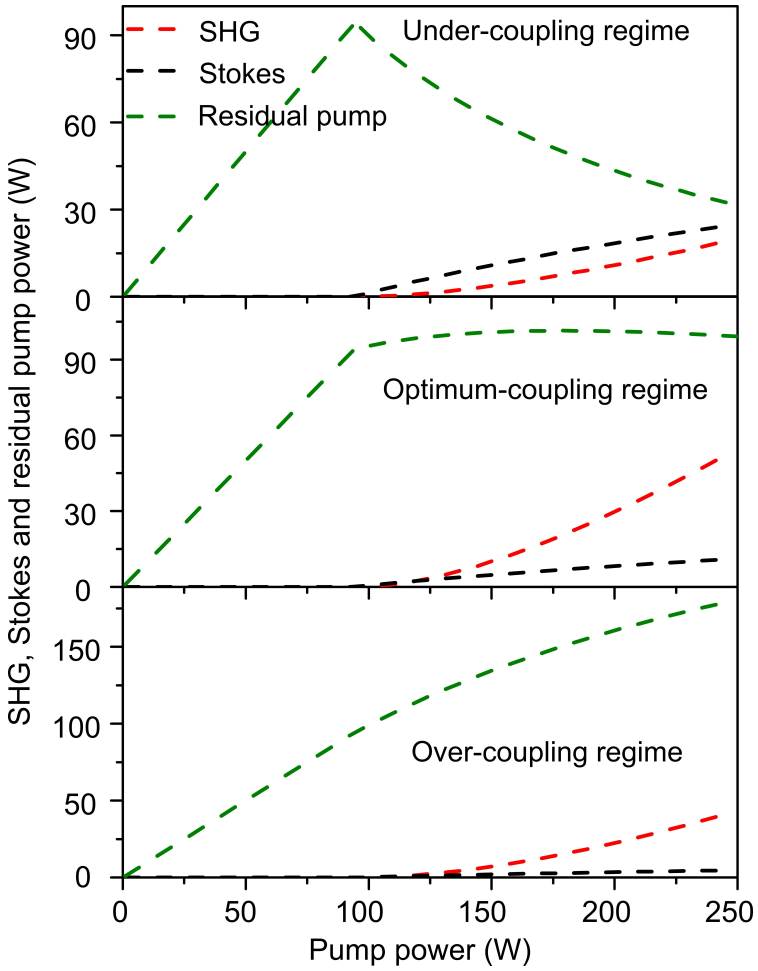

Figure 4.9: SHG, Stokes and residual pump as a function of pump power for w_{LBO}=450 µm (top figure), 155 µm (middle figure) and 70 µm (bottom figure) featured by under-, optimum and over-coupling regimes respectively. The parameters used for these plots are T = 0.5%, κ = 0.9%, α_{d} = 0.37%/cm, $\alpha_{\chi 2}$ = 0.37%/cm, L_{d} = 8 mm, $L_{\chi 2}$ = 10 mm, ω_{P} = 42 µm, ω_{S} = 47 µm, M^2_{P} = 1.5, and M^2_{S} = 1.0.

4.5 Model comparison with experiment

In this section, the model predictions are compared with the SHG and Stokes power characteristics of intracavity doubled DRLs investigated in Sec 4.3. Tab. 4.2 summarizes the parameters used for fitting the model results with the experimental results. The measurable parameters such as the output coupling, length of the diamond, length of the LBO, M^2 value of the pump and Stokes and second-order nonlinear coefficient d_{eff} (taken from SNLO) are taken as fixed parameters. The values for g_{S}, w_{P}, w_{S}, and parasitic losses (α_{d}, $\alpha_{\chi 2}$, and κ) are taken within a nominal range to fit the model results with the experiment. The Raman

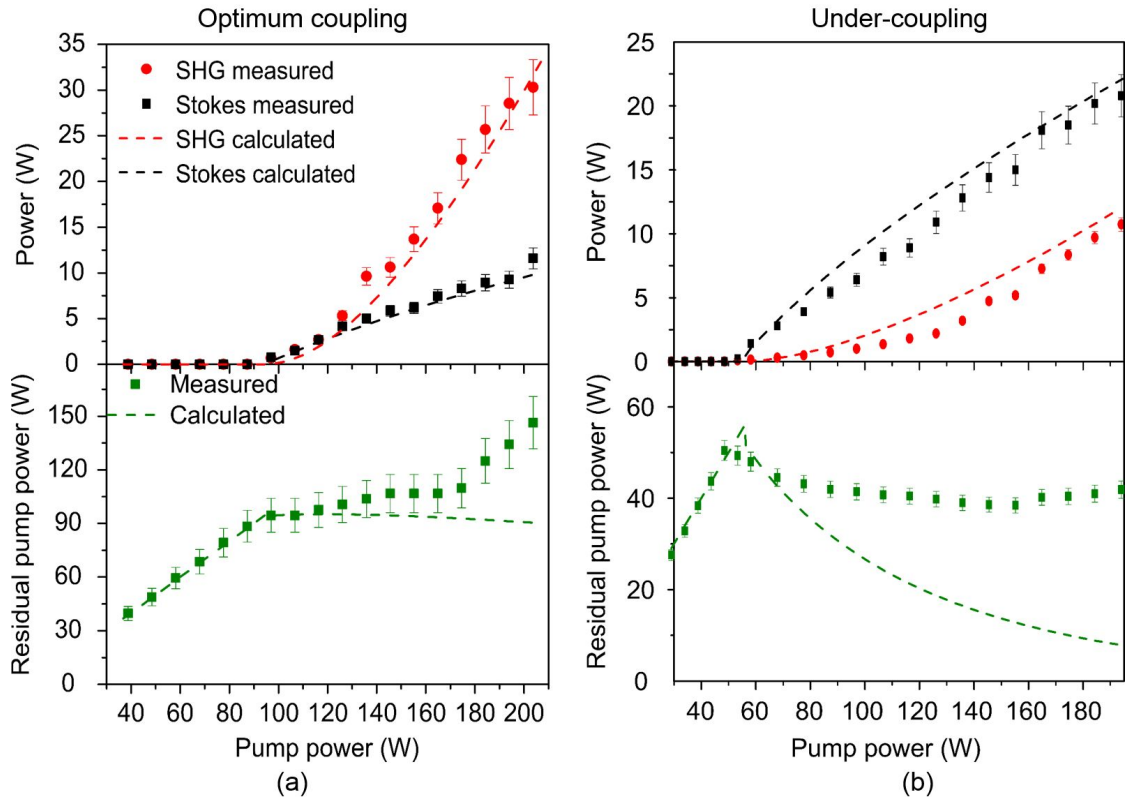

Figure 4.10: Modelled SHG and Stokes power (top figure) and residual pump power (bottom figure) as a function of incident pump power for Stokes beam radius in the LBO of (a) 155 μm and (b) 550 μm for experimental conditions given in (Tab.4.2). Experimental points are included for comparison. The dashed lines represent the model results and markers represent the measured results.

gain coefficient g_S of 8 cm/GW used for fitting the experiment is within the range of the reported values in the literature (8-15 cm/GW at 1064 nm, see also Sec.1.3) [116, 120]. The parameter α_d which accounts for the absorption and scattering losses in diamond is taken to be 0.37%/cm which is within the range expected for diamond samples with 20-40 ppb nitrogen content [123, 145]. The parameter $\alpha_{\chi 2}$ which accounts for the absorption and scattering loss for the LBO is taken to be 0.37%/cm which is slightly higher than the absorption coefficient value of about 0.1%/cm at 1064 nm given by the manufacturer (Castech Inc.). The reflection loss parameter κ is the sum of the reflection losses from diamond (approximately 0.1% per surface) and LBO (approximately 0.13% per surface) from the manufacturer's data sheet [182]. The pump and Stokes waist sizes are 35±5 μm and 40±5 μm, respectively. These values were calculated using LACAD laser design software from the known values

of incident pump beam radius, the focal length of the input lens, radii of curvature of the input and output couplers and cavity length, with the associated uncertainties determined by uncertainties in the pump beam parameters (M^2 and incident beam radius) and cavity parameters respectively.

Table 4.2: Simulation parameters used to model the optimum and under-coupled regions corresponding to the results in Fig. 4.3 (in the second column) and Fig. 4.7 (in the third column).

	Optimum	Under-coupled
Variable	30 W SHG power	10 W SHG output
T [%]	0.5	0.5
κ [%]	0.9	0.9
α_{d} [%/cm]	0.37	0.37
$\alpha_{\chi 2}$ [%/cm]	0.37	0.37
L_{d} [mm]	8	8
$L_{\chi 2}$ [mm]	10	10
d_{eff} $[As/V^2]$	8.5×10^{-24}	8.5×10^{-24}
g_{S} [cm/GW]	8	8
w_{LBO} [µm]	155	550
w_{P} [µm]	42	31
w_{S} [µm]	47	36
M^2_{P}	1.5	1.5
M^2_{S}	1.06	1.06

Figures. 4.10 (a) and (b) shows the measured and calculated SHG, Stokes and residual pump powers as a function of incident pump power for optimum- and under-coupling regimes. In both the regimes, the modelled threshold, Stokes power, and SHG power fit well with the experimental results. The measured threshold values in the under-coupling regime are notably lower than near optimum-coupling regime, which is attributed to variations in cavity alignment. The values for w_{P} and w_{S} in both the regimes are within the range expected for a given focusing lens, input and output couplers, the radius of the injected pump beam and position of diamond in the cavity.

There is a notable discrepancy between the measured and calculated residual pump powers

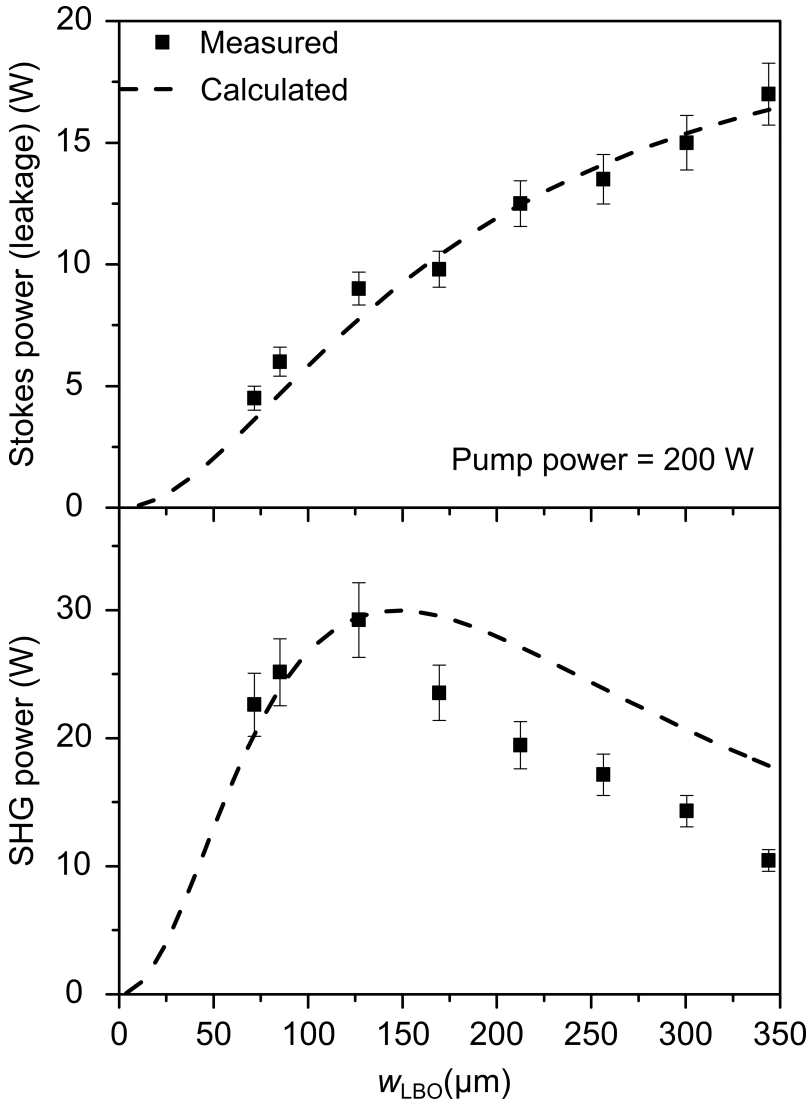

Figure 4.11: Measured and calculated Stokes power leakage (top figure) and SHG power (bottom figure) as a function of w_{LBO} at 200 W pump power. The parameters used for fitting the model plot is the same used for 30 W SHG power given in Tab. 4.2.

at higher injected pump powers (see Fig. 4.10 (a) and (b)). This is a well-known problem [86], which is assumed to be a result of the absence of a full two-dimensional model including the effects of diffraction. Hence, the deviation of the experimental residual pump power from the model indicates that the model derived loss and/or gain coefficients are likely to be over-estimated.

Figure. 4.11 show the measured and model-calculated Stokes leakage and SHG power as a function of the Stokes beam radius in the LBO at 200 W of pump power. The calculated values agree well with the measured values, except for consistently lower measured values of

SHG power for w_{LBO} greater than the optimum value. This discrepancy is attributed to the progressive misalignment of the cavity as the LBO was moved from the diamond towards the output coupler. Although the cavity was adjusted to compensate for the progressive misalignment, this was practically difficult to achieve due to highly sensitive laser behaviour with mirror adjustment. In addition, the discrepancy could also arise from the uncertainties in the fitting parameters such as the pump and Stokes beam-waist radii and loss parameters.

4.6 Optimization of parameters

The model presented in Sec.4.4 reasonably fits well with the observed laser behaviour with acceptable values of loss and Raman gain coefficients. Hence it can be used for optimization and predict its performance at higher pump powers.

Fig. 4.12 (a) shows the SHG power dependence on nonlinear output coupling Γ, which includes d_{eff}, $L_{\chi 2}$, and area of the Stokes beam (or w_{LBO}) in the LBO. The two design parameters in the nonlinear output coupling term that may be varied for optimizing the output are w_{LBO} (by changing the distance between diamond and LBO) and $L_{\chi 2}$. Figs. 4.12 (b) and (c) shows the variation of the SHG power with w_{LBO} and $L_{\chi 2}$ for fixed loss and focusing parameters. In practice, one of these parameters is fixed, and the other is varied to obtain the maximum SHG output. For a fixed $L_{\chi 2}$ = 10 mm, the optimum value of w_{LBO} is approximately 150 μm as expected from the experimental results (see the red dashed circle in Fig. 4.12 (b)). Similarly, for a fixed distance between the diamond and LBO, the optimum value of $L_{\chi 2}$ is 10 mm. In most of the cases, the length of the crystal is preselected and w_{LBO} is varied to obtain the maximum SHG power. Smaller crystal length may be used for reducing the losses, in which case the LBO should be placed closer to diamond (w_{LBO} should be smaller).

The diamond length is another important design parameter (Fig. 4.13) to maximize the SHG power. The intracavity Stokes power increases due to the increase in gain-length product and reaches a maximum point before succumbing to the increasing role of distributed losses in the crystal. As the SHG power depends on the intracavity Stokes power, it also follows the same trend. For the experimentally-derived optimal parameters (Column 1, Tab. 4.2), the optimum L_{d} is approximately 15 mm. This opens up the potential for further increase in SHG power by utilizing a longer diamond (for fixed focusing conditions).

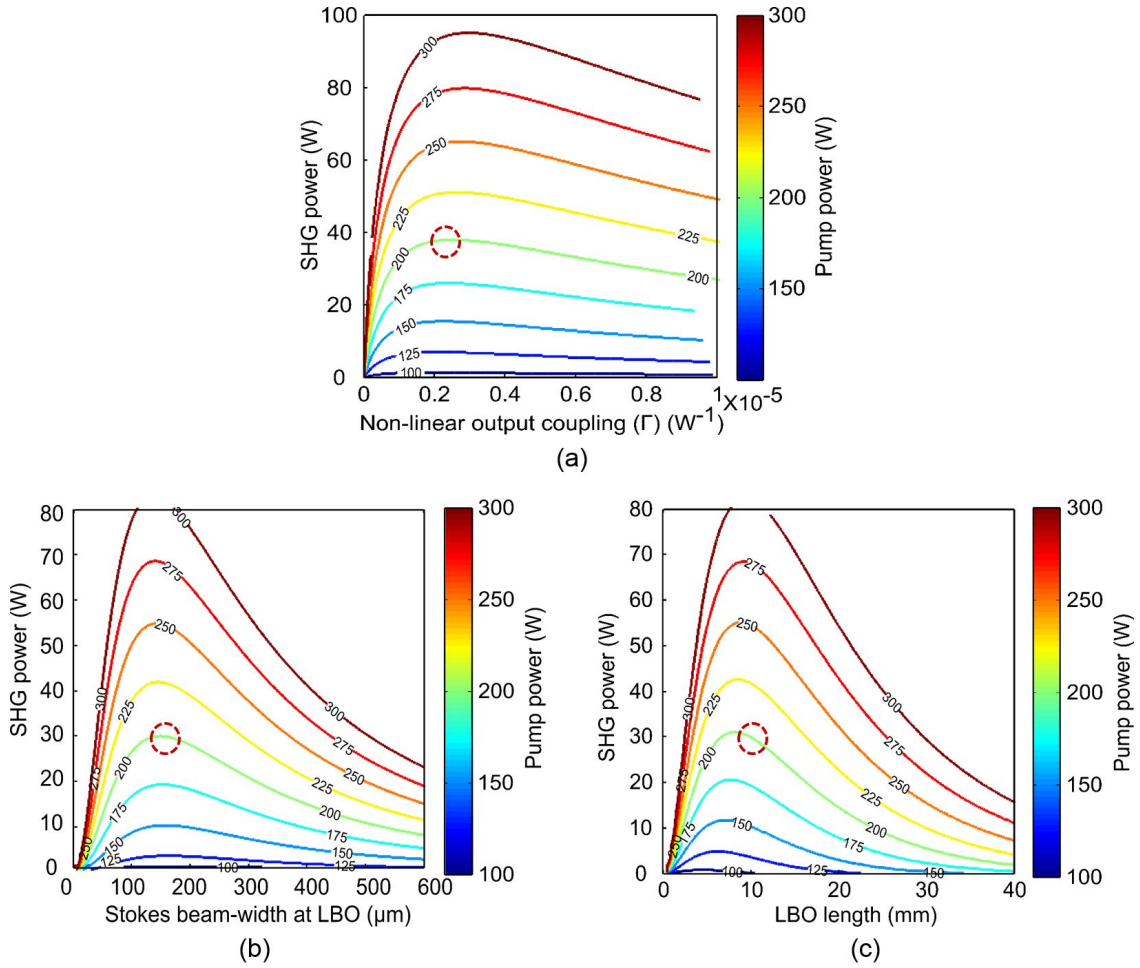

Figure 4.12: SHG power as a function of (a) nonlinear output coupling (b) beam width at LBO and (c) LBO length for pump powers in the range 100-300 W for T = 0.5%, κ = 0.9%, α_{d} = 0.37%/cm, $\alpha_{\chi 2}$ = 0.37%/cm, g_{S} = 8 cm/GW, w_{P} = 42 μm and w_{S} = 47 μm. The red dashed circle represent the investigated range for 30 W SHG output.

The pump and Stokes beam-waist radii are also important design parameters to be optimized for improving the laser performance. Fig. 4.14 shows the variation of SHG power as a function of w_{P}, assuming Stokes beam-waist is mode matched to the pump ($w_{\mathrm{P}} = 0.9 \times w_{\mathrm{S}}$ obtained from the experimental conditions given in Tab. 4.2) for fixed loss and diamond length. A tighter focusing is preferred for maximizing the SHG power, however, the SHG power saturates below a certain pump radius (approximately 25 μm for 200 W of pump power) and any further reduction in beam-radius would only result in a marginal increase (less than 5%). Hence, this plateau region is preferred, as smaller spot-size increases the possibility of laser-induced damage and may exacerbate the thermal effects when operating

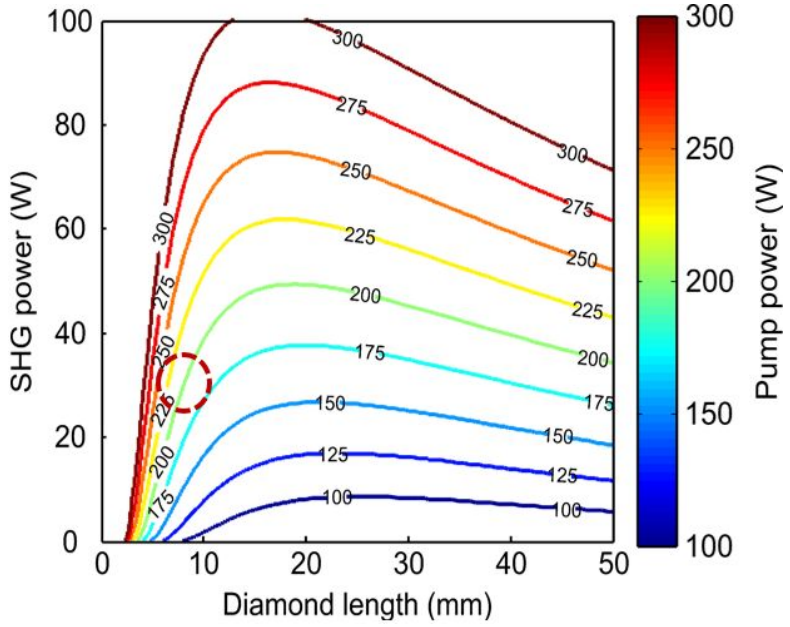

Figure 4.13: SHG power as a function of diamond length for pump powers in the range 100-300 W for T = 0.5%, κ = 0.9%, α_{d} = 0.37%/cm, $\alpha_{\chi 2}$ = 0.37%/cm, g_{S} = 8 cm/GW, w_{P} = 42 µm, w_{S} = 47 µm, $L_{\chi 2}$ = 10 mm and w_{LBO} = 155 µm. The red dashed circle represent the investigated range for 30 W SHG output.

at elevated power levels. Since the w_{P} for the 30 W SHG is larger than the optimum value (see the red-dashed circle in Fig. 4.14), an increase in the SHG power is expected with tighter focusing.

Losses in the laser cavity are crucial parameters determining the efficiency of the laser. Although losses will always be present, it can be reduced by improving the optical coatings and material quality. Fig. 4.15 shows the SHG power as a function of the total losses in the cavity including crystal losses (absorption, scattering and reflection losses) and Stokes output coupling loss. As expected, SHG power increases with reduced losses. The red dashed circle represents the estimated losses in the crystal for 30 W SHG output which is approximately 3.7%. For Stokes mirror leakages reduced from 0.5% to below 0.05%, which is easily within the capability of conventional laser mirror coatings, the SHG power may be increased from 30 W to 42 W (see black-dashed circle in Fig. 4.15). In addition, sourcing higher quality diamond and LBO (with lower absorption and scatter loss), will enable increased powers at the rate depicted in Fig. 4.15.

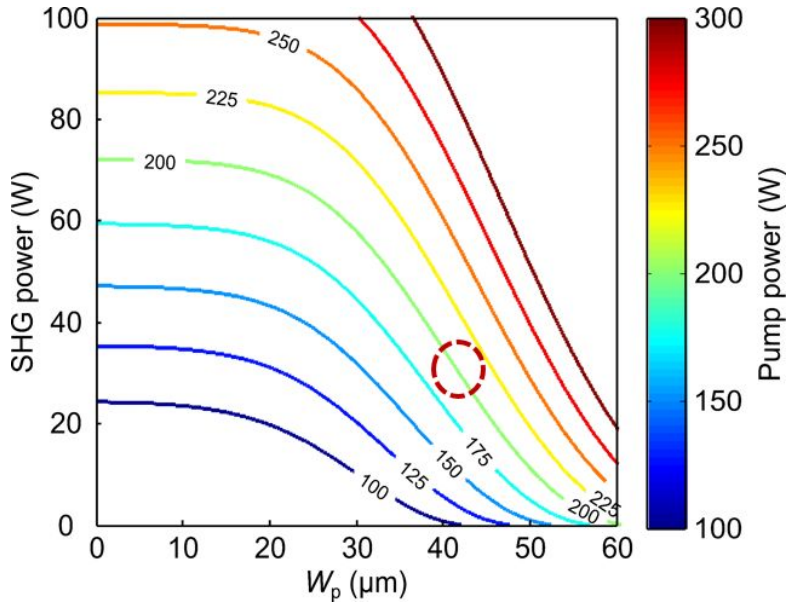

Figure 4.14: SHG power as a function of w_P for pump powers in the range 100-300 W for T = 0.5%, κ = 0.9%, α_d = 0.37%/cm, $\alpha_{\chi 2}$ = 0.37%/cm, g_S = 8 cm/GW, L_d = 8 mm, $L_{\chi 2}$ = 10 mm and w_{LBO} = 155 μm. The red dashed circle represent the investigated range for 30 W SHG output.

4.7 Thermal effects in diamond and LBO

The thermal effects in LBO and diamond need to be considered when increasing the pump power and pulse duration to the CW regime. In the quasi-CW regime used here, with 250 μs pump pulses, the steady state thermal gradients are established rapidly in the diamond (within a few tens of microseconds), due to its high thermal conductivity [93]. In contrast, the LBO requires approximately one thousand times longer due to its low thermal conductivity.

4.7.1 Thermal effects in diamond

In diamond, the major heating mechanisms are the decay of the optical phonons in the process of Stokes generation and the Stokes absorption due to impurities and defects in diamond. However, the nature of the decay of optical phonons and heat deposition is not completely understood and evidence suggest that the actual thermal lens is much weaker than calculated [92]. Nevertheless, an upper bound for the lens strength can be determined and is presented here.

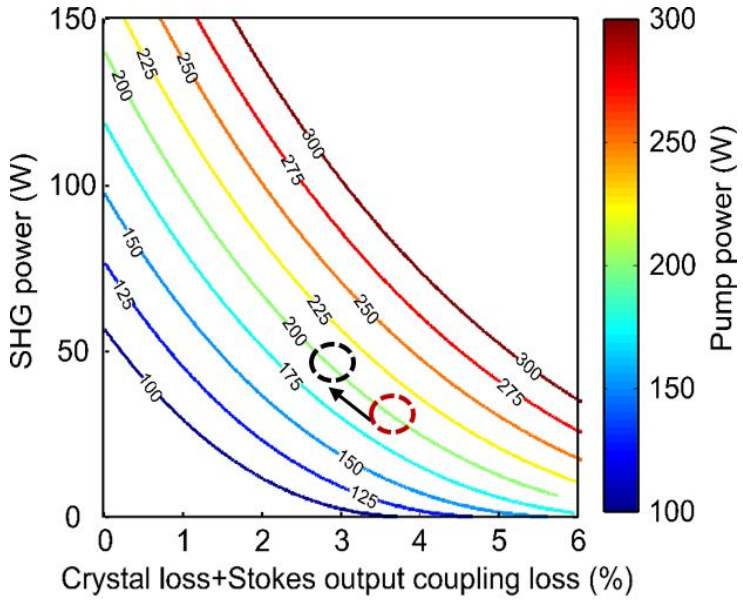

Figure 4.15: SHG power as a function of total loss including crystal losses and Stokes output coupling loss for pump powers in the range 100-300 W for g_S = 8 cm/GW, w_P = 42 µm, w_S = 47 µm, $L_{\chi 2}$ = 10 mm and w_{LBO} = 155 µm. The red dashed circle represent the investigated range for 30 W SHG output and the black-dashed circle represents the projected SHG power when the Stokes output coupling loss is reduced to less than 0.05%.

The thermal lens strength is calculated by assuming a uniform heat deposition along the crystal and is given by [116, 183]

$$\frac{1}{f_{\text{dia}}} = \frac{P_{\text{dep}}}{2\pi K_C w_P^2}\left[\frac{dn}{dT} + (n-1)(\nu+1)\alpha_T + n^3\alpha_T C_{r,\phi}\right] \tag{4.19}$$

where P_{dep} is the total heat load deposited, $\frac{dn}{dT}$ is the thermo-optic coefficient, n is the refractive index, ν is the Poisson's ratio, $C_{r,\phi}$ are the photoelastic coefficients in the cylindrical coordinates, K_C is the thermal conductivity (2200 W/mK), and α_T is the thermal expansion coefficient. Diamond has a moderately high $\frac{dn}{dT}$ and unusually small α_T and hence the major contributor to lensing in Eq. 4.19 is due to the thermo-optic term [116] and is the only term considered here.

The heat load due to phonon-decay is

$$P_{\text{ph}} = \left(\frac{\lambda_S}{\lambda_P} - 1\right) P_S^{OC} \tag{4.20}$$

and impurity absorption is

$$P_{\text{abs}} = P_S^{int}\alpha_d L_d. \tag{4.21}$$

From Eq. 4.20, the heat load due to phonon decay for 11 W of Stokes generated is calculated to be 1.82 W. From Eq. 4.21, and given the intracavity Stokes power of 4 kW and absorption coefficient of 0.1 %/cm (taken from Fig. 1.6 in Sec.1.3), the heat load contribution due to impurity absorption is calculated to be 3.2 W. With the same focussing parameters for 30 W SHG, the thermal lens focal length in diamond is calculated to be 33 cm. (Note that, the model determined α_{d} is not relevant in this context as it includes contributions from scattering and other parasitic losses in the cavity that do not lead to crystal heating). The current cavity can accommodate a thermal lens of focal length up to 2.6 cm (calculated using PSST) by adjusting the cavity length and hence the calculated thermal lens is an order of magnitude weaker.

In addition to lensing due to the thermal gradient, the absolute temperature rise is considered, in order to check its importance on Raman gain properties. The temperature rise due to SRS and impurity absorption is calculated using the equation (assuming a top-hat beam profile and unrestricted heat flow from the laser crystal to the heat sink) [184],

$$T_{\mathrm{max}} = T_{\mathrm{c}} + \frac{P_{\mathrm{dep}}\alpha_{\mathrm{d}}}{2\pi}\left[\frac{1}{2K_{\mathrm{C}}}\left(1 + 2\ln\frac{r_0}{w_{\mathrm{P}}}\right)\right], \tag{4.22}$$

where T_{max} is the maximum temperature reached in the diamond, T_{c} is the coolant temperature (the temperature of the copper block where the diamond is mounted), and r_0 is the radius of the laser crystal (approximately equal to the width of the diamond). Provided that the coolant temperature is approximately 20°C, the temperature gradient is calculated to be 5.5°C. Since the Raman gain or linewidth is only expected to be affected for temperature rise greater than 500 K, the absolute temperature rise is deduced to be negligible [119, 185].

4.7.2 Thermal effects in LBO

The major cause of heating in LBO is the absorption of the intracavity Stokes power due to the presence of defects and impurities. The thermal lens strength in LBO has been derived as [186]

$$\frac{1}{f_{\mathrm{LBO}}} = \frac{P_{\mathrm{S}}^{int}\alpha_{\chi 2}L_{\chi 2}}{\pi K_{\mathrm{C}} w_{\mathrm{LBO}}^2}\frac{\mathrm{d}n}{\mathrm{d}T}\ln 2 \tag{4.23}$$

where it was assumed that the end-face bulging of LBO was small and where $dn_x/dT = -9.3 \times 10^{-6}\ /^{\circ}C$, $dn_y/dT = -13.6 \times 10^{-6}\ /^{\circ}C$, and $dn_z/dT = -8.9 \times 10^{-6}\ /^{\circ}C$, $K_{\mathrm{C(x,y)}} =$

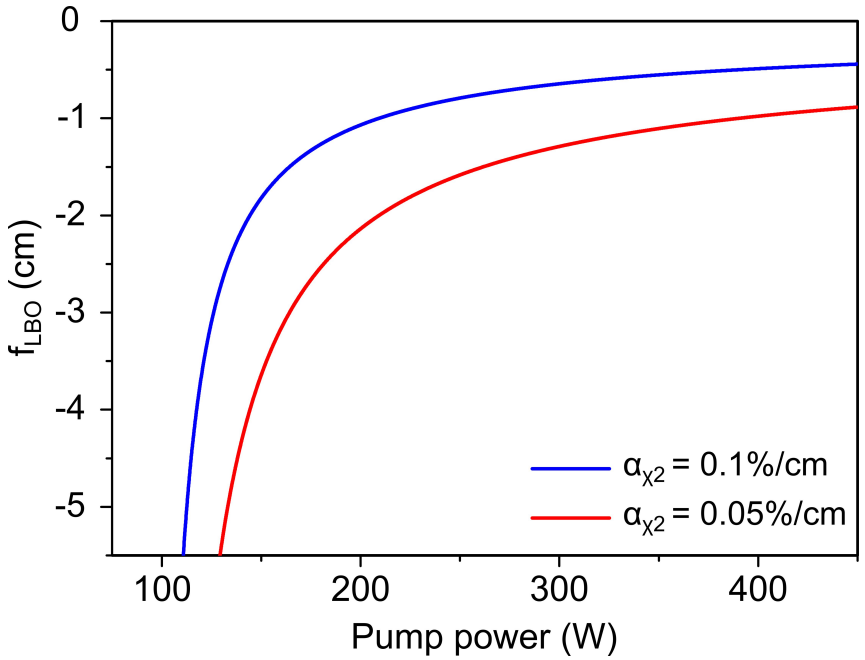

Figure 4.16: Thermal lens focal length in LBO as a function of input pump power for $\alpha_{\chi 2}$ = 0.1%/cm and $\alpha_{\chi 2}$ = 0.05%/cm.

3.97 W/mK and $K_{C(z)}$ = 3.03 W/mK. Since the thermal conductivity is anisotropic, the lens will be strictly astigmatic. However, the anisotropy is fairly small and hence it is neglected here, in order to obtain a first pass estimate of the lens strength. The minimum value of thermal conductivity along the z-direction is taken to predict the upper bound of the lens strength. Also, dn_z/dT is taken as the polarization is closely aligned to the z-axis. The absorption coefficient $\alpha_{\chi 2}$ of LBO, as given by the supplier's specification (Castech.Inc), is 0.1%/cm (here again, the model determined absorption coefficient is not taken due to the reasons described above). For an intracavity power of 4 kW, the total heat deposited in the LBO due to Stokes absorption is approximately 4 W. Additional heating due to red absorption is likely to be approximately 0.12 W, which is negligible compared to the contribution from Stokes absorption. The thermal lens strength in LBO is calculated to be more than an order of magnitude stronger which, like the time to attain steady-state profile, is a direct result of its much lower thermal conductivity compared to diamond. Hence the thermal effects in LBO is deduced to be the major limiting factor in power scaling.

Fig. 4.16 shows the thermal lens focal length f_{LBO} as a function of the incident pump power for two different $\alpha_{\chi 2}$ values, 0.1%/cm (as given in the data sheet) and 0.05%/cm (high optical quality LBO given in [187]). At the current operating pump level (204 W) with $\alpha_{\chi 2}$

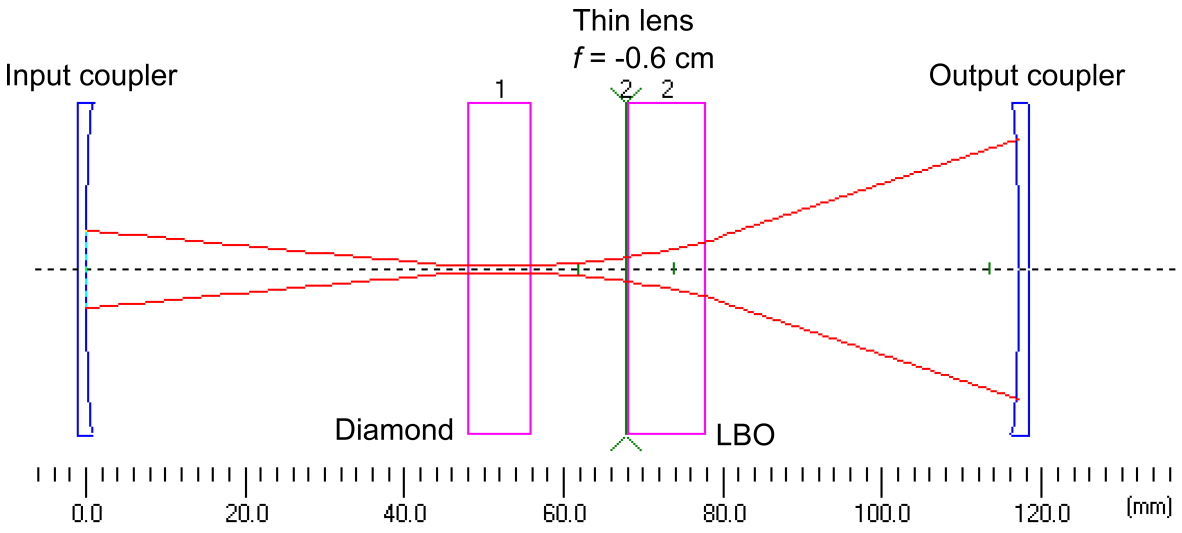

Figure 4.17: Stokes laser cavity after introducing -6 mm thin lens.

= 0.1%/cm, a thermal lens of focal length -1 cm is calculated. It is seen that by adjusting the cavity length, a thermal lens of up to -0.6 cm can be accommodated in the cavity (see Fig. 4.17 obtained using PSST). This implies that the pump power may be increased up to 320 W which would potentially yield up to 95 W of SHG output power. By using a low-loss LBO with $\alpha_{\chi 2}$ = 0.05%/cm given in Ref. [187], f is calculated to be approximately -2 cm at the current pump level (204 W) which potentially generates up to 50 W of SHG. The pump power may be increased up to 560 W, predicting SHG power of approximately 290 W before thermally-induced saturation. Although in this case the thermal lens may perturb the divergence of the Stokes beam in the cavity, this may be compensated by a combination of translating the LBO and adjusting cavity length.

4.8 Discussion

The laser demonstrated here shows the potential of intracavity doubled DRL to generate high power in the red spectral region. The power demonstrated here is high compared to other competing technologies such as frequency doubling of rare-earth doped lasers [39, 171–173], semiconductor disk lasers [174, 175], VECSELs [179, 180] and laser diodes [181]. In addition, the DRL approach has the advantage of good beam quality at higher output power (ie., high brightness) as a result of the combined effects of Raman beam clean-up in generating output of the fundamental spatial mode and the lack of thermally-induced saturation in the diamond.

As discussed in Sec.4.6, further improvement in SHG power may be attained by reducing the Stokes resonator loss, diamond and LBO crystal losses, increasing the diamond length and tighter pump focussing. For example, when T<0.1%, α_d <0.2%/cm (for 20 ppb CVD diamond, see also Fig. 1.6), $\alpha_{\chi 2}$ = 0.1%/cm (approximate absorption and scattering losses for low-loss LBO), L_d = 15 mm, and w_P = 30 μm (which is within the range for the current cavity), the SHG power potentially increases to more than 90 W with approximately 45% conversion efficiency at the current power level of 204 W (see Fig. 4.18). In addition, with these parameters, the SHG power may be increased up to 280 W for a pump power of 480 W without thermally-induced saturation.

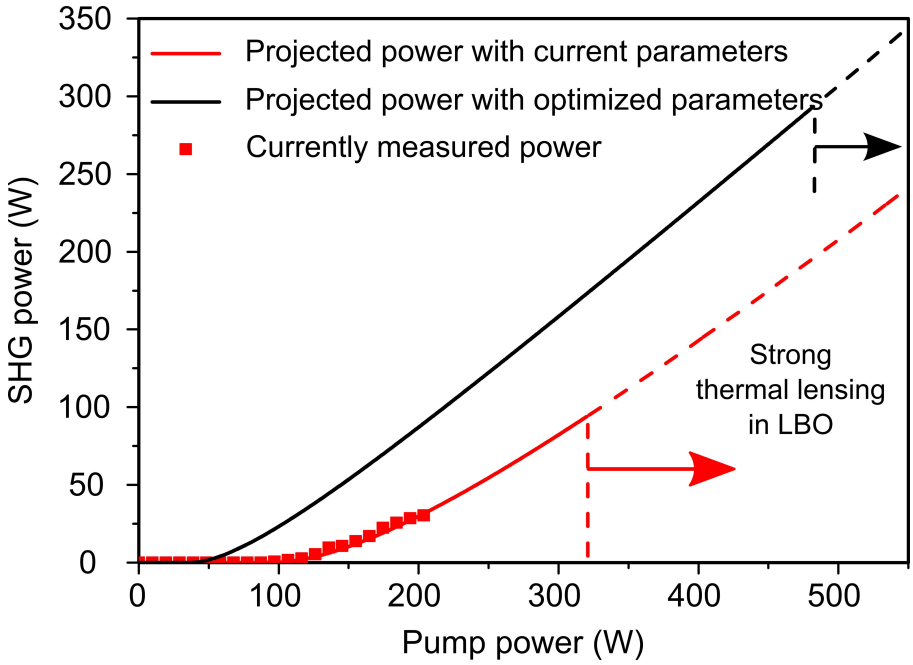

Figure 4.18: Projected SHG power with optimized parameters T<0.1%, α_d = 0.17%/cm, $\alpha_{\chi 2}$ = 0.1%/cm, w_P = 30 μm and L_d = 15 mm. Other parameters remains the same as 30 W SHG power. The measured and calculated SHG power with the current parameters are also shown for comparison. The red and black dashed lines represent strong thermal lens regime.

Furthermore, note that the Stokes was horizontally polarized and thus the Raman gain in the current configuration is 75% of the maximum achievable value. Improved laser performance is thus expected by orienting the LBO phase-matching plane, and hence the Stokes polarization, parallel to a ⟨111⟩ direction of the diamond (35.3° from horizontal).

The concept described in this chapter offers the potential to further explore more wavelengths in the visible and UV spectral regions by making use of higher order Stokes wavelength

as well as by using visible pump lasers. Although the design parameters for intracavity doubling of higher-order Stokes will be different, the basic principles are likely to be similar. High brightness output at 742.5 nm, for example, is feasible by making use of the second Stokes (1485 nm) and subsequent intracavity doubling. The secondary output lines of Nd lasers near 1320 nm may potentially enable generation of 1600 nm first Stokes or 2035 nm second Stokes with associated SHG wavelengths generates 800 nm (as an alternative for Ti:Sapphire laser) and 1018 nm respectively. Further wavelength options are also presented by using the broad tuning range offered by high-power Yb-doped fiber lasers. Fundamental output between 1010 nm and 1070 nm [188], for example, may be utilized to generate tunable first Stokes wavelength in the diamond from 1167-1248 nm and second Stokes from 1381-1496 nm and subsequent frequency doubling generates wavelengths ranging from 584-624 nm and 690-748 nm. This provides an alternative that is simpler and potentially more cost effective and that may be able to address applications in laser guide stars (589 nm) and atom cooling.

The concept is also further developed in the next chapter (Chapter 5), by utilizing a frequency-doubled Nd:YAG at 532 nm to generate 573 nm first Stokes output and with the view to intracavity frequency doubling to the deep-UV.

4.9 Chapter summary

The frequency extension of high power DRLs to visible wavelengths by intracavity frequency doubling has been demonstrated. A type I phase matched LBO was used in an external cavity DRL to generate quasi-CW 30 W output power at 620 nm with 15% conversion efficiency and excellent beam quality (M^2 = 1.1) for 204 W of available pump power. The first Stokes and the frequency doubled output was measured to have horizontal and vertical polarization respectively which agrees with the polarization behaviour of CW DRL described in Chapter 3. The SHG power as a function of the distance between the diamond and LBO was studied and found that the positioning of the LBO was crucial in determining the nonlinear output coupling and thus SHG efficiency.

A model was presented to provide insights for optimised operation and power scaling over a range of design parameters. Comparison of model and experiment provided a good understanding of the laser behaviour as a function of nonlinear coupling. It was found that

the length of the diamond, losses in the diamond and LBO, Stokes output coupling and pump focussing are the parameters to be optimized to generate more than 90 W of 620 nm at the current pump level.

Extension to higher power and from quasi-CW to CW operation was considered by examining the thermal effects that are expected to come into play in the diamond and LBO. In steady-state CW operation, the thermal lens strength in LBO is calculated to be more than an order of magnitude higher than in diamond, owing to the relatively low thermal conductivity of LBO and is the crucial factor in limiting the power scaling. The current cavity design and design parameters predicts CW power approaching 100 W for 320 W pump powers before thermal effects are likely to impact upon the performance. In addition, with optimized Stokes output coupling, low-loss LBO and diamond, focussing parameters, and length of the diamond, the SHG power may be increased to greater than 90 W at the current pump level and up to 280 W for 480 W pump power without significant thermal effects.

These results show the prospects for extending the wavelength range of diamond Raman lasers further by utilizing higher order Stokes as well as different pump wavelengths.

5

532 nm-pumped DRL: CW yellow and deep-UV generation

The previous chapter demonstrated a DRL operating in the IR with intracavity frequency doubling to generate visible output. The same approach is extended here, to generate Stokes in the yellow region by utilizing green pump source with the aim of further extending it to the deep-UV by intracavity frequency doubling.

CW yellow lasers find applications in skin and vascular medical treatments, ophthalmology, and laser displays. In the UV, applications include spectroscopy, atom cooling and trapping, photolithography, and material processing. High power CW lasers, especially in the deep-UV spectral region, are challenging due to scarcity of gain materials in this spectral range. To date, the main route to deep-UV has been through the SHG and SFG using cavity resonant frequency conversion [15, 16, 189–192] and intracavity frequency doubling [193]. An alternative technology is Ce doped lasers with emission in the deep-UV spectral region [194, 195]. However, the maximum power achievable using these technologies are

limited to few hundred milliwatts except at 266 nm with power reported up to 12 W. Also, at higher powers, it is difficult to maintain the beam quality. Hence, there is a need for high average power and high beam quality laser technology in this wavelength range.

Diamond Raman lasers pumped in the visible with intracavity frequency doubling offer the most promising technique for high power and high brightness lasers in the deep-UV spectral region. This chapter presents a DRL pumped with 532 nm CW pump laser to generate 573 nm Stokes. The basic laser design is presented and the fundamental laser characteristics are investigated. An analytical model is presented to provide insights into the characteristics and operation of visible DRL compared to near-IR. Also, ways of improving the laser performance by optimizing various design parameters are presented. These results were used to predict designs for high power deep-UV generation.

5.1 Experimental arrangement

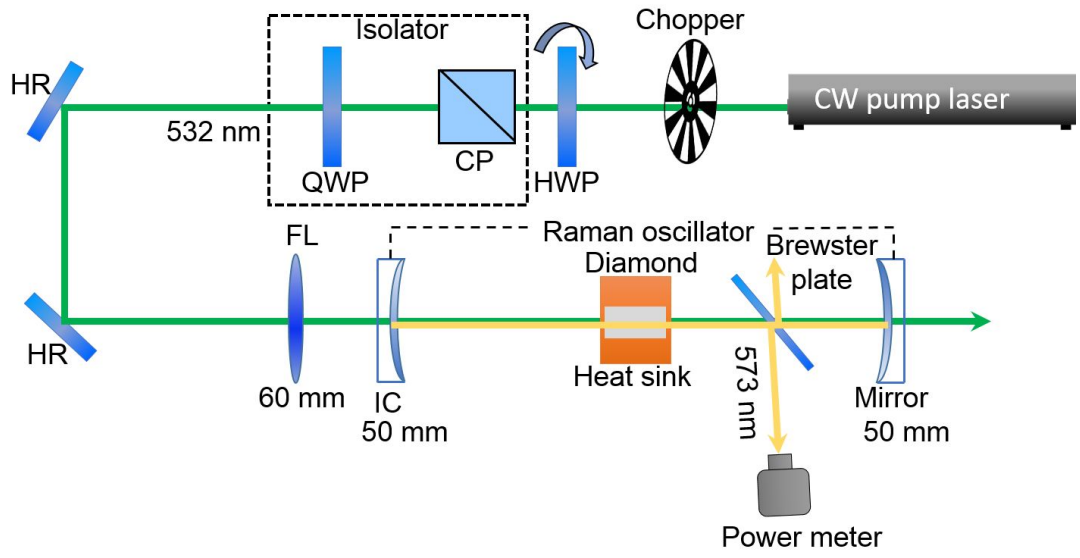

Figure 5.1: Experimental arrangement for a green pumped DRL. HWP - half-wave plate, CP - cube polarizer, QWP - quarter-wave plate, FL - focussing lens anf IC - input coupler.

The experimental arrangement for the green pumped DRL is shown in Figure. 5.1. The pump source used was a CW frequency doubled Yb-doped fiber laser (Model GLR 100, IPG photonics) with single longitudinal mode (line-width<1 MHz) and vertically polarized output at 532 nm. An optical chopper with 50% duty-cycle at 613 Hz frequency (0.8 ms pulse

duration) was used as a means of improving the safety. The thermal gradient in diamond establishes within a few tens of microseconds [93] enabling steady state operation within this pulse duration. A half-wave plate (HWP) and cube-polarizer (CP) (shown in Fig. 5.1) was used to provide variable attenuation of the pump power. The cube-polarizer and quarter-wave plate (QWP) provides optical isolation from the back-reflected pump beam resulting in a circularly polarized pump beam. This type of isolator works effectively when the pump polarization state is maintained throughout the laser cavity. Hence, any depolarization such as due to stress-induced birefringence in the diamond will reduce the optical isolation.

The Raman laser cavity consisted of a 104 mm-long near-concentric resonator consisting of an input coupler (radius of curvature = 50 mm), diamond as the gain medium, an end mirror (radius of curvature = 50 mm) and Brewster plate as the output coupler. A 60 mm focussing lens (FL in Fig. 5.1) was used to focus the pump beam into the centre of the diamond with a Rayleigh range of approximately 2 mm. The diamond used was an $8 \times 4 \times 1$ mm single-crystal CVD diamond, the same type as used for IR pumping (that is ultra-low birefringence material, Element Six Ltd) and was AR coated at 573 nm. The input coupler was highly transmitting for the pump beam (T>98%) and highly reflecting (R>99.9%) for the first Stokes at 573 nm. The same mirror was used as the end mirror providing a single pass for the pump and high-Q for the Stokes with near-zero transmission (T<0.1%) for the Stokes. Unlike the case of Chapters 2 and 3, single-pass pumping was used here due to the lack of a suitable Faraday isolator in the green and subsequently the concern of the strong depolarization in the diamond. A fused-silica Brewster plate was used to provide tunable output coupling for the Stokes beam.

Rotating the Brewster plate changes the reflectance of the p and s-polarized beam according to the Fresnel reflection. For the fused-silica (n=1.46), the Brewster angle is 55.4° where the reflection loss for the p-polarized light is zero. The s-polarized light, however, undergoes high reflection loss of 12.5%, and hence will not reach the threshold for lasing. For small angles of incidence from the Brewster angle, the total reflectance of the p-polarized light for double passing through both the Brewster plate surfaces is approximately four times the single surface reflectance. Fig. 5.2 shows the total reflectance of the p-polarized Stokes beam as a function of Brewster plate angle over the working range used in the experiment. It can be seen that the reflectance increases, as the Brewster plate is rotated away from the Brewster angle of 55.4° and the output coupling of the Stokes beam varies from 0.036% to

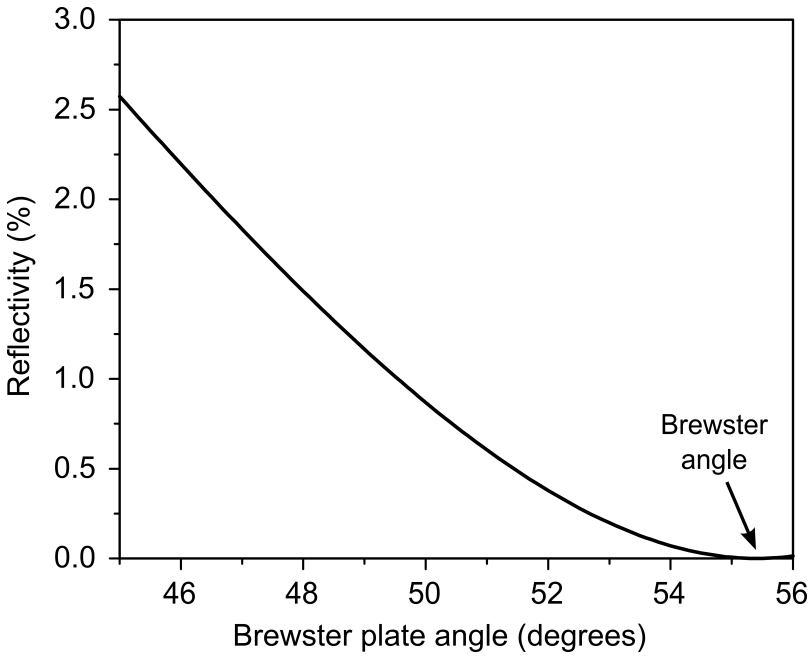

Figure 5.2: Reflectance of the *p*-polarized Stokes beam as a function of Brewster plate angle over the working range used in the experiment.

2% for a Brewster plate rotation from 54.5° to 46.5°.

5.2 Experimental results

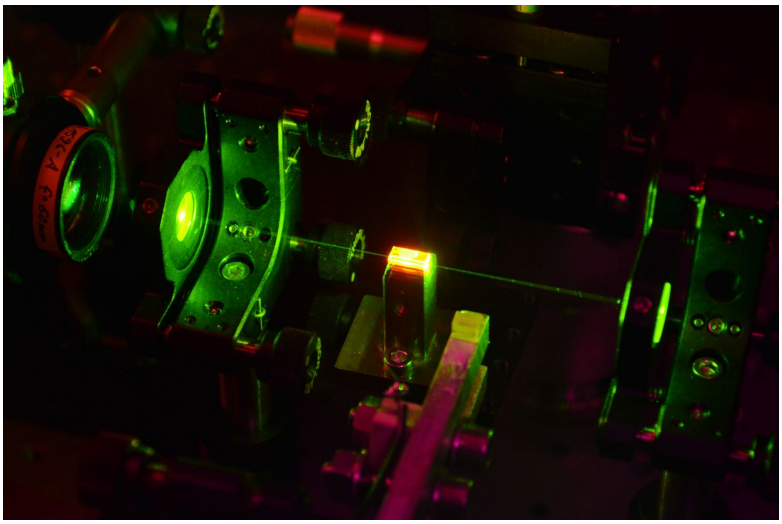

Figure 5.3: Photograph showing 573 nm Stokes generation in the Raman laser cavity.

At the Brewster plate angle of 54.5°, the onset of lasing was observed at a threshold pump power of 25 W generating 573 nm Stokes laser. Fig. 5.3 shows the photograph of 573 nm

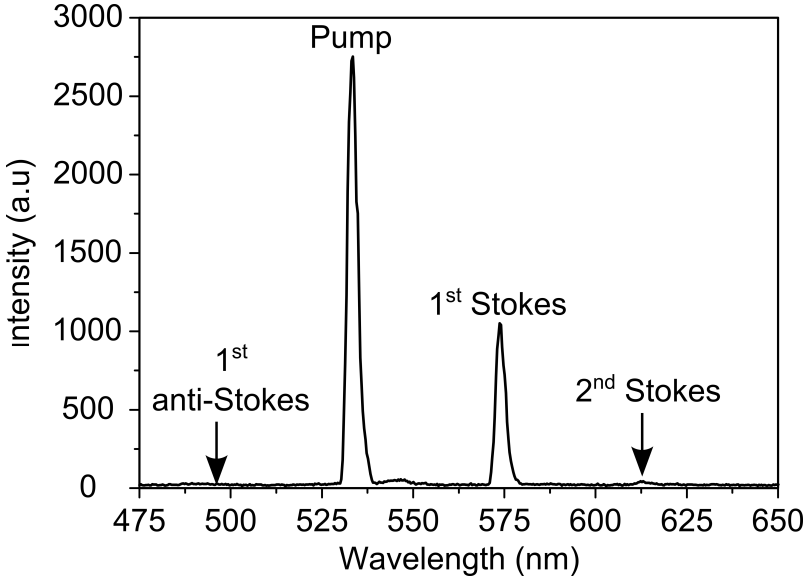

Figure 5.4: Output spectrum obtained when pumping with the 532 nm laser.

Stokes generation and Fig. 5.4 shows the output spectrum measured using Ocean Optics spectrometer. The spectrum shows pump, first Stokes as well as second Stokes photons. The second Stokes appeared as a ring around the first Stokes, a characteristic pattern of Raman-enhanced four-wave mixing of two Stokes photons and a pump photon [196]. No anti-Stokes was detected up to the maximum pump power (66 W).

The polarization of the Stokes was measured before and after placing the Brewster plate. Before inserting the Brewster plate, the Stokes beam leakage through the end mirror was measured to be horizontally polarized. Fig. 5.5 shows the Metripol determined birefringence map of the diamond sample along the [110] direction used in this experiment. It is seen that the magnitude of linear retardance is relatively uniform except for a small region towards the left-hand side with a maximum linear retardance up to 25° (Δn up to 5×10^{-6}). The linear retardance axis direction is also uniform across most of the crystals area and near 0° with respect to the horizontal. Hence, the measured DRL Stokes polarization is in good agreement with the results described in Chapter 3. Note that, the birefringence was characterized using Metripol technique and hence any effect of circular retardance (if present) on the linear birefringence measurement accuracy has not been taken into consideration. However, the circular birefringence is expected to be low (much less than 20 degrees) in this crystal as the overall retardances are substantially smaller than the crystal investigated in Chapter 2. The Brewster plate was inserted into the cavity with the tilt direction chosen to maintain the polarization in the horizontal direction.

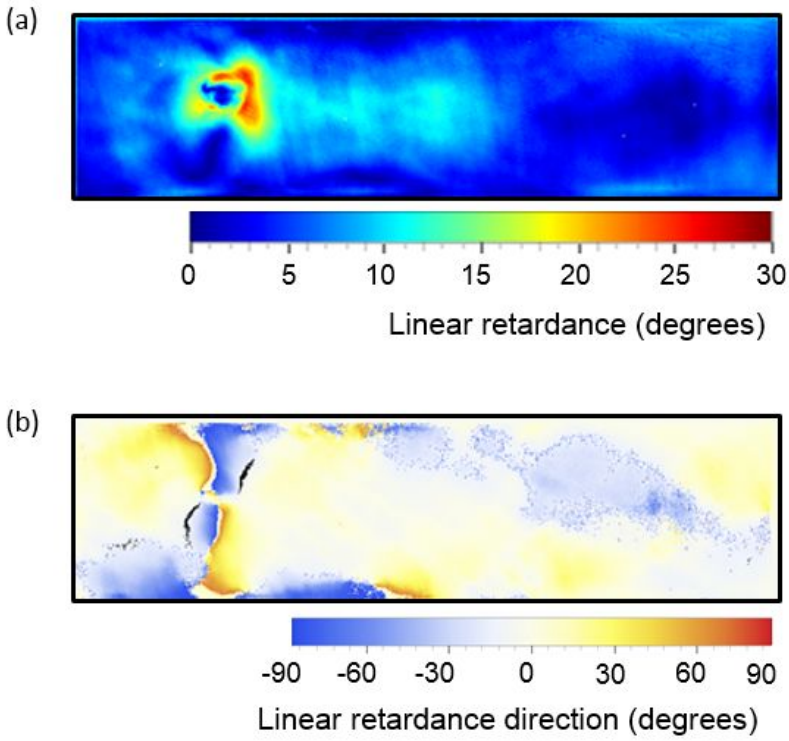

Figure 5.5: Metripol determined maps of linear birefringence (a) magnitude and (b) direction. 0° in the linear retardance direction map represents $\langle 1\bar{1}0 \rangle$ (horizontal axis).

Fig. 5.6 shows the dependence of the Brewster plate reflectivity, Stokes power (for a pump power of 66 W), threshold and slope efficiency on the Brewster plate angle. The absolute Brewster plate angle was calibrated using the angle giving the minimum slope efficiency (and hence lowest reflection). As the Brewster plate is rotated away from the Brewster angle (55.4°), the output coupled Stokes power increases, reaches a maximum value (15 W Stokes output) and then decreases. Above the optimal output coupling region, the losses in the cavity become higher, resulting in a reduction in intracavity Stokes power and thus a reduction in output power. The threshold pump power increases with output coupling as higher pump powers are required for compensating the output coupling loss. Also, the slope efficiency increases with increasing output coupling (Fig. 5.6 (d)) as expected due to the diminishing impact of parasitic losses.

Fig. 5.7 shows the Stokes power and the residual pump power as a function of pump power for the optimum Brewster plate angle 49° (output coupling $\simeq$ 1.2%). Starting with a threshold of 40 W, the maximum Stokes power of 15 W was obtained with a slope efficiency

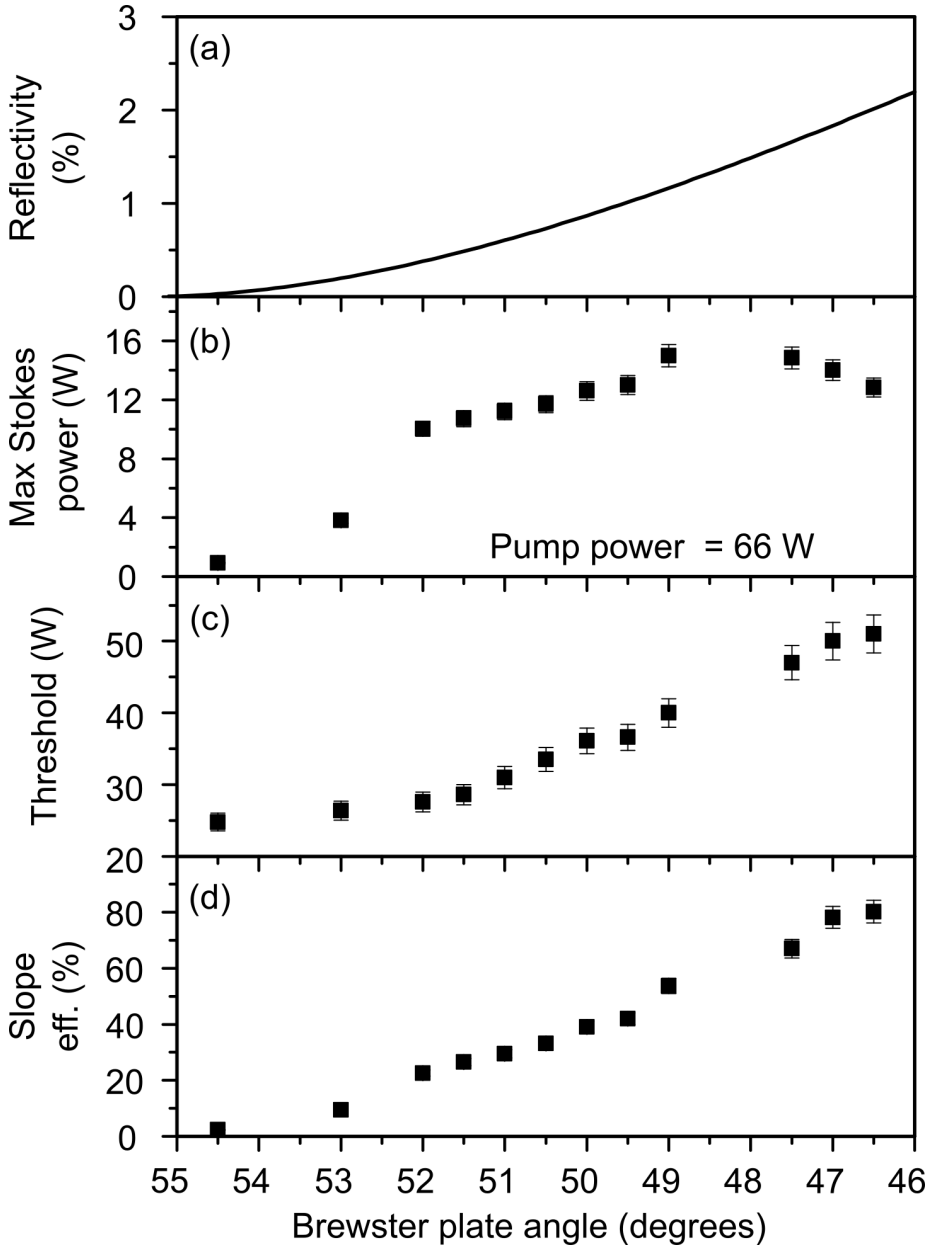

Figure 5.6: (a) Brewster plate reflectivity (Stokes output coupling) (b) Stokes power at 66 W of pump power (c) threshold pump power (d) and slope efficiency as a function of Brewster plate angle.

of 53.7% and maximum conversion efficiency of 22.7% and was limited by the available pump power (66 W). Note that, for the lower power measurements, the chopper was routinely removed to confirm that the 0.8 ms burst results are representative of genuine CW operation. The residual pump power increases with the incident power until it reaches the threshold, and then slightly decreases and remains approximately constant. The residual pump power is expected to decrease monotonically after the lasing threshold as a result of the pump depletion

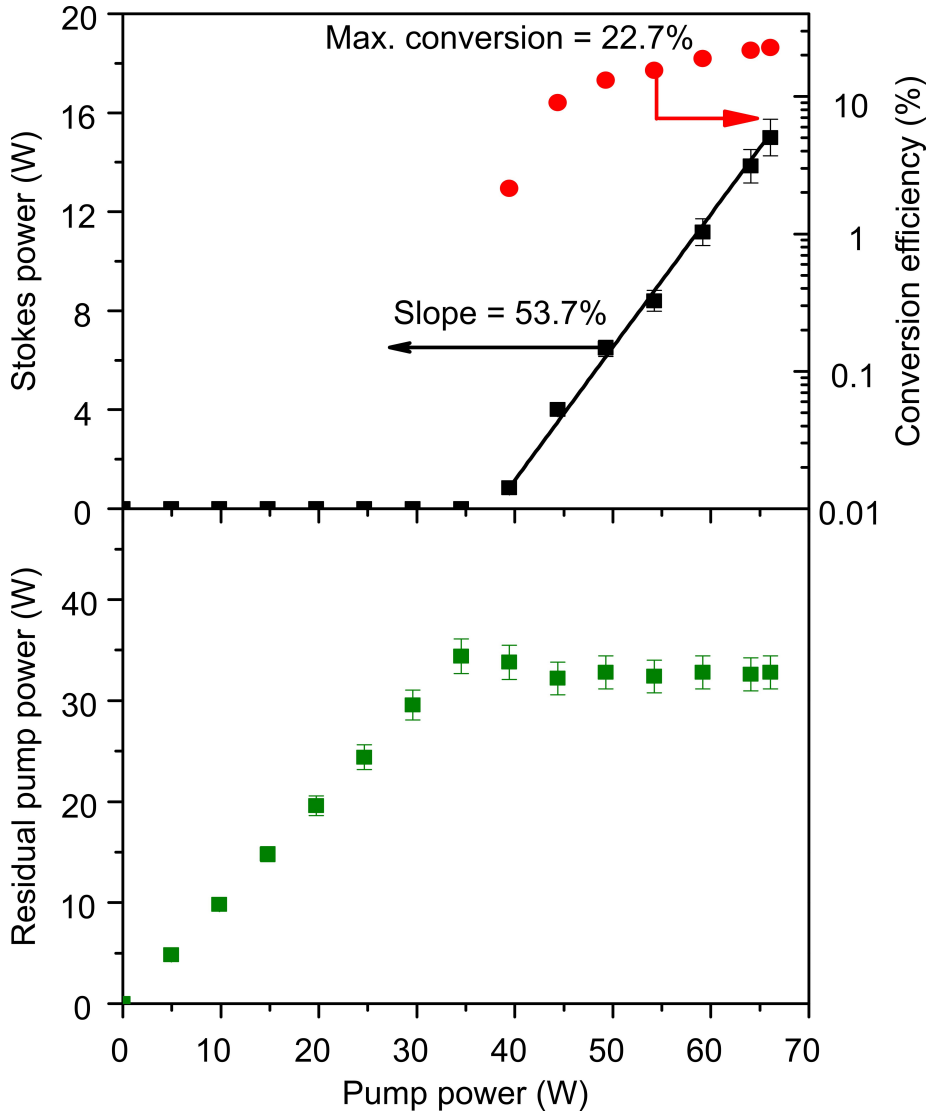

Figure 5.7: Measured Stokes power (top figure) and residual pump power (bottom figure) as a function of pump power for a Brewster plate angle of 49°.

by the growing Stokes intensity (see also Sec.5.3). However, depletion is highly sensitive to alignment and it is also likely that, in the limit of very large depletion, the conversion is hampered by deterioration in the spatial properties of the heavily depleted pump beam.

Measurement of the residual pump power enables a power budget for the laser to be constructed. Fig. 5.8 shows the flow of optical power from 532 nm pump to 573 nm Stokes at the maximum Stokes power level. The depleted pump power is distributed between the Stokes output coupling and the losses in the cavity. The ratio between the Stokes output coupling and the cavity losses determine the useful output. Here, the measured residual pump power is 32.8 W (at the maximum pump power), indicating 50% pump depletion. The pump depletion

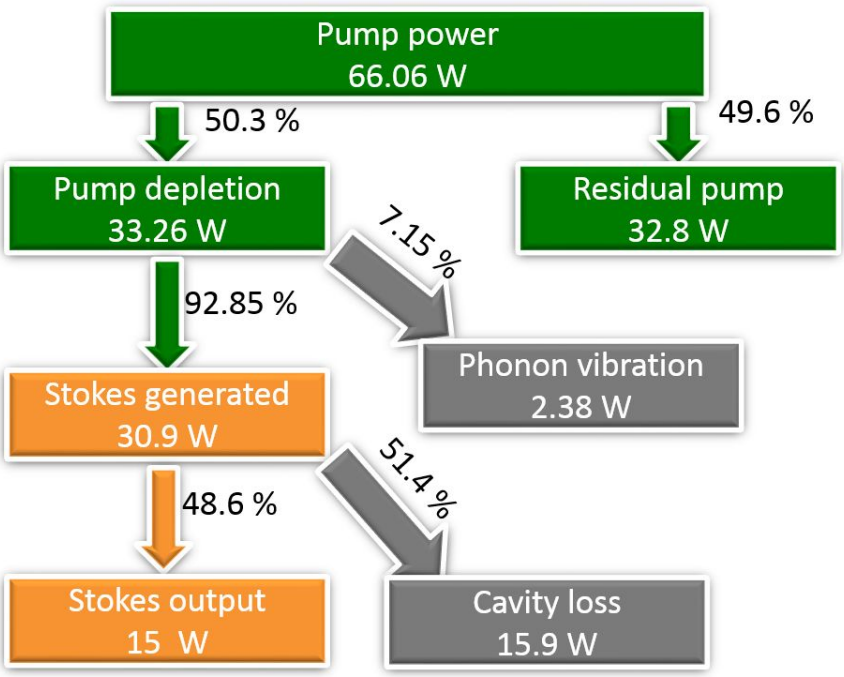

Figure 5.8: Power budget calculation of the 15 W yellow laser showing the distribution of input pump power throughout the system.

depends on the pump power as well as the mode overlap between the pump and Stokes. A higher depletion is expected with higher pump powers and for better overlap between the pump and Stokes mode, as will be discussed in the next section. Out of the 33.3 W of depleted pump power, 7.2% of the power is lost due to quantum defect and the remaining 30.9 W is available for the generation of intracavity Stokes field. The measured Stokes power was 15 W (48.6% of the total Stokes generated), and hence the remaining 15.9 W (51.4%) is attributed to the losses inside the cavity such as absorption, scattering, reflection and birefringence losses. Using the Stokes output coupling (approximately 1.2%) and the intracavity Stokes power, the combined absorption and scattering coefficient is deduced to be approximately 0.8-0.9%/cm. This is slightly higher than the absorption coefficient value (0.1-0.5%/cm at 532 nm) for low nitrogen (20 ppb) single crystal CVD diamond previously reported by the manufacturer [145]. Hence, the diamond crystal used here is likely to have a nitrogen content slightly higher at approximately 40 ppb. Further improvement in the Stokes output power, slope efficiency and conversion efficiency is predicted by improving the quality of the diamond as well as better overlap between the pump and Stokes fields/modes.

5.3 Laser model

The analytical model of the CW Raman laser of Kitzler *et al.* [86] is adapted here to understand the CW DRL characteristics in the visible. The model assumes that the pump beam, Stokes beam, and SHG beam are all Gaussian and the intracavity Stokes intensity is constant, owing to small gain and losses in the cavity. Following the equations from Chapter 4 (Sec.4.4),

$$P_{\mathrm{Res}} = P_{\mathrm{P}} \exp\left(-G P_{\mathrm{S}}^{int}\right). \tag{5.1}$$

And the total intracavity Stokes power generated is distributed between the output coupling loss P_{S}^{OC} and other resonator losses P_{S}^{loss}, such that

$$\begin{aligned} P_{\mathrm{S}}^{\mathrm{gen}} &= \eta P_{\mathrm{P}} \left[1 - \exp\left(-G P_{\mathrm{S}}^{int}\right)\right], \\ &= P_{\mathrm{S}}^{OC} + P_{\mathrm{S}}^{loss}. \end{aligned} \tag{5.2}$$

where $P_{\mathrm{S}}^{\mathrm{OC}}$ is (as given in Sec.4.4)

$$P_{\mathrm{S}}^{OC} = \frac{T}{2} P_{\mathrm{S}}^{int}. \tag{5.3}$$

Resonator losses P_{S}^{loss} includes absorption and scattering loss from the diamond (α_{d}) and the Brewster plate (α') as well as reflection loss from the diamond (κ). The reflection loss from Brewster plate is the output coupling P_{S}^{OC}.

$$P_{\mathrm{S}}^{loss} = \frac{2\alpha_{\mathrm{d}} L_{\mathrm{d}} + 2\alpha' L' + 2\kappa}{T} P_{\mathrm{S}}^{OC}. \tag{5.4}$$

where L' is the thickness of the Brewster plate.

The equation relating pump and Stokes power is obtained by substituting Eq. 5.3 and 5.4 in 5.2 [86, 127]

$$P_{\mathrm{P}} = \frac{T + 2\alpha_{\mathrm{d}} L_{\mathrm{d}} + 2\alpha' L' + 2\kappa}{\eta T \left[1 - \exp\left(-\frac{2G}{T} P_{\mathrm{S}}^{OC}\right)\right]} P_{\mathrm{S}}^{OC}. \tag{5.5}$$

The residual pump power is obtained by substituting Eq. 5.3 and 5.4 in Eq. 5.1

$$P_{\mathrm{Res}} = P_{\mathrm{P}} \exp\left(-\frac{2G}{T} P_{\mathrm{S}}^{OC}\right) = P_{\mathrm{P}} - \frac{T + 2\alpha_{\mathrm{d}} L_{\mathrm{d}} + 2\alpha' L' + 2\kappa}{\eta T} P_{\mathrm{S}}^{OC}. \tag{5.6}$$

The maximum conversion efficiency σ, is the slope of the Stokes versus pump power in the limit of infinite pump power (where the residual pump power approaches zero)

$$\sigma = \frac{\eta T}{T + 2\alpha_{\mathrm{d}} L_{\mathrm{d}} + 2\alpha' L' + 2\kappa}. \tag{5.7}$$

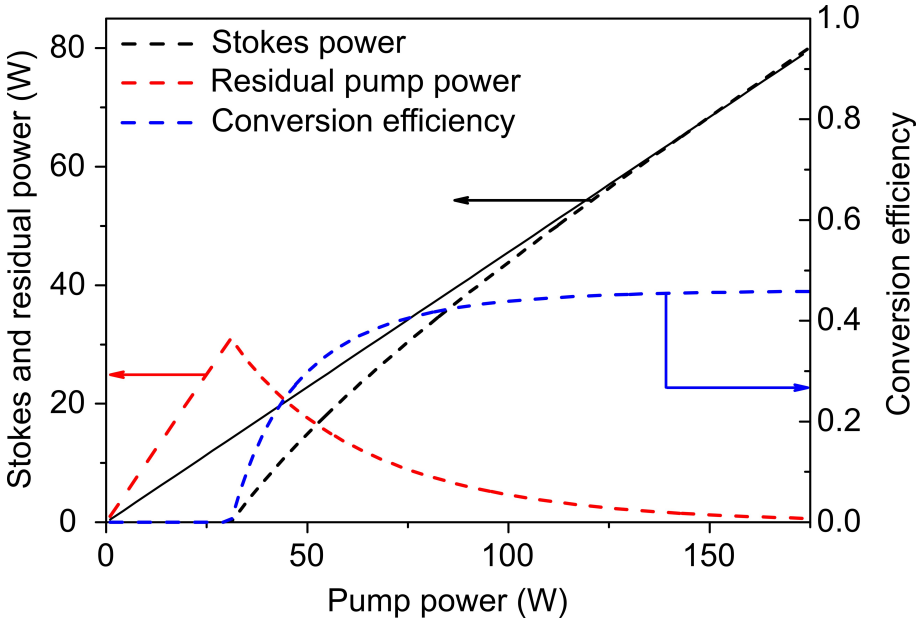

Figure 5.9: Output characteristics of green pumped DRL for $T = 1.2\%$, $\alpha_d = 0.5\%$/cm, $\alpha' = 0$, $w_P = 17$ μm, $w_S = 35$ μm, $L_d = 8$ mm, $M_P^2 = 2.0$ and $M_S^2 = 1.0$.

The threshold pump power is obtained by limiting the Stokes output P_S^{OC} to zero

$$P_P^{th} = \frac{T + 2\alpha_d L_d + 2\alpha' L' + 2\kappa}{2g_S \arctan(\zeta)}\Lambda. \tag{5.8}$$

Fig. 5.9 shows the behaviour of Stokes power, residual pump power and conversion efficiency as a function of pump power. Stokes power increases steeply just above threshold and thereafter approaches the linear rate according to Eq. 5.5. Above threshold, the residual pump power decreases following Eq. 5.6. For approximately 5 times above the threshold, the residual pump power closely approaches zero, and the conversion efficiency is given by Eq. 5.7.

5.4 Model comparison with experiment

In this section, the calculated Stokes and residual pump power from the analytical model in Sec.5.3 is compared with the experimental results from Sec.5.2. Here, the measurable parameters such as the output coupling, length of the diamond crystal and length of the Brewster plate are taken as fixed parameters. The Raman gain coefficient g_S of 14 cm/GW used was close to the previous measurements in the literature of approximately 15-20 cm/GW at 532 nm along the ⟨110⟩ (also refer Chapter 1). The beam widths of the pump and Stokes

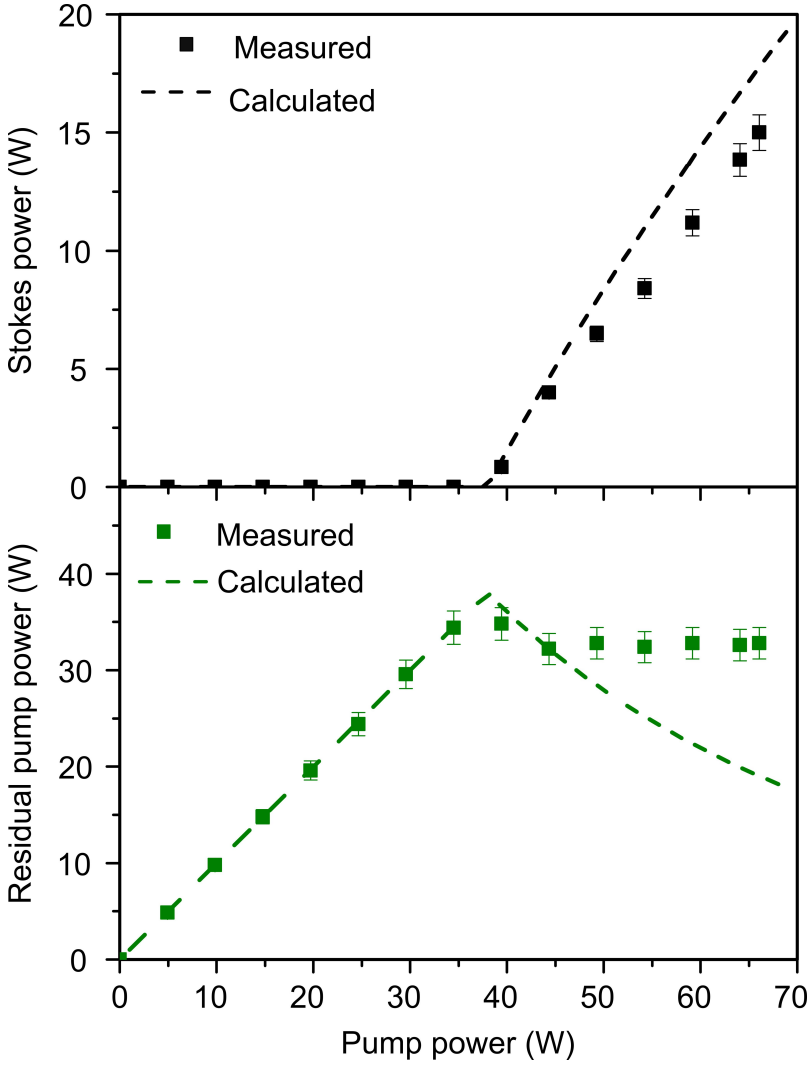

Figure 5.10: Measured (rectangular markers) and calculated (dashed line) Stokes power (top figure) and residual pump power (bottom figure) as a function of pump power for an output coupling of 1.2%.

were estimated using the LASCAD software for laser design (from the known values of pump beam radius of approximately 1.25 mm, radii of curvature of input and end mirrors and cavity length of 104 mm) to be approximately 17 μm and 35 μm respectively. The beam quality of the pump was not measured but was estimated to be approximately 2.0 as the pump beam passes through a series of optics including cube polarizer, a half-wave plate, quarter-wave plate and turning mirrors before it enters the DRL cavity. The Brewster plate precludes the straightforward measurement of M_S^2 considering the double image of the Stokes beam, however, is estimated to be 1.0 owing to the Raman beam clean-up and the consistently low M_S^2 values measured for all CW external cavity (or EC) DRLs to date. The parameter α_d,

which is the combined absorption and scattering coefficient of diamond at 573 nm is taken to be 0.9%/cm as determined from the power budget analysis in Sec.5.2. The reflection coefficient of the AR-coated diamond at 573 nm has been taken to be $\kappa = 0.1\%$ per surface.

Table 5.1: Simulation parameters used to model the experimental conditions corresponding to Fig. 5.7.

Variable	15 W Stokes power
T	1.2%
κ	0.2%
α_d	0.9%/cm
α'	0.03%/cm
L_d	8 mm
L'	2 mm
λ_P	532 nm
λ_S	573 nm
g_S	14 cm/GW
w_P	17 μm
w_S	35 μm
M_P^2	2.0
M_S^2	1.0

Fig. 5.10 shows the measured and calculated Stokes and residual power as a function of pump power and Tab. 5.1 summarizes the parameters used for fitting the model predicted results with the experimental results.

As shown in Fig. 5.10, the experimental results reasonably fit well with the model results. The notable discrepancy is in residual pump measurements where the experimental results indicate relatively low pump depletion, the reason for which was explained in Chapter 4. The poor pump depletion results in the deviation of Stokes output power from the calculated value when operating well above threshold.

Fig. 5.11 shows the measured and model determined maximum Stokes power (at 66 W of pump power), the threshold pump power and the initial slope efficiency as a function of output coupling. The maximum Stokes power and slope efficiency are slightly lower than the model predicted values due to the aforementioned problems with the model in replicating

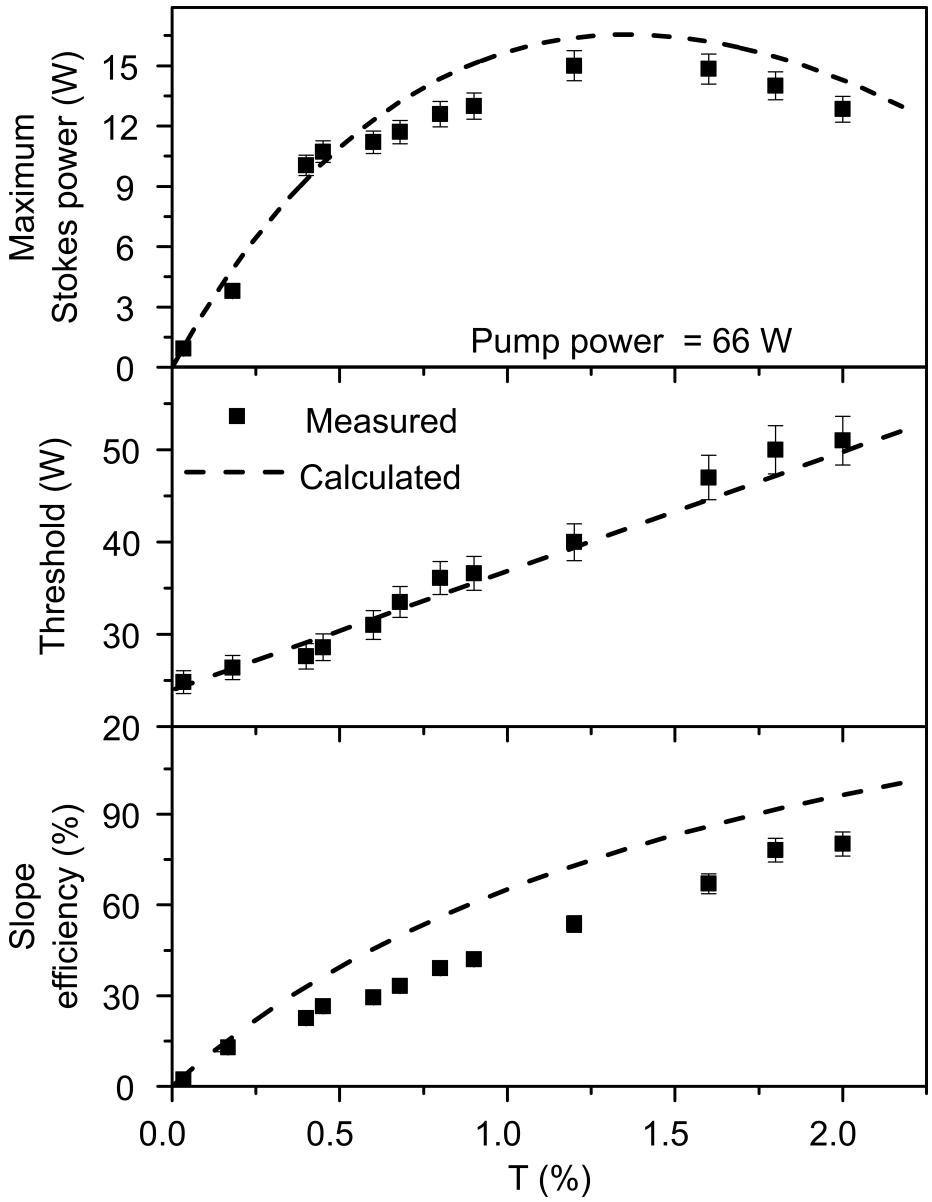

Figure 5.11: Measured (rectangular markers) and calculated (dashed line) Stokes power (at 66 W of pump power) (top figure), threshold pump power (middle figure) and initial slope efficiency (bottom figure) as a function of output coupling.

pump depletion at higher power. The measured thresholds fit well with the model predicted thresholds.

5.5 Optimizing laser performance

The model presented in Sec.5.3 is found to adequately describe the laser behaviour and hence it is valid to use it to study the influence on performance over a larger range of parameters.

In this section, we investigate parameters for optimising laser performance and predicting behaviour when using higher pump powers.

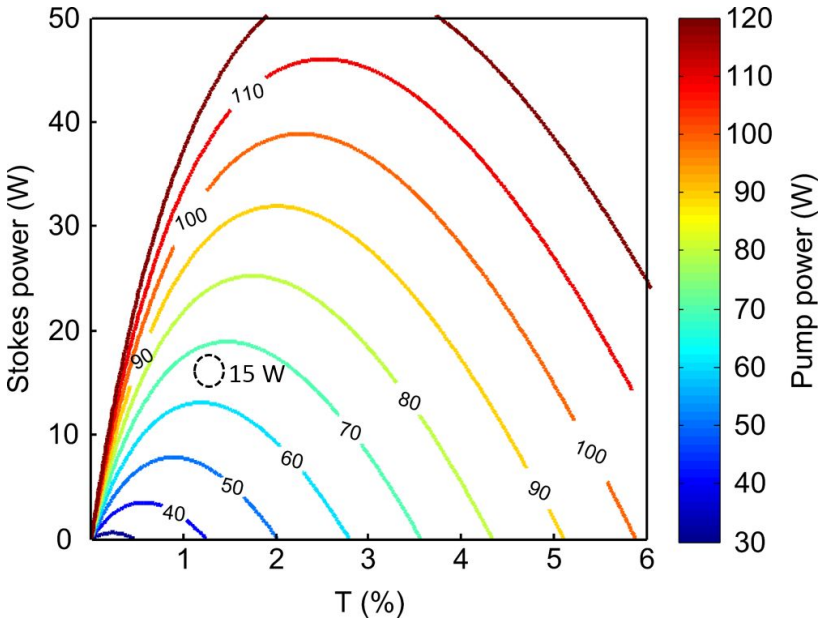

Figure 5.12: Stokes power as a function of output coupling T for different pump powers for w_P = 17 µm, w_S = 35 µm, L_d = 8 mm and α_d = 0.9%/cm. The region of operation for the 15 W Stokes for 66 W of pump power is indicated by the black dashed circle.

Fig. 5.12 shows the Stokes power dependence of output coupling for various pump powers. As the output coupling increases, the Stokes power also increases, reaches a maximum value and then decreases as discussed in Sec.5.2. The optimal output coupling increases for higher pump powers as shown the Fig. 5.12 as the output coupling affects the threshold and slope efficiency according to Eqs. 5.7 and 5.8. The plot was obtained for fixed focusing and loss parameters (from the Tab. 5.1). The region of operation of the 15 W Stokes power (indicated by the black dashed circle in Fig. 5.12) is the optimum output coupling for 66 W of pump power as expected (also shown in Fig. 5.11).

Fig. 5.13 shows the Stokes power as a function of the length of diamond crystal for various pump powers for fixed focusing and loss parameters (given in Tab. 5.1). Like the Stokes dependence of output coupling, there is an optimal length of the diamond crystal which results from trade-offs between Raman gain and parasitic losses. The optimum crystal length is found to increase slightly with pump power as higher parasitic losses can be tolerated. The model suggests that diamond length used in the experiment was slightly longer than the

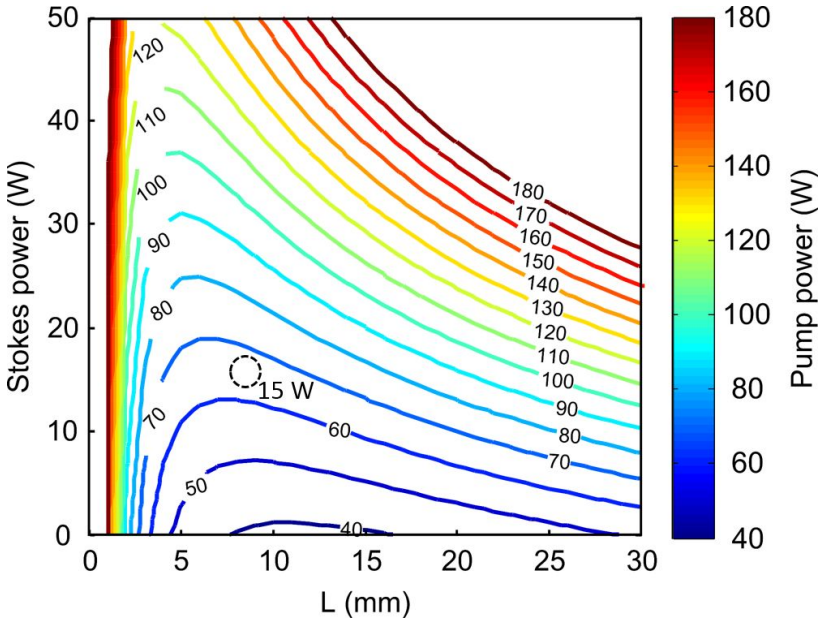

Figure 5.13: Stokes power as a function of length of the diamond L_d for different pump powers for w_P = 17 µm, w_S = 35 µm, T = 1.2% and α_d = 0.9%/cm. The region of operation for the 15 W Stokes for 66 W of pump power is indicated by the black dashed circle.

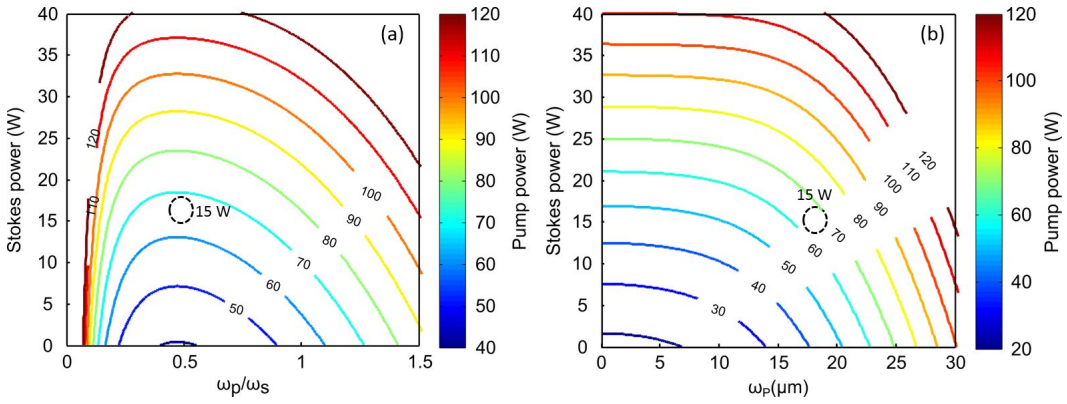

Figure 5.14: Stokes power as a function of (a) ratio of pump and Stokes beam waist radius (w_P/w_S) (b) Stokes mode matched pump beam waist (w_P) for different pump powers for T = 1.2%, α_d = 0.9%/cm and L_d = 8 mm. The region of operation for the 15 W Stokes for 66 W of pump power is indicated by the black dashed circle.

optimum value of 6-7 mm (see dashed circle in Fig. 5.13).

The pump and Stokes beam-waist radii are also important design parameters that can be varied to improve laser performance. Fig. 5.14 (a), shows that the ratio of w_P and w_S to obtain the maximum Stokes power is approximately 0.4. For a mode-matched pump and

Stokes beam ($w_P = 0.4 \times w_S$), Fig. 5.14 (b) shows the dependence of Stokes power with w_P. It is seen that tighter focusing is preferred for obtaining higher Stokes power, however, the Stokes power saturates below a certain pump beam radius (approximately 15 μm for 66 W of pump power) and any further reduction in the beam radius does not increase the Stokes power considerably. Hence, this w_P value is considered optimum as a further reduction increases the probability of laser-induced damage to the optical coatings and, if operating at very high power, exacerbates the thermally-induced lens as discussed in Chapter 4.

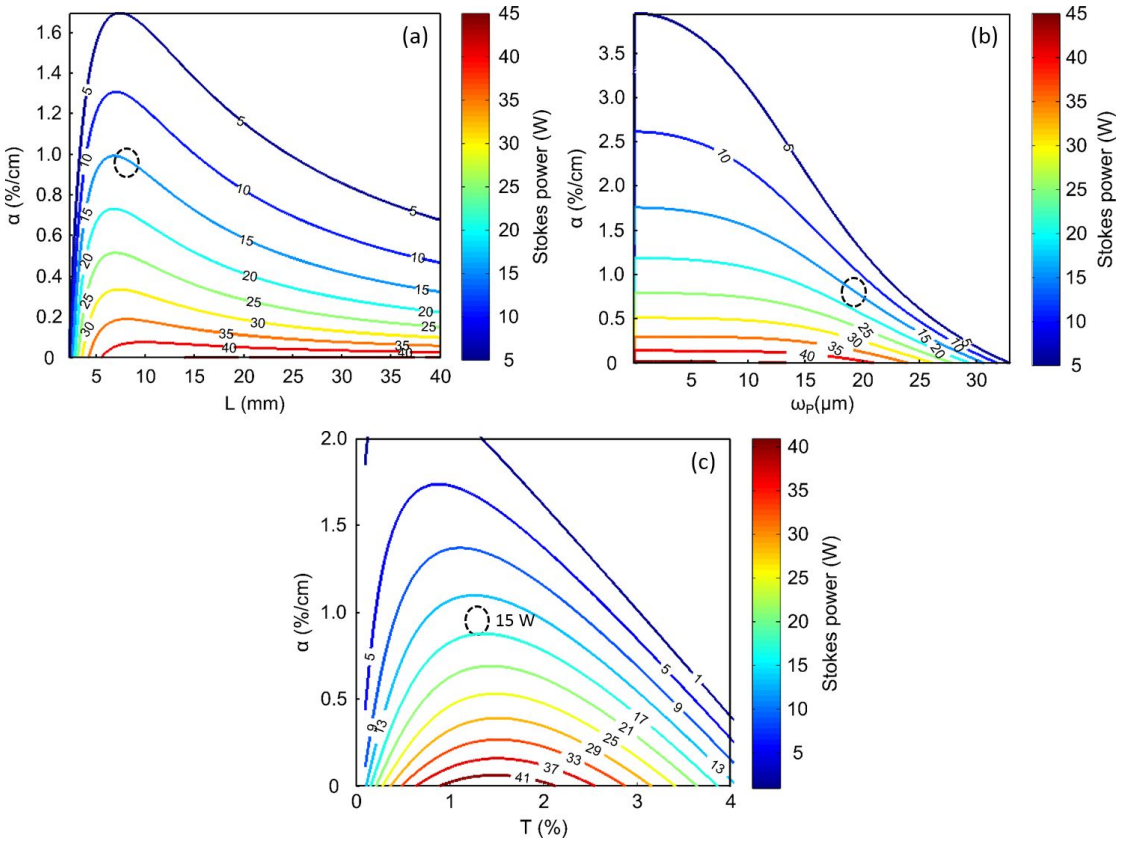

Figure 5.15: Stokes power as a function of absorption coefficient α_d and (a) crystal length L_d, (b) pump waist radius w_P, (c) output coupling T. The region of operation for the 15 W Stokes for 66 W of pump power is indicated by the black dashed circle.

The above plots were obtained when the diamond absorption coefficient α_d is kept at 0.9%/cm as derived from fitting the model results to the experimental results. In Fig. 5.15 (a), (b) and (c), the Stokes power dependence (for fixed pump power) as a function of α_d and L_d, w_P, and T respectively are shown. As expected, for a fixed pump power, the Stokes power decreases for higher crystal losses. The optimal crystal length also decreases for higher losses since, for a fixed focusing geometry, the round-trip losses increase at a faster rate than the

gain-length product. A tighter focusing in concert with shorter crystals are thus beneficial when using lossy crystals. For a given pump power, the optimal output coupling reduces with absorption loss (Fig. 5.15 (c)) in order to alleviate the impact of the loss on raising threshold.

5.6 Discussion

Although the 15 W Stokes power demonstrated here is in the quasi-CW regime, a significant reduction in the laser power or efficiency is not expected in the true CW regime as the Stokes power demonstrated here is much smaller than the previously demonstrated CW Stokes power of greater than 150 W in the IR [92]. Hence, the 15 W on-time Stokes power demonstrated here is likely to be readily achieved in the true CW regime.

The laser behaviour presented here in the visible is qualitatively similar to the previously reported near-IR CW diamond Raman lasers [86]. Higher efficiencies are predicted with a combination of reduced losses, shorter diamond, and tighter pump focussing as in the case of near-IR pumping. The major distinguishing factors in the visible are the higher Raman gain and absorption loss coefficients - approximately two and three times higher respectively. Also, the pump beam confocal parameter is longer in the visible (due to reduced diffraction), so that the optimum pump waist radius in the visible (approximately 20 μm) is smaller compared to the near-IR (approximately 40 μm). The combined result of these effects increases the optimum coupling in the visible to approximately 1-2% from 0.3-0.8% in the near-IR at comparable pump power levels.

In the present case, a Brewster plate was used to output couple the intracavity Stokes power which results in the output being distributed between two exiting beams (refer Fig. 5.1). Also, the Brewster plate may introduce additional losses in the cavity for regions in the diamond that suffer birefringence. Hence, replacing the Brewster plate with a mirror output coupler at the calculated optimum output coupling (1-2% T) would enable output that is more efficient and single-ended.

Furthermore, the end mirror was highly transmitting for the pump so that the diamond was only pumped with a single pass. Lower threshold and higher efficiency can therefore be obtained when using an end mirror highly reflecting for the pump beam. In this case, Eq. 5.5, 5.6 and 5.8 becomes:

$$P_{\mathrm{P}} = \frac{T + 2\alpha_{\mathrm{d}} L_{\mathrm{d}} + 2\alpha' L' + 2\kappa}{\eta T \left[1 - \exp\left(-\frac{4G}{T} P_{\mathrm{S}}^{OC}\right)\right]} P_{\mathrm{S}}^{OC}, \tag{5.9}$$

$$P_{\mathrm{Res}} = P_{\mathrm{P}} \exp\left(-\frac{4G}{T} P_{\mathrm{S}}^{OC}\right) = P_{\mathrm{P}} - \frac{T + 2\alpha_{\mathrm{d}} L_{\mathrm{d}} + 2\alpha' L' + 2\kappa}{\eta T} P_{\mathrm{S}}^{OC}, \tag{5.10}$$

and

$$P_{\mathrm{P}}^{th} = \frac{T + 2\alpha_{\mathrm{d}} L_{\mathrm{d}} + 2\alpha' L' + 2\kappa}{4 g_{\mathrm{S}} \arctan(\zeta)} \Lambda. \tag{5.11}$$

From Eqs. 5.10 and 5.11, the threshold halves compared to single pass pumping while the slope efficiency in the limit of higher pump power remains the same.

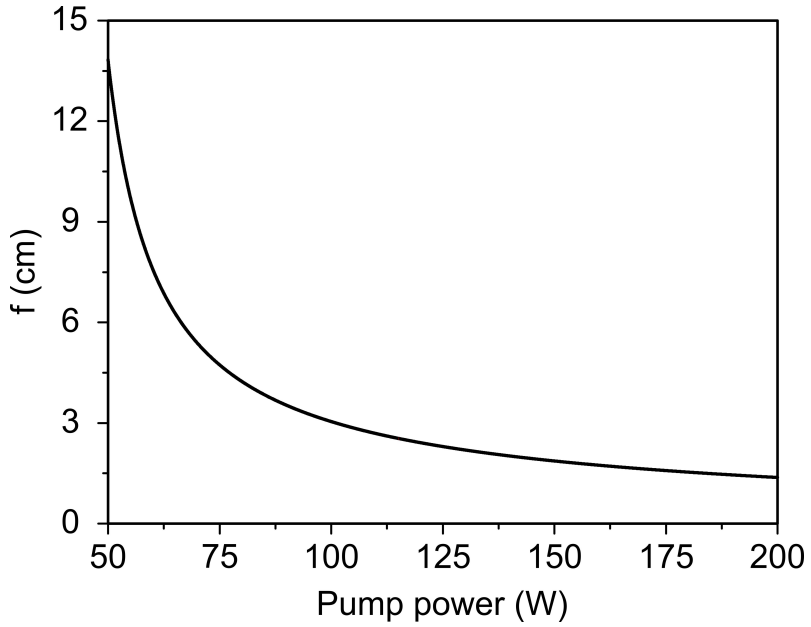

Figure 5.16: Predicted thermal lens focal length as a function of incident pump power.

The model presented in Sec.5.3 is only valid when the thermal lensing is weak and does not significantly change the pump and Stokes beam radii [86]. The thermal lens strength may be calculated by applying again here Eq. 4.19, which assumes that the thermo-optic contribution dominates over the photo-elastic and end-face curvature effects. Again, it should be noted that the calculations substantially over-estimates the lens strength [92] (see also Sec.4.7) and hence provides an upper bound of the real value.

The thermal lens is the result of the decay of Raman-generated optical phonons and impurity/defect absorption. The heat load deposited due to phonon-decay ($P_{\mathrm{ph}} = \left(\frac{\lambda_{\mathrm{S}}}{\lambda_{\mathrm{P}}} - 1\right) P_{\mathrm{S}}^{OC}$) for 15 W of Stokes output equates to 1.16 W. In addition, the heat load contribution due to

impurity absorption ($P_{\text{abs}} = P_{\text{S}}^{int} \times \alpha_{\text{d}} \times L_{\text{d}}$) is determined to be approximately 12 W based on the inferred intracavity Stokes power of 2.5 kW and the expected absorption coefficient of 0.6%/cm. Here, the absorption coefficient value is taken from Fig. 1.6 in Sec.1.3. (Note that the model-determined value for α_{d} of 0.9%/cm is not appropriate here, due to reasons discussed in Chapter 4). The thermal lens focal length f calculated as a function of incident pump power is shown in Fig. 5.16. At the current pump power (66 W), f is approximately 6 cm. The DRL cavity can accommodate a thermal lens of up to 2.6 cm by adjusting the cavity length, beyond which the Stokes mode radius increases by a factor of 1.5 above the no-lens case (determined using PSST). Thus a significant thermally-induced change in the pump and Stokes radii is not expected at the current levels and indeed up to pump powers up to 100 W. An f of 2.6 cm corresponds to a pump power of 114 W, which could potentially generate 40 W of Stokes output. In view of the fact that the thermal lens calculations only provide an upper bound, this analysis suggests output powers greater than 40 W are possible without thermally-induced saturation.

5.7 Extending the wavelength to deep-UV – intracavity frequency doubling

The high intracavity power (approximately 2.7 kW at 15 W Stokes power level) at 573 nm is sufficient to achieve further intracavity frequency conversion and highlights the potential to generate high power UV at 286.5 nm. Compared to the analogous near-IR pumped system generating visible output, the design becomes more complex due to the more limited options for the second harmonic crystal in the deep-UV. Following the discussions in Chapter 4, high nonlinear coefficient, wider acceptance angle, wider acceptance band-width, larger angular tolerance and smaller walk-off angle are the key parameters to consider for the appropriate choice of the nonlinear crystal. The divergence of the Stokes beam in the investigated linear cavity is less than 5 mrad and therefore, the nonlinear crystal should have an acceptance angle greater than this value, which further constrains the choice of the second harmonic crystal.

From Tab. 5.2, only type II phase-matched BBO crystal has a sufficiently wide acceptance angle but suffers from a smaller nonlinear coefficient, smaller angular tolerance, and larger walk-off angle compared to other crystals. In addition, the polarization behaviour of the CW DRL complicates the use of type II phase matching. For type II phase matching, the

polarization of the fundamental beam (in this case Stokes polarization) must be 45° with respect to the BBO optic axis. However, the polarization behaviour of CW DRL does not naturally satisfy this condition as it was found that the Stokes polarization orients itself parallel to the linear axis of the dominant birefringence element. One method around this problem may be found by inserting a 45° linear polarizer in the cavity. An additional complication arises due to the waveplate-like action of the BBO crystal, where the e- and o-rays experience a phase offset due to natural birefringence of the BBO. In this case, the polarization of the fundamental beam in general becomes elliptical as it propagates through the BBO and thus perturbs the polarization behaviour away from the ideal for both Raman conversion and harmonic generation. This may be avoided by introducing an intracavity quarter-wave plate at an appropriate orientation in order to restore the fundamental beam polarization [197]. It is to be noted that efficient CW UV generation relies on obtaining low-loss components (coatings and crystals) which become especially challenging in the deep-UV. On the flipside, higher losses can be tolerated when using visible pumping, due to higher Raman gain coefficient.

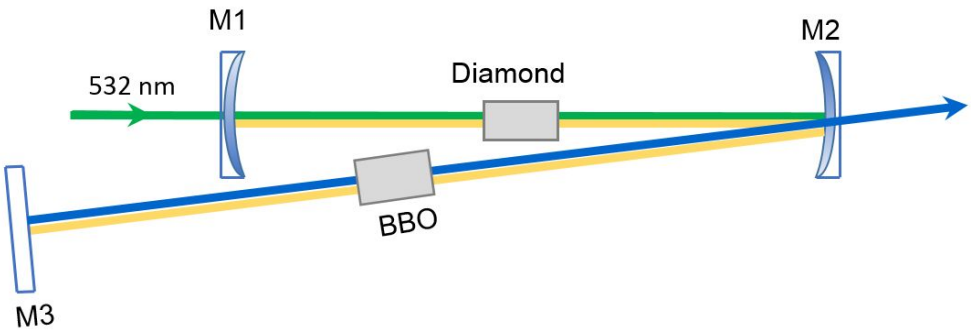

Figure 5.17: Folded Raman laser cavity with intracavity frequency doubling.

An alternative approach is to make use of a different cavity arrangement such as a folded cavity so as to enable collimated Stokes beam for the doubling crystal. Such a design would permit the use of crystals with narrower acceptance angle and type I phase matching. Fig. 5.17 shows one suggested basic arrangement using a single additional mirror to collimate the Stokes beam. Here, mirror M2 is highly reflecting for both the pump and Stokes and highly transmitting for UV and mirror M3 is highly reflecting for both Stokes and UV. Note that the folded cavity offers an additional advantage of avoiding passage of the UV through diamond, thereby reducing losses and the UV photo-chemical etching of the diamond surface

Table 5.2: Comparison of various nonlinear crystals. Data were taken from SNLO software.

Crystal	Phase-matching configuration	d_{eff}(pm/V)	walk-off (mrad) $(\omega(e), \omega(o), 2\omega)$	Angle tolerance (mrad cm)	Acceptance angle (mrad cm) (e, o)	Acceptance band-width $(cm^{-1}cm)$ (e, o)
LBO	Type I	0.283	0, 0, 11.40	1.55	3.11, 3.11	11.64, 11.64
BBO	Type I	1.84	0 0, 0, 83.92	0.20	0.41, 0.41	7.14, 7.14
	Type II	0.306	50.6, 0, 57.22	0.54	5.53, 0.60	5.68, 15.52
BIBO	Type I	1.32	0, 0, 31.37	0.47	0.93, 0.93	1.99, 1.99
KDP	Type I	0.422	0, 0, 23.79	0.80	1.60, 1.60	14.05, 14.05
NLBO	Type I	0.181	0, 0, 7.71	1.97	3.95, 3.95	4.84, 4.84
CLBO	Type I	0.71	0, 0, 36.78	0.52	1.04, 1.04	12.43, 12.43

that was observed in Ref. [198]. Suitable candidates for this type I phase-matching approach include BBO, CLBO and BIBO which offer moderately high d_{eff} compared to crystals listed in Tab. 5.2.

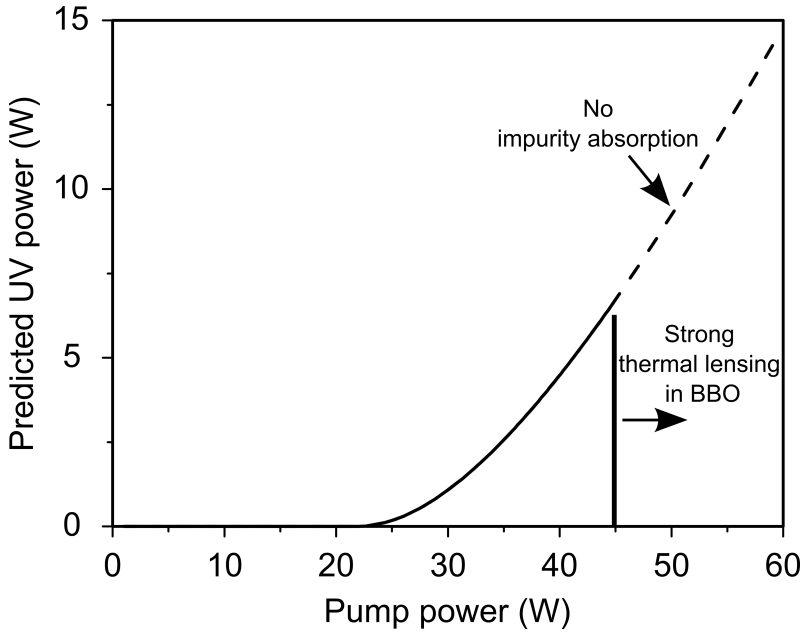

Figure 5.18: Predicted UV power as a function of pump power. The parameters used are T <0.05%, α_{d} = 0.9%/cm (same as used in Sec.5.4), $\alpha_{\chi 2}$ (absorption and scattering coefficient for BBO) = 1%/cm (from manufacturers data sheet), κ (reflection coefficient of diamond and BBO) = 0.6%/cm (from the manufacturers data sheet), ω_{P} = 17 μm, ω_{S} = 35 μm, M_{P}^2 = 2.0 and M_{S}^2 = 1.0 (same as used in Sec.5.4)

The model described in Sec.4.4 (Eq. 4.14) can be used to predict the UV power achievable, for example, in type I BBO, which has a relatively high d_{eff} compared to other commonly used crystals (see Tab. 5.2). With the same gain, loss, and focusing parameters used in Sec.5.4, the model predicts UV output power of up to approximately 6.5 W at 45 W pump power as shown in Fig. 5.18. Thermal lensing arising from impurity absorption in BBO is expected to be the major factor limiting the output power owing to its comparatively low thermal conductivity (K_{C} = 1.2 W/mK) compared to diamond (K_{C} = 2200 W/mK). The associated thermal lens focal length in BBO is calculated using Eq. 4.23 given in Sec.4.7, from the given parameters: $dn/dT = -9.3 \times 10^{-6}$ /°C, $\alpha_{\chi 2}$ = 1%/cm (taken from manufacturer's data sheet [199]), $L_{\chi 2}$ = 5 mm, and beam waist of the Stokes in the BBO = 125 μm. As the dn/dT is negative, the focal length of the lens is also negative. The current cavity can accommodate a lens with focal length -3 mm by adjusting the cavity length beyond which the cavity becomes unstable

(determined using PSST software for laser design), indicating that the thermal lens above 6.5 W will be too strong to maintain cavity stability in the current design.

Experiments to date have focussed on using a BBO crystal cut for type II phase-matching (theta=66.8°). It was verified that it is indeed crucial to introduce the above-mentioned polarizer and waveplate to enable efficient generation. Unfortunately, it was not possible within the timeframe of this thesis to source these components with sufficiently low loss to enable deep-UV generation. Future experiments may also benefit from using higher peak power pump pulses (eg. Q-switched) to more readily achieve the thresholds needed to investigate UV generation.

While the concept is promising for deep-UV generation based on visible pumps, it is also noted that a similar approach may also allow extension to even shorter wavelengths. By utilizing other convenient pump sources such as mature 355 nm CW lasers based on frequency tripled Nd:YAG, outputs at the 373 nm first Stokes and 186 nm frequency doubled output may be realized. Such a system would take advantage of the very high Raman gain at this shorter pump wavelength. However, there are various challenges involved in this vacuum-UV (VUV) spectral region such as the scarcity of suitable doubling crystals and requirement of low-loss optics and coatings. The potential options include $RbBe_2BO_3F_2$ (RBBF) and $KBe_2BO_3F_2$ (KBBF) [200, 201] with relatively low d_{eff} (in the range 0.2-0.3 pm/V) and narrower acceptance angle (0.4-0.5 mrad). Hence, such schemes would require the use of folded or ring cavity designs with optimized focusing conditions.

5.8 Chapter summary

An external cavity CW DRL for frequency conversion from green to yellow has been demonstrated. A maximum Stokes power of 15 W for CW periods of 0.8 ms at 573 nm with 53.7% slope efficiency and 22.7% conversion efficiency was obtained. The Stokes power dependence on output coupling was studied by utilizing a Brewster plate from which it was found that the optimum output coupling was approximately 1.2%.

A model was presented to provide insights into design optimization and predict performance over a greater range of parameters. When compared to the CW DRL performance in the near-IR, the visible operation is qualitatively similar, with the major exception that the optimum output coupling is higher (1-2% compared to 0.3-0.8% for the near-IR) as a

result of the higher Raman gain and loss coefficients in the visible. A combination of lower crystal losses, shorter crystal (6-8 mm), lower output coupling (1-2%) and tighter pump beam focussing (13 - 19 μm) are the key parameters for optimising the laser performance. Further power scaling to up to 40 W Stokes is predicted by the thermal lens calculations based on our current understanding of heat deposition in diamond, however, much higher power levels are expected, as previous evidences suggest that the lens strength is much weaker than the calculated value.

The chapter concluded with a study of the potential for CW deep-UV generation using intracavity frequency doubling. The nonlinear crystal choice and possible cavity designs were considered. A design based on Type II phase-matched BBO is attractive since its acceptance angle is better matched to the current cavity design. In order to satisfy polarization constraints, it was found to be necessary to insert an intracavity 45° linear polarizer and a quarter-wave plate. An alternative approach based on type I phase matching would require the use of folded cavity design. This has the advantage of permitting the use of nonlinear crystals with smaller acceptance angle and higher effective nonlinear coefficient such as type I BBO, BIBO and CLBO. For BBO, an output power of up to 6.5 W is predicted at the 45 W pump power, limited by the thermal lensing in the BBO.

The results in this chapter show the prospects of wavelength coverage of DRLs and opens up the potential for high brightness CW lasers in the challenging spectral region at wavelengths less than 300 nm.

6

Conclusion and future perspectives

This thesis builds on the recent developments in diamond Raman lasers – a highly promising technology for high power and high brightness wavelength conversion in the CW regime. To date, most work has been concentrated on the near-infrared. The work in this thesis has extended development to the visible and UV by combining the basic design with intracavity frequency doubling and using shorter wavelength pumps. A particular over-arching focus has been in understanding design issues for operation in the deep-UV to address the scarcity of high brightness CW technologies in this spectral region.

6.1 Summary of major findings

Since nonlinear frequency conversion is a polarization dependent process, understanding the detailed polarization behaviour of CW DRLs was the first step to understanding the factors that influence design. In anticipation of the importance of crystal birefringence on laser behaviour, the investigation in Chapter 2 has characterized in detail, birefringence and stress effects in

laser grade CVD single crystal diamond. Stress was found to induce substantial linear and circular birefringence when measured along the usual propagation direction ([110] direction). Surprisingly, the measured circular birefringence values, at least in one sample, were of the same order of linear birefringence. As well as this being an important consideration for Raman laser operation (Chapter 3), this knowledge may impact other areas in diamond optics such as on-chip diamond photonics and intra-cavity heatspreaders. In addition, the presence of circular birefringence is important to consider when characterizing birefringence using techniques that are unable to separate linear and circular components(such as Metripol).

The causes of birefringence were further investigated by measuring stress effects in the perpendicular direction and in the crystal growth direction ([001] direction). A complex pattern with spatially varying magnitudes and directions of linear birefringence were observed whose integrated effect results in circular birefringence along the [110] direction. Measurements of the stress-induced Raman frequency shift showed that, uniaxial and biaxial stresses present in the (001) plane, shift the Raman line by up to 0.7 cm^{-1} (corresponding to stress values up to 0.86 GPa). These results provided insights into the origin of depolarization along the laser axis and showed that piezo-Raman effects have negligible effect on the Raman gain.

In Chapter 3, the effect of these crystal anisotropies on the performance of CW diamond Raman lasers were investigated. By characterizing the Stokes polarization and laser threshold dependence on pump polarization, it was found that the output polarization is determined primarily by the local linear birefringence axis as measured along the beam axis. That is, the output polarization is parallel to the linear birefringence axis. This is in contrast to that observed previously in nanosecond pulsed (or low-Q cavity) DRLs where the Stokes polarization follows the maximum gain when pump polarization is rotated. This result enabled a greatly improved understanding of why some crystals, or some regions of a given crystal, exhibited large variations in threshold and polarization behaviour. Also, the results show that the threshold is lowest for regions in the diamond where the local linear birefringence axis is close to $\langle 111 \rangle$ and is pumped with a polarization close to $\langle 111 \rangle$. Although the experiments were conducted here for an external cavity Raman laser, the results are likely to be pertinent to other high-Q DRLs such as intracavity Raman lasers and synchronously pumped ultrafast lasers. The outcomes of this chapter form a firm foundation for understanding design and operation characteristics of intracavity frequency doubled external cavity DRLs.

Chapter 4 presented the first demonstration of a CW intracavity frequency doubled laser based on an external cavity crystalline Raman laser. A type I phase matched LBO crystal was used to generate 30 W of second harmonic at 620 nm with 15% conversion efficiency over periods of 0.2 ms. The output beam quality was excellent (M^2=1.1) as expected due to the high quality Stokes mode typically generated from diamond. The polarization behaviour was consistent with the results deduced from Chapter 3. The positioning of LBO crystal was crucial in the current design as the beam waist size, which dictates the nonlinear coupling, is a steep function of diamond and LBO separation. An analytical rate-equation model was found to adequately describe the observed laser behaviour and provided a useful tool for optimization. The model showed that the length and positioning of the LBO crystal in the cavity was near optimal at current pumping level. However, higher efficiencies are predicted by reducing the Stokes output coupling, increasing the length of the diamond crystal, tighter pump focussing as well as by using lower loss diamond and LBO. With such approximations, approximately 90 W of SHG power with 45% conversion efficiency is predicted using the current pump power level (200 W). Although thermal gradients in the diamond rapidly reach steady-state within the on-time pulse duration, this is not the case in the LBO. By calculating the thermal lens strength induced in the LBO crystal, laser performance in the steady-state CW regime was predicted. Due to the relatively low thermal conductivity of LBO, the lens strength was calculated to be an order of magnitude stronger than in diamond — given typical impurity absorption coefficients for LBO. The present cavity design is calculated to enable up to 95 W in the CW regime, above which the thermal lens in the LBO is expected to severely impact efficiency and beam quality.

The wavelength extension to shorter wavelengths was further investigated in Chapter 5 by using a pump laser at 532 nm. First Stokes output at 573 nm was demonstrated at 15 W for CW periods of 0.8 ms and with 53.7% slope and 22.7% overall conversion efficiency. Performance was analysed using a model similar to that developed in Chapter 4. Compared to performance in the near-IR, behaviour is qualitatively similar except for variations in threshold and efficiency that are consistent with the higher coefficients for Raman gain (approximately double) and loss (by approximately 3 times) for diamond in the visible. The higher losses increase the optimum output coupling to approximately 1.2%. As with operation in the near-infrared, higher efficiencies are predicted by using a combination of reducing loss, shorter diamond (6-8 mm) and tighter pump focussing (13-17 μm). Thermal lens calculations suggest

that much higher Stokes powers (>40 W) are achievable before temperature gradients induced in the crystal are likely to impact upon the performance.

The results obtained in Chapter 5 were used to predict the design considerations for deep-UV generation by utilizing intracavity frequency doubling. Design is more complex compared to that for the near-infrared pump, as there are greatly reduced options for the second harmonic crystal in the deep-UV. The choice of harmonic crystal is further constrained in the investigated linear cavity design due to the large acceptance angle required. Type II phase-matched BBO was considered owing to its larger acceptance angle, however, the polarisation mode properties of the CW DRL makes implementation non-trivial. Nevertheless, one approach based on adding additional polarization elements has been proposed that enables the polarization requirements of the Raman and $\chi^{(2)}$ process to be fulfilled. A potential alternative is to use type I phase-matched BBO, CLBO, or BIBO crystal in combination with a cavity design (such as a folded cavity) designed to provide a more collimated Stokes beam through the doubling crystal.

6.2 Implications and future outlook

There are number of outcomes from this thesis that may trigger novel research directions and warrant further investigation.

6.2.1 Birefringence and polarization behaviour of Raman lasers

The birefringence and polarization studies of Chapters 2 and 3 provide a firm basis for optimizing the threshold and efficiency of high-Q DRLs and intracavity doubled DRLs. DRLs with high-Q cavities correspond to designs that are aimed to achieve a low threshold and hence operate efficiently at low power. Birefringence effects need to be considered, and a custom birefringence analysis of the diamond sample is found to assist in reducing threshold, increasing efficiency and understanding polarization behaviour. The impact of birefringence diminishes for lower-Q DRLs, however, which is attributed to the reduced number of round trips of the Stokes field. This indicates that higher power DRLs, for which lower-Q cavities are optimally used, may readily avoid birefringence problems. In this case, the threshold and polarization behaviour return to values predicted by the Raman tensor calculations. A more direct approach to avoiding birefringence is through higher quality diamond synthesis. Lower

birefringence material is likely to be available in the future, either by CVD or HPHT growth. Since birefringence analysis of each diamond sample may be time-consuming, higher quality material will be an advantage. A further method for diminishing the effect of birefringence may be through tailoring the birefringence direction by applying stress to the diamond. This idea is speculative at this stage but may warrant investigation.

Further investigation is required to understand the disparity between the low-Q and high-Q DRLs. It would be interesting to study the cavity-Q dependence of the competition between the polarization-dependent Raman gain and birefringence and its role in determining the output Stokes threshold and polarization. A theoretical investigation could be developed based on solving for the polarization eigenmodes of the resonator (using for example a Jones matrix formalism). The contribution of magnitudes of linear and circular birefringence in determining polarization behaviour thus would be elucidated. The increased understanding would enable development of a comprehensive theory for predicting polarization behaviour across a wide range of laser designs and crystal birefringences.

This would not only provide an enhanced understanding of the polarization characteristics for diamond but also for other isotropic Raman media such as silicon and barium nitrate. Furthermore, the model may be readily extended to other cavity designs such as ring cavity and folded cavity designs.

6.2.2 Further wavelength extension and power scaling

The intracavity-doubled DRL presented in this thesis is a versatile technology for high brightness laser sources in the visible and UV and opens up prospects for further power scaling and wavelength coverage.

The current design enables power scaling to greater than 100 W power level by a careful choice of the design parameters derived from the analytical model (presented in Chapter 4 and 5). Since the impurity content in the nonlinear crystal was found to be a crucial parameter, utilizing a lower loss crystal would benefit threshold, power, and efficiency. Improved thermal management of the harmonic crystal also provides a path to further increase power. This could be achieved, for instance, by sandwiching the nonlinear crystal between two thin sapphire plates, thus enhancing the heat dissipation [202]. Such high power lasers in the visible may be of significant interest for use in applications such as laser guide stars and long range remote sensing.

As well as deep-UV generation by intracavity doubling of the yellow laser, other wavelengths may be targeted across the UV. For example, for a 355 nm pump source may enable a method for generating CW VUV at wavelengths less than 200 nm. The major challenge in this spectral range is the scarcity of appropriate nonlinear crystals – potential options include $RbBe_2BO_3F_2$ (RBBF) and $KBe_2BO_3F_2$ (KBBF) [200, 201]. Due to narrower acceptance angle in these crystals, alternative cavity designs such as folded cavity, z-cavity, and ring laser cavity are required to be considered for efficient frequency conversion. The requirement of low-loss crystals and optics are yet another challenge in this wavelength region. Deep UV wavelengths, which are especially challenging to generate in CW mode, are of interest for applications such as material processing, semiconductor photolithography and super-high-resolution photoemission spectrometers.

Another natural extension of intracavity harmonic in DRLs is to utilize higher-order Stokes generation to further diversify wavelength choice through either second harmonic or sum frequency generation. The design parameters, in this case, would be different from first Stokes due to the presence of additional interacting fields, however, the over-arching dynamics are likely to be governed by similar principles. For the example of a 1064nm pump, and when considering combination of the first and second Stokes fields, this would enable wavelengths at 620 nm, 573 nm, 676 nm and 743 nm.

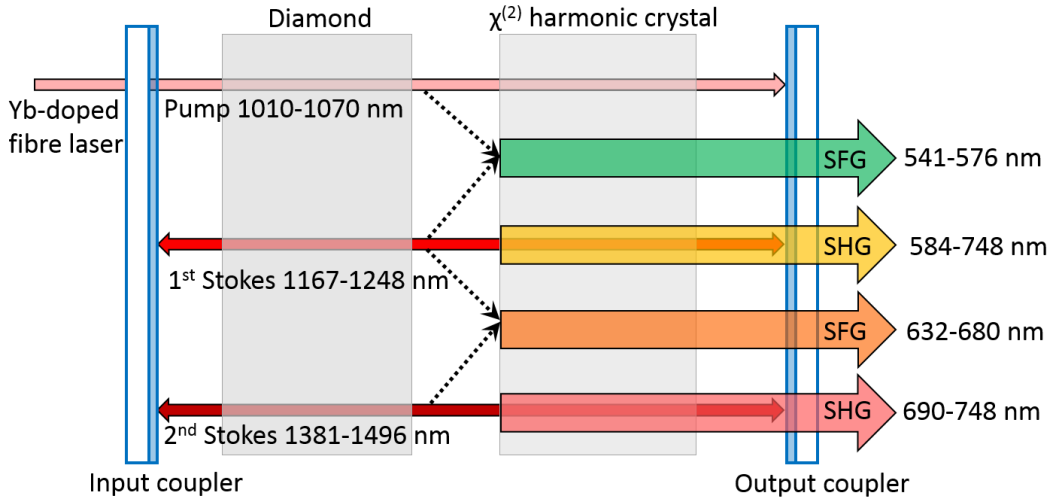

Figure 6.1: Schematic representation of the spectral coverage of external cavity diamond Raman laser with intracavity frequency mixing for the example case of tunable Yb fibre laser of nominal tuning range 1010-1070 nm.

Advances in high power and tunable Yb-fibre lasers provide an opportunity for developing continuously tunable output [188]. A DRL pumped with tunable Yb-doped fiber laser from 1010-1070 nm, for example, would provide first and second Stokes wavelengths up to 1496 nm and subsequent frequency doubling generates wavelengths in the range 584-624 nm and 690-748 nm. Fig. 6.1 shows the wavelength range achievable by utilizing higher order Stokes and frequency mixing. Temperature-tuned non-critical phase matched LBO crystal provides a suitable candidate for tunable operation in this wavelength range. Applications specific to atom cooling, photodynamic therapy, and atomic clocks would benefit from this wide range of wavelengths.

Clearly, intracavity mixing in DRLs in combination with higher order Stokes and tunable pump sources provides a novel and highly versatile approach to high brightness CW wavelength sources across the visible and UV.

6.2.3 Output linewidth

A further interesting direction for future work pertains to the linewidth of the frequency mixed output. In principle, single longitudinal mode operation in the current laser design may be readily achieved due to the absence of energy storage in the gain medium and thus the avoidance of the usual spatial hole burning mechanism that destabilizes longitudinal modes in standing wave inversion lasers. As shown recently [203], multi-watt Stokes output has been obtained without the use of any active frequency selective elements if the thermal expansion of the Raman medium (which leads to shifts in the effective cavity length and hence resonance frequency) is carefully managed. Hence, narrow-linewidth pump sources together with active cavity length stabilization are expected to also result in single mode frequency doubled output.

Lasers with high spectral purity are used in a range of applications such as in remote sensing of molecules, atom cooling, and spectroscopy. For example, the lasers in the visible to near-infrared with single longitudinal mode operation would be of particular interest in atom cooling experiments and spectroscopy. For example, 698 nm represents the wavelength of the $^1S_0 \rightarrow {}^3P_0$ clock transition in strontium atomic clocks [204].

6.3 Closing remarks

In short, the thesis provides a detailed birefringence characterization of laser grade single crystal CVD diamond with the underlying motivation to understand its role in high-Q diamond Raman lasers. The results enabled a detailed understanding of laser threshold, efficiency and polarization behaviour. As well as enabling diamond crystal selection and pump polarization optimization, the results aided design of external cavity devices employing intracavity harmonic generation. Devices in the red (620 nm) and yellow (573 nm) were demonstrated at power levels 30 W and 15 W in a temporal regime (quasi-CW) in which temperature gradients in the diamond were in steady-state. It is concluded that diamond Raman lasers are highly promising for the efficient generation of high brightness output at wavelengths in the visible and UV.

7

List of Publications

7.1 Peer-reviewed journal articles

- H. Jasbeer, R. J. Williams, O. Kitzler, A. McKay, S. Sarang, J. Lin and R. P. Mildren *Birefringence and piezo-Raman analysis of single-crystal CVD diamond and effects on Raman laser performance*. J. Opt. Soc. Am. B **33**, B56-B64 (2016).

- S. Sarang, R. J. Williams, O. Lux, O. Kitzler, A. McKay, H. Jasbeer, and R. P. Mildren *The high-gain 87* cm^{-1} *Raman line of KYW and its impact on continuous-wave Raman laser operation*, Opt.Express **24**, 21463–21473 (2016).

- O. Kitzler, H. Jasbeer, D. J. Spence and R. P. Mildren *Eigensolution of optical resonators containing polarization dependent diamond Raman gain and birefringence*, in preparation.

7.2 Conference presentations

- H. Jasbeer, R. J. Williams, A. McKay, O. Kitzler, S. Sarang and R. P. Mildren, *Circular and Linear birefringence in laser grade single crystal CVD diamond*, Paper No: 9744-11, Optical Components and Materials XIII, Photonics West 2016 (13-18 February 2016), San Francisco, USA. *Oral presentation*

- H. Jasbeer, R. J. Williams, A. McKay and R. P. Mildren, *Frequency extension of a high power diamond Raman laser by intracavity second harmonic generation*, Paper No: 9726-62, Solid State Lasers XXV: Technology and Devices, Photonics West 2016 (13-18 February 2016), San Francisco, USA. *Oral presentation*

- H. Jasbeer, R. J. Williams, O. Kitzler, A. McKay, J. Lin and R. P. Mildren, *Effect of birefringence on the performance of CW external cavity diamond Raman lasers*, ANZCOP 2015 (29 Nov-3 Dec 2015), University of Adelaide, Australia. *Poster presentation*

- H. Jasbeer, R. J. Williams, O. Kitzler, A. McKay, J. Lin and R. P. Mildren, *Stress induced optical rotation in CVD grown diamond*, CLEO-PR 2015 (24-28 Aug 2015), Busan, Korea. *Poster presentation*

- H. Jasbeer, R. J. Williams, O. Kitzler, A. McKay, J. Lin and R. P. Mildren, *Characterization of defect induced stress birefringence in CVD grown diamond*, AIP 2014 (7-11 Dec 2014), Australian National University, Canberra, Australia. *Poster presentation*

- Hadiya. V. M, R. J. Williams, O. Kitzler, J. Lin and R. P. Mildren, *Characterization of defect-induced stress birefringence in diamond using the Metripol technique*, KOALA 2013, University of Sydney. *Poster presentation*

- S. Sarang, R. J. Williams, O. Lux, O. Kitzler, A. McKay, H. Jasbeer and R. P. Mildren, *Impact of cascading on the efficiency of external cavity CW Raman laser*, CLEO-PR 2015 (24-28 Aug 2015), Busan, Korea. *Poster presentation*

- S. Sarang, R. J.Williams, O. Kitzler, A. Mckay, H. Jasbeer and R. P. Mildren, *Impact of cascading on efficiency of CW external cavity Raman lasers*, AIP 2014 (7-11 Dec 2014), Australian National University, Canberra, Australia. *Poster presentation*

- A. McKay, R. J. Williams, O. Kitzler, H. Jasbeer, S. Sarang and R. P. Mildren, *High Power Raman Beam Conversion in Synthetic Diamond*, Paper No. ATu4A.2, Advanced Solid State Lasers (ASSL) 2014 (16-21 Nov 2014), Shanghai, China. *Oral presentation*

- O. Kitzler, A. McKay, R. J. Williams, V. M. Hadiya and R. P. Mildren, *Fiber laser pumped continuous-wave external cavity diamond Raman laser*, ANZCOP, Fremantle, Western Australia (2013). *Oral presentation*

- O. Kitzler, A. McKay, V. M. Hadiya and R. P. Mildren, *Characterisation and optimization of external cavity continuous-wave diamond Raman laser*, Paper No. LTh2H.1, Frontiers in Optics, Orlando, Florida, United States (2013). *Oral presentation*

A

Voigt abbreviated notation

For a linear strain, stress (σ_{kl}) and strain (ϵ_{ij}) tensors are related by Hooke's law as [161]

$$\epsilon_{ij} = s_{ijkl}\sigma_{kl} \qquad i,j,k,l = 1,2,3 \tag{A.1}$$

where s_{ijkl} is the 4th rank elastic compliance tensor. In the abbreviated notation, Eq. A.1 is written as

$$\epsilon_{\lambda} = s_{\lambda\mu}\sigma_{\mu}, \tag{A.2}$$

where

$$\begin{aligned} \epsilon_{\lambda} &= \epsilon_{ij} && ij \leftrightarrow \lambda = 1,2,...6, \\ \sigma_{\mu} &= \sigma_{kl} && kl \leftrightarrow \mu = 1,2,...6, \\ s_{\lambda\mu} &= \begin{cases} s_{ijkl} & ij \leftrightarrow \lambda = 1,2,...6, kl \leftrightarrow \mu = 1,2,3 \\ 2s_{ijkl} & ij \leftrightarrow \lambda = 1,2,...6, kl \leftrightarrow \mu = 4,5,6 \end{cases} \end{aligned} \tag{A.3}$$

The relationship between the indices is written using the following convention

$$\begin{array}{cccccc} 11 & 22 & 33 & 23, 32 & 31, 13 & 12, 21 \\ 1 & 2 & 3 & 4 & 5 & 6 \end{array} \tag{A.4}$$

B

Related publications

B56 Vol. 33, No. 3 / March 2016 / Journal of the Optical Society of America B Research Article

Journal of the Optical Society of America B

OPTICAL PHYSICS

Birefringence and piezo-Raman analysis of single crystal CVD diamond and effects on Raman laser performance

Hadiya Jasbeer,* Robert J. Williams, Ondrej Kitzler, Aaron McKay, Soumya Sarang, Jipeng Lin, and Richard P. Mildren

MQ Photonics Research Centre, Department of Physics and Astronomy, Macquarie University, Sydney, NSW 2109, Australia
**Corresponding author: hadiya.valiyaveettil-mohamm@students.mq.edu.au*

Received 1 October 2015; revised 21 December 2015; accepted 23 December 2015; posted 24 December 2015 (Doc. ID 251269); published 12 February 2016

Defect-induced stress has been mapped in optical-grade synthetic diamond (chemical vapor deposition grown, low nitrogen, low birefringence) using Metripol polarimetry, Mueller polarimetry, and Raman microscopy. Large circular retardance was observed in the 8 mm long ⟨110⟩ cut crystal with values up to 28° for some paths along the major axis. Metripol-determined values for linear birefringence magnitude and fast-axis direction in such regions have significant error. Stress-induced shifts in Raman frequency were observed up to 0.7 cm^{-1}, which we deduce result from uniaxial and biaxial stresses up to 0.86 GPa. We also elucidate the effect of stress on diamond Raman laser performance. For high cavity Q Raman lasers, the direction of the linear birefringence axis is found to be a primary factor determining the laser threshold and the input–output polarization characteristics.

OCIS codes: (140.4480) Optical amplifiers; (260.1440) Birefringence; (190.5650) Raman effect; (180.5655) Raman microscopy; (310.4925) Other properties (stress, chemical, etc.); (310.5448) Polarization, other optical properties.

http://dx.doi.org/10.1364/JOSAB.33.000B56

1. INTRODUCTION

Diamond is an extreme material that has a suite of properties of interest for applications in optics such as in nanophotonics and optomechanics, intracavity heat spreaders, high-power laser windows, synchrotron and x-ray optics, quantum information processing, and Raman lasers [1–9]. High thermal conductivity, a wide bandgap, high Raman gain, and a wide transmission window are a few of its outstanding properties pertinent to optical and photonic applications. In recent years, advances in synthesis by chemical vapor deposition (CVD) has enabled production of material with reduced impurity content and lower residual stress [10–12] and has been an important driving factor for a range of new optical applications. Nevertheless, stress in diamond, an isotropic crystal, plays an important role in influencing the behavior of polarization-sensitive devices [2,13,14]. To date, characterization of defect-induced stresses built in CVD diamonds have been reported using the Metripol method [12], a simple and widely used technique for characterizing the magnitude and direction of linear retardance [15,16]. However, Metripol is unable to detect other polarization properties, such as circular birefringence and dichroism, and its accuracy can be compromised if these other polarization characteristics are also present [16]. Stress also causes splitting and/or a shift in the spontaneous Raman line in crystals via the piezo-Raman effect [17–26]. A complete characterization of CVD diamond has not been reported in the literature to date, despite the fact that these are important for optimizing the performance of polarization-dependent diamond devices.

In this paper, we have characterized stress effects in optical-grade synthetic diamond using Mueller polarimetry, which provides a complete characterization of the polarization properties of the sample [27,28], and Raman microscopy. Significant circular retardance was observed in some locations within the diamond, causing significant inaccuracies in the Metripol-measured values for linear retardance. Raman microscopy was used to determine the magnitude of stress and its spatial distribution in the crystal. As an example of the effects of stress in an optical device, the diamond was investigated as the active medium in a continuous-wave (cw) Raman laser. The behavior was characterized for several locations in the diamond sample and correlated with the local birefringence characteristics.

0740-3224/16/030B56-09$15/0$15.00 © 2016 Optical Society of America

Research Article Vol. 33, No. 3 / March 2016 / Journal of the Optical Society of America B B57

2. CVD DIAMOND CHARACTERIZATION

A. Experimental Methods

1. Diamond Sample

The dimensions and crystallographic orientation of the diamond sample are illustrated in Fig. 1. The sample was an 8 × 4 × 1 mm CVD diamond (Raman-grade or "ultra-low birefringence," Element Six Ltd) with nitrogen impurity of approximately 20 ppb and birefringence $<10^{-5}$ perpendicular to the growth direction (indicated also in Fig. 1). This crystal was selected out of a batch of three as it contained the largest variation of birefringence features as viewed through the long direction of the sample. This direction is featured in our characterization as it is also the direction of beam propagation in the Raman laser experiments in Section 3.

2. Metripol and Mueller Polarimetry

The Metripol method was performed using an in-house system to determine both the magnitude and direction of linear retardance of the optical sample, the details of which are described in Ref. [16]. It consisted of a collimated, narrow-band, incoherent beam (in this case from an incandescent lamp, a 589 nm notch filter, and a collimating lens) passing through a rotatable polarizer, the optical sample, followed by a quarter-wave plate and an analyzing polarizer. The analyzing polarizer was set to 45° of the fast axis of the quarter-wave plate and a 10 cm focal length lens was used to image the end face of the diamond onto a CCD camera (Spiricon SP620U).

The normalized intensity of the transmitted light after passing through the diamond and the polarization elements is given by [16]

$$\frac{I}{I_0} = \frac{1}{2}[1 + \sin 2(\alpha - \Phi) \sin \delta], \quad (1)$$

where α is the polarizer rotation angle, Φ is defined as the angle between the linear retardance axis of the sample and the horizontal, and δ is the magnitude of linear retardance. The transmitted intensity as a function of rotatable polarizer angle is a sine curve whose amplitude is $\sin \delta$ and phase is Φ.

The polarizer was rotated in steps of 10°, and the transmitted light was captured by the CCD camera. The intensity recorded at each pixel, corresponding to a specific location in the diamond, was fitted to a sine curve as a function of α from which the amplitude and phase values were extracted to provide the magnitude and direction of linear retardance. We calculate the measurement uncertainty in linear retardance to be ±2.5° ($\Delta n = \pm 5 \times 10^{-7}$), due to imperfect polarizers and wave plates.

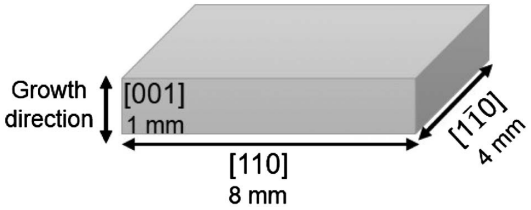

Fig. 1. Dimensions and crystallographic orientation of the diamond sample.

Mueller polarimetry, the principles of which are described in Ref. [27], was performed using a commercially available Mueller polarimeter (Exicor 150 XT from Hinds Instruments). The instrument launches a variety of known polarization states from a He–Ne laser (operating at 632.8 nm), polarizer, and computer-controlled polarization modulating photoelastic elements. The modulated light passes through the length of the sample whose polarization is further modulated by the birefringence in the sample. The instrument uses another pair of photoelastic modulators along with a polarizer, and photodetector to analyze the transmitted state of polarization from the sample under test corresponding to each launched state of polarization. Through the Mueller analysis of the recorded data (Ref. [27]), the system calculates all sixteen Mueller matrix elements of the sample under test. Metripol and Mueller polarimetry are based on intensity variations as a function of polarization and are therefore unaffected by scatter and absorption in diamond. Dichroism is found to be negligible in all cases.

3. Raman Microscopy

Raman spectra were recorded as a function of position in the sample using a confocal microscope equipped with a Raman spectrometer (Renishaw RM1000 Micro-Raman spectrometer). A 2400 lines/mm grating and 50 μm slit provided 5 cm^{-1} spectral resolution. The excitation source was a frequency-doubled Nd:YAG laser with 532 nm output. A 50 × objective lens with N.A. 0.75 provided a 1 μm probe beam spot size. A motorized stage was used to raster the sample in the X–Y plane in 25 μm step. To accurately determine the Raman shifts at each point in the crystal, each spectrum was fitted using a Gaussian function, thus enabling greatly enhanced resolution of the peak shift measurement to 0.17 cm^{-1}. Furthermore, averaging over many pixels in a particular region of interest increased the effective resolution of the peak position measurement to approximately 50–100 times greater than the Raman linewidth (depending on the chosen sample area for averaging), thus enabling very small shifts to be resolved.

B. Results and Discussion

1. Linear and Circular Birefringence

Figures 2(a) and 2(b) show maps of the magnitude and direction of linear retardance through the 1 × 4 mm end face obtained using Metripol and Mueller polarimetry. The qualitative features from the two methods are similar, showing a complex birefringence pattern across the sample. Both measurements reveal extended features in the growth direction in the central region of the crystal, and to the right of center, with linear retardance up to 55° (Δn up to 1.2×10^{-5}) as measured using Mueller polarimetry and up to 50° using Metripol. The values obtained using Mueller are systematically higher or lower than for Metripol, due to the contribution of circular retardance as discussed below. The direction of linear retardance likewise varies markedly across the sample from −90° to +90° showing some correlation with the linear retardance maps. Also, as with the magnitude of linear retardance, the orientations obtained using Mueller depart significantly from those obtained with Metripol in the central region of the crystal. Figure 2(c) shows the circular retardance map measured

B58 Vol. 33, No. 3 / March 2016 / Journal of the Optical Society of America B Research Article

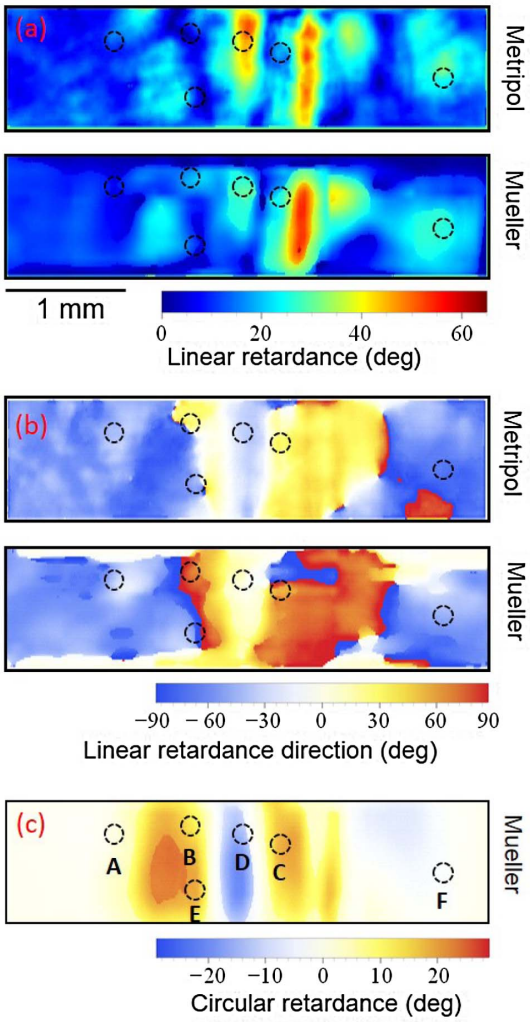

Fig. 2. Metripol and Mueller polarimetry-obtained values of (a) linear retardance magnitude and (b) direction. (c) Circular retardance obtained from Mueller polarimetry. Positive and negative values correspond to dextro and levo rotation, respectively. 0° represents the [1$\bar{1}$0] (horizontal in figure) direction. The black circles A, B, C, D, E, and F mark the six regions that were characterized under Raman laser operation. The circle (0.3 mm diameter) indicates the uncertainty in location of the laser spot.

using Mueller polarimetry. Significant circular retardance of up to 28° was measured at different locations in the sample. Some circular retardance is expected as the equivalent optical element for the path through a medium with varying magnitude and direction of linear retardance can be reduced to a single waveplate and rotator [29,30]. It is interesting, however, that the magnitude of circular retardance is up to approximately half of the maximum linear retardance observed in the crystal. Of the other polarization characteristics measured using Mueller polarimetry (e.g., linear and circular dichroism), none were detected in significant quantities in this sample.

2. Effect of Circular Retardance on Metripol Measurements

In order to quantify the effect of circular retardance on the accuracy of the Metripol-determined linear retardance, we introduce circular retardance χ into the Jones matrix of the sample under test, which for $\chi < \delta/2$ can be expressed as [16]

$$M = \begin{bmatrix} e^{\frac{i\delta}{2}} & -2\chi\frac{\sin\frac{\delta}{2}}{\delta} \\ 2\chi\frac{\sin\frac{\delta}{2}}{\delta} & e^{\frac{-i\delta}{2}} \end{bmatrix}. \quad (2)$$

Thus, the Jones matrix that describes the transmitted intensity through the entire Metripol setup becomes

$$A'' = \frac{1}{2}\begin{bmatrix} 1 & 1 \\ 1 & 1 \end{bmatrix}\begin{bmatrix} e^{\frac{i\pi}{4}} & 0 \\ 0 & e^{\frac{-i\pi}{4}} \end{bmatrix}\begin{bmatrix} e^{\frac{i\delta}{2}} & -2\chi\frac{\sin\frac{\delta}{2}}{\delta} \\ 2\chi\frac{\sin\frac{\delta}{2}}{\delta} & e^{\frac{-i\delta}{2}} \end{bmatrix} \times \begin{bmatrix} \cos\theta & \sin\theta \\ -\sin\theta & \cos\theta \end{bmatrix}\begin{bmatrix} 1 \\ 0 \end{bmatrix}, \quad (3)$$

where

$$\theta = \alpha - \Phi. \quad (4)$$

In this case, when the normalized intensity of the exiting beam is plotted against the rotation angle of the polarizer, there is a change in amplitude and phase of the sine curve which in turn affects the Metripol-measured magnitude and direction of linear retardance. Figure 3 shows the shift in magnitude and direction of linear retardance with circular retardance. The magnitude and direction of linear retardance increases with positive circular retardance and decreases with negative circular retardance. For example, for a region in the diamond having maximum linear retardance magnitude of 55° oriented at 75° and circular retardance of 25°, the Metripol-determined values for the magnitude and orientation of the linear retardance are 53° and 60°, respectively. Accordingly, in the Metripol birefringence map of Fig. 2(a), areas that have significant circular birefringence have errors attributable to circular birefringence of up to 5° in magnitude and 27° in orientation. In the central region of the crystal (the region of the crystal marked as D), the Metripol-determined values of magnitude and direction of linear retardance is found to be higher than Mueller-determined values because of negative circular retardance in this area as is evident from Fig. 3.

3. Birefringence and Piezo-Raman Effects for the (001) Face

In order to elucidate the cause of birefringence observed through the [110] face, the stress pattern for the major face of the crystal was revealed using Metripol polarimetry and Raman microscopy, as shown in Fig. 4. The Metripol polarimetry technique was used here as we were primarily interested in the stress distribution through the [110] face rather than the details of each Mueller matrix component. The linear and circular birefringence of Fig. 2 is the result of the integrated effect of stressed regions distributed along the 8 mm length. The magnitude of linear retardance [Fig. 4(a)] shows a complex pattern with values up to 60°. This corresponds to Δn values up to 1.1×10^{-4} which, as expected for the line-of-sight along the growth direction, is an order of magnitude higher than in the perpendicular direction [10,12]. Again, the magnitude

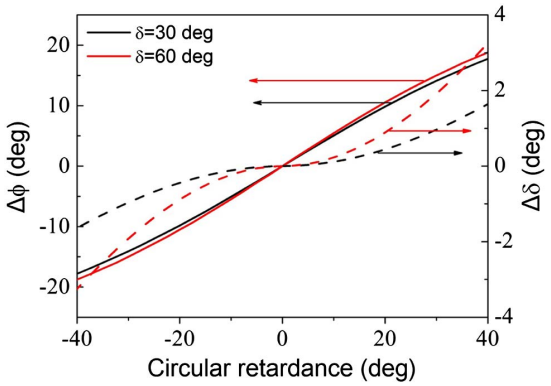

Fig. 3. Shift in Metripol-measured magnitude and direction of linear retardance as a function of circular retardance. Black and red solid lines indicate the shift in linear retardance direction with circular retardance for $\delta = 30°$ and $\delta = 60°$, respectively. Black and red dashed lines indicate the shift in linear retardance magnitude with circular retardance for $\delta = 30°$ and $\delta = 60°$, respectively.

and direction maps show some correlation. Stress features aligned along the [010] direction are observed on the left-hand side of the image. A notable feature with twofold symmetry is observed on the right-hand side slightly above center.

Stress may also cause splitting and/or a shift in the Raman line in crystals [17–26] depending upon the magnitude of the stress tensor components. Figure 4(c) shows the Raman frequency shift for backscattering along the [001] direction. No broadening of the peak is observed within the measurement uncertainty, indicating that the sampling volume is smaller than the granularity of the stress pattern. The shift in Raman peak is calculated with respect to the minimum stress value obtained at the bottom left-hand side of the birefringence map. A similar map is obtained for the laser focused 0.5 mm below the sample surface, indicating that the map is representative of the stress field throughout the 1 mm thick sample. Positive and negative shifts in frequency were observed, but the individual spectra showed no splitting of the Raman line. This is consistent with the polarization selection rules for Raman scattering, where only a singlet peak is observed for backscattering from a (001) surface in the cases of uniaxial or biaxial stresses acting in the (001) plane [19]. In diamond, positive and negative shifts correspond to compressive stress and tensile stress, respectively [23,26,31]. The Raman frequency map contains features that correspond to the two main features in the Metripol images; stress features that are elongated in the [010] and [100], and a region of large frequency shift that coincides with the twofold symmetric pattern (in the right-hand side above center). It is interesting to note that this latter region has the largest frequency shift while having relatively low birefringence. The peak shift is $+0.7$ cm^{-1}, which is approximately half the Raman linewidth in diamond, 1.5 cm^{-1} [32–34]. On average along the length of the crystal, the magnitude of the shift is less than 0.13 cm^{-1}. Since this is a small fraction of the Raman linewidth of diamond and the region only occupies a minor portion of the total length, we do not expect a

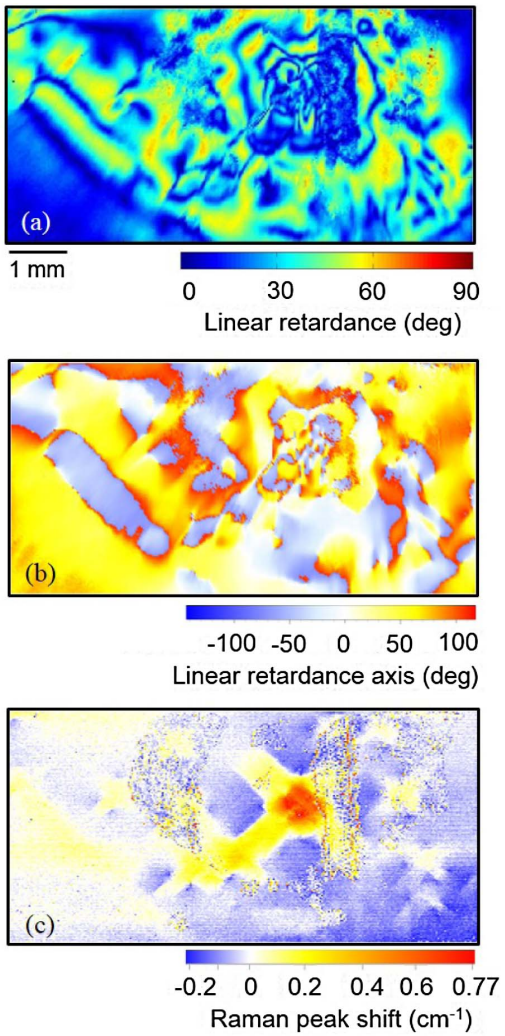

Fig. 4. (a),(b) Magnitude and direction of linear retardance across (001) plane obtained from Metripol (0° represents [110] direction), and (c) Raman peak shift map measured by backscattering from the (001) plane.

significant stress-induced decrease in the Raman gain of this crystal for beams propagating along [110].

The correspondence between birefringence and Raman frequency shift can be understood by considering the piezo-Raman and piezo-optic tensor in diamond. The change in dielectric impermittivity due to an applied stress σ_{ij} is given by [35]

$$\zeta_{ij} = \pi_{ijkl}\sigma_{kl} \qquad i, j, k, l = 1, 2, 3, \tag{5}$$

where π_{ijkl} is the fourth-rank piezo-optic tensor. For a biaxial stress, Eq. (5) (in the abbreviated notation) becomes

B60 Vol. 33, No. 3 / March 2016 / Journal of the Optical Society of America B Research Article

$$\zeta_\lambda = \begin{bmatrix} \pi_{11} & \pi_{12} & \pi_{12} & 0 & 0 & 0 \\ \pi_{12} & \pi_{11} & \pi_{12} & 0 & 0 & 0 \\ \pi_{12} & \pi_{12} & \pi_{11} & 0 & 0 & 0 \\ 0 & 0 & 0 & \pi_{44} & 0 & 0 \\ 0 & 0 & 0 & 0 & \pi_{44} & 0 \\ 0 & 0 & 0 & 0 & 0 & \pi_{44} \end{bmatrix} \begin{bmatrix} \sigma_{11} \\ \sigma_{22} \\ 0 \\ 0 \\ 0 \\ 0 \end{bmatrix} \quad (6)$$

$$= \begin{bmatrix} \sigma_{11}\pi_{11} + \sigma_{22}\pi_{12} \\ \sigma_{11}\pi_{12} + \sigma_{22}\pi_{11} \\ \sigma_{11}\pi_{12} + \sigma_{22}\pi_{12} \\ 0 \\ 0 \\ 0 \end{bmatrix}, \quad (7)$$

where the birefringence Δn is given in terms of ζ_λ as

$$\Delta n = \left(n_0 - \frac{n_0^3}{2}\zeta_1\right) - \left(n_0 - \frac{n_0^3}{2}\zeta_2\right), \quad (8)$$

which when viewing along [001] becomes

$$\Delta n = \frac{n_0^3}{2}(\sigma_{22} - \sigma_{11})(\pi_{11} - \pi_{12}). \quad (9)$$

Thus, the birefringence due to biaxial stress is proportional to the difference between the stress components σ_{11} and σ_{22}.

In contrast, the shift in Raman frequency $\Delta\omega_R$ due to biaxial stress is proportional to the sum of the stress components [20]:

$$\Delta\omega_R = \frac{1}{2\omega_0}[(\sigma_{11} + \sigma_{22})(pS_{12} + q(S_{11} + S_{12}))] \quad (10)$$

$$= -8.1576 \times 10^{-10}(\sigma_{11} + \sigma_{22}), \quad (11)$$

where p and q are the phonon deformation potentials, and S_{11} and S_{12} are the elastic compliance tensor components. Evaluation of Eq. (11) enables the stress values to be determined. The values of p and q were calculated from the mode Gruneisen parameter γ_G and the factor $(p - q)/2\omega_0^2$ given in Ref. [36]. The values of S_{11} and S_{12} were calculated from the elastic stiffness constants C_{11} and C_{12} given in Ref. [37]. The maximum frequency shift of $+0.7$ cm^{-1} corresponds to biaxial stress $(\sigma_{11} + \sigma_{22})$ of 0.86 GPa. Regions of the crystal with negative frequency shift indicate the action of tensile biaxial stress.

Hence, the region of low Δn and high $\Delta\omega_R$ of the twofold symmetric pattern is consistent with a transversely isotropic stress field (σ_{11} approximately equal to σ_{22}) in the (100) plane. For uniaxially stressed regions (σ_{11} or σ_{22} approximately equal to 0), $\Delta\omega_R$ increases with Δn which is consistent with scenarios on the left-hand side of the crystal.

3. EFFECTS ON RAMAN LASER BEHAVIOR

The combination of diamond's high Raman gain coefficient, damage threshold, and thermal conductivity, along with its low thermal expansion coefficient and wide transmission band, has led to the development of Raman lasers featuring outstanding output power capability approaching kW [13], high efficiency [38–43], and wide wavelength operating range [7,42,44–46]. However, understanding absorption losses and impurities, especially those of nitrogen, is important to laser design and optimization [7]. In cw Raman lasers in particular, minimization of intracavity losses is crucial to attaining high efficiency [7,10] due to their typically lower gain compared to pulsed devices. Recently, the presence of small amounts of birefringence has also been found to perturb performance. Furthermore, the polarization behavior of cw Raman lasers has been found to substantially deviate from that predicted from the Raman tensors, an effect that has been proposed to be due to stress-induced birefringence in the diamond [13,14]. In order to gain a more complete picture of Raman laser optimization, the effect of birefringence on laser performance is investigated here in detail.

The Raman gain coefficient is dependent on pump and Stokes polarizations according to [47]

$$g_s = k\sum_{i=1}^{3}(e_p R_i e_s)^2, \quad (12)$$

where the Raman tensor components R_1, R_2, and R_3 correspond to triply degenerate F_{2g} vibrational modes of diamond [48], and e_p and e_s are the pump and Stokes polarization unit vectors, respectively. The proportionality constant k is given by $k = 4\pi^2 N\omega_s/n_s n_p c_0^2 m\omega_R\Gamma$, where N is the number density of molecules, ω_s is the angular frequency of the Stokes photons, n_s and n_p are the refractive indices of diamond at the Stokes and pump frequencies, respectively, c_0 is the speed of light in vacuum, m is the reduced mass, and Γ is the Raman linewidth.

The Raman gain as a function of pump and Stokes polarizations for beam propagation along the [110] direction is shown in Fig. 5. The following behavior is shown: for a ⟨110⟩-polarized pump (labeled X in Fig. 5), the gain is uniform for all Stokes polarizations. For small angles of pump polarization, the gain has a maximum for a Stokes polarization near 45°. This angle counter-rotates as the pump polarization angle is increased. For a pump polarization of ⟨111⟩, the Stokes polarization is collinear and the Raman gain attains its maximum value. Upon further rotation of the pump polarization, the Stokes polarization continues to rotate until at X there is a flip in the Stokes polarization of 90°. Such polarization dynamics have been observed previously in a low-Q diamond Raman laser pumped with nanosecond pulses [41] and in similar lasers [40] investigated by some of the present authors when using diamond samples from the same batch and possessing similar birefringence characteristics to the sample used in this report. In these lasers, birefringence is not observed to influence the output Stokes polarization. However, for cw diamond Raman lasers in which the cavity Q is typically much higher, the circulating Stokes field experiences a large number of round trips before coupling out of the resonator. As a result, the influence of diamond birefringence on the polarization of the Stokes beam is increased leading to a substantial perturbation of the output polarization from that predicted by the Raman tensors [13,14].

A. Experiment

The Raman laser threshold, Stokes output polarization, and pump depolarization were studied as a function of pump polarization for areas of the diamond sample that provide a range of birefringence properties. Note that our current sample

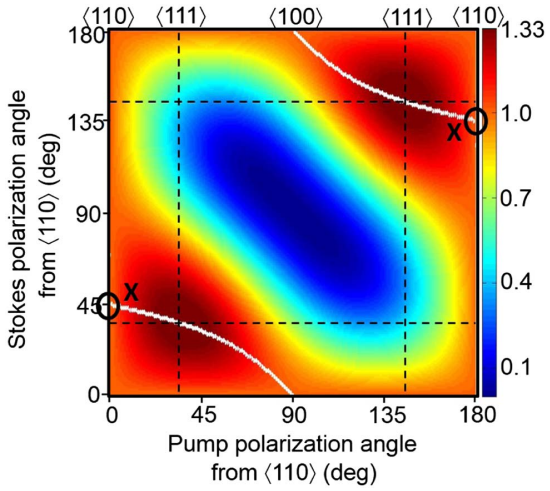

Fig. 5. Normalized Raman gain coefficient for propagation along the ⟨110⟩ direction as a function of pump and Stokes polarizations. Notable directions in diamond are represented by black dashed lines, and the maximum scattering efficiency amplitude is shown by the white loci.

under test is of the same type as that typically used in previous reports of cw diamond Raman lasers [13,14,38,39]

The diamond was placed on an X–Y–Z translation stage, allowing different regions in the crystal to be investigated. An IR camera was used to monitor the pump spot in the diamond in order to correlate the position in the diamond with the birefringence map, with an accuracy of 0.3 mm. The six regions marked A, B, C, D, E, and F in Fig. 2 were selected as these provided a range of δ, Φ, and χ values and was a sufficiently large set to characterize the observed features in polarization behavior. Regions A and F have the least amount of circular retardance (2°); B, C, D, and E have circular retardance of 12°, 19°, −13°, and 17°, respectively, as shown in Fig. 2. The magnitudes and directions of linear and circular retardance are summarized in Table 1.

Figure 6 shows the experimental setup providing simultaneous characterization of the Stokes polarization, lasing threshold, and pump depolarization. The pump source was a quasi-cw-pumped Nd:YAG laser with horizontally polarized output at 1064 nm, operating at 40 Hz repetition rate and 1% duty cycle (pulse duration approximately 250 μs). Variable attenuation of the pump beam was achieved with a rotatable half-wave plate and a polarizing cube. The diamond laser cavity was a 104 mm long near-concentric resonator consisting of concave mirrors with 50 mm radii of curvature. The input coupler was highly transmitting (>97%) at the pump and highly reflecting (99.98%) at the 1240 nm first Stokes. The output coupler was highly reflecting at the pump and provided 0.4% transmission at the first Stokes output wavelength. The antireflection-coated diamond was placed in the center of the cavity. A 50 mm focusing lens was used to focus the pump beam into the middle of the diamond. A half-wave plate (HWP 1 in Fig. 6) was used to rotate the injected pump polarization. In the following sections, the polarization angles are quoted with respect to the ⟨110⟩ direction. The total output Stokes power was monitored using an InGaAs photodiode (PD 1 in Fig. 6), while the degree and orientation of the Stokes polarization were determined using a half-wave plate and cube polarizer (rotating the half-wave plate and measuring the extinction). The depolarized pump power was monitored as a function of injected pump polarization as a check of the linear retardance axis measured using the Metripol technique and verifying the region in the diamond with respect to the birefringence map. This was achieved by removing the input coupler and measuring the backreflected, depolarized pump power on a photodetector.

B. Results

Figure 7 shows the output Stokes polarization (top row), measured and calculated threshold (middle row), and pump depolarization (bottom row) as a function of pump polarization for the four out of six regions shown in Fig. 2. The four regions A–D were selected as they were representative of the polarization behavior seen in all regions. The Stokes polarization, threshold, and pump depolarization for all the six regions investigated are given in Table 1. In each case, the Stokes polarization remains fixed to either of two orthogonal linear polarizations depending on the pump polarization. For all regions except D, the Stokes polarization is observed to switch between the orthogonal polarizations at a point in the cycle. The switching points, and the polarization directions, vary substantially for each region. The threshold for the different regions ranges from 18 to 55 W.

Table 1. Summary of the Magnitude and Direction of Linear and Circular Retardance (Measured Using Metripol and Mueller Polarimetry), Pump Depolarization, Stokes Polarization, and Minimum Threshold for the Crystal Locations A, B, C, D, E, and F Indicated in Fig. 2

	Region A	Region B	Region C	Region D	Region E	Region F
Δn (Metripol)	1.4×10^{-6}	2.5×10^{-6}	4.5×10^{-6}	7.2×10^{-6}	2.2×10^{-6}	4.8×10^{-6}
Δn (Mueller)	1.6×10^{-6}	3.9×10^{-6}	5.3×10^{-6}	6.7×10^{-6}	3.1×10^{-6}	5.2×10^{-6}
Principle axis (Metripol)	40°	40°	46°	26°	43°	41°
Principle axis (Mueller)	45°	59°	71°	1.7°	59°	37°
Circular retardance (Mueller)	2.5°	12°	18.3°	−13.2°	17°	2°
Depolarization axes	—	40°	50°	30°	40°	40°
Stokes polarization	45° and 135°	50° and 140°	62° and 152°	178°-no flip	52° and 142°	34° and 124°
Minimum threshold	18 W	24 W	25 W	53.5 W	27 W	28 W

B62 Vol. 33, No. 3 / March 2016 / Journal of the Optical Society of America B Research Article

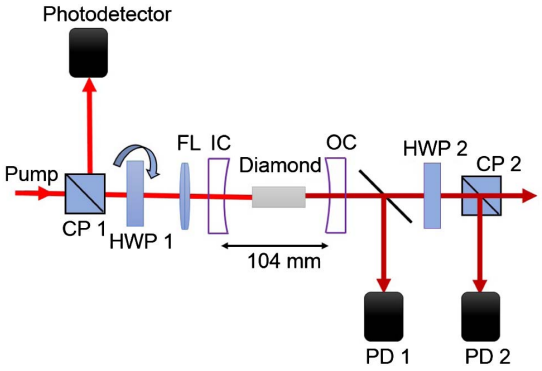

Fig. 6. Experimental arrangement for measuring laser threshold and polarization characteristics: CP, cube polarizer; HWP, half-wave plate; FL, focusing lens; IC, input coupler; OC, output coupler; PD, photodiode.

For region A, which has low circular retardance (2.5°), the linear birefringence axes obtained from Metripol (40°) and Mueller (46°) are in fair agreement. The two Mueller-obtained axes values closely match the two orthogonal Stokes polarizations (45° and 135°). A similar behavior is also observed for region F (Table 1). No significant pump depolarization was observed for region A as expected because of the low linear birefringence value ($\Delta n = 1.6 \times 10^{-6}$).

Regions B and C have significant circular retardance which substantially perturbs the Metripol-determined linear retardance direction. The direction obtained using the pump depolarization measurement matches the Metripol measurement as expected, since both measurements are unable to deconvolve the contributions of circular and linear retardance. For both the regions, the Stokes polarizations have directions closer to the Mueller-determined linear retardance axis. From Table 1, it can be seen that region E shows a similar behavior.

As for B and C, region D has large circular retardance and thus also a large difference between the linear retardance directions obtained using Metripol (24°) and Mueller (2°) polarimetry. However, as the circular retardance is negative, the Metripol-determined axis direction is overvalued in this case. Region D is also unique in that the output Stokes polarization state is constant at 178° for all pump polarizations. The reason for this is explained in the following section.

C. Analysis and Discussion

The above results reveal that the Stokes polarization is fixed to either of the axes of linear retardance. This is in stark contrast to the case of low-Q (nanosecond-pulsed) diamond Raman lasers whose polarization dynamics are dictated purely by the Raman tensors. In regions of large circular retardance, it is found that Mueller polarimetry is more suitable for predicting the output Stokes polarization.

Using the measured directions of the lasing Stokes polarizations, we have calculated the Raman laser threshold as a function of pump polarization according to the scattering efficiency [Eq. (12)]. The middle row of Fig. 7 shows the measured threshold (red and black rectangular markers) and calculated threshold using the observed Stokes polarizations. The calculated threshold has been scaled to the measured threshold to account for variations in diamond coating losses, surface quality, and cavity alignment.

It is seen that the Stokes polarization is fixed to the retardance axis that provides the highest gain according to the injected pump polarization. For example, for A, the threshold

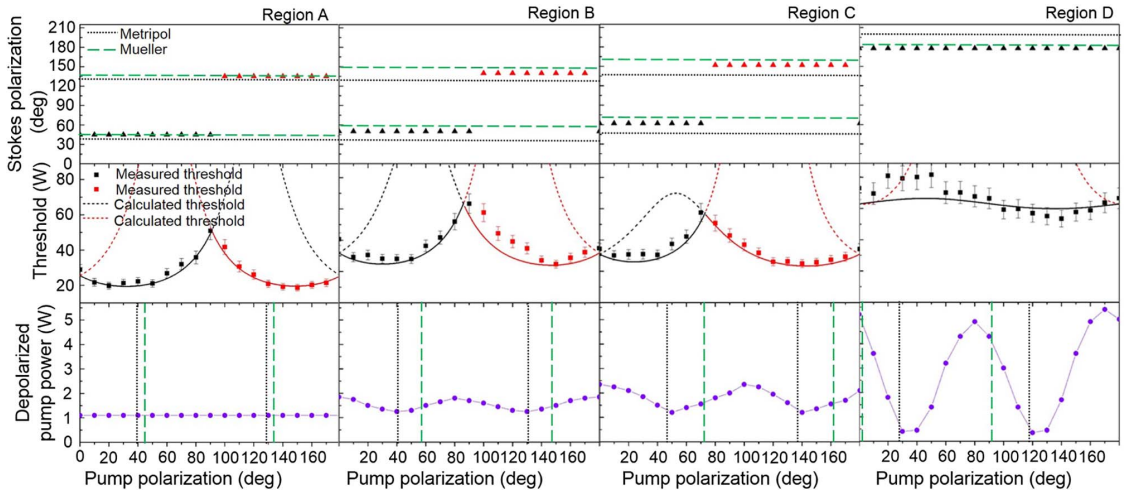

Fig. 7. Laser properties as a function of pump polarization for regions A, B, C and D. Top row: Stokes polarization (black and red triangular marker) along with the linear retardance axis direction obtained by Metripol (black dotted line) and Mueller (green dashed line). Middle row: threshold for the two orthogonal Stokes polarizations measured (black and red rectangular markers) and calculated (black and red dashed and solid lines). The solid lines indicate the calculated threshold corresponding to the polarization state with the highest Raman gain. Bottom row: pump depolarization (violet circular markers). As for the top row, the Metripol- and Mueller-measured linear retardance axis directions are shown.

Research Article Vol. 33, No. 3 / March 2016 / Journal of the Optical Society of America B B63

for 45° Stokes polarization is less than the threshold for 135° for pump polarizations in the range 0° to 91°, whereas the threshold for 135° Stokes polarization is less than for 45° for pump polarizations in the range 92° to 180°. Hence, we observe that the output polarization switches between birefringence axis directions according to which has the highest gain. The same behavior is observed for B and C (also for E and F). For D, the threshold for 178° Stokes polarization is less than its orthogonal Stokes polarization over the entire range of pump polarization angles consistent with the absence of a transition in the measured Stokes polarization.

The maximum scattering efficiencies for A, B, C, E, and F are of a similar magnitude as their birefringence axes are closely oriented to a ⟨111⟩ crystal direction. This is consistent with the similar minimum threshold for these five regions (18–28 W). The minimum threshold for D (50 W) is notably higher, partially due to the Stokes polarization being well away from the direction of maximum scattering efficiency. Note that slight variations in the coating and surface quality at each location, as well as precise alignment (which affects the pump/Stokes mode overlap), also contribute to the spread of observed thresholds.

These results show that weak stress-induced birefringence in the diamond crystal ($\Delta n \sim 10^{-6}$) affects the performance of cw diamond Raman lasers (DRLs), fixing the Stokes output polarizations to the local birefringence axes and thereby determining the maximum Raman gain coefficient achievable as a function of pump polarization. As the Stokes polarization is fixed to the local linear birefringence axis, pumping along ⟨111⟩ no longer provides maximum gain in all cases but only when Stokes polarization is aligned to ⟨111⟩. Hence, if the birefringence axis is not parallel to ⟨111⟩, the gain coefficient is less than the maximum achievable. Our results, for regions A–F and all other regions investigated, show no clear correlation between the magnitude of linear or circular retardance and DRL performance.

4. CONCLUSIONS

Here we have characterized the birefringence properties of single-crystal, CVD diamond and elucidated the effects of birefringence on cw Raman lasers. The sample showed significant circular birefringence in addition to linear birefringence, and thus the Mueller technique is a more appropriate tool for characterizing the birefringence magnitude and direction of CVD diamonds. We observed uniaxial and biaxial stresses in the (001) plane leading to shifts in the Raman line up to 0.7 cm^{-1} and corresponding to stress values up to 0.86 GPa.

We have shown that the Stokes polarization in cw Raman lasers is fixed to the local birefringence axes, in contrast to nanosecond-pulsed diamond Raman lasers for which the Stokes polarization follows the maximum Raman scattering efficiency predicted by Raman tensors. The greater susceptibility of cw devices to birefringence is attributed to the much greater number of round trips for the Stokes beam through the diamond medium. Since the Raman gain is dependent on both pump and Stokes polarizations, the Raman gain is maximized for locations in diamond where the retardance axis and pump polarization is aligned close to the ⟨111⟩ direction. These results have implications for optimizing high-Q cavity diamond Raman lasers and are expected to provide insights into the performance and optimization of other diamond-based optical devices.

Funding. ARC Discovery Grants (DP130103799, DP150102054); Air Force Research Laboratory (AFRL) (FA2386-15-1-4075); Macquarie University Research Excellence Scholarship; Macquarie University Research Fellowship.

Acknowledgment. The authors thank Hinds Instruments for the Mueller polarimetry measurements and Krystyna Drozdowicz-Tomsia for her assistance with the Raman microscope. H. Jasbeer received a Macquarie University Research Excellence Scholarship (2013). R. J. Williams received a Macquarie University Research Fellowship (2015).

REFERENCES

1. R. S. Balmer, J. R. Brandon, S. L. Clewes, H. K. Dhillon, J. M. Dodson, I. Friel, P. N. Inglis, T. D. Madgwick, M. L. Markham, T. P. Mollart, N. Perkins, G. A. Scarsbrook, D. J. Twitchen, A. J. Whitehead, J. J. Wilman, and S. M. Woollard, "Chemical vapour deposition synthetic diamond: materials, technology and applications," J. Phys. **21**, 364221 (2009).
2. F. van Loon, A. J. Kemp, A. J. Maclean, S. Calvez, J.-M. Hopkins, J. E. Hastie, M. D. Dawson, and D. Burns, "Intracavity diamond heat-spreaders in lasers: the effects of birefringence," Opt. Express **14**, 9250–9260 (2006).
3. D. H. Douglas-Hamilton, E. D. Hoag, and J. R. M. Seitz, "Diamond as a high-power-laser window," J. Opt. Soc. Am. **64**, 36–38 (1974).
4. B. J. M. Hausmann, I. B. Bulu, P. B. Deotare, M. McCutcheon, V. Venkataraman, M. L. Markham, D. J. Twitchen, and M. Lončar, "Integrated high-quality factor optical resonators in diamond," Nano Lett. **13**, 1898–1902 (2013).
5. B. J. M. Hausmann, T. M. Babinec, J. T. Choy, J. S. Hodges, S. Hong, I. Bulu, A. Yacoby, M. D. Lukin, and M. Lončar, "Single-color centers implanted in diamond nanostructures," New J. Phys. **13**, 045004 (2011).
6. B. J. M. Hausmann, M. Khan, Y. Zhang, T. M. Babinec, K. Martinick, M. McCutcheon, P. R. Hemmer, and M. Lončar, "Fabrication of diamond nanowires for quantum information processing applications," Diam. Relat. Mater. **19**, 621–629 (2010).
7. R. P. Mildren, A. Sabella, O. Kitzler, D. J. Spence, and A. M. McKay, "Diamond Raman laser design and performance," in *Optical Engineering of Diamond*, R. P. Mildren and J. R. Rabeau, eds. (Wiley-VCH Verlag GmbH, 2013), pp. 239–276.
8. A. K. Freund, J. Friedel Sellschop, K. Lieb, S. Rony, S.-B. Clemens, L. Schroeder, and J. Teyssier, "Recent diamond single crystal x-ray optics developments at the European synchrotron radiation facility," Proc. SPIE **3448**, 53–63 (1998).
9. O. J. L. Fox, L. Alianelli, A. M. Malik, I. Pape, P. W. May, and K. J. S. Sawhney, "Nanofocusing optics for synchrotron radiation made from polycrystalline diamond," Opt. Express **22**, 7657–7668 (2014).
10. I. Friel, S. L. Geoghegan, D. J. Twitchen, and G. A. Scarsbrook, "Development of high quality single crystal diamond for novel laser applications," Proc. SPIE **7838**, 783819 (2010).
11. I. Friel, "Optical quality diamond grown by chemical vapor deposition," in *Optical Engineering of Diamond*, R. P. Mildren and J. R. Rabeau, eds. (Wiley-VCH Verlag GmbH, 2013), pp. 35–69.
12. I. Friel, S. Clewes, H. Dhillon, N. Perkins, D. Twitchen, and G. Scarsbrook, "Control of surface and bulk crystalline quality in single crystal diamond grown by chemical vapour deposition," Diam. Relat. Mater. **18**, 808–815 (2009).
13. R. J. Williams, O. Kitzler, A. McKay, and R. P. Mildren, "Investigating diamond Raman lasers at the 100 W level using quasi-continuous-wave pumping," Opt. Lett. **39**, 4152–4155 (2014).

B64 Vol. 33, No. 3 / March 2016 / *Journal of the Optical Society of America B* **Research Article**

14. O. Kitzler, "External cavity diamond Raman lasers for high-power continuous-wave beam conversion," Ph.D. thesis (Macquarie University, 2014).
15. A. M. Glazer, J. G. Lewis, and W. Kaminsky, "An automatic optical imaging system for birefringent media," Philos. Trans. R. Soc. London Ser. A **452**, 2751–2765 (1996).
16. W. Kaminsky, K. Claborn, and B. Kahr, "Polarimetric imaging of crystals," Chem. Soc. Rev. **33**, 514–525 (2004).
17. F. Cerdeira, C. J. Buchenauer, F. H. Pollak, and M. Cardona, "Stress-induced shifts of first-order Raman frequencies of diamond-and zinc-blende-type semiconductors," Phys. Rev. B **5**, 580–593 (1972).
18. E. Anastassakis, A. Cantarero, and M. Cardona, "Piezo-Raman measurements and anharmonic parameters in silicon and diamond," Phys. Rev. B **41**, 7529–7535 (1990).
19. Y. von Kaenel, J. Stiegler, J. Michler, and E. Blank, "Stress distribution in heteroepitaxial chemical vapor deposited diamond films," J. Appl. Phys. **81**, 1726–1736 (1997).
20. I. De Wolf, "Relation between Raman frequency and triaxial stress in Si for surface and cross-sectional experiments in microelectronics components," J. Appl. Phys. **118**, 053101 (2015).
21. M. H. Grimsditch, E. Anastassakis, and M. Cardona, "Effect of uniaxial stress on the zone-center optical phonon of diamond," Phys. Rev. B **18**, 901–904 (1978).
22. J. W. Ager and M. D. Drory, "Quantitative measurement of residual biaxial stress by Raman spectroscopy in diamond grown on a Ti alloy by chemical vapor deposition," Phys. Rev. B **48**, 2601–2607 (1993).
23. A. Crisci, F. Baillet, M. Mermoux, G. Bogdan, M. Nesládek, and K. Haenen, "Residual strain around grown-in defects in CVD diamond single crystals: a 2D and 3D Raman imaging study," Phys. Status Solidi A **208**, 2038–2044 (2011).
24. K. E. Bennet, K. H. Lee, J. R. Tomshine, E. M. Sundin, J. N. Kruchowski, W. G. Durrer, B. M. Manciu, A. Kouzani, and F. S. Manciu, "Raman microscopic analysis of internal stress in boron-doped diamond," Materials **8**, 2782–2793 (2015).
25. H. Boppart, J. Van Straaten, and I. F. Silvera, "Raman spectra of diamond at high pressures," Phys. Rev. B **32**, 1423–1425 (1985).
26. E. J. D. Liscia, F. Alvarez, E. Burgo, E. Halac, H. Huck, and M. Reinoso, "Stress analysis on single-crystal diamonds by Raman spectroscopy 3D mapping," Mater. Sci. Appl. **4**, 191–197 (2013).
27. O. Arteaga, J. Freudenthal, B. Wang, and B. Kahr, "Mueller matrix polarimetry with four photoelastic modulators: theory and calibration," Appl. Opt. **51**, 6805–6817 (2012).
28. J. L. Pezzaniti, "Mueller matrix imaging polarimetry," Opt. Eng. **34**, 1558–1568 (1995).
29. L. S. Srinath and A. V. S. S. S. R. Sarma, "Effects of stress-induced optical activity in photoelasticity," J. Phys. D **5**, 883–895 (1972).
30. V. Yu, "Symmetry conditions for studying torsion stress-induced gradient piezogyration," Ukr. J. Phys. Opt. **14**, 91–95 (2013).
31. H. Kagi, S. Odake, S. Fukura, and D. A. Zedgenizov, "Raman spectroscopic estimation of depth of diamond origin: technical developments and the application," Russ. Geol. Geophys. **50**, 1183–1187 (2009).
32. R. P. Mildren, "Intrinsic optical properties of diamond," in *Optical Engineering of Diamond*, R. P. Mildren and J. R. Rabeau, eds. (Wiley-VCH Verlag GmbH, 2013), pp. 1–34.
33. K. C. Lee, B. J. Sussman, J. Nunn, V. O. Lorenz, K. Reim, D. Jaksch, I. A. Walmsley, P. Spizzirri, and S. Prawer, "Comparing phonon dephasing lifetimes in diamond using transient coherent ultrafast phonon spectroscopy," Diam. Relat. Mater. **19**, 1289–1295 (2010).
34. K. Ishioka, M. Hase, M. Kitajima, and H. Petek, "Coherent optical phonons in diamond," Appl. Phys. Lett. **89**, 231916 (2006).
35. A. Shtukenberg, Y. O. Punin, and B. Kahr, *Optically Anomalous Crystals* (Springer, 2007).
36. E. Anastassakis, A. Pinczuk, E. Burstein, F. Pollak, and M. Cardona, "Effect of static uniaxial stress on the Raman spectrum of silicon," Solid State Commun. **88**, 1053–1058 (1993).
37. P. Hess, "The mechanical properties of various chemical vapor deposition diamond structures compared to the ideal single crystal," J. Appl. Phys. **111**, 051101 (2012).
38. O. Kitzler, A. McKay, and R. P. Mildren, "Continuous-wave wavelength conversion for high-power applications using an external cavity diamond Raman laser," Opt. Lett **37**, 2790–2792 (2012).
39. R. J. Williams, J. Nold, M. Strecker, O. Kitzler, A. McKay, T. Schreiber, and R. P. Mildren, "Efficient Raman frequency conversion of high-power fiber lasers in diamond," Laser Photon. Rev. **9**, 405–411 (2015).
40. A. Mckay, O. Kitzler, and R. P. Mildren, "Simultaneous brightness enhancement and wavelength conversion to the eye-safe region in a high-power diamond Raman laser," Laser Photon. Rev. **8**, L37–L41 (2014).
41. A. Sabella, J. A. Piper, and R. P. Mildren, "1240 nm diamond Raman laser operating near the quantum limit," Opt. Lett. **35**, 3874–3876 (2010).
42. A. Sabella, J. A. Piper, and R. P. Mildren, "Efficient conversion of a 1064 μm Nd:YAG laser to the eye-safe region using a diamond Raman laser," Opt. Express **19**, 23554–23560 (2011).
43. J.-P. M. Feve, K. E. Shortoff, M. J. Bohn, and J. K. Brasseur, "High average power diamond Raman laser," Opt. Express **19**, 913–922 (2011).
44. R. P. Mildren, J. E. Butler, and J. R. Rabeau, "CVD-diamond external cavity Raman laser at 573 nm," Opt. Express **16**, 18950–18955 (2008).
45. E. Granados, D. J. Spence, and R. P. Mildren, "Deep ultraviolet diamond Raman laser," Opt. Express **19**, 10857–10863 (2011).
46. D. C. Parrotta, A. J. Kemp, M. D. Dawson, and J. E. Hastie, "Tunable continuous-wave diamond Raman laser," Opt. Express **19**, 24165–24170 (2011).
47. A. Penzkofer, A. Laubereau, and W. Kaiser, "High intensity Raman interactions," Prog. Quantum Electron. **6**, 55–140 (1979).
48. R. Loudon, "The Raman effect in crystals," Adv. Phys. **13**, 423–482 (1964).

Research Article | Vol. 24, No. 19 | 19 Sep 2016 | OPTICS EXPRESS 21463
Optics EXPRESS

High-gain 87 cm^{-1} Raman line of KYW and its impact on continuous-wave Raman laser operation

SOUMYA SARANG,* ROBERT J. WILLIAMS, OLIVER LUX, ONDREJ KITZLER, AARON MCKAY, HADIYA JASBEER, AND RICHARD P. MILDREN

MQ Photonics Research Centre, Department of Physics and Astronomy, Macquarie University, NSW 2109, Australia
*soumya.soumya@students.mq.edu.au

Abstract: We report a quasi-continuous-wave external cavity Raman laser based on potassium yttrium tungstate (KYW). Laser output efficiency and spectrum are severely affected by the presence of high gain Raman modes of low frequency (< 250 cm^{-1}) that are characteristic of this crystal class. Output spectra contained frequency combs spaced by the low frequency modes but with the overall pump-to-Stokes conversion efficiency at least an order of magnitude lower than that typically obtained in other crystal Raman lasers. We elucidate the primary factors affecting laser performance by measuring the Raman gain coefficients of the low energy modes and numerically modeling the cascading dynamics. For a pump polarization aligned to the N_g crystallo-optic axis, the 87 cm^{-1} Raman mode has a gain coefficient of 9.2 cm/GW at 1064 nm and a dephasing time T_2 = 9.6 ps, which are both notably higher than for the 765 cm^{-1} mode usually considered to be the prominent Raman mode of KYW. The implications for continuous-wave Raman laser design and the possible advantages for applications are discussed.

OCIS codes: (140.3550) Lasers, Raman; (140.3580) Lasers, solid-state.

References and links

1. H. M. Pask, "The design and operation of solid-state Raman lasers," Prog. Quantum Electron. **27**(1), 3–56 (2003).
2. V. G. Savitski, I. Friel, J. E. Hastie, M. D. Dawson, D. Burns, and A. J. Kemp, "Characterization of single-crystal synthetic diamond for multi-watt continuous-wave Raman lasers," IEEE J. Quantum Electron. **48**(3), 328–337 (2012).
3. A. S. Grabtchikov, V. A. Lisinetskii, V. A. Orlovich, M. Schmitt, R. Maksimenka, and W. Kiefer, "Multimode pumped continuous-wave solid-state Raman laser," Opt. Lett. **29**(21), 2524–2526 (2004).
4. O. Kitzler, A. McKay, D. J. Spence, and R. P. Mildren, "Modelling and optimization of continuous-wave external cavity Raman lasers," Opt. Express **23**(7), 8590–8602 (2015).
5. O. Kitzler, A. McKay, and R. P. Mildren, "Continuous-wave wavelength conversion for high-power applications using an external cavity diamond Raman laser," Opt. Lett. **37**(14), 2790–2792 (2012).
6. R. J. Williams, J. Nold, M. Strecker, O. Kitzler, A. McKay, T. Schreiber, and R. P. Mildren, "Efficient Raman frequency conversion of high-power fiber lasers in diamond," Laser Photonics Rev. **9**(4), 405–411 (2015).
7. R. P. Mildren and J. R. Rabeau, *Optical Engineering of Diamond* (John Wiley & Sons, 2013), Chap. 8.
8. Y. Romanyuk, "Liquid-phase epitaxy of doped $KY(WO_4)_2$ layers for waveguide lasers," Thesis, Swiss Federal Institute of Technology in Lausanne (2005).
9. A. Kaminskii, A. Konstantinova, V. Orekhova, A. Butashin, R. Klevtsova, and A. Pavlyuk, "Optical and nonlinear laser properties of the $\chi^{(3)}$-active monoclinic α-$KY(WO_4)_2$ crystals," Crystallogr. Rep. **46**(4), 665–672 (2001).
10. A. Sabella, D. J. Spence, and R. P. Mildren, "Pump–probe measurements of the Raman gain coefficient in crystals using multi-longitudinal-mode beams," IEEE J. Quantum Electron. **51**(12), 1–8 (2015).
11. I. V. Mochalov, "Laser and nonlinear properties of the potassium gadolinium tungstate laser crystal $KGd(WO_4)_2$: Nd^{3+}-(KGW: Nd)," Opt. Eng. **36**(6), 1660–1669 (1997).
12. R. Mildren, M. Convery, H. Pask, J. Piper, and T. McKay, "Efficient, all-solid-state, Raman laser in the yellow, orange and red," Opt. Express **12**(5), 785–790 (2004).
13. H. M. Pask, "Continuous-wave, all-solid-state, intracavity Raman laser," Opt. Lett. **30**(18), 2454–2456 (2005).
14. L. Macalik, J. Hanuza, and A. Kaminskii, "Polarized Raman spectra of the oriented $NaY(WO_4)_2$ and $KY(WO_4)_2$ single crystals," J. Mol. Struct. **555**(1–3), 289–297 (2000).

#269876 http://dx.doi.org/10.1364/OE.24.021463
Journal © 2016 Received 12 Jul 2016; revised 29 Aug 2016; accepted 29 Aug 2016; published 7 Sep 2016

Research Article Vol. 24, No. 19 | 19 Sep 2016 | OPTICS EXPRESS 21464
Optics EXPRESS

15. D. Kasprowicz, T. Runka, A. Majchrowski, and E. Michalski, "Low-temperature vibrational properties of $KGd(WO_4)_2$:(Er, Yb) single crystals studied by Raman spectroscopy," J. Phys. Chem. Solids **70**(9), 1242–1247 (2009).
16. J. Hanuza and L. Macalik, "Polarized infra-red and Raman spectra of monoclinic α-$KLn(WO_4)_2$ single crystals (Ln= Sm—Lu, Y)," Spectrochim. Acta Am. **43**(3), 361–373 (1987).
17. D. C. Parrotta, W. Lubeigt, A. J. Kemp, D. Burns, M. D. Dawson, and J. E. Hastie, "Continuous-wave Raman laser pumped within a semiconductor disk laser cavity," Opt. Lett. **36**(7), 1083–1085 (2011).
18. A. Kaminskii, O. Lux, H. Rhee, H. Eichler, H. Yoneda, A. Shirakawa, K. Ueda, R. Rückamp, L. Bohatý, and P. Becker, "Manifestations of nonlinear optical effects in a novel SRS-active crystal—natural topaz, $Al_2(F_{1-x}(OH)_x)_2SiO_4$: many-phonon $\chi^{(3)}$-lasing, more than sesqui-octave Stokes and anti-Stokes multi-wavelength comb lasing, cascaded and cross-cascaded $\chi^{(3)} \leftrightarrow \chi^{(3)}$ Raman-induced interactions under single-and dual-wavelength picosecond collinear coherent pumping, THG and combined SRS-promoting phonon modes," Laser Phys. Lett. **10**(7), 073001 (2013).
19. R. P. Mildren and J. A. Piper, "Increased wavelength options in the visible and ultraviolet for Raman lasers operating on dual Raman modes," Opt. Express **16**(5), 3261–3272 (2008).
20. R. J. Williams, O. Kitzler, A. McKay, and R. P. Mildren, "Investigating diamond Raman lasers at the 100 W level using quasi-cw pumping," Opt. Lett. **39**(14), 4152–4155 (2014).
21. A. McKay, O. Kitzler, and R. P. Mildren, "Thermal lens evolution and compensation in a high power KGW Raman laser," Opt. Express **22**(6), 6707–6718 (2014).
22. B. Denker and E. Shklovsky, *Handbook of solid-state lasers: Materials, systems and applications* (Elsevier, 2013).
23. D. Chunaev, T. Basiev, V. Konushkin, A. Papashvili, and A. Y. Karasik, "Synchronously pumped intracavity YLF–Nd–KGW picosecond Raman lasers and LiF: F^-_2 amplifiers," Laser Phys. Lett. **5**(8), 589–592 (2008).
24. J. Jakutis-Neto, J. Lin, N. U. Wetter, and H. Pask, "Continuous-wave watt-level Nd:YLF/KGW Raman laser operating at near-IR, yellow and lime-green wavelengths," Opt. Express **20**(9), 9841–9850 (2012).
25. S. Ding, X. Zhang, Q. Wang, J. Chang, S. Wang, and Y. Liu, "Modeling of actively Q-switched intracavity Raman lasers," IEEE J. Quantum Electron. **43**(8), 722–729 (2007).
26. S. Ding, X. Zhang, Q. Wang, F. Su, S. Li, S. Fan, S. Zhang, J. Chang, S. Wang, and Y. Liu, "Theoretical models for the extracavity Raman laser with crystalline Raman medium," Appl. Phys. B **85**(1), 89–95 (2006).
27. A. A. Demidovich, A. S. Grabtchikov, V. A. Lisinetskii, V. N. Burakevich, V. A. Orlovich, and W. Kiefer, "Continuous-wave Raman generation in a diode-pumped Nd^{3+}:$KGd(WO_4)_2$ laser," Opt. Lett. **30**(13), 1701–1703 (2005).
28. V. Lisinetskii, A. Grabtchikov, A. Demidovich, V. Burakevich, V. Orlovich, and A. Titov, "Nd: KGW/KGW crystal: efficient medium for continuous-wave intracavity Raman generation," Appl. Phys. B **88**(4), 499–501 (2007).
29. L. Batay, A. Kuzmin, A. Grabtchikov, V. Lisinetskii, V. Orlovich, A. Demidovich, A. Titov, V. Badikov, S. Sheina, V. Panyutin, M. Mond, and S. Kück, "Efficient diode-pumped passively Q-switched laser operation around 1.9 μm and self-frequency Raman conversion of Tm-doped $KY(WO_4)_2$," Appl. Phys. Lett. **81**(16), 2926–2928 (2002).
30. A. McKay, O. Kitzler, and R. P. Mildren, "High power tungstate-crystal Raman laser operating in the strong thermal lensing regime," Opt. Express **22**(1), 707–715 (2014).
31. C. Y. Tang, W. Z. Zhuang, K. W. Su, and Y. F. Chen, "Efficient continuous-wave self-Raman Nd: KGW laser with intracavity cascade emission based on shift of 89 cm^{-1}," IEEE J. Sel. Top. Quantum Electron. **21**(1), 142–147 (2015).
32. R. Chulkov, V. Markevich, V. Orlovich, and M. El-Desouki, "Steady-state Raman gain coefficients of potassium-gadolinium tungstate at the wavelength of 532 nm," Opt. Mater. **50**, 92–98 (2015).
33. A. McKay, O. Kitzler, and R. P. Mildren, "Simultaneous brightness enhancement and wavelength conversion to the eye-safe region in a high-power diamond Raman laser," Laser Photonics Rev. **8**(3), L37–L41 (2014).
34. A. McKay, D. J. Spence, D. W. Coutts, and R. P. Mildren, "Non-collinear beam combining of kilowatt beams in a diamond Raman amplifier," in *Advanced Solid State Lasers*, OSA Technical Digest (online) (Optical Society of America, 2014), paper ATu5A.1.

1. Introduction

Solid state Raman lasers are convenient and efficient devices for extending the wavelength range of inversion based lasers [1]. External cavity Raman lasers (ECRLs) offer simplicity and flexibility over other configurations for designing the resonator in terms of thermal-lens management and mirror reflectivities by placing the Raman crystal in a separate cavity singly resonant to the Stokes wavelength [2]. However, achieving continuous-wave (CW) operation is challenging as high-intensity pumping, small mode sizes and low-loss resonators are required to achieve moderate lasing thresholds [3–5]. The first CW ECRL used barium nitrate and was limited to 5% conversion efficiency and 164 mW output power due to strong thermal lensing in the crystal [3]; whereas more recent work using diamond has enabled conversion

Research Article Vol. 24, No. 19 | 19 Sep 2016 | OPTICS EXPRESS 21465
Optics EXPRESS

efficiency exceeding 60% and output powers up to 380 W due to diamond's excellent thermal properties and high Raman gain [6]. However, since the Raman shift in diamond is relatively large (1332 cm^{-1}), there is still demand for crystalline Raman lasers with greater flexibility in terms of output wavelength, despite having less output power potential.

Table 1. Comparison of KYW Properties with Other Raman Crystals Used in CW-ECRLs

	Barium nitrate (cubic) [7]	Diamond (cubic) [7]	KYW (monoclinic) [8,9]
Raman shift (cm^{-1})	1047.3	1332.3	765 (E ‖ N_g) 905 (E ‖ N_m)
Raman gain for 1064 nm pumping (cm/GW)	11	10[a]	3.6 (765 cm^{-1}) 3.6 (905 cm^{-1})
Thermal Conductivity (W/m.K)	1.2	2000	3.3[b]

[a]For polarizations parallel to a [111] direction [10].
[b]Average value over the three principal directions.

The class of double metal tungstates—of which potassium gadolinium tungstate ($KGd(WO_4)_2$, KGW) and potassium yttrium tungstate ($KY(WO_4)_2$, KYW) are prominent examples—offer the distinct advantage of two strong phonon modes around 765 cm^{-1} and 905 cm^{-1} that have similar Raman gain coefficients and can be accessed separately by changing the polarization state of the pump radiation with respect to the crystallographic axes of the crystal [8, 9]. As shown in Table 1, they also have thermal conductivity approximately three times that of barium nitrate [11], a moderate Raman gain coefficient, a high optical damage threshold and robust mechanical properties [12, 13]. The two aforementioned modes correspond to the symmetric stretching vibrations of the WOOW and WO molecular groups, respectively [14–16]. Although most reports on double metal tungstate Raman lasers utilize these two phonon modes, others have been observed. Kaminskii et al. [9] and Hanuza and Macalik [16] reported strong Raman modes of frequency 87 cm^{-1} and 225 cm^{-1} in the spontaneous Raman spectrum of KYW that have been attributed to a librational mode of WO_n and a translation mode of Y^{3+} ions, respectively. Laser operation on a low frequency mode (84 cm^{-1}) was observed in an intra-cavity KGW Raman laser which was designed for lasing on the prominent 768 cm^{-1} mode [17]. In this work, the output wavelengths resulted successive Stokes shifts from the 768 cm^{-1} and 84 cm^{-1} modes. Following [18], we refer to this process of cascaded stimulated Raman scattering (SRS) via two or more different phonons as cross-cascading. Cross-cascading has also been observed in single-pass excitation of other crystals. On the other hand, lasing on the 225 cm^{-1} phonon mode has not been observed to our knowledge. Similar cross-cascading processes have been utilized for multi-wavelength Raman lasers in other double metal tungstate devices [19]. Therefore double metal tungstate crystals offer a greater choice of Stokes wavelengths than diamond or barium nitrate, in addition to reduced susceptibility to thermal effects compared with barium nitrate.

In this paper, we demonstrate a quasi-CW ECRL employing KYW pumped at 1064 nm to generate laser radiation at 1158 nm and 1177 nm, corresponding to the first Stokes components of the two prominent high-energy phonon modes. However, we find that cross-cascading involving the 87 cm^{-1} and 225 cm^{-1} Raman modes plays a critical role in determining the output spectrum and laser efficiency. Polarization-dependent spontaneous Raman spectra of the crystal have been recorded to understand the manifestation of the observed phonon modes for different pumping conditions, and a numerical model was developed to analyze the role of cross-cascading and its impact on ECRLs. The 87 cm^{-1} mode has been found to have a gain coefficient, significantly higher than the two modes often regarded as the primary Raman modes.

Research Article Vol. 24, No. 19 | 19 Sep 2016 | OPTICS EXPRESS 21466
Optics EXPRESS

2. Experimental setup

2.1 Raman laser setup

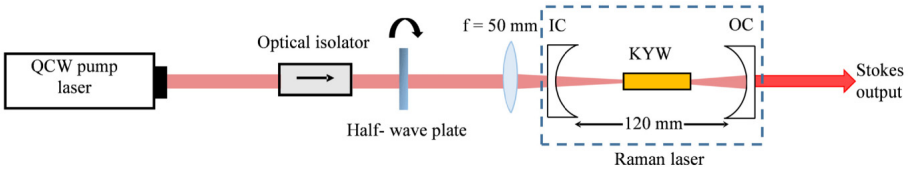

Fig. 1. Schematic diagram of the experimental setup. IC = input coupler; OC = output coupler.

The pump source was a polarized Nd:YAG laser, multimode at 1064 nm, delivering 200 W of power in 250 μs pulses at 40 Hz repetition rate and having M^2 less than 1.5 [20]. A half-wave plate was utilized to align the pump polarization along either the N_g or N_m crystallo-optic axis. The pump beam was focused into a 50 mm long KYW crystal which was placed in a near concentric 120 mm long cavity, as shown in Fig. 1. The end faces of the KYW crystal were coated with broadband AR coatings from 1000 to 1200 nm to reduce reflection losses.

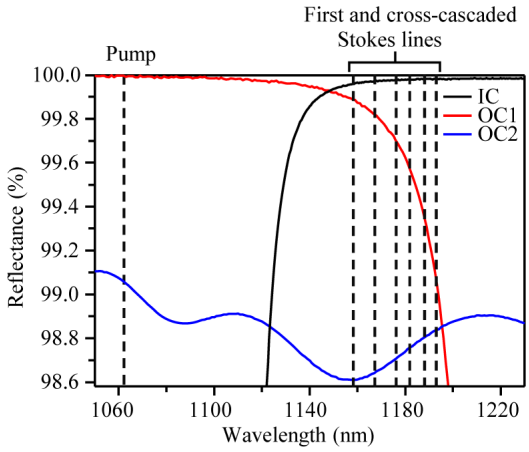

Fig. 2. Reflectance of the input coupler (IC) and the two output couplers (OC1 and OC2) used in the KYW Raman laser. The measurement uncertainty is 0.2% and 0.5% for measurements of OC1 and OC2, respectively. The vertical dashed lines indicate the reflectance at pump and different Stokes wavelengths observed experimentally (as shown in Fig. 3(b)).

Fig. 2 shows the reflectance spectra of the input coupler and output couplers which formed the linear Raman oscillator, obtained using a spectrophotometer (Cary 5000). The input coupler (IC) was highly transmitting (T = 96.8%) at 1064 nm and highly reflective (R > 99.9%) at the first Stokes wavelength (1158 nm) and at the observed cascaded Stokes wavelengths which are indicated by vertical dashed lines in the figure. The following experiments were carried out using two different output couplers OC1 and OC2, with reflectance of 99.89% and 98.6% at 1158 nm, respectively.

The Stokes output power was measured using a thermal power sensor. The output spectrum was recorded using a spectrometer (Ocean Optics NIR 512), and the spatial beam profile was measured employing a CCD camera (WinCamD, DataRay Inc.).

2.2 Raman microscopy

A high-resolution (< 1 cm^{-1}) Raman spectrometer (LabRAM HR Evolution, HORIBA Ltd.) incorporating a 532 nm laser was employed to record the spontaneous Raman scattering spectra. The probe beam was propagated along the crystallographic *b*-axis (the lasing direction) with its polarization vector varied using a half-wave plate.

Research Article | Vol. 24, No. 19 | 19 Sep 2016 | OPTICS EXPRESS 21467
Optics EXPRESS

3. Results

3.1 Laser performance

For OC1, the first Stokes at 1158 nm had a threshold of 18 W. Above 60 W of pump power, the Stokes output increases with a slope efficiency of 0.1%, reaching a maximum conversion efficiency of 0.04% (see Fig. 3(a)). The efficiency was fifty times lower than that obtained with a CW barium nitrate ECRL [3] and a thousand times lower than in a CW diamond ECRL [6]. There was no evidence of output saturation and the spatial beam profile of the Stokes output remained TEM_{00} across the investigated power range (see inset of Fig. 3(a)). Therefore, the cause of the inefficiency was deduced to be primarily non-thermal in nature. The time constant for establishing steady-state thermal gradients in KYW for a pump spot radius of 23 μm is approximately 500 μs [20, 21], thus the laser pulses are in a regime of thermal non-equilibrium and the temperature gradients are even smaller than expected for the stated output power. Measurements of the residual pump power show that the amount of pump depletion in the Raman crystal was negligible, confirming that a non-thermal mechanism was inhibiting power transfer in the Raman crystal.

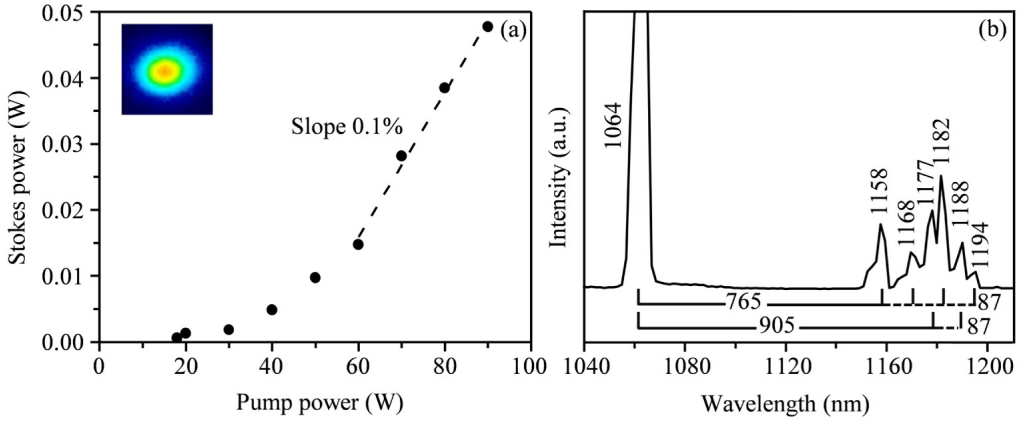

Fig. 3. (a). Output Stokes peak power versus pump peak power when using OC1. The pump polarization direction was parallel to the N_g axis. The inset shows the Stokes beam profile at 92 W pump power. (b). Laser output spectrum at 50 W pump power, containing the pump line at 1064 nm and various Stokes components. The brackets indicate the Raman modes responsible for the various output wavelengths (765 cm^{-1}, 905 cm^{-1} and 87 cm^{-1}, respectively).

The Raman laser output spectrum shown in Fig. 3(b) reveals, in addition to the first Stokes lines at 1158 nm and 1177 nm corresponding to 765 cm^{-1} and 905 cm^{-1} shifts, several emission lines spaced by approximately 10 nm which is consistent with the 87 cm^{-1} phonon mode in KYW. At pump powers near the Raman laser threshold, only the first Stokes line at 1158 nm was attained. However, when the pump power was slightly increased (less than 1.2 times threshold), cross-cascaded Stokes generation involving the 87 cm^{-1} mode occurred, generating radiation at 1168 nm. With further increase in pump power to about 26 W, the Stokes line at 1177 nm corresponding to the 905 cm^{-1} Raman mode was also observed, followed by a Stokes shift from 1177 nm to 1188 nm via the 87 cm^{-1} Raman mode. This is followed by further cascaded Stokes shifts from 1168 nm to 1182 nm and from 1182 nm to 1194 nm via 87 cm^{-1} Raman mode.

Research Article Vol. 24, No. 19 | 19 Sep 2016 | OPTICS EXPRESS 21468
Optics EXPRESS

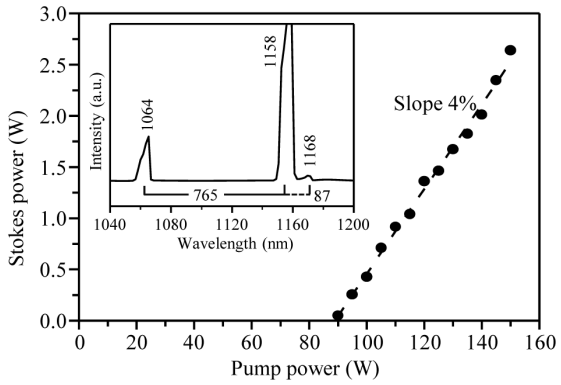

Fig. 4. Output Stokes peak power versus pump peak power when using OC2. The laser output spectrum in the inset was measured at 110 W pump power and the pump intensity is attenuated using a long pass filter. (Note that the shoulders on the short-wavelength side of the more intense lines in the inset is an artifact of the spectrometer.) The brackets indicate the Raman modes responsible for the Stokes wavelengths (765 cm^{-1} and 87 cm^{-1}, respectively).

For OC2, which showed higher transmission at the Stokes wavelengths, the laser exhibited a higher threshold pump power of 90 W, as expected. The Stokes power increased linearly with a slope efficiency of 4%, as shown in Fig. 4. The maximum conversion efficiency was 2% which is comparable to the aforementioned CW ECRL based on barium nitrate [3]. As for OC1, thermal effects in the Raman laser were negligible and the output spectrum exhibited a cross-cascaded spectral line due to the 87 cm^{-1} mode. At 110 W pump power, the output spectrum contained the primary 765 cm^{-1} Stokes mode and a single cross-cascaded line at 1168 nm (see inset of Fig. 4).

In a further experiment, we oriented the pump laser polarization along the N_m crystallo-optic axis using OC1, which suppressed lasing on the 765 cm^{-1} shift and enabled first Stokes lasing via the 905 cm^{-1} Raman mode. The threshold was 42 W, while cross-cascading to 1209 nm involving the 225 cm^{-1} mode was observed for pump powers above 50 W (see Fig. 5). For 90 W of input power, the first cross-cascaded line was stronger than the 905 cm^{-1} shifted line which we attribute in part to a higher transmission for the longer wavelengths for this output coupler. The threshold pump power for the second 225 cm^{-1} Stokes shift to 1241 nm was 90 W.

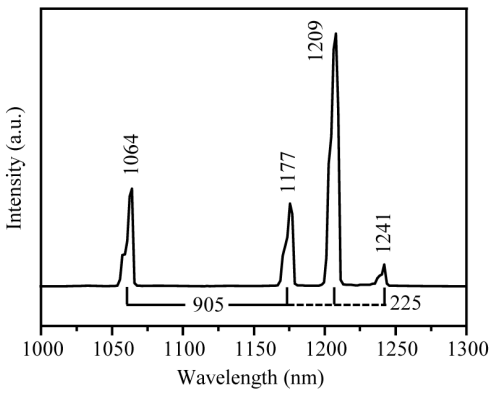

Fig. 5. Output spectrum at 90 W pump peak power for the pump polarization aligned to the N_m axis and when using OC1. The spectrum shows the pump wavelength at 1064 nm and three Stokes-shifted wavelengths generated from the 905 cm^{-1} and cross-cascaded 225 cm^{-1} phonon modes. The brackets indicate the Raman modes responsible for the first and cascaded Stokes wavelengths (905 cm^{-1} and 225 cm^{-1}, respectively).

Research Article Vol. 24, No. 19 | 19 Sep 2016 | OPTICS EXPRESS 21469
Optics EXPRESS

Similar to the observation for a N_g pump polarization, the higher output coupling provided by OC2 led to an increase in threshold (to 120 W). Cross-cascading by the 225 cm^{-1} mode was observed at a pump power of 130 W.

3.2 Raman spectrum of KYW

Although the 87 cm^{-1} and 225 cm^{-1} Raman modes have been previously identified, their gain coefficients have not been previously reported. In order to determine the gain coefficients for these shifts, we recorded high-resolution spontaneous Raman spectra for the two principal crystallo-optic directions.

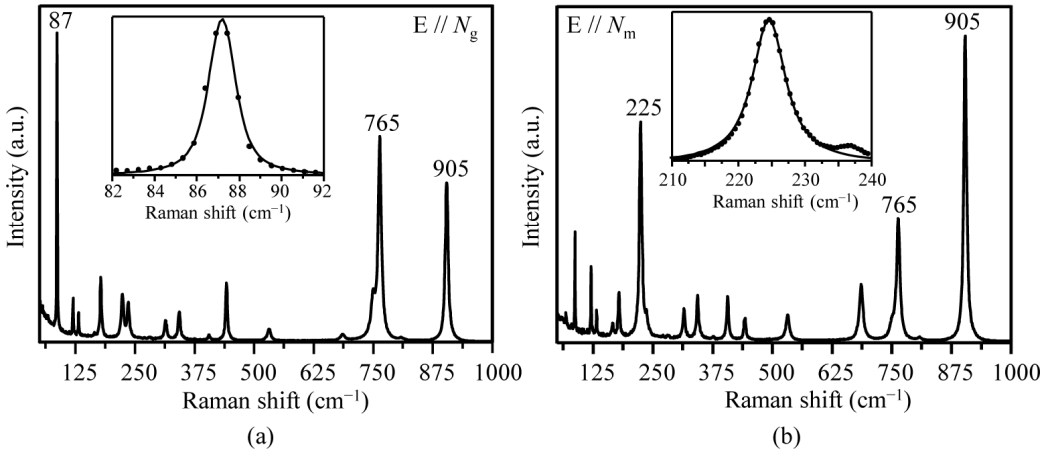

Fig. 6. Spontaneous Raman spectra of KYW for the pump polarization (E) parallel to (a) the N_g and (b) the N_m crystallo-optic axis. The insets to (a) and (b) show fitted line shapes (after baseline correction) of the 87 cm^{-1} and the 225 cm^{-1} modes, respectively.

For the pump polarization oriented parallel to N_g, as shown in Fig. 6(a), there are three main lines at 87, 765 and 905 cm^{-1}. The peak value of the 87 cm^{-1} mode is substantially higher than for the 765 cm^{-1}, indicating a higher stationary Raman gain coefficient. As is clearly apparent in the figure, the linewidth of the 87 cm^{-1} mode is much narrower than that of the 765 cm^{-1} mode, which suggests that the higher gain coefficient is in part attributable to a much longer dephasing time. Voigt profiles were fitted to the individual peaks of the instrument-broadened spontaneous Raman spectra after baseline correction in order to determine the Raman linewidths as well as the ratio of the gain coefficients. The results, summarized in Table 2, show that the stationary Raman gain coefficient of the 87 cm^{-1} mode is higher than that of the primary modes. It has a Raman linewidth of 1.1 cm^{-1}, corresponding to a dephasing time $T_2 \approx 9.6$ ps which, for comparison, is slightly longer than the first-order mode in diamond ($T_2 \approx 7.1$ ps), but shorter than for the primary (A_g) mode in barium nitrate ($T_2 \approx 26$ ps) [7]. For the pump polarization aligned parallel to N_m, shown in Fig. 6(b), the 905 cm^{-1} line has the highest peak value with the 225 cm^{-1} line slightly lower. The linewidths of the primary Raman modes at 765 cm^{-1} and 905 cm^{-1} are in agreement with previously published values to within measurement uncertainty [22]. By referencing to a reported value of 3.6 cm/GW in the literature for the 905 cm^{-1} gain coefficient [9] and comparing the relative peak intensities of the respective Raman modes, we determined the gain coefficients at 1064 nm for the 87 cm^{-1} and 225 cm^{-1} to be 9.2 cm/GW and 2.5 cm/GW, respectively.

Research Article Vol. 24, No. 19 | 19 Sep 2016 | OPTICS EXPRESS 21470
Optics EXPRESS

Table 2. Linewidths and Relative Peak Intensities of the Raman Modes for N_g and N_m Axes

Raman mode (cm^{-1})	Linewidth (cm^{-1})[a]	Relative peak intensities[a]
87	1.11 ± 0.01 E || N_g	2.564 ± 0.013 E || N_g
	0.57 ± 0.02 E || N_m	0.51 ± 0.03 E || N_m
765	8.69 ± 0.02 E || N_g	1.21 ± 0.05 E || N_g
	8.82 ± 0.02 E || N_m	0.39 ± 0.04 E || N_m
905	6.88 ± 0.003 E || N_g	1.0 ± 0.01 E || N_g
	6.89 ± 0.003 E || N_m	1.0 ± 0.01 E || N_m
225	5.89 ± 0.013 E || N_m	0.7 ± 0.03 E || N_m

[a]Error values are derived from fits to Voigt profiles.

4. Model analysis

We have observed that the presence of the low-energy Raman modes has a profound effect on the quasi-CW performance of a KYW ECRL. However, according to previous reports of KYW and KGW Raman lasers in other configurations (i.e. either pulse-pumped, intra-cavity, or both) [12, 23, 24], highly efficient operation (many tens of percent) can, in principle, be obtained without noticeable impact from low-energy modes. In order to elucidate the disparity between our observations and previous work, we have developed a numerical model to describe the power performance and spectral properties of the KYW ECRL. It is based on coupled rate equations describing the amplification and depletion of the pump and different Stokes fields via SRS [25, 26]. In this model, the pump and Stokes intensities are considered uniform as a function of position inside the cavity, and anti-Stokes generation, Raman four-wave mixing and dispersion effects are neglected. The generalized equations for the pump and first Stokes fields are:

$$\frac{dI_p}{dt} = \frac{I_{pump}}{t_{rt}} - \frac{2l_R g_a}{t_{rt}} I_p I_a - \frac{2l_R g_b}{t_{rt}} I_p I_b - \frac{L_s - \log(R_{1p}R_{2p})}{t_{rt}} I_p, \quad (1)$$

$$\frac{dI_a}{dt} = \frac{2l_R g_a \eta_a}{t_{rt}} I_p I_a - \frac{2l_R g_c \eta_c}{t_{rt}} I_a I_{ai} - \frac{L_s - \log(R_{1a}R_{2a})}{t_{rt}} I_a + \frac{2Kl_R}{t_{rt}} I_a, \quad (2)$$

$$\frac{dI_b}{dt} = \frac{2l_R g_b \eta_b}{t_{rt}} I_p I_b - \frac{2l_R g_c \eta_c}{t_{rt}} I_b I_{bi} - \frac{L_s - \log(R_{1b}R_{2b})}{t_{rt}} I_b + \frac{2Kl_R}{t_{rt}} I_b. \quad (3)$$

where I_{pump} is the initial pump intensity, g_a and g_b are the gain coefficients of the primary Raman modes at 765 cm^{-1} and 905 cm^{-1}, respectively, g_c denotes the gain coefficient of the 87 cm^{-1} mode, at the pumping wavelength, and η_i is the quantum defect for the i^{th} Stokes shift from the pump. K is the spontaneous Raman scattering factor, l_R is the Raman crystal length, t_{rt} is the round-trip time of the cavity, L_s is the dissipative loss excluding the out-coupling loss, and R_{1p} and R_{2p}, and $R_{1a,b}$ and $R_{2a,b}$ are the input and output coupler reflectivities at the pump and Stokes wavelengths, respectively. The mirror reflectivities at each of the Stokes wavelengths were obtained from transmission measurements of Fig. 2. The cavity length was 120 mm and the pump spot sizes were 23 μm and 39 μm for OC1 and OC2, respectively. The model agreed well with the experimental observations when the round trip intracavity dissipative losses (scatter and absorption) were taken to be in the range 0.8% to 1.0%. I_p is the intracavity intensity for the pump, $I_{a,b}$ and $I_{ai,bi}$ are the intracavity intensities for the first Stokes and cascaded Stokes components respectively. Equations for cascaded Stokes fields were also used in the model, where the pump field is replaced by the first or next-lower order Stokes field. These intracavity intensities were solved numerically using Mathematica, and

Research Article | Vol. 24, No. 19 | 19 Sep 2016 | OPTICS EXPRESS 21471
Optics EXPRESS

the corresponding output powers were calculated and compared to the experimental data. The best agreement was achieved when the ratio of the gain coefficients for the 87 cm^{-1} and 765 cm^{-1} modes with respect to the 905 cm^{-1} mode was set to 2.5 and 1.25, respectively, which are within the uncertainty range of the gain coefficients derived from the spontaneous Raman spectra (compare Tables 2 and 3).

Table 3. Raman Gain Coefficients Obtained by the Numerical Model (for Pump Polarization Parallel to N_g, Pump Wavelength: 1064 nm) by Comparison with Experiment

Raman modes (cm^{-1})	Gain coefficients (cm/GW)
87	9.0
765	4.5
905	3.6

The model yields the intensities for each Stokes wavelength as a function of pump power. For a visual comparison with the experimental laser spectrum along N_g, we plotted the model results as Lorentzian lines at each Stokes wavelength with a linewidth of 0.7 nm. The modelled spectra are shown as dashed lines in Fig. 7(a) and (b) for OC1 and 2, respectively, along with the measured spectra (solid lines). Since we used an ECRL configuration which is non-resonant at wavelengths near the pump, first Stokes laser operation at 1074 nm generated directly from the pump via the 87 cm^{-1} mode does not reach threshold.

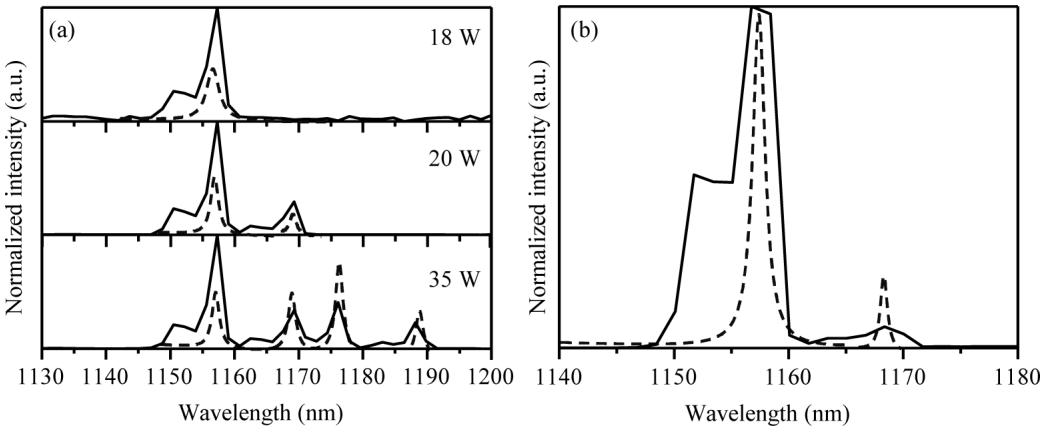

Fig. 7. Measured spectra (solid lines) and corresponding modelled spectra (dashed lines) for (a) OC1 at different pump powers and (b) OC2 at 110 W.

In all cases the model qualitatively reproduces what was observed experimentally: the onset of cascaded Stokes shifts at low thresholds accompanied by poor pump depletion and poor conversion efficiency. Using the coefficients in Table 3, the calculated laser threshold at 1158 nm for OC1 was 17.8 W in close agreement with the experimental value of 18 W. The model also shows that, with only a slight increase in pump power of about 2 W, the threshold for cross-cascaded Stokes at 1168 nm is achieved. This leads to clamping of the intracavity first Stokes intensity which subsequently stalls the transfer of pump power to the first Stokes. This is confirmed by a stepwise increase in residual pump power (not shown here). For a further rise in pump power by 5 W, the first Stokes related to the 905 cm^{-1} mode (at 1177 nm) is also seen, followed by a cross-cascaded Stokes line at 1187 nm owing to the interaction with the 87 cm^{-1} mode. The OC1 reflectivities for all the Stokes wavelengths are high and approximately equal (99.7 ± 0.1%), and thus promote the cross-cascading process.

In the case of OC2, the calculated threshold for lasing at 1158 nm (765 cm^{-1} mode) is 95 W, which is close to the measured threshold of 90 W. The first Stokes component corresponding to the 905 cm^{-1} mode (at 1177 nm) is obtained after an increase in pump power

Research Article Vol. 24, No. 19 | 19 Sep 2016 | OPTICS EXPRESS 21472
Optics EXPRESS

of approximately 30 W. These values agree well with those measured, confirming the accuracy of the model and the deduced Raman gain coefficients. It is evident from the model that the number of cascaded Stokes wavelengths is larger for OC1 compared to OC2 owing to the former's higher reflectivity.

Although cross-cascading leads to clamping of a first Stokes line accompanied by stalling of the Stokes conversion efficiency, the model also shows that for pump powers higher than the threshold for a further cascade leads to a large recovery in the slope efficiency. This is because the cross-cascaded Stokes intensity becomes clamped which in turn unclamps the first Stokes intensity and power transfer from the pump. Indeed, using the model it was found generally that the slope efficiency changes from low to high values in an alternating fashion for odd and even number of cascades. The reason the laser efficiency remains poor overall is because the threshold for the odd-order cascade is very close to the previous one causing the slope efficiency to remain low for most of the power range. Although model derived thresholds are highly sensitive to losses, it reproduces well the higher efficiency observed for OC2 compared to OC1 and confirms that this is facilitated by the offsetting of cross-cascading to higher powers.

5. Discussion

The experimental results and the model show that the low frequency Raman modes have a major impact on the performance of the KYW laser, due to their high gain and the high output coupler reflectivity at wavelengths within 250 cm^{-1} of the first Stokes lines. The resultant low-threshold cross-cascaded Stokes shifting obstructs the efficient conversion of power from the pump to the first Stokes line, thus limiting the overall conversion efficiency. Therefore the impact of these modes must be taken into account when designing Raman lasers based on KYW or crystals with similar Raman spectral features. However, there have been numerous reports of efficient Raman lasers using double-metal-tungstate crystals such as KYW and KGW (which has a very similar structure and Raman spectrum to KYW) [12, 17, 19, 23, 24, 27–31], and only one that considers cross-cascading as a power-limiting factor [32].

One possible reason that these devices exhibited higher efficiency and were not apparently severely impacted by cross-cascading is that they operate with pump polarization along the N_m axis where the gain coefficient of the 225 cm^{-1} mode is lower than the 87 cm^{-1} and 905 cm^{-1} Raman modes [12, 19, 23, 24, 27–29]. In addition to the lower gain for this mode, the cross-cascaded wavelength is about 20 nm apart from the first Stokes so the output coupler reflectivity for the cascaded shift may be more differentiated from that of the first Stokes. Nevertheless, cross-cascading from the first Stokes mode (901 cm^{-1}) via the 204 ± 3 cm^{-1} mode in KGW (equivalent to the 225 cm^{-1} mode in KYW) has been reported in a nanosecond-pulsed ECRL [30]. In that case they could not achieve slope efficiency similar to that obtained in other ECRLs and attributed it mainly to thermal effects in the crystal and the poor pump beam quality (cross-cascading was not discussed).

There are several papers which have reported cross-cascading in KGW lasers with pump polarization along N_g. In the case of a ns-pulse pumped KGW ECRL with a low-reflectivity output coupler [32], cross-cascading via the 84 cm^{-1} mode was observed at elevated powers, coinciding with a sudden decrease in slope efficiency. This may be evidence that cross-cascading is playing a similar role in limiting efficiency as observed in our work. In some CW intracavity and self-Raman lasers operating with low output coupling, cross-cascading on the low frequency Raman mode has been observed, although any adverse effects of cross-cascading on the laser efficiency was not discussed [17, 31]. Since the boundary conditions for power flow in intracavity Raman lasers are different to ECRLs, we cannot directly compare their results with our observations. Finally, there are other reports of efficient KGW and KYW lasers operating in the same orientation in which cross-cascading was not observed [12, 19, 23, 24]. This could be due to the specific loss properties of the resonators used (e.g. mirror coatings) or insufficient resolution in the characterization of the output spectrum.

Research Article | Vol. 24, No. 19 | 19 Sep 2016 | OPTICS EXPRESS 21473
Optics EXPRESS

Typically cross-cascading would be considered a parasitic process that should be avoided to improve laser efficiency. This can be achieved by tailoring the OC reflectivity at the first and cross-cascaded Stokes wavelengths in order to extend the range of pump power between the first and cascaded-Stokes thresholds. However, this would require sophisticated mirror coatings with significant changes in reflectivity (tens of percent) over a spectral range of only a few to a few tens of nanometers. This is likely to be costly and impractical. Introducing wavelength selective elements such as etalons or gratings into the cavity is an alternative approach for suppressing cross-cascading.

Even though the low frequency Raman mode at 87 cm^{-1} reduced the efficiency of this laser, it may be advantageous for other applications. This high gain mode could be used to simultaneously generate multiple closely spaced wavelengths which may be of use in spectroscopy or in terahertz radiation generation at integer multiples of 2.6 THz (87 cm^{-1}) through difference frequency mixing of first and/or cross-cascaded Stokes waves. Furthermore, Raman beam conversion for the purposes of either brightness enhancement [33] through the Raman beam cleanup effect, or beam combination [34], can be enabled with much lower quantum defect than with conventional Raman modes in crystals. This may pave the way for an alternative approach to diamond in terms of high-power Raman lasers with possible advantages arising from the ease of growth of large tungstate crystals with good damage threshold and moderate thermal properties.

6. Conclusion

We have demonstrated an external cavity quasi-CW KYW Raman laser operating at multiple Stokes wavelengths. Cross-cascading involving the 765 cm^{-1} mode and the 87 cm^{-1} mode was observed when the pump polarization was aligned along the N_g axis, while a similar effect was present via 905 cm^{-1} and 225 cm^{-1} modes when the pump polarization was parallel to the N_m axis. Numerical modelling and experimental results confirmed that the early onset of cascaded Stokes components severely limits the pump depletion and thus, lowers the overall conversion to the output Stokes beam. The gain coefficients and dephasing times of the low frequency modes were calculated from high-resolution spontaneous Raman spectra. It is concluded that for a Raman crystal with one or more strong, low-frequency Raman modes, cross-cascading can be a major factor for consideration in Raman cavity design, particularly for CW systems that rely on highly-resonant cavities. The high gain coefficient of the 87 cm^{-1} Raman mode in KYW (9.2 cm/GW at 1064 nm) indicates potential for future applications as multi-wavelength laser sources of high beam quality and as a low-quantum-defect Raman material for brightness enhancement and/or beam combination.

Funding

Australian Research Council Discovery Grant (DP130103799); US Air Force Research Laboratory (FA2386-15-1-4075); German Research Foundation (DFG) (LU2018/1-1).

Acknowledgment

The authors thank David Adams for his assistance with the Raman spectrometer.

List of Figures

References

[1] T. H. Maiman. *Stimulated optical radiation in ruby*. Nature **187**(4736), 493 (1960).

[2] A. A. Kaminskii. *Laser crystals: their physics and properties*, vol. 14 (Springer, 2013).

[3] W. Koechner. *Solid-state laser engineering*, vol. 1 (Springer, 2013).

[4] A. Javan, W. R. Bennett Jr, and D. R. Herriott. *Population inversion and continuous optical maser oscillation in a gas discharge containing a He-Ne mixture*. Physical Review Letters **6**(3), 106 (1961).

[5] A. White and J. Rigden. *Continuous Gas Maser Operation in Visible*. Proceedings of the Institute of Radio Engineers **50**(7), 1697 (1962).

[6] E. Gordon, E. Labuda, and W. Bridges. *Continuous visible laser action in singly ionized argon, krypton, and xenon*. Applied Physics Letters **4**(10), 178 (1964).

[7] C. K. N. Patel. *Continuous-wave laser action on vibrational-rotational transitions of CO_2*. Physical review **136**(5A), A1187 (1964).

[8] O. Peterson, S. Tuccio, and B. Snavely. *CW operation of an organic dye solution laser*. Applied Physics Letters **17**(6), 245 (1970).

[9] Z. Kiss and R. Duncan. *CROSS – PUMPED $Cr^{3+} - Nd^{3+}$: YAG LASER SYSTEM*. Applied Physics Letters **5**(10), 200 (1964).

[10] H. Statz, C. Tang, and J. Lavine. *Spectral output of semiconductor lasers*. Journal of Applied Physics **35**(9), 2581 (1964).

[11] O. G. Okhotnikov. *Semiconductor disk lasers: physics and technology* (John Wiley & Sons, 2010).

[12] R. W. Boyd. *Nonlinear optics* (Academic press, 2003).

[13] Y. Lv, H. Tan, and L. Qian. *All-solid-state doubly resonant sum-frequency continuous-wave laser at 555 nm*. Chinese Optics Letters **4**(1), 25 (2006).

[14] C. Adams and A. Ferguson. *Tunable narrow linewidth ultra-violet light generation by frequency doubling of a ring Ti:sapphire laser using lithium tri-borate in an external enhancement cavity*. Optics communications **90**(1-3), 89 (1992).

[15] T. Sudmeyer, Y. Imai, H. Masuda, N. Eguchi, M. Saito, and S. Kubota. *Efficient 2^{nd} and 4^{th} harmonic generation of a single-frequency, continuous-wave fiber amplifier*. Optics express **16**(3), 1546 (2008).

[16] M. Scheid, F. Markert, J. Walz, J. Wang, M. Kirchner, and T. W. Hänsch. *750 mW continuous-wave solid-state deep ultraviolet laser source at the 253.7 nm transition in mercury*. Optics letters **32**(8), 955 (2007).

[17] H. Kumagai, Y. Asakawa, T. Iwane, K. Midorikawa, and M. Obara. *Efficient frequency doubling of 1-W continuous-wave Ti: sapphire laser with a robust high-finesse external cavity*. Applied optics **42**(6), 1036 (2003).

[18] L. S. Cruz and F. C. Cruz. *External power-enhancement cavity versus intracavity frequency doubling of Ti: sapphire lasers using BIBO*. Optics express **15**(19), 11913 (2007).

[19] H. Schnitzler, U. Fröhlich, T. K. Boley, A. E. Clemen, J. Mlynek, A. Peters, and S. Schiller. *All-solid-state tunable continuous-wave ultraviolet source with high spectral purity and frequency stability*. Applied optics **41**(33), 7000 (2002).

[20] M. Fallahi, L. Fan, Y. Kaneda, C. Hessenius, J. Hader, H. Li, J. V. Moloney, B. Kunert, W. Stolz, S. W. Koch, J. Murray, and R. Bedford. *5-W yellow laser by intracavity frequency doubling of high-power vertical-external-cavity surface-emitting laser*. IEEE Photonics Technology Letters **20**(20), 1700 (2008).

[21] E. Kantola, T. Leinonen, S. Ranta, M. Tavast, and M. Guina. *High-efficiency 20 W yellow VECSEL*. Optics express **22**(6), 6372 (2014).

[22] V. Ostroumov, W. Seelert, L. Hunziker, C. Ihli, A. Richter, E. Heumann, and G. Huber. *UV generation by intracavity frequency doubling of an OPS-pumped Pr : YLF laser with 500 mW of cw power at 360 nm*. In *Lasers and Applications in Science and Engineering*, pp. 645103–645103 (International Society for Optics and Photonics, 2007).

[23] W.-L. Zhou, Y. Mori, T. Sasaki, S. Nakai, K. Nakano, S. Niikura, and B. Craig. *Intracavity frequency doubling of a continuous wave Ti: sapphire laser with over 70% conversion efficiency*. Applied physics letters **66**(19), 2463 (1995).

[24] W.-L. Zhou, Y. Mori, T. Sasaki, and S. Nakai. *High-efficiency intracavity continuous-wave ultraviolet generation using crystals $CsLiB_6O_{10}$, β-BaB_2O_4 and LiB_3O_5*. Optics communications **123**(4), 583 (1996).

[25] Y. Lü, G. Sun, X. Fu, Z. Liu, and J. Chen. *Diode-pumped doubly resonant all-intracavity continuous-wave ultraviolet laser at 336 nm*. Laser Physics Letters **7**(8), 560 (2010).

[26] S. C. Kumar, G. Samanta, and M. Ebrahim-Zadeh. *High-power, single-frequency, continuous-wave second-harmonic-generation of ytterbium fiber laser in PPKTP and MgO: sPPLT*. Optics express **17**(16), 13711 (2009).

[27] S. V. Tovstonog, S. Kurimura, I. Suzuki, K. Takeno, S. Moriwaki, N. Ohmae, N. Mio, and T. Katagai. *Thermal effects in high-power CW second harmonic generation in Mg-doped stoichiometric lithium tantalate*. Optics express **16**(15), 11294 (2008).

[28] F. Kontur, I. Dajani, Y. Lu, and R. Knize. *Frequency-doubling of a CW fiber laser using PPKTP, PPMgSLT, and PPMgLN*. Optics express **15**(20), 12882 (2007).

[29] Z. M. Liao, S. A. Payne, J. W. Dawson, A. D. Drobshoff, C. A. Ebbers, D. M. Pennington, I. Jovanovic, and L. R. Taylor. *Thermally induced dephasing in periodically poled $KTiOPO_4$ nonlinear crystals*. In *Nonlinear Optics: Materials, Fundamentals and Applications*, p. WD17 (Optical Society of America, 2004).

[30] N. Yu, C. Jung, D. Ko, J. Lee, O. Louchev, S. Kurimura, and K. Kitamura. *Thermal dephasing of quasi-phase-matched second-harmonic generation in periodically poled stoichiometric $LiTaO_3$ at high input power*. Journal of the Korean Physical Society **49**(2), 528 (2006).

[31] K. Mizuuchi, A. Morikawa, T. Sugita, K. Yamamoto, N. Pavel, and T. Taira. *Continuous-wave ultraviolet generation at 354 nm in a periodically poled $MgO : LiNbO_3$ by frequency tripling of a diode end-pumped $Nd : GdVO_4$ microlaser*. Applied physics letters **85**(18) (2004).

[32] N. Pavel, T. Taira, K. Mizuuchi, A. Morikawa, T. Sugita, and K. Yamamoto. *Continuous-wave ultraviolet generation at 354 nm in a periodically poled $MgO : LiNbO_3$*. In *Nonlinear Optics: Materials, Fundamentals and Applications*, p. TuA2 (Optical Society of America, 2004).

[33] R. White, I. McKinnie, S. Butterworth, G. Baxter, D. Warrington, P. Smith, G. Ross, and D. Hanna. *Tunable single-frequency ultraviolet generation from a continuous-wave Ti: sapphire laser with an intracavity PPLN frequency doubler*. Applied Physics B **77**(6-7), 547 (2003).

[34] J. Bai and G. Chen. *Continuous-wave diode-laser end-pumped $Nd : YVO_4/KTP$ high-power solid-state green laser*. Optics & Laser Technology **34**(4), 333 (2002).

[35] N. Aubert, T. Georges, C. Chauzat, R. Le Bras, and P. Feron. *Diode-pumped low noise CW 355-nm intra-cavity tripled laser up to 20 mW*. In *Photonics Europe*, pp. 61900E–61900E (International Society for Optics and Photonics, 2006).

[36] M. Oka, L. Y. Liu, W. Wiechmann, N. Eguchi, and S. Kubota. *All solid-state continuous-wave frequency-quadrupled $Nd : YAG$ laser*. IEEE Journal of Selected Topics in Quantum Electronics **1**(3), 859 (1995).

[37] C. Czeranowsky, E. Heumann, and G. Huber. *All-solid-state continuous-wave frequency-doubled $Nd : YAG - BiBO$ laser with 2.8-W output power at 473 nm*. Optics letters **28**(6), 432 (2003).

[38] Z. Quan, Y. Yi, Q. Dapeng, Z. Kai, L. Yang, and Z. Ling. *All-solid-state 556 nm*

yellow-green laser generated by frequency doubling of a diode-pumped Nd : YAG laser. JOSA B **26**(10), 1939 (2009).

[39] R. Zhou, S. Ruan, C. Du, and J. Yao. *High-power continuous-wave diode-end-pumped intracavity-frequency-doubled Nd : $GdVO_4$/LBO red laser*. Optics Communications **282**(4), 605 (2009).

[40] I. Lee, M. Jalali, N. Vanasse, Z. Prezkuta, and W. J. Alford. *High average power 589 nm generation in LBO*. In *Advanced Solid-State Photonics*, p. MC18 (Optical Society of America, 2008).

[41] I. Lee, M. Jalali, N. Vanasse, Z. Prezkuta, K. Groff, J. Roush, N. Rogers, E. Andrews, G. Moule, B. Tiemann, A. K. Hankla, S. M. Adkins, and C. d'Orgeville. *20 W and 50 W guidestar laser system update for the Keck I and Gemini South telescopes*. In *SPIE Astronomical Telescopes+ Instrumentation*, pp. 70150N–70150N (International Society for Optics and Photonics, 2008).

[42] S. Lin, Y. Y. Lin, R. Y. Tu, T. D. Wang, and Y. C. Huang. *Fiber-laser-pumped CW OPO for red, green, blue laser generation*. Optics express **18**(3), 2361 (2010).

[43] G. Samanta and M. Ebrahim-Zadeh. *Continuous-wave, single-frequency, solid-state blue source for the 425–489 nm spectral range*. Optics letters **33**(11), 1228 (2008).

[44] C. Drag and F. Bretenaker. *Single-frequency and tunable operation of a continuous intracavity-frequency-doubled singly resonant optical parametric oscillator*. Optics letters **33**(13), 1455 (2008).

[45] T. Petelski, R. Conroy, K. Bencheikh, J. Mlynek, and S. Schiller. *All-solid-state, tunable, single-frequency source of yellow light for high-resolution spectroscopy*. Optics letters **26**(13), 1013 (2001).

[46] F. Colville, M. Padgett, A. Henderson, J. Zhang, and M. Dunn. *Continuous-wave parametric oscillator pumped in the ultraviolet*. Optics letters **18**(13), 1065 (1993).

[47] U. Strößner, J.-P. Meyn, R. Wallenstein, P. Urenski, A. Arie, G. Rosenman, J. Mlynek, S. Schiller, and A. Peters. *Single-frequency continuous-wave optical parametric oscillator system with an ultrawide tuning range of 550 to 2830 nm*. JOSA B **19**(6), 1419 (2002).

[48] J.-M. Melkonian, F. Bretenaker, and C. Drag. *High spectral purity and tunable operation of a continuous singly resonant optical parametric oscillator emitting in the red*. Optics letters **32**(5), 518 (2007).

[49] I. Breunig, D. Haertle, and K. Buse. *Continuous-wave optical parametric oscillators: recent developments and prospects*. Applied Physics B **105**(1), 99 (2011).

[50] S. Calvez, J. E. Hastie, M. Guina, O. G. Okhotnikov, and M. D. Dawson. *Semiconductor disk lasers for the generation of visible and ultraviolet radiation*. Laser & Photonics Reviews **3**(5), 407 (2009).

[51] J. Chilla, Q.-Z. Shu, H. Zhou, E. Weiss, M. Reed, and L. Spinelli. *Recent advances in optically pumped semiconductor lasers*. In *Lasers and Applications in Science and Engineering*, pp. 645109–645109 (International Society for Optics and Photonics, 2007).

[52] A. Henderson and R. Stafford. *Intra-cavity power effects in singly resonant cw OPOs*. Applied Physics B **85**(2-3), 181 (2006).

[53] A. Smekal. *Zur quantentheorie der dispersion*. Naturwissenschaften **11**(43), 873 (1923).

[54] K. KRISHNAN. *A new class of spectra due to secondary radiation Part I*. Indian J. Phys **2**, 399 (1928).

[55] E. Woodbury and W. Ng. *Ruby laser operation in near IR* (1962).

[56] G. Eckhardt, R. Hellwarth, F. McClung, S. Schwarz, D. Weiner, and E. Woodbury. *Stimulated Raman scattering from organic liquids*. Physical Review Letters **9**(11), 455 (1962).

[57] A. Penzkofer, A. Laubereau, and W. Kaiser. *High intensity Raman interactions*. Progress in Quantum Electronics **6**(2), 55 (1979).

[58] Y. R. Shen and N. Bloembergen. *Theory of stimulated Brillouin and Raman scattering*. Physical Review **137**(6A), A1787 (1965).

[59] C.-S. Wang. *Theory of stimulated Raman scattering*. Physical Review **182**(2), 482 (1969).

[60] G. D. Boyd, W. D. Johnston Jr, and I. P. Kaminow. *Optimization of the stimulated Raman scattering threshold*. Quantum Electronics, IEEE Journal of **5**(4), 203 (1969).

[61] G. Placzek. *Rayleigh-streuung und Raman-effekt*, vol. 2 (Akad. Verlag-Ges., 1934).

[62] R. L. Sutherland. *Handbook of nonlinear optics* (CRC press, 2003).

[63] R. C. Powell. *Physics of solid-state laser materials*, vol. 1 (Springer Science & Business Media, 1998).

[64] S. Ding, X. Zhang, Q. Wang, F. Su, S. Li, S. Fan, S. Zhang, J. Chang, S. Wang, and Y. Liu. *Theoretical models for the extracavity Raman laser with crystalline Raman medium*. Applied Physics B **85**(1), 89 (2006).

[65] D. Von der Linde, M. Maier, and W. Kaiser. *Quantitative investigations of the stimulated Raman effect using subnanosecond light pulses*. Physical Review **178**(1), 11 (1969).

[66] G. Willenberg, U. Hübner, and J. Heppner. *Far infrared cw raman lasing in NH_3*. Optics Communications **33**(2), 193 (1980).

[67] R. Marx, U. Hubner, I. Abdul-Halim, J. Heppner, Y.-C. Ni, G. Willenberg, and C. Weiss. *Far-infrared CW Raman and laser gain of $14NH_3$*. IEEE Journal of Quantum Electronics **17**(6), 1123 (1981).

[68] S. N. Jabr. *Gain and noise characteristics of a continuous-wave Raman laser*. Optics letters **12**(9), 690 (1987).

[69] M. Poelker and P. Kumar. *Sodium Raman laser: direct measurements of the narrow-band Raman gain*. Optics letters **17**(6), 399 (1992).

[70] J. Brasseur, K. Repasky, and J. Carlsten. *Continuous-wave Raman laser in H_2*. Optics letters **23**(5), 367 (1998).

[71] H. M. Pask. *The design and operation of solid-state Raman lasers*. Progress in Quantum Electronics **27**(1), 3 (2003).

[72] L. Zhang, C. Liu, H. Jiang, Y. Qi, B. He, J. Zhou, X. Gu, and Y. Feng. *Kilowatt ytterbium-Raman fiber laser*. Optics express **22**(15), 18483 (2014).

[73] Y. Feng, L. R. Taylor, and D. B. Calia. *150 W highly-efficient Raman fiber laser*. Optics express **17**(26), 23678 (2009).

[74] V. Supradeepa and J. W. Nicholson. *Power scaling of high-efficiency 1.5 μm cascaded Raman fiber lasers*. Optics letters **38**(14), 2538 (2013).

[75] A. Grabtchikov, V. Lisinetskii, V. Orlovich, M. Schmitt, R. Maksimenka, and W. Kiefer. *Multimode pumped continuous-wave solid-state Raman laser*. Optics letters **29**(21), 2524 (2004).

[76] H. M. Pask. *Continuous-wave, all-solid-state, intracavity Raman laser*. Optics letters **30**(18), 2454 (2005).

[77] J. A. Piper and H. M. Pask. *Crystalline Raman lasers*. IEEE Journal of Selected Topics in Quantum Electronics **13**(3), 692 (2007).

[78] L. Fan, Y.-X. Fan, Y.-Q. Li, H. Zhang, Q. Wang, J. Wang, and H.-T. Wang. *High-efficiency continuous-wave Raman conversion with a $BaWO_4$ Raman crystal*. Optics letters **34**(11), 1687 (2009).

[79] V. Orlovich, V. Burakevich, A. Grabtchikov, V. Lisinetskii, A. Demidovich, H. Eichler, and P. Turpin. *Continuous-wave intracavity Raman generation in $PbWO_4$ crystal in the $Nd : YVO_4$ laser*. Laser Physics Letters **3**(2), 71 (2005).

[80] L. Fan, Y. Fan, Y. Duan, Q. Wang, H. Wang, G. Jia, and C. Tu. *Continuous-wave intracavity Raman laser at 1179.5 nm with $SrWO_4$ Raman crystal in diode-end-pumped $Nd : YVO_4$ laser*. Applied Physics B **94**(4), 553 (2009).

[81] A. Demidovich, A. Grabtchikov, V. Lisinetskii, V. Burakevich, V. Orlovich, and W. Kiefer. *Continuous-wave Raman generation in a diode-pumped $Nd^{3+} : KGd(WO_4)_2$ laser*. Optics letters **30**(13), 1701 (2005).

[82] V. Burakevich, V. Lisinetskii, A. Grabtchikov, A. Demidovich, V. Orlovich, and V. Matrosov. *Diode-pumped continuous-wave $Nd : YVO_4$ laser with self-frequency Raman conversion*. Applied Physics B **86**(3), 511 (2007).

[83] K. S. Repasky, L. Meng, J. K. Brasseur, J. L. Carlsten, and R. C. Swanson. *High-efficiency, continuous-wave Raman lasers*. JOSA B **16**(5), 717 (1999).

[84] J. K. Brasseur, R. F. Teehan, P. A. Roos, B. Soucy, D. K. Neumann, and J. L. Carlsten. *High-power deuterium Raman laser at 632 nm*. Applied optics **43**(5), 1162 (2004).

[85] P. Roos, J. Brasseur, and J. Carlsten. *Diode-pumped nonresonant continuous-wave Raman laser in H_2 with resonant optical feedback stabilization*. Optics letters **24**(16), 1130 (1999).

[86] O. Kitzler, A. McKay, D. J. Spence, and R. P. Mildren. *Modelling and optimization of continuous-wave external cavity Raman lasers*. Optics express **23**(7), 8590 (2015).

[87] O. Kitzler, A. McKay, and R. P. Mildren. *Continuous-wave wavelength conversion for high-power applications using an external cavity diamond Raman laser*. Optics letters **37**(14), 2790 (2012).

[88] V. G. Savitski, I. Friel, J. E. Hastie, M. D. Dawson, D. Burns, and A. J. Kemp. *Characterization of single-crystal synthetic diamond for multi-watt continuous-wave Raman lasers*. Quantum Electronics, IEEE Journal of **48**(3), 328 (2012).

[89] W. Lubeigt, G. M. Bonner, J. E. Hastie, M. D. Dawson, D. Burns, and A. J. Kemp. *An intra-cavity Raman laser using synthetic single-crystal diamond*. Optics express **18**(16), 16765 (2010).

[90] W. Lubeigt, V. G. Savitski, G. M. Bonner, S. L. Geoghegan, I. Friel, J. E. Hastie, M. D. Dawson, D. Burns, and A. J. Kemp. *1.6 W continuous-wave Raman laser using low-loss synthetic diamond*. Optics express **19**(7), 6938 (2011).

[91] D. C. Parrotta, A. J. Kemp, M. D. Dawson, and J. E. Hastie. *Tunable continuous-wave diamond Raman laser*. Optics express **19**(24), 24165 (2011).

[92] R. J. Williams, J. Nold, M. Strecker, O. Kitzler, A. McKay, T. Schreiber, and R. P. Mildren. *Efficient Raman frequency conversion of high-power fiber lasers in diamond*. Laser & Photonics Reviews **9**(4), 405 (2015).

[93] R. J. Williams, O. Kitzler, A. McKay, and R. P. Mildren. *Investigating diamond Raman lasers at the 100 W level using quasi-continuous-wave pumping*. Optics letters **39**(14), 4152 (2014).

[94] E. Ammann. *Simultaneous stimulated Raman scattering and optical frequency mixing in lithium iodate*. Applied Physics Letters **34**(12), 838 (1979).

[95] P. Dekker, H. M. Pask, and J. A. Piper. *All-solid-state 704 mW continuous-wave yellow source based on an intracavity, frequency-doubled crystalline Raman laser*. Optics letters **32**(9), 1114 (2007).

[96] H. Pask, P. Dekker, R. Mildren, D. Spence, and J. Piper. *Wavelength-versatile visible and UV sources based on crystalline Raman lasers*. Progress in Quantum Electronics **32**(3), 121 (2008).

[97] A. J. Lee, H. M. Pask, J. A. Piper, H. Zhang, and J. Wang. *An intracavity, frequency-doubled $BaWO_4$ Raman laser generating multi-watt continuous-wave, yellow emission*. Optics express **18**(6), 5984 (2010).

[98] Y. Lü, W. Cheng, Z. Xiong, J. Lu, L. Xu, G. Sun, and Z. Zhao. *Efficient CW laser at 559 nm by intracavity sum-frequency mixing in a self-Raman $Nd : YVO_4$ laser under direct 880 nm diode laser pumping*. Laser Physics Letters **7**(11), 787 (2010).

[99] Y. Bu, C. Tan, and N. Chen. *Continuous-wave yellow light source at 579 nm based on intracavity frequency-doubled $Nd : YLF/SrWO_4/LBO$ Raman laser*. Laser Physics Letters **8**(6), 439 (2011).

[100] A. Kananovich, A. Demidovich, M. Danailov, A. Grabtchikov, and V. Orlovich. *All-solid-state quasi-CW yellow laser with intracavity self-Raman conversion and sum frequency generation*. Laser Physics Letters **7**(8), 573 (2010).

[101] A. J. Lee, D. J. Spence, J. A. Piper, and H. M. Pask. *A wavelength-versatile, continuous-wave, self-Raman solid-state laser operating in the visible*. Optics express **18**(19), 20013 (2010).

[102] X. Li, A. J. Lee, H. M. Pask, J. A. Piper, and Y. Huo. *Efficient, miniature, cw yellow source based on an intracavity frequency-doubled $Nd : YVO_4$ self-Raman laser*. Optics letters **36**(8), 1428 (2011).

[103] W. Liang, X. Zhang, and J. Xia. *Efficient continuouswave laser at 560 nm by intracavity frequency summation of fundamental and first-stokes wavelengths in a $Nd : YVO_4 - BaWO_4$ Raman laser*. Laser Physics **21**(4), 667 (2011).

[104] J. Lin and H. Pask. *Nd : $GdVO_4$ self-Raman laser using double-end polarised pumping at 880 nm for high power infrared and visible output*. Applied Physics B **108**(1), 17 (2012).

[105] J. Jakutis-Neto, J. Lin, N. U. Wetter, and H. Pask. *Continuous-wave watt-level Nd : YLF/KGW Raman laser operating at near-IR, yellow and lime-green wavelengths*. Optics express **20**(9), 9841 (2012).

[106] Y. Lü, X. Zhang, S. Li, J. Xia, W. Cheng, and Z. Xiong. *All-solid-state cw sodium D_2 resonance radiation based on intracavity frequency-doubled self-Raman laser operation in double-end diffusion-bonded Nd^{3+} : $LuVO_4$ crystal*. Optics letters **35**(17), 2964 (2010).

[107] D. C. Parrotta, A. J. Kemp, M. D. Dawson, and J. E. Hastie. *Multiwatt, continuous-wave, tunable diamond Raman laser with intracavity frequency-doubling to the visible region*. Selected Topics in Quantum Electronics, IEEE Journal of **19**(4), 1400108 (2013).

[108] R. Mildren and J. Piper. *Increased wavelength options in the visible and ultraviolet for Raman lasers operating on dual Raman modes*. Optics express **16**(5), 3261 (2008).

[109] R. P. Mildren, H. Ogilvy, and J. A. Piper. *Solid-state Raman laser generating discretely tunable ultraviolet between 266 and 320 nm*. Optics letters **32**(7), 814 (2007).

[110] R. P. Mildren, J. E. Butler, and J. R. Rabeau. *CVD-diamond external cavity Raman laser at 573 nm*. Optics express **16**(23), 18950 (2008).

[111] R. Balmer, J. Brandon, S. Clewes, H. Dhillon, J. Dodson, I. Friel, P. Inglis, T. Madgwick, M. Markham, T. Mollart, N. Perkins, S. GA, D. Twitchen, A. Whitehead, J. Wilman, and S. Woollard. *Chemical vapour deposition synthetic diamond: materials, technology and applications*. Journal of Physics: Condensed Matter **21**(36), 364221 (2009).

[112] F. Van Loon, A. J. Kemp, A. J. Maclean, S. Calvez, J.-M. Hopkins, J. E. Hastie, M. D. Dawson, and D. Burns. *Intracavity diamond heatspreaders in lasers: the effects of birefringence*. Optics express **14**(20), 9250 (2006).

[113] D. Douglas-Hamilton, E. Hoag, and J. Seitz. *Diamond as a high-power-laser window*. JOSA **64**(1), 36 (1974).

[114] B. J. Hausmann, I. Bulu, P. Deotare, M. McCutcheon, V. Venkataraman, M. Markham, D. Twitchen, and M. Loncar. *Integrated high-quality factor optical resonators in diamond*. Nano letters **13**(5), 1898 (2013).

[115] B. J. Hausmann, T. M. Babinec, J. T. Choy, J. S. Hodges, S. Hong, I. Bulu, A. Yacoby, M. D. Lukin, and M. Lončar. *Single-color centers implanted in diamond nanostructures*. New Journal of Physics **13**(4), 045004 (2011).

[116] R. P. Mildren, A. Sabella, O. Kitzler, D. J. Spence, and A. M. McKay. *Diamond Raman laser design and performance*. Optical Engineering of Diamond pp. 239–276 (2013).

[117] Y. Romanyuk. *Liquid-phase epitaxy of doped $KY(WO_4)_2$ layers for waveguide lasers* (2005).

[118] P. Loiko, K. Yumashev, N. Kuleshov, and A. Pavlyuk. *Thermo-optical properties of pure and Yb-doped monoclinic $KY(WO4)_2$ crystals*. Applied Physics B **106**(3), 663 (2012).

[119] R. P. Mildren. *Intrinsic optical properties of diamond*. Optical Engineering of Diamond pp. 1–34 (2013).

[120] A. Sabella, D. J. Spence, and R. P. Mildren. *Pump–Probe Measurements of the Raman Gain Coefficient in Crystals Using Multi − Longitudinal − Mode Beams*. IEEE Journal of Quantum Electronics **51**(12), 1 (2015).

[121] V. G. Savitski, S. Reilly, and A. J. Kemp. *Steady-state Raman gain in diamond as a function of pump wavelength*. IEEE Journal of Quantum Electronics **49**(2), 218 (2013).

[122] V. Savitski, D. Burns, and A. Kemp. *Low-loss synthetic single-crystal diamond: Raman gain measurement and high power Raman laser at 1240 nm*. In *The European Conference on Lasers and Electro-Optics*, p. CA12_2 (Optical Society of America, 2011).

[123] I. Friel. *Optical quality diamond grown by chemical vapor deposition*. Optical engineering of diamond pp. 35–69 (2013).

[124] A. Sabella, J. A. Piper, and R. P. Mildren. *1240 nm diamond Raman laser operating near the quantum limit*. Optics letters **35**(23), 3874 (2010).

[125] A. Sabella, J. A. Piper, and R. P. Mildren. *Efficient conversion of a 1.064 μm Nd : YAG laser to the eye-safe region using a diamond Raman laser*. Optics express **19**(23), 23554 (2011).

[126] R. Loudon. *The Raman effect in crystals*. Advances in Physics **13**(52), 423 (1964).

[127] O. Kitzler. *External cavity diamond Raman lasers for high-power continuous-wave beam conversion*. Ph.D. thesis, Macquarie University (2014).

[128] F. Cerdeira, C. Buchenauer, F. H. Pollak, and M. Cardona. *Stress-induced shifts of first-order Raman frequencies of diamond-and zinc-blende-type semiconductors*. Physical Review B **5**(2), 580 (1972).

[129] E. Anastassakis, A. Cantarero, and M. Cardona. *Piezo-Raman measurements and anharmonic parameters in silicon and diamond*. Physical Review B **41**(11), 7529 (1990).

[130] Y. Von Kaenel, J. Stiegler, J. Michler, and E. Blank. *Stress distribution in heteroepitaxial chemical vapor deposited diamond films*. Journal of applied physics **81**(4), 1726 (1997).

[131] I. De Wolf. *Relation between Raman frequency and triaxial stress in Si for surface and cross-sectional experiments in microelectronics components*. Journal of Applied Physics **118**(5), 053101 (2015).

[132] M. Grimsditch, E. Anastassakis, and M. Cardona. *Effect of uniaxial stress on the zone-center optical phonon of diamond*. Physical Review B **18**(2), 901 (1978).

[133] J. W. Ager III and M. D. Drory. *Quantitative measurement of residual biaxial stress by Raman spectroscopy in diamond grown on a Ti alloy by chemical vapor deposition*. Physical Review B **48**(4), 2601 (1993).

[134] A. Crisci, F. Baillet, M. Mermoux, G. Bogdan, M. Nesládek, and K. Haenen. *Residual strain around grown-in defects in CVD diamond single crystals: A 2D and 3D Raman imaging study*. physica status solidi (a) **208**(9), 2038 (2011).

[135] K. E. Bennet, K. H. Lee, J. R. Tomshine, E. M. Sundin, J. N. Kruchowski, W. G. Durrer, B. M. Manciu, A. Kouzani, and F. S. Manciu. *Raman microscopic analysis of internal stress in boron-doped diamond*. Materials **8**(5), 2782 (2015).

[136] H. Boppart, J. Van Straaten, and I. F. Silvera. *Raman spectra of diamond at high pressures*. Physical Review B **32**(2), 1423 (1985).

[137] E. Di Liscia, F. Alvarez, E. Burgos, E. Halac, H. Huck, and M. Reinoso. *Stress analysis on single-crystal diamonds by Raman spectroscopy 3D mapping*. Materials Sciences and Applications **4**, 191 (2013).

[138] C. Bradac, T. Gaebel, and J. R. Rabeau. *Nitrogen-vacancy color centers in diamond: Properties, synthesis, and applications*. Optical Engineering of Diamond pp. 143–175 (2013).

[139] P. Martineau, M. Gaukroger, R. Khan, and D. Evans. *Effect of steps on dislocations in CVD diamond grown on {001} substrates*. physica status solidi (c) **6**(8), 1953 (2009).

[140] N. Davies, R. Khan, P. Martineau, M. Gaukroger, D. Twitchen, and H. Dhillon. *Effect of off-axis growth on dislocations in CVD diamond grown on {001} substrates*. In *Journal of Physics: Conference Series*, vol. 281, p. 012026 (IOP Publishing, 2011).

[141] H. Pinto and R. Jones. *Theory of the birefringence due to dislocations in single crystal CVD diamond*. Journal of Physics: Condensed Matter **21**(36), 364220 (2009).

[142] P. Martineau, M. Gaukroger, K. Guy, S. Lawson, D. Twitchen, I. Friel, J. Hansen, G. Summerton, T. Addison, and R. Burns. *High crystalline quality single crystal chemical vapour deposition diamond*. Journal of Physics: Condensed Matter **21**(36), 364205 (2009).

[143] M. Gaukroger, P. Martineau, M. Crowder, I. Friel, S. Williams, and D. Twitchen. *X-ray topography studies of dislocations in single crystal CVD diamond*. Diamond and Related materials **17**(3), 262 (2008).

[144] J. E. Butler and I. Oleynik. *A mechanism for crystal twinning in the growth of diamond by chemical vapour deposition*. Philosophical Transactions of the Royal Society of London A: Mathematical, Physical and Engineering Sciences **366**(1863), 295 (2008).

[145] I. Friel, S. L. Geoghegan, D. J. Twitchen, and G. A. Scarsbrook. *Development of high quality single crystal diamond for novel laser applications*. In *Security+ Defence*, pp. 783819–783819 (International Society for Optics and Photonics, 2010).

[146] A. Glazer, J. Lewis, and W. Kaminsky. *An automatic optical imaging system for birefringent media*. In *Proceedings of the Royal Society of London A: Mathematical, Physical and Engineering Sciences*, vol. 452, pp. 2751–2765 (The Royal Society, 1996).

[147] M. Born and E. Wolf. *Principles of optics: electromagnetic theory of propagation, interference and diffraction of light* (CUP Archive, 2000).

[148] I. Wood and A. Glazer. *Ferroelastic phase transition in $BiVO_4$ I. birefringence measurements using the rotating-analyser method*. Journal of Applied Crystallography **13**(3), 217 (1980).

[149] W. Kaminsky, K. Claborn, and B. Kahr. *Polarimetric imaging of crystals*. Chemical Society Reviews **33**(8), 514 (2004).

[150] B. Wang. *Linear birefringence measurement instrument using two photoelastic modulators*. Optical Engineering **41**(5), 981 (2002).

[151] O. Arteaga, J. Freudenthal, B. Wang, and B. Kahr. *Mueller matrix polarimetry with four photoelastic modulators: theory and calibration*. Applied optics **51**(28), 6805 (2012).

[152] B. Wang and T. C. Oakberg. *A new instrument for measuring both the magnitude and angle of low level linear birefringence*. Review of scientific instruments **70**(10), 3847 (1999).

[153] B. B. Wang. *Measurement of circular and linear birefringence in chiral media and optical materials using the photoelastic modulator*. In *Photonics East (ISAM, VVDC, IEMB)*, pp. 294–302 (International Society for Optics and Photonics, 1999).

[154] H. Hurwitz and R. C. Jones. *A New Calculus for the Treatment of Optical SystemsII. Proof of Three General Equivalence Theorems*. JOSA **31**(7), 493 (1941).

[155] O. Kvasnyuk, B. Zapeka, Y. Vasylkiv, M. Kostyrko, and R. Vlokh. *Symmetry conditions for studying torsion stress-induced gradient piezogyration*. Ukrainian journal of physical optics (14,âĎŰ 2), 91 (2013).

[156] L. Srinath and A. Sarma. *Effects of stress-induced optical activity in photoelasticity*. Journal of Physics D: Applied Physics **5**(5), 883 (1972).

[157] I. Friel, S. Clewes, H. Dhillon, N. Perkins, D. Twitchen, and G. Scarsbrook. *Control of surface and bulk crystalline quality in single crystal diamond grown by chemical vapour deposition*. Diamond and Related Materials **18**(5), 808 (2009).

[158] H. Kagi, S. Odake, S. Fukura, and D. Zedgenizov. *Raman spectroscopic estimation of depth of diamond origin: technical developments and the application*. Russian Geology and Geophysics **50**(12), 1183 (2009).

[159] K. Lee, B. J. Sussman, J. Nunn, V. Lorenz, K. Reim, D. Jaksch, I. Walmsley, P. Spizzirri, and S. Prawer. *Comparing phonon dephasing lifetimes in diamond using transient coherent ultrafast phonon spectroscopy*. Diamond and Related Materials **19**(10), 1289 (2010).

[160] K. Ishioka, M. Hase, M. Kitajima, and H. Petek. *Coherent optical phonons in diamond*. Applied physics letters **89**(23), 231916 (2006).

[161] J. F. Nye. *Physical properties of crystals* (1957).

[162] A. G. Shtukenberg, I. O. Punin, and B. Kahr. *Optically anomalous crystals* (Springer, 2007).

[163] S. Ganesan, A. Maradudin, and J. Oitmaa. *A lattice theory of morphic effects in crystals of the diamond structure*. Annals of Physics **56**(2), 556 (1970).

[164] E. Anastassakis. *Selection rules of Raman scattering by optical phonons in strained cubic crystals*. Journal of applied physics **82**(4), 1582 (1997).

[165] E. Anastassakis, A. Pinczuk, E. Burstein, F. Pollak, and M. Cardona. *Effect of static uniaxial stress on the Raman spectrum of silicon*. solid state Communications **8**(2), 133 (1970).

[166] P. Hess. *The mechanical properties of various chemical vapor deposition diamond structures compared to the ideal single crystal*. Journal of Applied Physics **111**(5), 051101 (2012).

[167] M. P. Murdough and C. A. Denman. *Mode-volume and pump-power limitations in injection-locked TEM_{00} Nd : YAG rod lasers*. Applied optics **35**(30), 5925 (1996).

[168] J. Frougier, G. Baili, I. Sagnes, D. Dolfi, J.-M. George, and M. Alouini. *Accurate measurement of the residual birefringence in VECSEL: Towards understanding of the polarization behavior under spin-polarized pumping*. Optics express **23**(8), 9573 (2015).

[169] G. Bouwmans, B. Segard, P. Glorieux, P. Khandokhin, N. Milovsky, and E. Y. Shirokov. *Polarization dynamics of longitudinally monomode bipolarized microchip solid-state lasers*. Radiophysics and quantum electronics **47**(10-11), 729 (2004).

[170] N. N. Nath. *The dynamical theory of the diamond lattice. i*. In *Proceedings of the Indian Academy of Sciences-Section A*, vol. 1, pp. 333–345 (Springer, 1934).

[171] Q. Zheng, J.-Y. Wang, and L. Zhao. *2.23 W diode-pumped Nd : YVO_4/LBO Laser at 671nm*. Optics & Laser Technology **36**(6), 485 (2004).

[172] F. Jia. *High power continues wave laser diode array end pumped Nd : YAG/LBO red lasers operated at 669 nm and 659 nm*. Laser physics **20**(7), 1559 (2010).

[173] Y. Inoue, S. Konno, T. Kojima, and S. Fujikawa. *High-power red beam generation by frequency-doubling of a Nd : YAG laser*. IEEE journal of quantum electronics **35**(11), 1737 (1999).

[174] A. Härkönen, J. Rautiainen, M. Guina, J. Konttinen, P. Tuomisto, L. Orsila, M. Pessa, and O. G. Okhotnikov. *High power frequency doubled GaInNAs semiconductor disk laser emitting at 615 nm*. Optics express **15**(6), 3224 (2007).

[175] A. Rantamäki, A. Sirbu, A. Mereuta, E. Kapon, and O. G. Okhotnikov. *3 W of 650 nm red emission by frequency doubling of wafer-fused semiconductor disk laser*. Optics express **18**(21), 21645 (2010).

[176] A. Richter, E. Heumann, G. Huber, V. Ostroumov, and W. Seelert. *Power scaling of semiconductor laser pumped praseodymium-lasers*. Optics express **15**(8), 5172 (2007).

[177] T. Gün, P. Metz, and G. Huber. *Power scaling of laser diode pumped Pr^{3+} : $LiYF_4$ cw lasers: efficient laser operation at 522.6 nm, 545.9 nm, 607.2 nm, and 639.5 nm*. Optics letters **36**(6), 1002 (2011).

[178] P. W. Metz, F. Reichert, F. Moglia, S. Müller, D.-T. Marzahl, C. Kränkel, and G. Huber. *High-power red, orange, and green Pr^{3+} : $LiYF_4$ lasers*. Optics letters **39**(11), 3193 (2014).

[179] T. Schwarzbäck, M. Eichfelder, W.-M. Schulz, R. Roßbach, M. Jetter, and P. Michler. *Short wavelength red-emitting AlGaInP-VECSEL exceeds 1.2 W continuous-wave output power*. Applied Physics B **102**(4), 789 (2011).

[180] J. E. Hastie, S. Calvez, M. D. Dawson, T. Leinonen, A. Laakso, J. Lyytikäinen, and M. Pessa. *High power CW red VECSEL with linearly polarized TEM 00 output beam*. Optics Express **13**(1), 77 (2005).

[181] J. Osinski, B. Lu, H. Zhao, and B. Schmitt. *High power continuous-wave operation of 630 nm-band laser diode arrays*. Electronics Letters **34**(24), 2336 (1998).

[182] Castech Inc. URL http://www.castech-us.com/caslbo.htm.

[183] S. C. Tidwell, J. F. Seamans, M. S. Bowers, and A. K. Cousins. *Scaling CW diode-end-pumped Nd : YAG lasers to high average powers*. Quantum Electronics, IEEE Journal of **28**(4), 997 (1992).

[184] S. Chénais, F. Druon, S. Forget, F. Balembois, and P. Georges. *On thermal effects in solid-state lasers: The case of ytterbium-doped materials*. Progress in Quantum Electronics **30**(4), 89 (2006).

[185] M. S. Liu, L. A. Bursill, S. Prawer, and R. Beserman. *Temperature dependence of the first-order Raman phonon line of diamond*. Physical Review B **61**(5), 3391 (2000).

[186] N. P. Barnes and J. A. Williams-Byrd. *Average power effects in parametric oscillators and amplifiers*. JOSA B **12**(1), 124 (1995).

[187] A. Kokh, N. Kononova, G. Mennerat, P. Villeval, S. Durst, D. Lupinski, V. Vlezko, and K. Kokh. *Growth of high quality large size LBO crystals for high energy second harmonic generation*. Journal of Crystal Growth **312**(10), 1774 (2010).

[188] R. Royon, J. Lhermite, L. Sarger, and E. Cormier. *High power, continuous-wave ytterbium-doped fiber laser tunable from 976 to 1120 nm*. Optics express **21**(11), 13818 (2013).

[189] T. Gün, P. Metz, and G. Huber. *Efficient continuous wave deep ultraviolet Pr^{3+} : $LiYF_4$ laser at 261.3 nm*. Applied Physics Letters **99**(18), 181103 (2011).

[190] D. J. Berkeland, F. C. Cruz, and J. C. Bergquist. *Sum-frequency generation of continuous-wave light at 194 nm*. Applied optics **36**(18), 4159 (1997).

[191] S. Bourzeix, B. De Beauvoir, F. Nez, F. De Tomasi, L. Julien, and F. Biraben. *Ultraviolet light generation at 205 nm by two frequency doubling steps of a cw titanium-sapphire laser*. Optics communications **133**(1), 239 (1997).

[192] Y. Kaneda, J. Yarborough, L. Li, N. Peyghambarian, L. Fan, C. Hessenius, M. Fallahi, J. Hader, J. V. Moloney, Y. Honda, M. Nishioka, Y. Shimizu, K. Miyazono, H. Shimatani, M. Yoshimura, Y. Mori, Y. Kitaoka, and T. Sasaki. *Continuous-wave all-solid-state 244 nm deep-ultraviolet laser source by fourth-harmonic generation of an optically pumped semiconductor laser using $CsLiB_6O_{10}$ in an external resonator*. Optics letters **33**(15), 1705 (2008).

[193] Y. Taira. *High-power continuous-wave ultraviolet generation by frequency doubling of an argon laser*. Japanese journal of applied physics **31**(6A), L682 (1992).

[194] B. Wellmann, D. J. Spence, and D. W. Coutts. *Tunable Continuous Wave Ultraviolet Cerium LiCAF Lasers*. In *Advanced Solid State Lasers*, pp. ATh2A–47 (Optical Society of America, 2014).

[195] O. Kitzler, B. Wellmann, D. Coutts, and D. Spence. *Continuous-wave ultraviolet Ce : LiCAF laser*. In *Advanced Solid State Lasers*, pp. ATh3A–7 (Optical Society of America, 2015).

[196] G. S. He. *Stimulated scattering effects of intense coherent light*. Progress in Optics **53**, 201 (2009).

[197] K.-c. Liu. *Frequency doubling a laser beam by using intracavity type II phase matching* (1986). US Patent 4,618,957.

[198] E. Granados, D. J. Spence, and R. P. Mildren. *Deep ultraviolet diamond Raman laser*. Optics express **19**(11), 10857 (2011).

[199] Castech Inc. URL http://www.castech.com/products_detail/&productId=100.html.

[200] C. Chen, S. Luo, X. Wang, G. Wang, X. Wen, H. Wu, X. Zhang, and Z. Xu. *Deep* UV *nonlinear optical crystal:* $RbBe_2(BO_3)F_2$. JOSA B **26**(8), 1519 (2009).

[201] L. Kang, S. Luo, H. Huang, T. Zheng, Z. Lin, and C. Chen. *Ab initio studies on the optical effects in the deep ultraviolet nonlinear optical crystals of the* $KBe_2BO_3F_2$ *family*. Journal of Physics: Condensed Matter **24**(33), 335503 (2012).

[202] R. Riedel, J. Rothhardt, K. Beil, B. Gronloh, A. Klenke, H. Höppner, M. Schulz, U. Teubner, C. Kränkel, J. Limpert, A. Tünnermann, M. J. Prandolini, and F. Tavella. *Thermal properties of borate crystals for high power optical parametric chirped-pulse amplification*. Optics express **22**(15), 17607 (2014).

[203] O. Lux, S. Sarang, O. Kitzler, D. J. Spence, and R. P. Mildren. *Intrinsically stable high-power single longitudinal mode laser using spatial hole burning free gain*. Optica **3**(8), 876 (2016).

[204] T. Nicholson, S. Campbell, R. Hutson, G. Marti, B. Bloom, R. McNally, W. Zhang, M. Barrett, M. Safronova, G. Strouse, W. Tew, and J. Ye. *Systematic evaluation of an atomic clock at* 2×10^{-18} *total uncertainty*. Nature communications **6** (2015).